



UNIVERSIDAD DEL PAIS VASCO

# Analysis and Control of Transient Spectra Using Time-Dependent Density Functional Theory

by

Jessica Walkenhorst

**Supervisors:**

Prof. Angel Rubio

Dr. Alberto Castro

A thesis submitted in partial fulfillment for the  
degree of Doctor of Philosophy

in the

Faculty of Physics, Chemistry and Materials Science  
Department of Materials Physics

December 2015



---

*“To my parents”*





# Acknowledgements

---

*“If I have seen further it is by standing on the shoulders of giants.”*

*- Sir Isaac Newton*

*“Don’t cry because it’s over, smile because it happened.”*

*- Dr. Seuss*

---

First and foremost I would like to thank Angel Rubio and Alberto Castro for being my supervisors during my PhD. Without their guidance, advice and support, none of this work would have been possible. Thank you for letting me see further. Thanks to Alberto also for letting me stay in his group my first month in Spain and helping me with all the paperwork at a time, when everything, that Spanish people said still sounded French to me. Also for extensive proof reading.

Thanks to my collaborators Umberto De Giovannini in San Sebastian, Heiko Appel in Berlin and Nicole Helbig in Jülich for their time, ideas and fruitful discussions. Special thanks go to Heiko for teaching me that computers are friends, not enemies. Thanks to Heiko and Nicole also for inviting me to spend time at their groups and to the people in their groups, especially Tanja Dimitrov and Johannes Flick for making this time not only productive, but also enjoyable.

Thank you to all my friends and colleagues in the NanoBio Spectroscopy group, young and old, permanent or still or there way, still here or already gone: The last six years would not have been the same without you.

Thanks to Cristina Garcia and Cecilia Benguria for their neverending help with fighting the paper-dragon.

---

Thank you to the people from the San Sebastian Judo Club: to Iñigo Matxain and Gorka Sagastume, for helping me to rediscover my love for the martial arts and to my fellow judokas for their companionship and many exchanged bruises. Special thanks to Aitzol Yubero, Alberto Neves, Jorge Iparragirre and Jorge Reverendo: I will miss our combats.

Thanks to my friends here, there, from the past, the present and (hopefully) the future: Marius Wanko, Johanna Fuks, Aina Casaponsa, Juliana Martinez, Marisa Unrein, Silvina Romero, Isabel Murillo to name just a few. May our friendships last.

Thanks to my flatmates during my time in San Sebastian, but special thanks to two of them: JessMex and Saio, without you, this house ain't no home.

I would also like to thank Edmund for his love, support and patience over the past 4 years. Thanks also to Crispin Barnes for providing me with a place to work, when being at Cambridge.

Last, but not least and most importantly, I would like to thank my mother, my brother, my grandfather and all the rest of my family, old and new, for their love and support. Thank you for being the harbour that I can always come back to.

## List of Publications

- **Simulating Pump-Probe Photoelectron and Absorption Spectroscopy on the Attosecond Timescale with Time-Dependent Density Functional Theory**

(The article was selected for the inner cover of the journal.)

Umberto De Giovannini, Gustavo Brunetto, Alberto Castro, Jessica Walkenhorst, Angel Rubio, ChemPhysChem **14** (7), 1363-1376 (2013)

- **Tailored Pump & Probe Transient Spectroscopy with Time-Dependent Density-Functional Theory: Controlling Absorption Spectra**

Jessica Walkenhorst, Umberto De Giovannini, Alberto Castro, Angel Rubio, submitted to EPJB (arXiv: 1601.04544)



# Abstract

Attosecond-transient absorption spectroscopy (TAS) and attosecond time-resolved photo-electron spectroscopy (TRPES) based on pump-probe setups, in which a system response (absorption or electron emission) to a probe pulse is measured, have recently become an experimental reality due to the availability of ultra-fast pulsed laser sources. These experiments follow the electronic motion at its natural time-scale, allowing the characterization of electronic excited states and transitions while neglecting the influence of the nuclear degrees of freedom.

Molecular absorption and photo-electron spectra can be efficiently simulated with real-time time-dependent density-functional theory (TDDFT), which is normally used for the description of systems in their ground state. In this thesis, I demonstrate how this technique can be extended to study time-resolved pump-probe experiments. I show how the extra degrees of freedom (pump pulse duration, intensity, frequency, and time-delay), which are absent in a conventional steady state experiment, provide additional information about the electronic structure and the dynamics, which can be used to improve a system characterization.

In addition to gaining insight by numerical simulations, a microscopical, theoretical understanding of the processes would be useful. It is well known, that photo absorption spectra of systems at equilibrium can be written in terms of the dipole-dipole response function. In pump-driven systems, the photo-absorption spectrum is not an intrinsic property of the system under investigation, but additionally depends on the shape of the probe. In this thesis, I reexamine the Lehmann representation of the response function of a pump-driven system in the non-overlapping regime, deriving some general properties of the excited state spectra, including position and shape of their resonance peaks. I demonstrate how this Lehmann representation can be used to understand laser-induced line shape changes.

Measurement and control of ultrafast processes are inherently intertwined. In this work,

---

I assess the possibility of using tailored pumps in order to enhance (or reduce) some given features of the probe absorption (for example, absorption in the visible range of otherwise transparent samples). This type of manipulation of the system response could be helpful for its full characterization, since it would allow us to visualize transitions that are obscured when using un-shaped pulses. In order to investigate this possibility, I firstly combine the derived Lehmann representation with a simple numerical model of the Hydrogen atom to show how Hydrogen can be manipulated to loose its transparency in the visible. I then proceed to investigate the feasibility of using time-dependent density-functional theory as a means to implement, theoretically, this absorption-optimization idea for more complex atoms or molecules.

# Contents

<b>Acknowledgements</b>	<b>v</b>
<b>List of Publications</b>	<b>vii</b>
<b>Abstract</b>	<b>ix</b>
<b>List of Figures</b>	<b>xv</b>
<b>List of Tables</b>	<b>xxvii</b>
<b>Acronyms</b>	<b>xxix</b>
<b>1. Introduction</b>	<b>1</b>
<b>2. Theory</b>	<b>17</b>
2.1. Born-Oppenheimer and Clamped-Ion Approximation . . . . .	22
2.2. Linear Response Theory . . . . .	24
2.2.1. General Time-Dependent Linear Response Theory . . . . .	25
2.2.2. Frequency Dependent Response Function and Generalized Lehmann Representation . . . . .	28
2.2.3. Kramers–Kronig Relations . . . . .	33
2.2.4. Spectroscopic Observables . . . . .	34
2.2.5. Properties of the Generalized Lehmann Representation . . . . .	35
2.3. Resonance Line Shapes . . . . .	38
2.4. Time-Dependent Density Functional Theory for Response Calculations . .	42
2.4.1. Static Density Functional Theory . . . . .	43
2.4.1.1. The Energy Functionals . . . . .	46
2.4.1.2. Pseudopotentials . . . . .	48
2.4.2. Time-Dependent Density Functional Theory . . . . .	48

2.4.3.	Time-Resolved Photoabsorption Spectroscopy - The Density-Density Response . . . . .	49
2.4.4.	Kohn-Sham Linear Response Function . . . . .	52
2.4.5.	Absorption Spectra from the Time-Evolution . . . . .	53
2.4.6.	Time-Resolved Photoelectron Spectroscopy – The Mask Method . .	54
2.5.	Few-Electron Systems and Model-Hamiltonians . . . . .	58
2.5.1.	Model Hamiltonians . . . . .	59
2.5.2.	Rabi-Oscillations . . . . .	60
2.5.2.1.	Rabi-Oscillations in Two-Level Systems . . . . .	60
2.5.2.2.	Rabi-like Oscillations in Three-Level Systems . . . . .	61
2.6.	Quantum Optimal Control Theory . . . . .	64
2.6.1.	General Aspects of Quantum Optimal Control Theory . . . . .	65
2.6.2.	Derivation of the Quantum-OCT Equations for the Optimization of Response Functions . . . . .	69
2.6.3.	Derivation of a Gradient-Free Algorithm for Quantum Optimal Control Theory . . . . .	70
2.7.	The Colour Perception of the Human Eye . . . . .	72
<b>3.</b>	<b>Simulating Attosecond Pump-Probe Spectroscopy with TDDFT</b>	<b>75</b>
3.1.	One-dimensional Model Helium . . . . .	77
3.2.	Helium Atom in 3D . . . . .	82
3.2.1.	Transient Absorption Spectroscopy . . . . .	82
3.2.2.	Time-Resolved Photo-Electron Spectroscopy . . . . .	85
3.3.	Ethylene Molecule . . . . .	88
3.3.1.	Transient Absorption Spectroscopy . . . . .	88
3.3.2.	Time-Resolved Photo-Electron Spectroscopy . . . . .	89
3.4.	Conclusions . . . . .	93
<b>4.</b>	<b>Control of Optical Properties – The Case of the Hydrogen Atom</b>	<b>95</b>
4.1.	Excited State Spectroscopy . . . . .	96
4.1.1.	Converting Lorentzians Into Rayleigh Resonances and Viceversa . .	99
4.1.2.	Convergence Tests . . . . .	102
4.1.3.	Transient Absorption Spectroscopy and the Change of Colour . . .	104



4.2. Control . . . . .	108
4.2.1. Equations of Control . . . . .	109
4.2.1.1. Time-independent Envelope Functions . . . . .	109
4.2.1.2. Time-dependent Envelope Functions . . . . .	112
4.2.2. Numerical Example . . . . .	113
4.3. Summary and Conclusion . . . . .	114
<b>5. Control of Optical Properties – Many-Electron Systems</b>	<b>117</b>
5.1. Approach I: Direct Optimization . . . . .	118
5.1.1. One-dimensional Model Hydrogen . . . . .	119
5.1.2. One-dimensional Helium . . . . .	122
5.1.3. One-dimensional Singly-Ionized Beryllium . . . . .	128
5.1.4. Methane . . . . .	129
5.2. Approach II: Spectrum of an Excited Kohn-Sham Orbital . . . . .	138
5.3. Summary and Conclusions . . . . .	143
<b>6. Conclusions and Outlook</b>	<b>147</b>
<b>A. The Downhill-Simplex Algorithm</b>	<b>155</b>
<b>B. The Optimization Procedure - Scheme 1</b>	<b>159</b>
B.1. The Octopus Class . . . . .	160
B.2. The Optimization Class . . . . .	160
B.3. The Main Program . . . . .	162
B.4. Implementation of the Simplex-Downhill - Amoeba or fmin . . . . .	162
B.5. General Comments on the Implementation . . . . .	163
<b>C. Many-Body Tunneling in Exact and Density Functional Theory</b>	<b>165</b>
C.1. Introduction . . . . .	165
C.2. A Simple Donor-Acceptor Many-Body Model . . . . .	166
C.3. Exact calculations . . . . .	168
C.3.1. Tunneling Points From Ionization Potential and Electron Affinity .	171
C.3.2. Energy Corrections . . . . .	173
C.3.3. Three and Four Electrons . . . . .	177
C.3.4. Lineshape of Electronic Transport . . . . .	179

## Contents

---

C.4. Tunneling in Density-Functional Theory . . . . .	183
C.4.1. Tunneling with Different Functionals . . . . .	184
C.4.2. Constructing the Exact KS Potential for Tunneling . . . . .	185
C.4.3. Eigenenergies - Exact vs. DFT . . . . .	189
C.5. Summary . . . . .	190

<b>Bibliography</b>	<b>193</b>
---------------------	------------

# List of Figures

1.1.	Pump-probe spectroscopy setup. The pump pulse triggers the dynamics, and after a certain delay time, the reaction of the system to a probe pulse is measured. Depending on the time-scale, electronic, vibrational and rotational properties can be measured. On the sub-femtosecond time-scale, the electronic-only dynamics can be observed. If we look at time-scales longer than tens or hundreds of femtoseconds, the atomic structure will have time to re-arrange, giving rise to the field of femtochemistry. . . .	4
1.2.	TAS of Krypton ions as obtained by Goulielmakis <i>et al.</i> : The ionization of Krypton can be observed as a function of time. This figure was published as Fig. 2 in Ref. [1]. Copyright © 2010 by the Nature Publishing Group (NPG). . . . .	7
1.3.	(left) Laser controlled amplification of resonant light in the EUV. (A) Spectrum of transmitted EUV light without control laser: The Helium resonant absorption lines can be observed as local minima in an otherwise smoothly varying spectrum centered at a vertical position of 0 mm. (B) Spectrum of transmitted and amplified EUV light in the presence of the control laser. Amplification can be observed exactly at the He resonance positions corresponding to absorption in (A). (right) Transforming asymmetric Fano spectral absorption lines into symmetric Lorentzian absorption peaks in doubly excited He (A, B) and vice versa, from Lorentz to Fano in singly excited He (C, D). This figure is an adaption of Figs. 3 and 4 in Ref. [2]. Copyright © 2013 by the American Association for the Advancement of Science (AAAS). . . . .	12
2.1.	Illustration of the times used in the derivation of the generalized Lehmann representation of the response function. . . . .	31

## LIST OF FIGURES

---

- 2.2. Schematic description of the space partition implemented by the mask method. A mask function (a) is used to implement the spatial partitions (b). In region A (interaction region) the TDKS equations are numerically solved in real space while in B (free propagation region) electrons are evolved analytically as free particles in momentum space. Region C is where  $\varphi_A$  and  $\varphi_B$  overlap. This figure was published as Fig. 1 in our publication [3]. Copyright © 2013 Wiley-VCH Verlag GmbH & Co. KGaA, Weinheim. . . . . 56
  
- 2.3. Gradient-free optimization procedure to optimize the response-function of an excited-state system using the real-time, real-space TDDFT code **octopus**. . . . . 71
  
- 2.4. (left) The CIE standard observer colour matching functions. (right) The CIE 1931 chromaticity diagram (taken from the Encyclopedia Britannica (<http://global.britannica.com/science/tristimulus-system>)). . . . 74
  
  
- 3.1. Out of equilibrium absorption spectrum as function of the pump laser frequency for one-dimensional Helium. The system is driven out of equilibrium by 45 cycle  $\sin^2$  envelope laser pulses of intensity  $I = 5.26 \times 10^{11}$  W/cm<sup>2</sup>, at different carrier frequencies and then probed right after. Maximal response is observed for frequencies close to the first optical transition  $\omega_P = 0.533$  a.u.. . . . . 78
  
- 3.2. Comparison of absorption spectra calculated in different approximations for a one-dimensional Helium model. The filled curves are the spectra for the unperturbed systems while the solid lines are the spectra of the system excited by a laser as in Figure 3.1 resonant with the first allowed optical transition: exact time-dependent Schrödinger equation  $\omega_P = 0.533$  a.u. (in blue), EXX  $\omega_P = 0.549$  a.u. (in red), and LDA  $\omega_P = 0.475$  a.u. (in green). The dashed blue line is the absorption of the system perturbed by a 180 cycle laser and probed at  $t = 30.62$  fs, where the population on the excited state is maximal. The lines have been shifted by a vertical constant to facilitate the comparison between results. . . . . 79

3.3.	Exact population on the ground $ \gamma_0(t) ^2 =  \langle \Psi_0   \Psi(t) \rangle ^2$ (solid lines) and first excited $ \gamma_1(t) ^2 =  \langle \Psi_1   \Psi(t) \rangle ^2$ (dashed lines) states as a function of time for different laser pulses. In red a 45 cycles pulse with parameters as in Figure 3.2, and in blue a longer 180 cycles pulse with the same parameters.	81
3.4.	Comparison of the absorption spectra of unperturbed (filled curve) and perturbed He atom probed at $\tau = 5.32$ fs (solid line) and after the end of the pulse $\tau = 8.68$ fs (dashed line). The spectrum range is below the ionization threshold. The atom is excited by a 45 cycle $\sin^2$ envelope laser pulse polarized along the $x$ -axis with carrier $\omega_P = 0.79$ a.u. resonant with the first optical transition, intensity $I = 2.6 \times 10^{12}$ W/cm <sup>2</sup> .	83
3.5.	Helium transient absorption spectrum scan for different time delays $\tau$ . The pump laser pictured in the upper panel is the same as in Figure 3.4.	84
3.6.	Helium transient photoelectron spectrum in logarithmic scale. The pump laser (upper panel) is the same as in Figure 3.4 and the probe is a 40 cycles trapezoidal laser pulse with 8 cycles ramp, $\omega_p = 1.8$ a.u., $I = 5.4 \times 10^9$ W/cm <sup>2</sup> aligned with the pump pulse.	85
3.7.	Energy- and angular- resolved photoelectron spectra for Helium at fixed delay $\tau = 8.99$ fs. Panel (c) displays a logarithmic scale PES $P(E)$ comparison at fixed delays $\tau = -1.69$ fs (red) and $\tau = 8.99$ fs (green). The other panels depict normalized PADs $P(\theta, \phi, E)$ with polar coordinates referred to axis $z$ at fixed delay $\tau = 8.99$ fs and energy: (a) $E_1 = 0.66$ a.u., (b) $E_2 = 0.88$ a.u., and (d) $E_3 = 1.67$ a.u.. White crosses mark the intersection between the probe polarization axis and the cutting sphere.	87
3.8.	Comparison of the absorption spectra of unperturbed (filled curve) and perturbed (solid line) Ethylene molecule below the ionization threshold. The molecule is excited by a 45 cycle $\sin^2$ envelope laser pulse polarized along the $x$ -axis with carrier frequency $\omega_P = 0.297$ a.u. of intensity $I = 1.38 \times 10^{11}$ W/cm <sup>2</sup> .	89
3.9.	TAS of the Ethylene molecule. The pump laser pictured in the upper panel is the same as in Figure 3.4.	90
3.10.	Logarithmic scale TRPES for C <sub>2</sub> H <sub>4</sub> . The molecule is probed at different delays with a 40 cycles trapezoidal laser pulse with 8 cycles ramp, $\omega_p = 1.8$ a.u. and $I = 5.4 \times 10^9$ W/cm <sup>2</sup> polarized along the $z$ -axis perpendicular to the pump. The pump laser (upper panel) is the same as in Figure 3.9.	91

- 3.11. Angular- and energy-resolved photoelectron spectra for  $C_2H_4$  at two fixed delay times. Panel (a) shows the geometry of the process:  $\mathbf{p}$  indicates the photoelectron direction,  $\mathbf{A}$  is the pump polarization vector, and  $\mathbf{A}_p$  the probe one. Panel (d) shows the logarithmic scale PES  $P(E)$  for  $\tau = -1.69$  fs (red) and  $\tau = 3.63$  fs (green). The other panels depict normalized PADs  $P(\theta, \phi, E)$  at  $\tau = 3.63$  fs and energies marked in (d): (b)  $E_1 = 0.16$  a.u., (c)  $E_2 = 1.37$  a.u. and (e)  $E_3 = 1.67$  a.u.. White marks indicate the position of the probe polarization vector (c), (e) (at the corners) and the pump one (b) on the sphere. . . . . 92
- 4.1. Absorption coefficient  $\bar{\sigma}(\omega)$  of the the state  $\Psi_T = \sqrt{0.4}|2p_z\rangle + \sqrt{0.6}e^{i\varphi}|3p_z\rangle$  for  $\varphi = 0, 1/2\pi, \pi$  and  $3/2\pi$ . The total spectrum (black line) is the sum of the two phase-independent terms  $0.4\bar{\sigma}_{2p_z}$  (red shaded) and  $0.6\bar{\sigma}_{3p_z}$  (blue shaded) coming from the excited state spectra of the respective states multiplied by the absolute values of their expansion coefficients squared plus the phase-dependent interference term  $\bar{\sigma}^{IN}(\omega, \Theta)$  (green dashed line), which is responsible for the change of the spectrum with the delay time  $\tau$ . 100
- 4.2. Average photoabsorption coefficient  $\bar{\sigma}$  of  $|\Psi_T\rangle = \sqrt{0.4}|2p_z\rangle + \sqrt{0.6}|3p_z\rangle$  of Hydrogen. Analytic result including states up to  $n = 9$  (shaded) in comparison to (top) numerical results (solid lines) obtained through the generalized Lehmann representation with numerically obtained eigenenergies and dipole matrix elements for boxes with radii  $r = 30$  (blue),  $r = 45$  (black) and  $r = 60$  a.u. (red) and to (bottom) numerical results obtained through the generalized Lehmann representation (solid line) and through time-propagation (dashed), both in a box with  $r = 60$  a.u.. The shaded blue area indicates the visible range of the spectrum (350 nm - 750 nm). 102
- 4.3. Time-resolved spectrum of the  $\sqrt{0.4}|2p_z\rangle + \sqrt{0.6}|3p_z\rangle$  of Hydrogen. Because the phases of the  $|2p\rangle$  and  $|3p\rangle$  states evolve with different velocities, the spectral weights of each of the peaks changes with time, leading to a time-dependent spectrum with a periodicity of  $T = \frac{2\pi}{\varepsilon_{2p} - \varepsilon_{3p}} \approx 91 a.u.$ . The first 100 eigenstates were included, continuum contributions neglected. . . 105

- 4.4. (top) CIE 1931 colour matching functions  $\bar{x}$ ,  $\bar{y}$  and  $\bar{z}$  and the spectral power distribution of the sun (orange). (center) Average absorption coefficient of  $|\Psi_T\rangle = \sqrt{0.4}|2p_z\rangle + \sqrt{0.6}|3p_z\rangle$  (solid) and the part taken into account in the calculation of the colour (shaded). (bottom) Power distribution of sun light after having passed through a gas of atoms in the state  $|\Psi_T\rangle$  with a pathlength of  $l = 1$  a.u. (blue) and  $l = 5$  a.u. (pink). . . . . 106
- 4.5. (top): Colour associated to the time-dependent spectrum of the  $\sqrt{0.4}|2p_z\rangle + \sqrt{0.6}|3p_z\rangle$  state of Hydrogen for a path in the gas of length  $l = 1$  a.u. (left) and of  $l = 5$  a.u. (right). From left to right, from top to bottom each square shows the colour at a time  $\Delta t = 1.01$  a.u. later than the previous one. (bottom) The colours above shown in a chromaticity diagram, illustrating the periodic changes in colour with time. (inset) Time-averaged colours. . . 107
- 4.6. Time-evolution of the populations of the  $1s$ -,  $2p_z$ - and  $3p_z$ - state. Dashed lines show the analytic model, solid lines the numerical results. The total pump-laser (upper panel, black) has two carrier-frequencies, one resonant to the transition  $|\Phi_{1s}\rangle \rightarrow |\Phi_{2p}\rangle$  (green), the other resonant to the transition  $|\Phi_{1s}\rangle \rightarrow |\Phi_{3p}\rangle$  (blue). The bottom panel shows the phase difference  $\varphi_{3p} - \varphi_{2p}$ . . . . . 114
- 5.1. Optimization of the one-dimensional soft-Coulomb Hydrogen atom. (Top) Comparison of initial (green) and optimized pump laser (Fourier transforms). Peaks are labeled by their basis wave length and the number  $n$  of their harmonic  $2n + 1$ . (Bottom) Ground state (shaded) and excited state (solid lines) spectra. Results for the initial pump laser are shown in green, results for the optimized pump laser (after 100 iterations) are shown in blue. The numbers label the transitions. The grey shaded box marks the optimization area, the blue shaded one the visible range of the spectrum (350 nm - 750 nm). (Top inset) Populations of the ground state (red), the first excited state (green) and the second excited state (blue) under the influence of the pump pulse. The black line shows the number of electrons in the system. (Lower Inset) The function  $\varepsilon^A$  as a function of the number of iterations. . . . . 120

- 5.2. (Middle and bottom) Ground state (shaded) and excited state (solid lines) spectra of one-dimensional Helium in a box of (middle)  $r = 50$  a.u. and (bottom)  $r = 100$  a.u.. In the bottom panel, the excited state transitions of the exact calculations are indicated. (Top) Comparison of initial (green) and optimized pump laser (Fourier transforms). Peaks are labeled by their basis wave length and the number  $n$  of their harmonic  $2n + 1$ . (Inset, middle) The control function  $\varepsilon^A$  as a function of the number of iterations. (Inset, bottom)  $|\langle \Psi(t) | \Psi_i \rangle|^2$  of the exact time propagation under the influence of the optimized pump pulse for the (red) ground state, (green) first excited state, (blue) second excited state, (pink) third excited state and (turquoise) fourth excited state. In all panels, results obtained by exact propagation are shown in blue, results obtained by (TD)DFT using the adiabatic spin-polarized exact exchange functional are shown in red. The grey shaded box marks the optimization area, the blue shaded one the visible range of the spectrum (350 nm - 750 nm). . . . . 123

- 5.3. (Middle and bottom) Ground state (shaded) and excited state (solid lines) spectra of one-dimensional Helium in a box of  $r = 100$  a.u.. (Middle) Spectrum optimized with the adapted search space using TDEXX after 550 iterations. Features in the visible have emerged. (Bottom) Optimized spectra after 100 iterations: Comparison of the exact optimization (blue) with the TDEXX optimization in the adapted search space (black). (Top) Optimization lasers in energy space: (shaded green) adapted initial laser and (green line) original initial laser as well as optimized laser with TDEXX after (black) 100 iterations and (red) 550 iterations. (Inset) Target function  $\varepsilon^A$  for the adapted TDEXX optimization (red) and original exact optimization (blue). . . . . 125



- 5.4. (Top) Transient Absorption Spectrum of Helium after the excitation with a 45 cycle  $\sin^2$  laser pulse of intensity  $I = 5.26 \cdot 10^{11} \text{ W cm}^{-2}$  with a carrier frequency resonant to the excitation energy from the ground state to the first excited state for (left) exact and (right) adiabatic EXX description. (Bottom) Time-evolution of the cross section tensor at selected energies  $E_n = 0.2$  (red), 0.4 (blue), 0.6 (purple) 0.8 (turquoise) a.u. for (left) exact and (right) adiabatic EXX description. In the exact case, the curve at 0.6 a.u. is offset for clarity. In all cases, the time interval  $T = 2\pi/\epsilon_1 - \epsilon_0$  is shown. . . . . 126
- 5.5. (Middle and bottom) Ground state (shaded) and excited state (solid lines) spectra of one-dimensional singly-ionized Beryllium in a box of (middle)  $r = 50$  a.u. and (bottom)  $r = 100$  a.u. (Top) Comparison of initial (green) and optimized pump pulse (Fourier transforms). Peaks are labeled by their basis wave length and the number  $n$  of their harmonic  $2n + 1$ . (Inset) The target function  $\epsilon_\tau^{A,m}$  as a function of the iteration number  $m$ . The grey shaded box marks the optimization area, the blue shaded one the visible range of the spectrum (350 nm - 750 nm). . . . . 128
- 5.6. Structure of Methane: A Carbon atom tetrahedrally surrounded by four Hydrogen atoms. Taken from <https://commons.wikimedia.org/wiki/File:Methane-3D-balls.png>. . . . . 129
- 5.7. (Middle and bottom) Ground state (shaded) and excited state (solid lines) spectra of Methane ( $\text{CH}_4$ ) in a box of (middle)  $r = 15$  a.u. and (bottom)  $r = 30$  a.u. for two different laser pulses. The grey shaded box marks the optimization area, the blue shaded one the visible range of the spectrum (350 nm - 750 nm). The spectra within the optimization area are shown enhanced by a factor of 5. (Top) Comparison of initial (green) and optimized lasers (Fourier transforms). Peaks are labeled by their basis wave length and the number  $n$  of their harmonic  $2n + 1$ . (Inset) The spectra shifted to lower energies to coincide with the ground state spectrum. . . . 130
- 5.8. Ground state spectrum of doubly-ionized Methane  $\text{CH}_4^{2+}$ . Peaks are numbered for later reference. The the blue area marks the visible range of the spectrum (350 nm - 750 nm). . . . . 133

## LIST OF FIGURES

---

- 5.9. (Middle and bottom) Ground state (dark grey) and excited state spectra of doubly-ionized Methane ( $\text{CH}_4^{2+}$ ) in a box of (middle)  $r = 15$  a.u. and (bottom)  $r = 30$  a.u. for two different pump pulses  $\mathcal{E}^I$  (brown) and  $\mathcal{E}^{II}$  (green). The grey shaded box marks the optimization area, the blue shaded one the visible range of the spectrum (350 nm - 750 nm). (Top) Comparison of initial (shaded) and optimized (solid lines) pump pulses (Fourier transforms). (Inset) Chromaticity diagram with colours obtained by excitation of the system by the pump pulses. . . . . 135
- 5.10. (Middle and bottom) Laser spectra obtained by exposure of  $\text{CH}_4^{2+}$  to selected frequency components of the pump pulse  $\mathcal{E}^I$ . The shaded line shows the spectrum obtained by the full pulse. (top) Many-body excitation energies obtained through analysis of the ground state spectrum. The x axis denotes the excitation energy, the y axis the excited state, from where the excitation takes place. . . . . 136
- 5.11. Ground state spectrum of Methane using the LDA-ADSIC functional. . . 141
- 5.12. (Bottom) Excited-state spectra of  $\text{CH}_4$  according to scheme II and (inset) the chromaticity diagram with the resulting colours. (Top) Many-body excitation energies of  $\text{CH}_4$  obtained through calculating the energy differences of the ground state spectrum. The x axis denotes the excitation energy, the y axis is the excited state, from where the excitation takes place. . . . . 142
- A.1. The four methods used in the Downhill-Simplex algorithm. (a) Reflection, (b) expansion, (c) contraction, and (d) compression. Taken from [4]. . . . 157
- C.1. The external potential  $V_{ext}(x)$  is a double well potential surrounded by vacuum of the energy  $V_V$ . The right well is located between  $x_{BD}$  and  $x_D$  and serves as donor (D). Its potential is  $V_D$  and can be varied. The left well is located between  $x_A$  and  $x_{AB}$  and serves as electron acceptor (A). Its potential is fixed to zero for all calculations. Donor and acceptor are separated by a barrier of variable height  $V_B$ , which is fixed to two different heights. . . . . 167

- 
- C.2. (Top) The number of electrons on the acceptor  $N_A$  as a function of the donor potential  $V_D$  for the case of  $N = 2$  for the truncated electron-electron interaction  $\hat{V}_{ee}^{(2)}$  (C.4), and for the full electron-electron interaction  $\hat{V}_{ee}^{(1)}$  (C.3). Panels a) and b) display to the high-barrier case, and c) and d) display the low-barrier case. For comparison a) shows in grey the result as obtained by DFT calculations using the LDA functional. (Bottom) The derivatives of the number of electrons on the acceptor with respect to the donor potential  $dN_A/dV_D$  normalized to its maximum. The tunneling points are identified by the local maxima of  $dN_A/dV_D$ . The vertical lines show the predicted tunneling points, in blue for the IP-EA prediction (C.11), and in green for the predictions corrected with the Hartree interaction  $C_H$  (C.18). . . . . 170
- C.3. The external potentials of the isolated subsystems (dashed red). These were used to calculate the ionization potentials, the electron affinities and the wave functions of the isolated subsystems. On the left we show the potential  $V_{ext}^A(x)$  of the isolated acceptor, on right side we display the potential  $V_{ext}^D(x)$  of the isolated donor. For comparison  $V_{ext}(x)$  of the combined system is shown underlying in black. . . . . 171
- C.4. a) Hartree correction (C.18) and b) exchange correction (C.19) for high-barrier case (I) (orange) and low-barrier case (II) (red). The vertical dashed blue lines show the tunneling points of case (II) as predicted by the IP-EA approach. They mark the donor potentials  $V_D$ , where in the naive correction scheme the energy corrections to predict the tunneling points of the fully interacting system would be calculated. For the high-barrier case (I), the corrections can be calculated at any point. The strong increase of the energy corrections of case (II) is due to the break-down of our wave function approximation, which is caused by the delocalization of the donor wave-function  $\varphi_D$  for donor-potentials  $V_D$  which are at the order of the barrier height  $V_B$ . . . . . 174

## LIST OF FIGURES

---

- C.5. (Top) Number of electrons on the acceptor  $N_A$  as a function of the donor potential  $V_D$  in the low-barrier case (II) for a)  $N = 3$  (dark orange) and b)  $N = 4$  (dark violet) electrons. For comparison the case of  $N = 2$  electrons is shown in black. A system of  $N$  electrons exhibits  $N$  tunneling points. The behaviour of three and four electrons is qualitatively similar as the one of two electrons. (Bottom) The derivate  $dN_A/dV_D$  as a function of the donor potential for c)  $N = 3$  and d)  $N = 4$ . In each panel, the predicted tunneling points are shown as dashed vertical lines. The light orange (violet) dashed line shows the IP-EA predicted tunneling points, the slightly darker orange (violet) dashed line the Hartree corrected predictions. . . . 177
- C.6. Tunneling of (top) three and (bottom) four electrons in a 9-site model. The figure shows the numerical data in comparison with our model, both for the full and the truncated interaction. In both cases, our model reproduces the numerical results on the shown scale. Figs. C.7 and C.8 show zooms into the relevant regions for three and four electrons respectively. . . . . 179
- C.7. Comparison of the tunneling behaviour predicted by our model and the corresponding numerical data for an asymmetric double-well potential with three electrons (zoom into the regions of the different tunneling points).180
- C.8. Comparison of the tunneling behaviour predicted by our model and the corresponding numerical data for an asymmetric double-well potential with four electrons (zoom into the regions of the different tunneling points).181
- C.9. Number of electrons on the acceptor as a function of donor potential  $V_D$  for two electrons in an asymmtric double-well potential. The red line indicates the exact many-body solution, the other lines DFT solutions with different functionals: LDA (green), LDA-ADSIC (blue) and spin-polarized LDA-PZSIC (pink). The spin-polarized LDA-PZSIC solution has multiple solutions. If one chooses the one with minimal energy, it exhibits a step-like behaviour like the exact solution. . . . . 184

- 
- C.10. KS potentials  $v_{KS}$  and the respective ground-state densities for exact, spin-polarized LDA-PZSIC and LDA calculations. The top row shows the situation where both electrons are on the donor, the middle one, the one, where one is on the donor, one has already tunneled to the acceptor and the bottom row shows the situation where both electrons have tunneled to the acceptor. The left column shows the exact  $V_{KS}$  (red) with its respective density (blue), the middle one the spin-polarized LDA-SIC potentials (red and green) with their respective spin-densities (blue and pink) and the right column finally shows the LDA potential (red) with its density in blue. Note, that the offsets of the potentials are arbitrary and have no physical meaning. . . . . 186
- C.11. Number of electrons on the acceptor  $N_A$  in dependence of the donor potential  $V_D$  for the exact case, as obtained with the wrong spin-symmetry with spin-polarized LDA-PZSIC, with our proposed scheme with the correct spin-symmetry using  $V_{\text{eff}}^{(i)} = \min(V_{\uparrow}, V_{\downarrow})$ ,  $V_{\text{eff}}^{(ii)} = \min(V_{\uparrow}, V_{\downarrow}) + S_{\uparrow\downarrow}$  and  $V_{\text{eff}}^{(iii)} = \min(V_{\uparrow}, V_{\downarrow}) + S_{\uparrow\downarrow} + P_{\uparrow\downarrow}$ .  $V_{\text{eff}}^{(i)}$  does not produce a plateau,  $V_{\text{eff}}^{(ii)}$  produces first hints of a plateau in the center and  $V_{\text{eff}}^{(iii)}$  produces a plateau, even though it is still too narrow. LDA is shown for comparison. 188
- C.12.(top) Number of electrons on the acceptor  $N_A$  as a function of the donor potential  $V_D$  (as in Fig. C.11) and (i) - (iv) the corresponding KS eigenvalues: (i) exact KS, (ii)  $V_{\text{eff}}^{(i)} = \min(V_{\uparrow}, V_{\downarrow})$ , (iii)  $V_{\text{eff}}^{(ii)} = \min(V_{\uparrow}, V_{\downarrow}) + S_{\uparrow\downarrow}$  and (iv)  $V_{\text{eff}}^{(iii)} = \min(V_{\uparrow}, V_{\downarrow}) + S_{\uparrow\downarrow} + P_{\uparrow\downarrow}$ . Eigenvalues are plotted as differences to the lowest eigenvalue. . . . . 189



# List of Tables

5.1. Numerical parameters: spacing $\Delta x$ , radius $r$ , absorbing boundary width $w$ , time step $dt$ , pump pulse duration $T_{\mathcal{P}}$ , delay $\tau$ and spectrum time $T_S$ , both during the optimization (opt) and for the fully converged calculations (conv). All values are given in a.u.. . . . .	121
5.2. Laser frequencies (in a.u.) and the corresponding resonances of the search spaces of the optimization of $\text{CH}_4^{2+}$ . Nomenclature as in Figure 5.8, $\epsilon_H$ is minus the energy of the highest occupied KS state. $\omega_3^I$ is the average of $\epsilon_1 = 0.337$ a.u. and $\epsilon_3 - \epsilon_1 = 0.353$ a.u.. Since the frequencies are broadened by the finite pulse duration, $\omega_3^I$ covers both resonances. . . . .	134
B.1. Attributes of the octopus clase. . . . .	161
B.2. Attributes of the optimization clase. . . . .	161





# Acronyms

<b>ADSIC</b>	<b>A</b> verage <b>D</b> ensity <b>S</b> elf <b>I</b> nteraction <b>C</b> orrection
<b>DFT</b>	<b>D</b> ensity <b>F</b> unctional <b>T</b> heory
<b>EXX</b>	<b>E</b> xact <b>E</b> xchange
<b>HK</b>	<b>H</b> ohenberg- <b>K</b> ohn
<b>HOMO</b>	<b>H</b> ighest <b>O</b> ccupied <b>M</b> olecular <b>O</b> rbital
<b>KLI</b>	<b>K</b> rieger <b>L</b> i <b>I</b> afrate
<b>KS</b>	<b>K</b> ohn- <b>S</b> ham
<b>LDA</b>	<b>L</b> ocal <b>D</b> ensity <b>A</b> pproximation
<b>LUMO</b>	<b>L</b> owest <b>U</b> noccupied <b>M</b> olecular <b>O</b> rbital
<b>OEP</b>	<b>O</b> ptimized <b>E</b> ffectice <b>P</b> otential
<b>PAD</b>	<b>P</b> hotoelectron <b>A</b> ngular <b>D</b> istribution
<b>PES</b>	<b>P</b> hotoelectron <b>S</b> pectroscopy
<b>QOCT</b>	<b>Q</b> uantum <b>O</b> ptimal <b>C</b> ontrol <b>T</b> heory
<b>SIC</b>	<b>S</b> elf- <b>I</b> nteraction <b>C</b> orrected
<b>TAS</b>	<b>T</b> ransient <b>A</b> bsorption <b>S</b> pectroscopy
<b>TD</b>	<b>T</b> ime- <b>D</b> ependent
<b>TRPES</b>	<b>T</b> ime- <b>R</b> esolved <b>P</b> hotoelectron <b>S</b> pectroscopy



# 1. Introduction

---

*“The beginning is the most important part of the work.”*

*- Plato, The Republic*

---

In this thesis I have addressed the microscopical, theoretical analysis and the control of transient spectra using time-dependent density functional theory. Here, the topics of non-equilibrium (attosecond) spectroscopy of molecular systems and optimal control theory are united under the technical framework of time-dependent density functional theory.

**The Attosecond Time Scale.** Structure and dynamics in the microcosm are inherently connected by the laws of quantum mechanics. Take, for example, a particle in a linear combination of its ground state  $\Psi_0$  with energy  $E_0$  and its first excited state  $\Psi_1$  with energy  $E_1$ . This is called a wave-packet and the change in the position of its center of mass is the closest quantum mechanical analog to a classical trajectory [5]. The solution of the Schrödinger equation leads to an oscillatory motion with the period  $T_{osc} = 2\pi/(\Delta E)$  where  $\Delta E = E_1 - E_0$ . The larger the energy separation  $\Delta E$ , the faster is the oscillatory motion. This energy separation is dictated by the spatial extent of the confining potential in addition to the particle’s mass. Therefore, quantum mechanics connects the rapidity of a problem with its spatial scale. Furthermore, for a wave-packet made of two bound eigenstates, the oscillation period  $T_{osc}$  also determines the response time of the system to an external perturbation. For example, a two-level atom responds to the radiation field similarly to a classical damped electron oscillator of eigenfrequency  $\omega_0 = 2\pi/T_{osc}$  [5, 6, 7]. The situation is similar for electron plasmas, where the plasma oscillation

frequency is inversely proportional to the square root of its density [8]. For a mean distance comparable to atomic dimensions  $l_{mean} \approx 0.1$  nm, we obtain  $T_{osc} = 120$  as. This is close to the oscillation period of valence electron wave-packets in bound atomic or molecular systems: a semiclassical electron orbits a hydrogen atom in 150 as. Thus the motion of electrons inside atoms, in molecular orbitals or confined in nanometer-scale potentials, like the collective dynamics of free electrons in high-density ionized gases, is naturally measured in attoseconds, and attosecond science is the science of electrons in motion, both collective and individual.

**The Road Towards Attosecond Time Scales.** Being able to measure with high resolution in space and time requires access to physical quantities with well-defined spatial and temporal gradients. They can both be provided by waves, whose wave length and oscillation period define the spatial and temporal steepness. In waves, the oscillations are periodic, which can be used to extract temporal information by measuring in the frequency domain and using the Kramers-Kronig relations [9, 10]. However, obtaining accurate results becomes more challenging with larger distances in space and time. Moreover, stationary metrology fails in describing non-linear response phenomena [5]. In these cases, isolated spatial temporal gradients are necessary. Direct space- and time-domain approaches offer transparent and intuitive measurement tools. In space, these methods carry the name microscopy, while its time-equivalent is called chronoscopy or *time-resolved metrology*. The evolution in the field of time-resolved metrology from the nanosecond to the attosecond regime was done in three steps, each triggered by new technologies.

First, the invention of the transistor brought the time-scale down from nanoseconds to picoseconds using wave lengths in the radio- to microwave regime. However, in this regime, the refractive index of typical materials varies strongly due to lattice vibrations. This strong dependence of the refractive index on the wave length limits the path length of distortion-free propagation. Since this path length scales quadratically with the duration of the transients, the path length of distortion-free propagation sets an upper limit for the signal speed. The refractive index of transparent optical materials is nearly constant in the visible and near-infrared. This gives rise to the mode-locking technique [11], which is based on the constructive interference of phase-modulated modes in a laser cavity and the resulting possibility of coherent light amplification if the phases are locked accordingly.

---

Non-linear optical phenomena, like the optical Kerr-effect and negative group delay dispersion, play a key-role in the process [12, 13]. These techniques have for example been implemented in mirror dispersion controlled Kerr Lens mode locked Ti:Sapphire lasers [14, 15]. To further shorten the pulse durations, the bandwidth of the cavity is increased using hollow-fiber wave guides [16, 17, 18, 19] and afterwards compressed with for example chirped mirrors [20]. By combining these techniques, the pulse duration reached the 1fs-barrier by 2000 (see e.g. the review articles [21, 22]). Nevertheless, the pulse lengths are limited by the increasing dispersion towards the ultraviolet due to electronic transitions.

An alternative approach to the generation of ultrashort pulses are free electron lasers (FEL) [23], proposed by Madey in 1971 [24], and firstly used by Deacon in 1977 [25]. Current FELs are based on the Self Amplified Spontaneous Emission (SASE) technique [26, 27, 28, 29] and produce radiation in the extreme ultraviolet to soft x-ray regime [30, 31] and the hard x-ray regime [32, 33] with durations in the femtosecond regime. They have been used to study the photoionization of atoms like Neon [34], Argon [35] and Xenon [36], which was theoretically studied in [37].

Finally, at the beginning of the 21st century, attosecond-pulse laser sources became available [38, 39]: In 2001 Hentschel *et al.* reported on the generation of single  $650 \pm 150$  as long soft x-ray pulses [38] and in 2004 Kienberger *et al.* reported on the generation of 250 as long XUV pulses. The generation of attosecond pulses is based on high-harmonic generation (HHG) [5, 40, 41, 42] and is described by a three-step model [43, 44, 45]: In the first step, the laser ionizes an electron from an atom. The ionized electron is then accelerated by the laser field and recombines with its parent atom, releasing its kinetic energy in the form of a photon [46, 47]. The trajectory of the electron and its resulting kinetic energy depend on its time of release, with a maximal energy of  $\omega_{max} = I_P + 3.17U_P$ , where  $I_P$  is the ionization potential of the system and  $U_P$  the ponderomotive potential. Combining the different electron trajectories, for example by passing them through a thin aluminium-film [48], finally leads to the generation of attosecond pulses. An important variable in this context is the carrier-envelope phase (CEP), which is defined as the phase difference between the highest half-cycle of the electric field under the envelope and the envelope itself and was predicted [21, 49] and later observed [50] to play an important role in strong-field laser-matter interaction. Its control is crucial for the generation and measurement of reproducible isolated attosecond pulses [51] and the control of electron

emission from atoms [52]. The emission of attosecond pulses through high-harmonic generation can happen either in single-cycle mode [53, 54, 55] or as a train of pulses [56, 57], which are coherent and can be phase matched among multiple emitting atoms [58, 59, 60]. One distinguishes between in-situ and ex-situ measurements (for a recent review see [46]). By 2014, the shortest individual pulse obtained had a duration of 67 as [46, 61].

In addition to the generation, the ability to measure attosecond pulses is important. Duration and shape of attosecond-pulses can for example be measured by streak-imaging [62, 63]. The advent of attosecond-pulse laser sources and the possibility to adequately characterize the resulting pulses has given birth to a new field of physics – attosecond physics, where electron dynamics can be observed in real time [5, 42].

**Pump-Probe Spectroscopy.** Pump-probe experiments are the preferred technique to study the dynamical behaviour of atoms and molecules: the dynamics triggered by the pump pulse can be monitored by the time-dependent reaction of the system to the probe pulse (see Fig. 1.1), a reaction that can be measured in terms of, for example, the absorption of the pulse intensity, or of the emission of electrons .

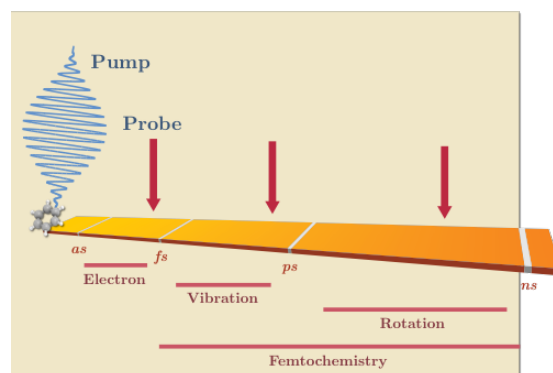


Figure 1.1.: Pump-probe spectroscopy setup. The pump pulse triggers the dynamics, and after a certain delay time, the reaction of the system to a probe pulse is measured. Depending on the time-scale, electronic, vibrational and rotational properties can be measured. On the sub-femtosecond time-scale, the electronic-only dynamics can be observed. If we look at time-scales longer than tens or hundreds of femtoseconds, the atomic structure will have time to re-arrange, giving rise to the field of femtochemistry.

---

Before 1900 it was already known, that short flashes of light permit the recording of rapid phenomena using a technique called spark photography [5]. In 1864 Toepler extended this technique to study microscopic dynamics, where he used one spark to trigger a sound wave and a subsequent, delayed one to record it [64]. By taking pictures of the sound wave as a function of the delay time, he obtained a complete history of sound-wave phenomena. Pump-probe spectroscopy was born.

The time resolution of these experiments is mainly limited by the duration of the pulses – although it is also limited by the ability of the experimenter to ascertain their relative time delay and shape. In order to precisely fix this delay, the two pulses are coherently synchronized – in fact, they have the same origin, or one of them is used to generate the other – so that the delay is gauged by an optical path difference. This technique was developed in 1899 by Abraham and Lemoine, who were the first to derive pump and probe from the same spark [65]. The resultant synchronism allowed the improvement of the time resolution to the limit of the flash duration. This completed the conceptual framework of studying transient phenomena, limiting its progress to the development of shorter light pulses and techniques for its measurement.

A wealth of possibilities of potential setups exists, depending on the frequencies, durations and intensities of the two pulses. A common set-up in attosecond physics employs an XUV attosecond pulse and the relatively more intense, longer (few femtoseconds) NIR or visible pulse used for its generation. This set-up has two caveats: (i) Experiments are performed in the regime of temporal overlap of pump and probe pulse. The behaviour is complex and the results are difficult to interpret [66]. (ii) In some experimental setups, the NIR controls the system more than it probes it [67]. One way to circumvent this problem is by combining two XUV attosecond pulses. This is in principle possible (and has been theoretically analysed [68]), but unfortunately the low outputs of current XUV attosecond pulses lead to significantly too weak signals. To distinguish the attosecond pump-probe signal from the pump-only and probe-only background, the probability of the two-photon process involving a pump and a probe photon must be considerably higher than the one of the one-photon processes involving only a pump or only a probe photon. This requires focused intensities of  $10^{15}$  W/cm<sup>2</sup> [67]. Intensities of  $10^{14}$  W/cm<sup>2</sup> have been achieved for pulse trains [69, 70]. Another choice to make is the final observable, i.e. what kind of system reaction is to be measured as a function of the time delay. In this work we focus on two common choices: (i) Observing the emission of electrons

(their energies, angular distribution, or total yield) from the pumped system due to the probe pulse. This can be called time-resolved photo-electron spectroscopy (TRPES). (ii) Observing the optical absorption of the probe signal, which can be called time resolved absorption spectroscopy, or transient absorption spectroscopy (TAS).

Both techniques can of course be used to look at longer time resolutions. If we look at molecular reactions on the scale of tens or hundreds of femtoseconds, the atomic structure will have time to re-arrange. These techniques are thus mainly employed to observe modification, creation, or destruction of bonds, a field triggered by Zewail [71, 72], which is now called *femtochemistry*. TAS, for example, has been successfully employed to *watch* the first photo-synthetic events in chlorophylls and carotenoids [73], that transform the energy gained by light absorption into molecular rearrangements. A review describing the essentials of this technique can be found in Ref. [74]. Note that in addition to following chemical reactions, femtosecond-long pulses may also be used for example for characterizing the final electronic quantum state of ionized atoms [75] and many more processes.

In TRPES, the probe pulse generates free electrons through photo-ionization, and one measures their energy or angular distribution as a function of time; if this time is on the femtosecond scale one can follow molecular dynamics in the gas phase, as demonstrated already in the mid 1990s [76, 77], although this technique had already been employed to follow electronic dynamics on surfaces [78]. For review articles on the topic, see the recent articles [79, 80, 81, 82, 83].

If the goal –as in this work– is to study the electronic dynamics *only*, disentangling them from the vibronic degrees of freedom, then one must move down these spectroscopic methods to the attosecond regime [84]. In this regime, both TAS and TRPES have recently been demonstrated. Goulielmakis *et al.* for example performed a TAS experiment on the strong-field ionization of Krypton atoms, where the valence electron motion was observed in real-time [1]. For the obtained TAS see Figure 1.2. Another prototypical example for TAS is the recent experiment of Holler *et al.* where the transient absorption of an attosecond pulse train (created by high harmonic generation) by a Helium gas target, was studied in the presence of an intense IR pulse. The absorption was observed to oscillate as a function of the time-delay of pump and probe [85].

Several cases of use of TRPES with attosecond pulses have also been recently reported; an early example is the use of attosecond TRPES to investigate the time-resolved Auger



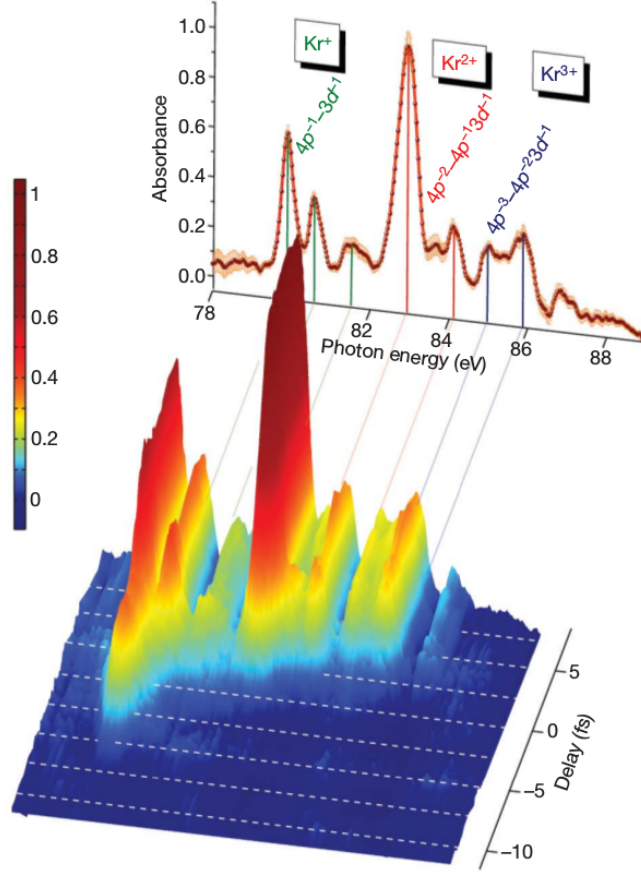


Figure 1.2.: TAS of Krypton ions as obtained by Goulielmakis *et al.*: The ionization of Krypton can be observed as a function of time. This figure was published as Fig. 2 in Ref. [1]. Copyright © 2010 by the Nature Publishing Group (NPG).

decay in Krypton by Drescher *et al.* [86]. In fact, one of the major successes of attosecond science has been the measurement of the delays of electron ejection. Using a method called streak-field detection [5, 39, 87], the difference in electron ejection times can be measured on the order of tens of attoseconds [66]. In the streak-field method, a strong field from a NIR pulse is used to shift the momentum of an electron released into a laser field, giving it a time-stamp at the time of its birth. With this method, Schultze *et al.* were able to measure the delay of electrons emitted from the 2p orbital in Neon in comparison to the ones emitted from the 2s orbital by 100 eV photons to a precision

of  $21 \pm 5$  as [88]. Uiberacker *et al.* could observe in real time the light induced electron tunneling provoked by a strong NIR pulse, demonstrating how this electron tunneling can be used to probe short lived electronic states [89]. Smirnova *et al.* studied the ionization of an atom by an attosecond XUV pulse in the presence of an intense laser pulse, as a function of the time delay between both [90]. Johnsson *et al.* employed attosecond pulse trains and a Helium target to not only control the timing but also the probability of electron ejection [91]. Attosecond photoelectron spectroscopy was also demonstrated to yield useful information for condensed matter systems; e.g. Cavalieri *et al.* performed experiments on single-crystal Tungsten, where they measured the delay time between electrons emitted from the core and from the conduction bands [92].

**Theoretical Spectroscopy.** All these advances demand appropriate theoretical modelling. The use of more than one pulse of light intrinsically requires us to go beyond any “linear spectroscopy” technique – although if the pulses are weak a perturbative treatment may still be in order. This non-linear behavior provides much more information about the system at the cost of an increasingly difficult analysis. The use of two (or more) coherent pulses of light, with fine control over their shape (sometimes called a “multidimensional analysis”), permits a deeper characterization. This fact was already acknowledged in the field of nuclear magnetic resonance, or later in femtochemistry – see for example Refs. [93] and [94] for theoretical treatments of these cases.

A recent theoretical analysis of attosecond TAS based on perturbation theory was given by Baggesen *et al.* [68]. Gaarde *et al.* presented a study for relatively weak pumping IR pulses in combination with XUV ultrafast probes, for Helium targets and based on the single active electron approximation [95]. Very recently, the experiment reported by Ott *et al.* [2], in which the ultrafast TAS of Helium displayed features beyond the single active electron approximation, was theoretically analyzed in Ref. [96], utilizing an exact solution of the time-dependent Schrödinger equation, that cannot however be easily extended to larger systems. Finally, the above-mentioned experiment of Goulielmakis *et al.* [1] was analyzed with the model described in Ref. [97], which treated the pump IR pulse non-perturbatively.

Indeed, it would be desirable to analyze these processes with a fully non-perturbative theory (since at least one of the pulses is usually very intense), which at the same time

---

is capable of going beyond the single active electron approximation and accounting for many-electron interaction effects. This last fact is relevant since the attosecond time resolution obtained in this type of experiments is able to unveil the fast dynamical electron-electron interaction effects. The single active electron approximation, which essentially assumes that only one electron actively responds to the laser pulse, has been successfully used to interpret many strong-field processes. However, its range of validity is limited, and roughly speaking it is expected to fail whenever the energies of multielectron excitations become comparable to the laser frequencies or the single electron excitations [98].

Time-dependent density functional theory (TDDFT) [99] meets all these requirements: it may be used non-perturbatively, includes the electron-electron interaction and can handle out-of-equilibrium situations. It has been routinely used in the past decades to study the electron dynamics in condensed matter *in equilibrium*. By this we mean that, usually, one computes the linear or non-linear response properties of systems in the ground state (or at thermal equilibrium). In pump-probe experiments, however, one must compute the response of a system that is being driven out of equilibrium by an initial pulse. In this work, we have developed the theoretical framework and implemented it in the code `octopus` [100, 101, 102, 103] to explore the usability of TDDFT for this purpose, and show how, at least for the two cases of TAS and TRPES, the extension is straightforward.

However, in addition to mere numerical modelling, a more theoretical understanding of pump-probe experiments would be helpful. It is known, that ground state photo absorption spectra can be analyzed using the dipole-dipole response function, which can be conveniently cast into frequency space. The resulting Lehmann-representation of the response function provides an intuitive interpretation of photo absorption spectra in terms of the many-body excitation energies. In pump-driven systems, obtaining a similar mathematical interpretation is more complicated. Recently, several groups have published results on the theoretical modelling of these pump-probe situations [68, 95, 104, 105, 106]. In this thesis, I recast the Lehmann representation of the interacting response function of a driven system in the non-overlapping regime for short probe pulses and analyze some of its properties, paying particular attention to the lineshapes of the spectral peaks. A similar analysis has been published recently by Perfetto and Stefanucci [107], who also included the treatment of long probes and the overlapping regime. We also address how, the Lehmann representation in the non-equilibrium case can be used

to understand laser-induced lineshape changes.

**Optimal Control Theory.** The measurement and control of ultrafast processes are inherently intertwined. In fact, quantum optimal control theory [108, 109] (Quantum-OCT) can be viewed as the *inverse* of theoretical spectroscopy: rather than attempting to predict the reaction of a quantum system to a perturbation, it attempts to find the perturbation that induces a given reaction. It is the quantum version, first developed in the 80s [110, 111, 112], of a more general mathematical framework, *control theory* [113, 114], which is commonly applied in engineering, for example to design trajectories for satellites and space probes [109]. This quantum version of control was needed given the fast advances in experimental quantum control – or *coherent control of quantum systems*, as it is sometimes called.

The experimental control of quantum systems was born in the field of photo-chemistry: the goal was to achieve the selective destruction or creation of bonds by means of suitably tailored laser fields. It was therefore a consequence of the raise of the field of *femtochemistry*. Numerous techniques were invented in a short period of time, such as the control of quantum interference proposed by Brumer and Shapiro (also called *coherent control scheme*) [115, 116, 117], the “pump-dump” control proposed by Tannor and Rice [118, 119] (where the probe pulse not only probes, but in fact partially “dumps” the excited state wave-packet on the ground state), stimulated Raman adiabatic passage [120], wave-packet interferometry [121], etc.

However, the most successful technique – since it can be considered in fact a generalization of all the previous ones – has been found to be the adaptive feedback control (AFC) first proposed by Judson and Rabitz [122] and first realized in 1997 [123]. Using AFC, groundbreaking results were achieved in the control of chemical reactions [124], and in many related experiments such as the control of the efficiency of photosynthesis processes [125]. Even the photo-isomerization of the retinal molecule in rhodopsin proteins (a process that is crucial e.g. for vision in higher organisms) was optimized [126].

There are various degrees of freedom in the control pulse that can be manipulated. Take, for example, the previously mentioned carrier-envelope phase that has been used to control the electronic motion during the dissociation of diatomic molecules [127]. Recently, this approach has been extended to more complex polyatomic molecules (namely Acety-

---

lene, Ethylene, Butadiene) by Xie *et al.* [128, 129].

Another recent development in coherent control is the scheme based on the nonresonant dynamic Stark effect, developed by Sussman, Stolow and coworkers [130, 131, 132], which is based on a three-pulse scheme: the pump pulse starting the dynamics, a manipulating pulse and a probe pulse. For a comprehensive review, I refer the reader to [133] and to [134] for a perspective on the field of strong field laser control. Experimental control of absorption spectrum features of methyl iodide ( $\text{CH}_3\text{I}$ ) using the dynamic Stark effect has been recently demonstrated by Corrales *et al.* [135, 136]. In 2006, Stolow *et al.* used the nonresonant dynamic Stark effect to control the photodissociation of  $\text{IBr}$  [131]. They showed, that the dissociation yield depends critically on the delay between pump and control pulse. The same system was later investigated theoretically by Sanz-Sanz *et al.* [137]. The nonresonant dynamic Stark effect also provides a framework to understand light-induced avoided crossings and their counterpart light-induced conical intersections. An experimental exploitation of light-induced conical intersections was recently used to control the photo dissociation of a polyatomic molecule ( $\text{CH}_3\text{I}$ ) [138].

Since the advent of attosecond physics, investigating autoionizing resonances in a time-resolved manner has drawn much attention both from experimentalists [139, 140, 141, 142] and theorists [105, 143, 144, 145, 146]. Autoionizing states were first observed by Beutler in 1935 in the photoabsorption spectra of rare gases [147]. Their characteristic shape was later explained by Fano in 1961 [148] - giving them their name. Recently, interest has also been focused not only on their time-resolved observation, but also on their modification and control of resonance shapes using laser dressing [95, 105, 139, 140, 144, 145, 149]. The simultaneous interaction with two light-fields in these experiments, directly connects them to phenomena like electromagnetically induced transparency [150, 151]. Works like [2, 152] use the NIR pulse of the pump-probe setup to impart a specific phase to the system under investigation, demonstrating the change from a Fano into a Lorentz line shape and vice versa (see Fig. 1.3).

All these advances in experimental quantum control require a theoretical counterpart, provided by Quantum-OCT. In this work, I have concentrated on its possible application to attosecond dynamics of many-electron systems. For that purpose, the possibility of combining Quantum-OCT with TDDFT was recently established [153]. Furthermore it has been shown, that it can be used to optimize strong-field ionization [154], photo-induced dissociation [155] and is compatible with Ehrenfest dynamics [156]. Very

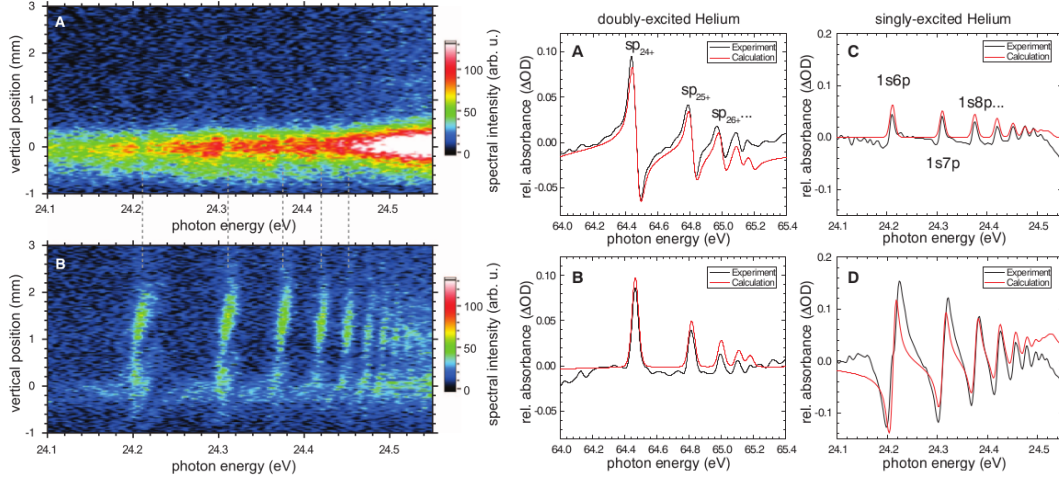


Figure 1.3.: (left) Laser controlled amplification of resonant light in the EUV. (A) Spectrum of transmitted EUV light without control laser: The Helium resonant absorption lines can be observed as local minima in an otherwise smoothly varying spectrum centered at a vertical position of 0 mm. (B) Spectrum of transmitted and amplified EUV light in the presence of the control laser. Amplification can be observed exactly at the He resonance positions corresponding to absorption in (A). (right) Transforming asymmetric Fano spectral absorption lines into symmetric Lorentzian absorption peaks in doubly excited He (A, B) and vice versa, from Lorentz to Fano in singly excited He (C, D). This figure is an adaption of Figs. 3 and 4 in Ref. [2]. Copyright © 2013 by the American Association for the Advancement of Science (AAAS).

recently, Krieger *et al.* used TDDFT to study intense, short, laser pulse-induced demagnetization in bulk Fe, Co, Ni, which can take place on time scales of  $<20$  fs [157]. They studied the influence of laser intensity, frequency and duration on the demagnetization process.

In this thesis, the goal was to apply Quantum-OCT techniques, possibly in combination with TDDFT, in order to manipulate optical properties of atoms or molecules. This is strongly related to the topic of electromagnetically induced transparency: the goal may be to reduce or to enhance the absorption of light – how much and at which wave length. In particular, I have assessed the possibility of using tailored pumps in order to enhance the absorption in the visible range of otherwise transparent samples.

Finally, I have related the obtained results to the concept of perceived colour in humans.

---

Indeed, one of the most important ways of perceiving (and consequently interacting) with our environment as human beings is sight. The human vision is restricted to a very small spectral range, roughly between 350 and 750 nm. The human eye has three types of light receptors, each with different sensitivities for different wave lengths. When light enters the eye, each receptor perceives a different intensity, sending the corresponding electrical signal to the brain. The human brain then converts this so-called tristimulus into the colour that we “see”. Which colour would be perceived by the human eye is an interesting question in the field of dyes and has for example been addressed in [158]. The colour of a material depends on its electronic response to light (or, at very high temperatures, on its intrinsic emission), and is therefore subject to manipulation if one has control over the electronic state. This has been the control route whose viability has been assessed in this work.

**Outline.** The thesis is structured as follows. In Chapter 2, I present the necessary theoretical background for the thesis. I start by introducing the Born-Oppenheimer approximation, which allows us to separate the electronic from the nuclear degrees of freedom. Using the clamped-ion approximation for the rest of the thesis, I exclusively focus on the electronic part of the problem. Then I present the linear response theory for a general excited system, in the overlapping or non-overlapping regime in Section 2.2. This includes linear response theory for a system in its ground state as a special case. For the non-overlapping regime and short probe-pulses, I present a closed form of the Lehmann-representation of the response function and analyze some of its properties like the time-independence of its poles and the time-dependence of its spectral weights. After describing line-broadening mechanisms in Section 2.3, I show how the generalized Lehmann-representation can be used to understand lineshape changes in non-equilibrium systems. In Section 2.4, I present the foundations of (TD)DFT and describe how it can be used for the calculation of transient spectra. In Section 2.5.1, I present the model Hamiltonians used in this thesis, present the general theory of Rabi oscillations and show how this theory can be extended to three-level systems. In Section 2.6, I present the basic concepts of Quantum-OCT and how it can be used to optimize spectral properties of laser-excited systems. Finally in Section 2.7, I describe how spectra can be translated into human colour perception.

After having derived and presented the theory, I show how these concepts can be brought

together in spectroscopic applications in chapters 3, 4 and 5.

In Chapter 3, I show examples, where I use both, models and TDDFT to simulate pump-probe photo-electron and absorption spectroscopy in the overlapping and non-overlapping regime. First, the transient absorption spectrum of a one-dimensional model of He is studied using the exactly solvable model, showing how transient spectra can be interpreted using Rabi physics. The results are then compared to TDDFT calculations using the LDA and the EXX functional, where I identify and point out some shortcomings of the functionals due to their lack of memory. Afterwards, I present TAS and TRPES simulations for the real three-dimensional Helium, showing how both techniques can be combined to obtain a more complete picture of the photo-induced dynamics. Finally, I extend the study to the Ethylene molecule, which features a  $\pi \rightarrow \pi^*$  transition in the transient spectra.

In Chapter 4, I use the example of analytically solvable Hydrogen to demonstrate how the Lehmann representation for excited state spectra can be used to interpret transient absorption spectra in the non-overlapping regime. I compare analytic and numerical results and investigate the difficulties of simulating spectroscopy of highly excited states. I demonstrate how the excited-state spectrum of a non-stationary state changes in time, how this time-dependence influences the colour and how the oscillatory behaviour of the spectrum in time manifests in a chromaticity diagram. Finally, I show how the previously derived Rabi-formalism in a three-level system can be used to control the excitation of Hydrogen into a state, that absorbs light in the visible.

In Chapter 5, I focus on bringing together TDDFT with the control of transient spectra. I present the details of the derived algorithm to optimize spectra and demonstrate results for exactly solvable Hydrogen. Then I compare its performance using the exact formalism with its TDDFT performance using the case of one-dimensional Helium. This comparison demonstrates the importance of an intelligent choice of the optimization space, and it also becomes clear that TDDFT brings about its own special challenges. I also demonstrate the time-dependence of the excited-state spectrum of Helium in the TDDFT case and compare it to the exact case as demonstrated in the previous chapter. Singly ionized Beryllium is investigated as the final single-atom system before I extend the approach to molecules, where I look at neutral and doubly-ionized Methane. For doubly-ionized Methane, in addition to presenting the optimization results for two different search spaces, I perform a pulse-cleaning, where I analyse the dynamics of the excitation process by



---

exposing the molecule to only certain parts of the optimized pulse. Finally I present an alternative approach to the optimization process where, instead of directly optimizing the spectrum, one first finds an excited state with the desired properties, and then uses gradient-based optimization algorithms to excite the system into this target state.

In Chapter 6, I summarize the work at hand, its main conclusions and point out open questions and possible future work. Finally, two appendices provide further details on the computational methods and a third provides calculations, where we analyze tunneling in many-particle systems and its description in DFT. The bibliography can be found at the end of thesis.



## 2. Theory

### Contents

<b>2.1. Born-Oppenheimer and Clamped-Ion Approximation . . . . .</b>	<b>22</b>
<b>2.2. Linear Response Theory . . . . .</b>	<b>24</b>
2.2.1. General Time-Dependent Linear Response Theory . . . . .	25
2.2.2. Frequency Dependent Response Function and Generalized Lehmann Representation . . . . .	28
2.2.3. Kramers–Kronig Relations . . . . .	33
2.2.4. Spectroscopic Observables . . . . .	34
2.2.5. Properties of the Generalized Lehmann Representation . . . . .	35
<b>2.3. Resonance Line Shapes . . . . .</b>	<b>38</b>
<b>2.4. Time-Dependent Density Functional Theory for Response     Calculations . . . . .</b>	<b>42</b>
2.4.1. Static Density Functional Theory . . . . .	43
2.4.2. Time-Dependent Density Functional Theory . . . . .	48
2.4.3. Time-Resolved Photoabsorption Spectroscopy - The Density- Density Response . . . . .	49
2.4.4. Kohn-Sham Linear Response Function . . . . .	52
2.4.5. Absorption Spectra from the Time-Evolution . . . . .	53
2.4.6. Time-Resolved Photoelectron Spectroscopy – The Mask Method	54
<b>2.5. Few-Electron Systems and Model-Hamiltonians . . . . .</b>	<b>58</b>
2.5.1. Model Hamiltonians . . . . .	59
2.5.2. Rabi-Oscillations . . . . .	60
<b>2.6. Quantum Optimal Control Theory . . . . .</b>	<b>64</b>
2.6.1. General Aspects of Quantum Optimal Control Theory . . . . .	65

2.6.2.	Derivation of the Quantum-OCT Equations for the Optimization of Response Functions . . . . .	69
2.6.3.	Derivation of a Gradient-Free Algorithm for Quantum Optimal Control Theory . . . . .	70
<b>2.7.</b>	<b>The Colour Perception of the Human Eye . . . . .</b>	<b>72</b>

---



---

*“Everything should be as simple as possible, but not simpler.”*

*- Albert Einstein*

---

In this thesis, we investigate the reaction of atoms and molecules to the irradiation with electromagnetic fields on the attosecond time scale. The dynamics of non-relativistic, quantum-mechanical systems are governed by the time-dependent Schrödinger equation

$$i \frac{\partial}{\partial t} |\Xi\rangle = \hat{H}(t) |\Xi\rangle \quad (2.1)$$

with the wave function  $|\Xi\rangle$  and the time-dependent Hamiltonian

$$\hat{H}(t) = \hat{T}_I + \hat{T}_e + \hat{V}_{II} + \hat{V}_{ee} + \hat{V}_{Ie} + \hat{V}_{ext}(t), \quad (2.2)$$

---

where  $\hat{V}_{ext}(t)$  is the external potential and

$$\begin{aligned}
\hat{T}_I &= - \sum_I \frac{\nabla_I^2}{2M_I}, \\
\hat{V}_{II} &= \frac{1}{2} \sum_{IJ} \frac{Z_I Z_J}{|\hat{\mathbf{R}}_I - \hat{\mathbf{R}}_J|}, \\
\hat{T}_e &= - \sum_i \frac{\nabla_i^2}{2m}, \\
\hat{V}_{ee} &= \frac{1}{2} \sum_{ij} \frac{1}{|\hat{\mathbf{r}}_i - \hat{\mathbf{r}}_j|}, \\
\hat{V}_{eI} &= \sum_{iI} \frac{Z_I}{|\hat{\mathbf{r}}_i - \hat{\mathbf{R}}_I|},
\end{aligned} \tag{2.3}$$

where  $\hat{\mathbf{r}}_i$  are the positions of the electrons,  $m$  is the electronic mass and  $\hat{\mathbf{R}}_I$ ,  $\mathbf{M}_I$  and  $Z_I$  are the positions, masses and charges of the nuclei. Note, that atomic units will be used throughout the whole thesis.

Solving (2.1) is computationally challenging and in practice becomes unfeasible for systems with more than two or three degrees of freedom. Therefore a range of approximations have to be applied.

One, that is commonly used to separate the electronic from the nuclear degrees of freedom, is the Born-Oppenheimer approximation [159, 160]. The Born-Oppenheimer approximation states, that due to the mass difference between atoms and electrons, atomic and electronic motion happen on different time-scales and therefore the combined Schrödinger equation (2.1) can be separated into a nuclear and an electronic part.

In this thesis, we look at electron dynamics at the attosecond time scale. Since we want to focus on the electronic part, we use the Born-Oppenheimer approximation in combination with the Clamped-Ion Approximation, in which the motion of the nuclei is completely neglected.

In this chapter, I present the theoretical background to the work done. I start by introducing the Born-Oppenheimer approximation in 2.1. Afterwards, I will exclusively focus on the electronic problem. The response of a system to an external perturbation is the topic of response theory, where the connection between perturbation and response is given by the respective response function. If the perturbation is sufficiently weak, one

neglects higher orders in the response function, leading to the linear response theory, which is presented in 2.2. Whilst the theory of linear response is usually based on a system in its ground state, where the external perturbation is used to probe the system, I show, how the formalism can be adapted to describe the response of systems out of equilibrium. This formalism is useful to describe pump-probe experiments, where external fields are not only used to probe, but also to excite the system. A generalized Lehmann representation of the response function for the non-overlapping regime, (where the probe arrives after the end of the pump), is presented in 2.2.2 followed by some general comments about the connection between real and imaginary part of the response function in Section 2.2.3. Up to here, everything was about general response functions. How the optical spectrum can be obtained from one of them – namely the dipole-dipole response, is presented in Section 2.2.4. With this connection in mind, in Section 2.2.5, I analyze the consequences of the time-dependency of the developed Lehmann representation for the spectra of excited states.

In our formalism, excited bound states have an infinitely long life time and spectroscopic peaks are  $\delta$ -functions, which have to be broadened artificially in order to mimic spontaneous emission and other decay mechanisms that could be present in experiments. Different broadening mechanisms and the resulting line shapes are discussed in Section 2.3. Furthermore, it is shown, how different line shapes are connected with each other and can be converted into each with the help of lasers.

At the beginning of this chapter, I said, that solving the time-dependent Schrödinger equation (2.1) is computational challenging. For many-electron systems, only applying the Born-Oppenheimer approximation is not enough to make the problem solvable. Further approximations have to be made for the electronic part of the problem. One way to tackle the electronic problem is Density Functional Theory (DFT) and its time-dependent counterpart TDDFT, which replace the many-body wave function by the far more manageable electronic density.

Section 2.4 marries the concepts of response functions with the concept of treating electronic systems using TDDFT. After a brief introduction, in Section 2.4.1, I present the Hohenberg-Kohn (HK) theorem, which states, that indeed there is one-to-one correlation between the external potential (and therefore the many-body wave function) and its ground state density. The HK variational principle then finds the ground state density by minimizing the energy functional, which is a functional of the density. This is mostly

---

done using the Kohn-Sham (KS) equations, where the density is constructed using a system of fictitious non-interacting electrons occupying the so-called KS orbitals. Whilst DFT is in principle exact, this functional is not known analytically and in practice has to be approximated. Section 2.4.1.1 presents the approximations used in this thesis. For time-dependent problems, a similar theory exists, connecting the time-dependent density to the time-dependent external potential using time-dependent KS orbitals. A short introduction into TDDFT and how to propagate the KS orbitals in time is given in Section 2.4.2.

After the introduction into (TD)DFT it should be clear, that the most important observable in this context is the time-dependent density. How the time-dependent density can be used to obtain the density-density response function and how the density-density response function is coupled to the dipole-dipole response function, which at the end provides the optical spectrum of a system is shown in Section 2.4.3 followed by the connection between many-body and KS-response function in Section 2.4.4. In practice, solving the response equations can be done using several approaches, e.g. by linearizing the time-dependent Kohn-Sham (TDKS) equations in the frequency domain and casting them into matrix eigenvalue form or by propagating the same equations in real time applying a sufficiently weak dipole perturbation. While the first one mostly focuses on ground state spectrum, the extension of the latter to the case of excited state spectroscopy is straightforward and our method of choice. A small introduction into its principles can be found in Section 2.4.5.

Finally in Section 2.4.6, I explain how to perform time-resolved photo-electron spectroscopy (TRPES) calculation in TDDFT using the mask method.

Whilst for bigger systems methods like (TD)DFT have to be used, it is instructive to test theories for smaller systems, which can be solved either analytically or numerically exactly. In this thesis, calculations for several model systems (in one or three dimensions) are used. This is the topic of Section 2.5.1. For the analysis of excited state spectra in the exact case, the concept of Rabi-oscillations assuming a two-level system is used throughout this thesis. Section 2.5.2 gives a short introduction into the text-book derivation of Rabi oscillations. This concept is then extended to certain cases of three-level systems.

As mentioned before, this thesis not only deals with spectroscopy, but combines excited state spectroscopy with control. Not only how to probe, but also how to create and control excited states is addressed. The general concept of control is presented in Section 2.6 as

well as the general procedure to derive an algorithm to control spectra.

Finally, we analyze optical spectra in the context of their perception by us - human beings. We argue, that by controlling the spectrum of a system, one can control its colour. In this context, one has to understand, how the light, that is perceived by the human retina is translated into human colour perception. This question is addressed in Section 2.7.

## 2.1. Born-Oppenheimer and Clamped-Ion Approximation

Thanks to the large difference in masses between nuclei and electrons, a great simplification in the problem of studying a system combining both types of particles can be achieved by making use of the so-called Born-Oppenheimer approximation [159, 160]. With it, the problem posed by the Hamiltonian (2.2) can be split into two steps: one that involves the resolution of an electronic-only problem (yet, in principle, one problem for each possible nuclear configuration), and one that involves the solution of an equation for the nuclei only, moving on some “potential surfaces” constructed in the previous step. First, one defines an “electronic Hamiltonian” for each nuclear configuration  $\mathbf{R} = \{\mathbf{R}_I\}$ :

$$\hat{H}_e(\mathbf{R}) = \hat{T}_e + V_{II}(\mathbf{R}) + \hat{V}_{ee} + \hat{V}_{Ie}(\mathbf{R}). \quad (2.4)$$

Note that, here,  $\mathbf{R}$  are *parameters*, and not operators. Next, we consider an orthonormal basis for the electronic Hilbert space, also at each nuclear configuration:  $\{\Psi_k(\mathbf{r}; \mathbf{R})\}_k$ . Using this basis, we may expand (without, yet, any approximation) the full solution of the Schrödinger equation

$$\hat{H}\Xi(\mathbf{r}, \mathbf{R}) = E\Xi(\mathbf{r}, \mathbf{R}) \quad (2.5)$$

as:

$$\Xi(\mathbf{r}, \mathbf{R}) = \sum_k \Psi_k(\mathbf{r}; \mathbf{R}) \chi_k(\mathbf{R}). \quad (2.6)$$

The substitution of this expression into Eq. (2.5) yields, after some algebra:

$$\left[ \hat{T}_I + T'_{kk}(\hat{\mathbf{R}}) + T''_{kk}(\hat{\mathbf{R}}) + U_{kk}(\hat{\mathbf{R}}) - E \right] |\chi_k\rangle = - \sum_{k' \neq k} \left[ U_{kk'}(\hat{\mathbf{R}}) + T'_{kk'}(\hat{\mathbf{R}}) + T''_{kk'}(\hat{\mathbf{R}}) \right] |\chi_{k'}\rangle, \quad (2.7)$$



where:

$$U_{kk'}(\mathbf{R}) = \langle \Psi_k(\mathbf{r}; \mathbf{R}) | \hat{H}_e(\mathbf{R}) | \Psi_{k'}(\mathbf{r}; \mathbf{R}) \rangle, \quad (2.8)$$

$$T'_{kk'}(\mathbf{R}) = - \sum_I \frac{1}{M_I} \mathbf{d}_{kk'}^I(\mathbf{R}) \cdot \nabla_{\mathbf{R}} \quad (2.9)$$

$$T''_{kk'}(\mathbf{R}) = - \sum_I \frac{1}{2M_I} \langle \Psi_k(\mathbf{r}; \mathbf{R}) | \nabla_{\mathbf{R}}^2 | \Psi_{k'}(\mathbf{r}; \mathbf{R}) \rangle \quad (2.10)$$

$$\mathbf{d}_{kk'}^I(\mathbf{R}) = \langle \Psi_k(\mathbf{r}; \mathbf{R}) | \nabla_{\mathbf{R}} | \Psi_{k'}(\mathbf{r}; \mathbf{R}) \rangle \quad (2.11)$$

After these manipulations, one may attempt a solution of the full Schrödinger equation in two steps, where the first step is the construction of the electronic basis and the computation of the previous objects and the second step is the solution of the nuclear Eq. (2.7).

Normally, the orthonormal basis is chosen to be the eigenbasis of the electronic Hamiltonian:

$$\hat{H}_e(\mathbf{R}) | \Psi_k(\mathbf{r}; \mathbf{R}) \rangle = U_{kk}(\mathbf{R}) | \Psi_k(\mathbf{r}; \mathbf{R}) \rangle, \quad (2.12)$$

so that the off-diagonals  $U_{kk'}(\mathbf{R}) = 0$  ( $k \neq k'$ ) vanish. Also, usually (especially if the electronic eigenstates can be chosen to be real),  $T'_{kk}(\mathbf{R}) = 0$ . However, the Born-Oppenheimer approximation, essentially, amounts to neglecting the right hand side off-diagonal ( $k \neq k'$ ) terms  $T_{kk'}$  and  $T''_{kk'}$  (the “non-adiabatic couplings”), and the BO diagonal correction  $T''_{kk}$ . In this manner, the nuclear wave functions are completely decoupled:

$$\left[ \hat{T}_I + U_{kk}(\hat{\mathbf{R}}) \right] | \chi_k \rangle = E | \chi_k \rangle. \quad (2.13)$$

A perturbation theory analysis permits to understand that the neglect of the terms assumed in the Born-Oppenheimer approximation is good if the ratio of electronic to nuclear masses is small.

This analysis can be extended to the time-dependent Schrödinger equation, and one may propagate “nuclear wave packets” moving on the electronic “potential surfaces”  $U_{kk}(\mathbf{R})$ . Some subtleties arise whenever the nuclear wave packets approach regions in configuration space where the potential surfaces cross, rendering the Born-Oppenheimer approximation invalid.

As a further step, one may “complete” the Born-Oppenheimer approximation by taking

a classical limit for the nuclear degrees of freedom, arriving to the realm of “molecular dynamics”. This limit can also be taken *before* the neglect of the non-adiabatic terms, arriving to some form of non-adiabatic molecular dynamics.

In any case, for this work we can in fact ignore the nuclear movement (due to the very fast phenomena we wish to study), and assume the **Clamped-Ion Approximation**. Therefore, we are only concerned with the electronic Hamiltonian (2.4), for nuclear positions fixed at the equilibrium positions (in fact, we may safely remove from the electronic Hamiltonian the nucleus-nucleus interaction term  $V_{II}(\mathbf{R})$ , since it is now merely a constant).

## 2.2. Linear Response Theory

When a time-dependent electromagnetic pulse passes through a sample, the molecules polarize and this polarization modifies the otherwise free propagation of light, leading to e.g. its partial absorption. In a dilute gas, assuming the electric dipole approximation and a sufficiently weak pulse, the dipole–dipole linear dynamic polarizability entirely determines the polarization of the medium and therefore the amount of absorption. Usually this is understood at equilibrium: the gas is supposed to be at thermal equilibrium and the only light pulse present is the one, the absorption of which we want to measure. The pump-probe situation discussed in this thesis is slightly different. Here, we want to measure the absorption of a probe pulse by a gas, that is also irradiated by a pump-pulse, either simultaneously (overlapping regime) or with a certain delay (non-overlapping regime). In this situation, the task is to compute the electric dipole of a system, which is evolving in time with and without the probe pulse – the difference is the excess of polarization, which is responsible for the absorption of the probe.

In this chapter, I first derive a generalized Kubo formula of the retarded response function of a system governed by a time-dependent Hamiltonian. This Kubo formula is valid in the overlapping as well as in the non-overlapping regime. For the non-overlapping regime, I then proceed to write-down a generalized Lehmann formula of the response function that will help us gain microscopical understanding of the mechanisms behind pump-probe experiments. After shortly presenting the Kramers–Kronig relations and showing the connection between the dipole–dipole response function and the photoabsorption cross-section I present a detailed analysis of the generalized Lehmann formula and the

information, that it holds in the case of transient absorption spectroscopy.

### 2.2.1. General Time-Dependent Linear Response Theory

Here, we give a short overview about general time-dependent linear response theory. For a more detailed description, we refer the reader to [3, 161, 162, 163, 164].

We consider a system described by the Hamiltonian

$$\hat{H}_0[\mathcal{E}](t) = \hat{\mathcal{H}} + \mathcal{E}(t)\hat{V}, \quad (2.14)$$

where  $\hat{\mathcal{H}}$  is the static Hamiltonian, that describes the system itself and  $\mathcal{E}(t)\hat{V}$  is the coupling to a pump laser pulse. Note, that we only treat the electric part of the electromagnetic field, neglecting the magnetic part.  $\hat{H}_0[\mathcal{E}](t)$  is the “unperturbed” Hamiltonian, which contains only the pump pulse. The full Hamiltonian results from the addition of the time-dependent perturbation  $\hat{H}_1(t) = F(t)\hat{V}$ , where  $F(t)$  describes the probe pulse:

$$\hat{H}(t) = \hat{\mathcal{H}} + \mathcal{E}(t)\hat{V} + F(t)\hat{V}. \quad (2.15)$$

The time evolution of the system is given by

$$i\frac{\partial}{\partial t}\hat{\rho}(t) = [\hat{H}(t) + F(t)\hat{V}, \hat{\rho}(t)] \quad (2.16)$$

and initially ( $t_{-\infty} \leq t_0$ , some time before the arrival of both pump and probe laser), the system is at equilibrium

$$[\hat{\mathcal{H}}, \hat{\rho}(t_{-\infty} \leq t_0)] = 0. \quad (2.17)$$

For a given pump  $\mathcal{E}(t)$ , we may assume the evolution of the system to be a functional of the probe shape  $\hat{\rho} = \hat{\rho}[F]$  and we can expand  $\hat{\rho}$  in a Taylor series (in a functional sense) around the case of no perturbation  $F(t) = 0$ :

$$\hat{\rho}[F] = \sum_{n=0}^{\infty} \hat{\rho}_n[F], \quad (2.18)$$

where  $\hat{\rho}_0$  is the unperturbed system evolution ( $F(t) = 0$ , only the pump pulse is present)

and  $\hat{\rho}_n$  is  $n$ th order in the perturbing field  $F(t)$ :

$$\hat{\rho}[\lambda F] = \lambda^n \hat{\rho}[F]. \quad (2.19)$$

A similar Taylor expansion is possible for any expectation value  $O(t)$  of an observable  $\hat{O}$ :

$$O(t) = \text{Tr} \left\{ \hat{\rho}(t) \hat{O} \right\} = \sum_{n=0}^{\infty} O_n(t) \quad (2.20)$$

with

$$O_n(t) = \text{Tr} \left\{ \hat{\rho}_n(t) \hat{O} \right\}. \quad (2.21)$$

$O(t) - O_0(t)$  is called the **response** of  $\hat{O}$  to the perturbation  $F(t)\hat{V}$ , where  $O_1(t)$  is the linear,  $O_2(t)$  the quadratic response and so on. There is no proof that this expansion is convergent, but normally one assumes that it does as long as the perturbing field  $F(t)$  is sufficiently weak. Note, that in the case of no pump-laser,  $O_0$  is time-independent and we recover the usual formalism of linear response from the ground state.

For sufficiently weak probes, we are only interested in the linear response

$$\delta O(t) = O(t) - O_0(t) \approx O_1(t) = \text{Tr} \left\{ \hat{\rho}_1(t) \hat{O} \right\}, \quad (2.22)$$

where  $\hat{\rho}_1(t)$  is the solution to the linearized equation

$$i \frac{\partial}{\partial t} \rho_1(t) = \left[ \hat{H}_0(t), \hat{\rho}_1(t) \right] + \left[ F(t) \hat{V}, \hat{\rho}_0(t) \right] \quad (2.23)$$

with the initial condition  $\hat{\rho}_1(t_0) = 0$ . To obtain the solution  $\hat{\rho}_1(t)$  of Eq. (2.23), we introduce the propagator  $\hat{U}[\mathcal{E}](t, t')$  for the unperturbed time evolution in presence of only the pump  $\mathcal{E}(t)$ :

$$\hat{U}[\mathcal{E}](t, t') = \hat{T} \exp \left\{ -i \int_{t'}^t d\tau \hat{H}_0[\mathcal{E}](\tau) \right\}, \quad (2.24)$$

where  $\hat{T} \exp\{\dots\}$  is the usual time-ordered exponential [165]. For the moment, we skip the explicit notation of the functional dependence on  $\mathcal{E}$ , but will put it back later.

Eq. (2.24) is the formal solution to the equation of motion for the propagator

$$i \frac{\partial}{\partial t} \hat{U}(t, t') = \hat{H}_0(t) \hat{U}(t, t') \quad (2.25)$$

with the boundary condition  $\hat{U}(t, t) = \hat{I}$ . Using Eq. (2.25), we find the solution to Eq. (2.23) as

$$\hat{\rho}_1(t) = -i \int_{t_0}^t dt' \hat{U}(t, t') \left[ F(t') \hat{V}, \hat{\rho}_0(t') \right] \hat{U}(t', t), \quad (2.26)$$

where the differentiation of the propagators yields the first term of the right-hand side of Eq. (2.23), while the differentiation with respect to the upper limit of the  $t'$  integral yields the second term. Inserting  $\hat{\rho}_1(t)$  into Eq. (2.22) yields the linear response

$$O_1(t) = -i \int_{t_0}^t dt' F(t') \text{Tr} \left\{ \hat{\rho}(t_0) \left[ \hat{O}_I(t), \hat{V}_I(t') \right] \right\}, \quad (2.27)$$

with the operators  $\hat{O}(t)$  in the interaction representation being defined as

$$\hat{O}_I(t) := \hat{U}(t_0, t) \hat{O} \hat{U}(t, t_0) = \hat{U}^\dagger(t, t_0) \hat{O} \hat{U}(t, t_0). \quad (2.28)$$

Finally we rewrite the linear response as

$$O_1[\mathcal{E}](t) = \int_{-\infty}^{\infty} dt' F(t') \chi_{\hat{O}, \hat{V}}[\mathcal{E}](t, t'), \quad (2.29)$$

where

$$\chi_{\hat{O}, \hat{V}}[\mathcal{E}](t, t') = -i \theta(t - t') \text{Tr} \left\{ \hat{\rho}(t_0) \left[ \hat{O}_I[\mathcal{E}](t), \hat{V}_I[\mathcal{E}](t') \right] \right\} \quad (2.30)$$

is the **retarded response function**. In Eq. (2.29) we replaced the lower integral limit by  $-\infty$ , because of Eq. (2.17) and we could replace the upper integral limit by  $\infty$  because of the step-function in the response-function. The step-function ensures the causality requirement, that any response at time  $t$  is due to a perturbation at an earlier time  $t' < t$ . Eq. (2.29) has the standard form of **Kubo's formula** [166] with one minor difference. In our case, the unperturbed Hamiltonian  $\hat{H}_0(t)$  is time-dependent and therefore the time-propagation of the operators has to be done using the time-ordered exponentials (2.24). For systems at equilibrium (i.e. the Hamiltonian  $\hat{H}_0$  is time-independent and the system is initially at equilibrium), one makes use of the time-translational invariance, since one may prove that the expression for the response function only depends on  $t - t'$ , and not

on both times independently. This permits to define a response function that has only one time argument (the difference  $t - t'$ ) and only depends on properties of the system in absence of the probe.

In contrast, in Eqs. (2.29) and (2.30) we explicitly mention the functional dependence on  $\mathcal{E}$  to stress that in the more general case, the response function is a property of both the system (defined by the static Hamiltonian  $\hat{\mathcal{H}}$ ) and of the pump shape  $\mathcal{E}$  and explicitly depends on both times  $t$  and  $t'$ . The response itself is a functional of both pump and probe pulses, and after taking its Fourier transform can be written as

$$O_1[\mathcal{E}, F](\omega) = \int_{-\infty}^{\infty} dt' F(t') \chi_{\hat{O}, \hat{V}}[\mathcal{E}](\omega, t'). \quad (2.31)$$

In the next subsection we look closer at  $\chi_{\hat{O}, \hat{V}}[\mathcal{E}](\omega, t')$  and show, how one can derive a Lehmann-like representation of the frequency-dependent response function in the non-overlapping case, where the pump pulse has ended and the system evolves under the influence of the static Hamiltonian  $\hat{\mathcal{H}}$ .

### 2.2.2. Frequency Dependent Response Function and Generalized Lehmann Representation

In linear-response theory it is more common to work in the frequency domain than to consider the response in real time, because replacing the time by the frequency as variable enables us to extract the excitation energies of a system from its linear response. For a stationary initial state  $\rho(t_0)$  and a static Hamiltonian  $\hat{\mathcal{H}}$ , one makes use of the time-translational invariance of the response function, Fourier-transforms with respect to the time difference  $t - t'$  and arrives at the Lehmann representation of the frequency-dependent response function.

We are interested in a situation, in which at the arrival of the probe the system is not in its ground state, but in an excited state, due to its excitation by a previous pump laser. We can show, that while for a general non-stationary state it is not possible to define a time-**independent** response function, one can still write down the Lehmann representation of the response function in closed form, which then additionally depends on the delay between pump and probe. Here, we present the time-dependent Lehmann representation for the non-overlapping regime, i.e. for the case, where the pump pulse has finished before the probe pulse arrives. In [107], a similar expression is presented,

that includes the overlapping regime.

In the non-overlapping regime, the situation is conceptually equivalent to considering a Hamiltonian

$$\hat{H}(t) = \hat{\mathcal{H}} + F(t)\hat{V} \quad (2.32)$$

with an arbitrary initial state described by the density operator  $\hat{\rho}[\mathcal{E}](t_0)$ , which the system has reached because of the former influence of the pump field  $\mathcal{E}$ . Hereafter, the time  $t_0$  is fixed after the pump pulse, and before the arrival of the probe. In contrast to the very general case described in Section 2.2.1, the unperturbed Hamiltonian is now time-independent (but the unperturbed evolution of the system is not).

We recall the time-dependent linear response function (2.30)

$$\chi_{\hat{O},\hat{V}}[\mathcal{E}](t,t') = -i\theta(t-t') \text{Tr} \left\{ \hat{\rho}(t_0) \left[ \hat{O}_I[\mathcal{E}](t), \hat{V}_I[\mathcal{E}](t') \right] \right\}. \quad (2.33)$$

We now perform several steps at once. First we write the density operator as

$$\hat{\rho}[\mathcal{E}](t_0) = \sum_{n=1}^{\infty} s_n |\Psi_n(t_0)\rangle \langle \Psi_n(t_0)|, \quad \sum_n s_n = 1 \quad (2.34a)$$

with

$$\text{Tr} \left\{ \hat{\rho}[\mathcal{E}](t_0) \hat{O} \right\} = \sum_n s_n \langle \Psi_n(t_0) | \hat{O} | \Psi_n(t_0) \rangle, \quad (2.34b)$$

where  $s_n$  is the probability of the system to be in the state  $|\Psi_n(t_0)\rangle$  at  $t = t_0$ . For ease of notation, we assume, that the system is in a pure state, i.e. that all  $s_n$  are zero except for one, which is one. This reduces the trace to

$$\text{Tr} \left\{ \hat{\rho}[\mathcal{E}](t_0) \hat{O} \right\} = \langle \Psi(t_0) | \hat{O} | \Psi(t_0) \rangle \quad (2.34c)$$

with an arbitrary wave function  $|\Psi(t_0)\rangle$ , which in the eigenbasis of  $\hat{\mathcal{H}}$  is expressed as

$$|\Psi(t_0)\rangle = \sum_{j=1}^{\infty} \gamma_j |\Phi_j\rangle, \quad \hat{\mathcal{H}} |\Phi_j\rangle = \varepsilon_j |\Phi_j\rangle \quad (2.34d)$$

where the sum includes both bound and continuum eigenstates  $|\Phi_j\rangle$ ; for the latter, the sum over states has to be converted into the integral over a continuum of states. The

expansion coefficients  $\gamma_j$  are complex with

$$\gamma_j = |\gamma| e^{i\varphi_j} \quad (2.34e)$$

and depend on the end-time  $t_0$  of the pump pulse, which is the time, when we do the projection. Finally we make use of the interaction representation

$$\hat{V}_I = e^{i\hat{\mathcal{H}}(t-t_0)} \hat{V} e^{-i\hat{\mathcal{H}}(t-t_0)} \quad (2.34f)$$

while inserting the completeness relation

$$1 = \sum_{j=1}^{\infty} |\Phi_j\rangle\langle\Phi_j|. \quad (2.34g)$$

Using Eqs. (2.34), Eq. (2.33) turns into

$$\chi_{\hat{O},\hat{V}}[\mathcal{E}](t,t') = -i\theta(t-t') \sum_{jkm} \gamma_j^* \gamma_k \langle\Phi_j|\hat{O}|\Phi_m\rangle \langle\Phi_m|\hat{V}|\Phi_k\rangle e^{-i(\varepsilon_m-\varepsilon_j)(t-t')} e^{-i(\varepsilon_k-\varepsilon_j)(t'-t_0)} + cc.$$

Finally we substitute the step-function  $\theta(t-t')$  by the integral representation

$$\theta(t-t') = \lim_{\eta \rightarrow 0^+} \frac{i}{2\pi} \int_{-\infty}^{\infty} d\omega' \frac{e^{-i\omega'(t-t')}}{\omega' + i\eta} \quad (2.35)$$

and Fourier transform in order to arrive to a generalized **Lehmann representation** of the linear response function (here and in the following,  $\lim_{\eta \rightarrow 0^+}$  is understood):

$$\chi_{\hat{O},\hat{V}}[\mathcal{E}](\omega, t_0 + \tau) = \sum_{jkm} \left\{ \frac{\gamma_j^* \gamma_k \langle\Phi_j|\hat{O}|\Phi_m\rangle \langle\Phi_m|\hat{V}|\Phi_k\rangle}{\omega - (\varepsilon_m - \varepsilon_j) + i\eta} e^{-i(\varepsilon_k - \varepsilon_j)\tau} - \frac{\gamma_j \gamma_k^* \langle\Phi_j|\hat{O}|\Phi_m\rangle^* \langle\Phi_m|\hat{V}|\Phi_k\rangle^*}{\omega + (\varepsilon_m - \varepsilon_j) + i\eta} e^{i(\varepsilon_k - \varepsilon_j)\tau} \right\}, \quad (2.36)$$

where we introduced the “delay time”

$$\tau = t' - t_0. \quad (2.37)$$



For an illustration see Fig. 2.1. If the operators  $\hat{V}$  and  $\hat{O}$  are real, we can always chose

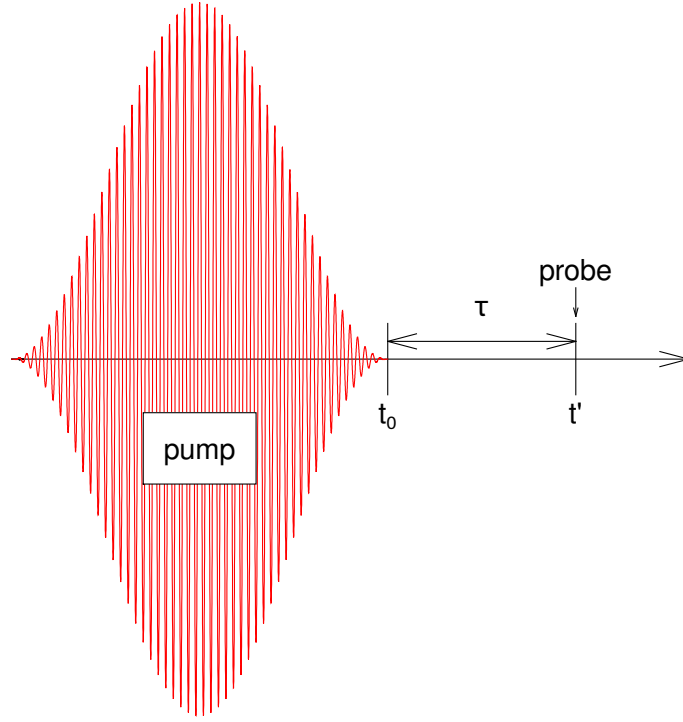


Figure 2.1.: Illustration of the times used in the derivation of the generalized Lehmann representation of the response function.

the basis set  $\{|\Phi_i\rangle\}$  to be real and Eq. (2.36) simplifies to

$$\chi_{\hat{O},\hat{V}}[\mathcal{E}](\omega, t_0+\tau) = \sum_{jkm} \langle \Phi_j | \hat{O} | \Phi_m \rangle \langle \Phi_m | \hat{V} | \Phi_k \rangle \left\{ \frac{\gamma_j^* \gamma_k e^{-i(\varepsilon_k - \varepsilon_j)\tau}}{\omega - (\varepsilon_m - \varepsilon_j) + i\eta} - \frac{\gamma_j \gamma_k^* e^{i(\varepsilon_k - \varepsilon_j)\tau}}{\omega + (\varepsilon_m - \varepsilon_j) + i\eta} \right\}, \quad (2.38)$$

which, using

$$\gamma_j(\tau) := \gamma_j e^{-i\varepsilon_j\tau} = |\gamma_j| e^{-i(\varepsilon_j\tau - \varphi_j)} \quad (2.39)$$

and

$$\omega_{jm} = \varepsilon_m - \varepsilon_j \quad (2.40)$$

can be rewritten as

$$\chi_{\hat{O}, \hat{V}}[\mathcal{E}](\omega, t_0 + \tau) = \sum_{jkm} \langle \Phi_j | \hat{O} | \Phi_m \rangle \langle \Phi_m | \hat{V} | \Phi_k \rangle \left\{ \frac{\gamma_j^*(\tau) \gamma_k(\tau)}{\omega - \omega_{jm} + i\eta} - \frac{\gamma_j(\tau) \gamma_k^*(\tau)}{\omega + \omega_{jm} + i\eta} \right\}. \quad (2.41)$$

The Lehmann representation is one of the most important results in linear response theory because it shows explicitly how a frequency-dependent perturbation couples to the excitation spectrum of a system. Here, we present a generalization to a pump-probe situation, where the probe arrives with some positive delay to the pump pulse (non-overlapping regime).

Before we continue to the derivation of the Kramers–Kronig relations, let us firstly introduce some useful notation. For further discussions, we divide the linear response function into its real and its imaginary part

$$\chi(\omega) = \chi'(\omega) + i\chi''(\omega). \quad (2.42)$$

We note, that  $\chi'(\omega)$  is an even function

$$\chi'(-\omega) = \chi'(\omega) \quad (2.43)$$

and unchanged under time-reversal  $t \rightarrow -t$ . It is called the **reactive** part of the response function. In contrast, the imaginary part  $\chi''(\omega)$  is an odd function

$$\chi''(-\omega) = -\chi''(\omega) \quad (2.44)$$

and changes its sign under time reversal. It is called **dissipative** or **absorptive** part of the response function and is also known as the **spectral function**.

I will now proceed to present the Kramers–Kronig relations for general response functions before pointing out, how the the density-density response function, a variable that can be readily obtained with the help of TDDFT, relates to the photoabsorption cross-section of a system. With this a bit more concrete example in mind, I will finally present a detailed analysis of Eq. (2.41), pointing out the differences to the usual ground-state formalism.

### 2.2.3. Kramers–Kronig Relations

The Kramers–Kronig relations relate the real and imaginary part of the response function (defined as in Eq. (2.42)) to each other via

$$\chi'(\omega) = \frac{1}{\pi} P \left[ \int_{-\infty}^{\infty} d\omega' \frac{\chi''(\omega')}{\omega - \omega'} \right] \quad (2.45a)$$

$$\chi''(\omega) = -\frac{1}{\pi} P \left[ \int_{-\infty}^{\infty} d\omega' \frac{\chi'(\omega')}{\omega - \omega'} \right], \quad (2.45b)$$

where  $P$  denotes the Cauchy principal value. The Kramers–Kronig relations are derived as follows. Cauchy’s residue theorem states, that, since the response function is analytic in the upper half of the complex plane,

$$\oint d\omega' \frac{\chi(\omega')}{\omega' - \omega} = 0 \quad (2.46)$$

for any contour within this region. We choose the contour to trace the real axis and come back via a large semicircle in the upper half plane. The integral over the semicircle vanishes because  $\chi(\omega)$  vanishes faster than  $1/|\omega|$  and we are left with the integral along the real axis. Using the relation

$$\lim_{\eta \rightarrow 0^+} \frac{1}{\omega - \omega' + i\eta} = P \left[ \frac{1}{\omega - \omega'} \right] - i\pi\delta(\omega - \omega') \quad (2.47)$$

we get

$$0 = \oint d\omega' \frac{\chi(\omega')}{\omega' - \omega} = P \left[ \int_{-\infty}^{\infty} d\omega' \frac{\chi(\omega')}{\omega' - \omega} \right] - i\pi\chi(\omega). \quad (2.48)$$

Reordering Eq. (2.48) leads to the Kramers–Kronig relation

$$\chi(\omega) = \frac{1}{i\pi} P \left[ \int_{-\infty}^{\infty} d\omega' \frac{\chi(\omega')}{\omega' - \omega} \right]. \quad (2.49)$$

Separating this with respect to real and imaginary part finally leads to Eqs. (2.45). Transforming the integrals into one of definite parity by multiplying the denominator by  $\omega' + \omega$  and using the symmetry relation  $\chi(-\omega) = \chi^*(\omega)$ , we can collapse the integration along the real axis and arrive to the version of the Kramers–Kronig relations, that is

often found in literature about response calculations

$$\chi'(\omega) = \frac{2}{\pi} P \left[ \int_0^\infty d\omega' \omega' \frac{\chi''(\omega')}{\omega'^2 - \omega^2} \right] \quad (2.50a)$$

$$\chi''(\omega) = -\frac{2\omega}{\pi} P \left[ \int_0^\infty d\omega' \frac{\chi'(\omega')}{\omega'^2 - \omega^2} \right]. \quad (2.50b)$$

#### 2.2.4. Spectroscopic Observables

The linear optical properties of finite systems are characterized by the frequency dependent **dipole-dipole polarizability**  $\alpha_{\mu\nu} = \chi_{\hat{D}_\mu, \hat{D}_\nu}$ , where the dipole operator is defined as

$$\hat{D}_\mu = - \sum_{i=1}^N \hat{r}_\mu^{(i)} \quad (2.51)$$

in which  $N$  is the number of electrons. As we will see in Section 2.4.3, the dipole-dipole polarizability can be easily obtained from the density-density response function, providing a straightforward way of using time-dependent density functional theory to simulate absorption spectroscopy experiments. This is especially true, since the expectation value of the required observable in this case – the dipole operator – is an explicit functional of the density: while in principle, all observables are functionals of the time-dependent density, in practice their functional form may be unknown.

The dipole-dipole polarizability describes the induced **electronic polarization**  $\mathbf{p}(t)$  of a system, that is caused by a perturbing electric field  $\mathbf{E}(t)$ . If  $\mathbf{E}(t)$  is monochromatic of frequency  $\omega$  with a wave lengths long enough to apply the dipole approximation (i.e. we assume, that the system exposed to the laser is small in comparison to the wave length  $2\pi/\lambda x \ll 1$ ) and linearly polarized along the  $r_\nu$ -direction ( $r_\nu$  being one of the Cartesian coordinates  $x, y, z$ ) with amplitude  $E_0$ , the time-dependent dipole-dipole polarizability tensor  $\alpha_{\mu\nu}(t, t')$  relates the induced **electronic polarization** in the  $\mu$ -direction  $p_\mu(t, t')$  with the perturbing electric field in the  $r_\nu$ -direction  $E_\nu = E_0 e^{-i\omega t}$  like

$$p_\mu(t, t') = \sum_\nu \alpha_{\mu\nu}(t, t') E_\nu(t). \quad (2.52)$$

From the absorptive part of the polarizability tensor in frequency space  $\alpha_{\mu\nu}(\omega, t_0 + \tau)$ ,

we obtain the **photoabsorption cross-section** like ([165])

$$\sigma_{\mu\nu}(\omega, t_0 + \tau) = \frac{4\pi\omega}{c} \Im \alpha_{\mu\nu}(\omega, t_0 + \tau) \quad (2.53)$$

and finally the **average absorption coefficient**

$$\bar{\sigma}(\omega, t_0 + \tau) = \frac{1}{3} \text{Tr} \sigma(\omega, t_0 + \tau). \quad (2.54)$$

### 2.2.5. Properties of the Generalized Lehmann Representation

The following analysis is similar to an analysis, that was published by Perfetto and Stefanucci [107]. Nonetheless, the results were obtained independently.

In Section 2.2.2 we arrived to the generalized Lehmann representation (2.41) of a general response function from an arbitrary excited state under the influence of an ultra-short (delta-kick) probe pulse. Since in this work we are interested in the average absorption coefficient and therefore in the trace of the polarizability tensor, in the following we focus on its diagonal elements:

$$\alpha_{\mu\mu} [\mathcal{E}] (\omega, t_0 + \tau) = \sum_{jkm} d_{jm} d_{mk} \left\{ \frac{\gamma_j(\tau) \gamma_k^*(\tau)}{\omega + \omega_{jm} + i\eta} - \frac{\gamma_j^*(\tau) \gamma_k(\tau)}{\omega - \omega_{jm} + i\eta} \right\} \quad (2.55)$$

with the dipole matrix elements

$$d_{jm} = \langle \Phi_j | \hat{D}_\mu | \Phi_m \rangle. \quad (2.56)$$

Eq. (2.55) can be rewritten as

$$\alpha_{\mu\mu} [\mathcal{E}] (\omega, t_0 + \tau) = \sum_{jkm} d_{jm} d_{mk} |\gamma_j \gamma_k| \left\{ \frac{e^{i\Theta_{kj}(\tau)}}{\omega + \omega_{jm} + i\eta} - \frac{e^{-i\Theta_{kj}(\tau)}}{\omega - \omega_{jm} + i\eta} \right\} \quad (2.57)$$

with the time-dependent phase

$$\Theta_{kj}(\tau) = \varphi_j - \varphi_k - \omega_{kj}\tau. \quad (2.58)$$

We now discuss Eqs. (2.57) in more detail. The first thing to notice is that the time-

dependence of  $\alpha_{\mu\mu}[\mathcal{E}](\omega, t_0 + \tau)$  stems exclusively from the time-dependence of the expansion coefficients  $\gamma(\tau)$  and enters only through the phase factors. Therefore, the peak positions of the spectrum do not change, they are an intrinsic property of the many-body system and located at the many-body transition energies. The time-dependence is exclusively in the spectral weights, which we look at now.

We distinguish three cases. In case (i) we choose  $\gamma_j = \delta_{j0}$ , recovering the usual (time-independent) Lehmann representation of the polarizability tensor of the ground state

$$\alpha_{\mu\mu}[\mathcal{E}](\omega) = \sum_m |d_{0m}|^2 \left\{ \frac{1}{\omega + \omega_{0m} + i\eta} - \frac{1}{\omega - \omega_{0m} + i\eta} \right\} \quad (2.59)$$

which for  $\eta \rightarrow 0$  and using Eq. (2.47) leads to

$$\Im \alpha_{\mu\mu}[\mathcal{E}](\omega) = \sum_m |d_{0m}|^2 \{ \delta(\omega - \omega_{0m}) - \delta(\omega + \omega_{0m}) \}, \quad (2.60)$$

which is proportional to the spectrum. Since  $\omega_{0m} = \varepsilon_m - \varepsilon_0 > 0$  for all  $m$ , the spectrum is positive at all positive frequencies (and consequently negative at all negative frequencies).

In case (ii), we consider the simplest example of a non-equilibrium state: an excited, but still stationary state  $|\Psi_\xi\rangle \neq |\Psi_0\rangle$ , i.e.  $\gamma_j = \delta_{j\xi}$  in Eq. (2.55). The polarizability tensor has the same shape as in Eq. (2.60) but now the transition frequencies  $\omega_{\xi m}$  can be either positive or negative leading to a spectrum, where the peaks for  $\omega > 0$  (which we denote by  $\omega^+$ ) can be either positive or negative, leading to either absorption (positive) or emission (negative):

$$\Im \alpha_{\mu\mu}[\mathcal{E}](\omega)_{\omega>0} = \sum_{\xi < m} |d_{\xi m}|^2 \delta(\omega - \omega_{\xi m}) - \sum_{\xi > m} |d_{\xi m}|^2 \delta(\omega + \omega_{\xi m}). \quad (2.61)$$

It is noteworthy, that for a stationary state, the spectral weights of the peaks are time-independent and therefore in the same way that the ground state spectrum is independent of the time, the spectrum of a stationary state is independent of the delay between pump and probe.

Finally, in case (iii) we look at the spectrum of an arbitrary non-stationary state, which

assuming real basis functions  $\{|\Phi\rangle\}_i$  is

$$\Im \alpha_{\mu\mu}[\mathcal{E}](\omega, t_0 + \tau) = \sum_{jkm} d_{jm} d_{mk} |\gamma_j \gamma_k| \cos \Theta_{kj}(\tau) \{ \delta(\omega - \omega_{jm}) - \delta(\omega + \omega_{jm}) \}. \quad (2.62)$$

We see, that in the case, that the excited state is a linear combination of degenerate states, the spectrum is again time-independent. The only time-dependence occurs if the involved eigenstates are non-degenerate. In this case, we divide the spectrum into two parts:

$$\Im \alpha_{\mu\mu}[\mathcal{E}](\omega^+, t_0 + \tau) = \Im \alpha_{\mu\mu}^{EQ}[\mathcal{E}](\omega^+) + \Im \alpha_{\mu\mu}^{IN}[\mathcal{E}](\omega^+, t_0 + \tau), \quad (2.63a)$$

one part being the time-independent sum over equilibrium spectra of the eigenstates involved, scaled by their occupation:

$$\Im \alpha_{\mu\mu}^{EQ}[\mathcal{E}](\omega^+) = \sum_j |\gamma_j|^2 \left\{ \sum_{j < m} |d_{jm}|^2 \delta(\omega - \omega_{jm}) - \sum_{j > m} |d_{jm}|^2 \delta(\omega + \omega_{jm}) \right\}, \quad (2.63b)$$

the other one being a time-dependent interference term between the involved states:

$$\begin{aligned} \Im \alpha_{\mu\mu}^{IN}[\mathcal{E}](\omega, t_0 + \tau) = \sum_{j \neq k; m} d_{jm} d_{mk} |\gamma_j \gamma_k| & \left\{ \cos(\Theta_{kj}(\tau)) \delta(\omega - \omega_{jm}) \right. \\ & \left. - \cos(\Theta_{kj}(\tau)) \delta(\omega + \omega_{jm}) \right\}. \end{aligned} \quad (2.63c)$$

The equilibrium term depends neither on time nor on the initial phase differences  $\varphi_j - \varphi_k$ . It is influenced by the pump only through the occupations  $|\gamma_j|^2$ . The phase- and time-dependency of the spectrum enters exclusively through the interference terms, which are governed by the phase differences  $\Theta_{kj}(\tau)$ , which have contributions from both the phase difference  $\varphi_j - \varphi_k$  at the end of the laser and from its time evolution  $\omega_{kj}\tau$ , leading to a periodic beating pattern, which was firstly observed by Goulielmakis *et al* [1]. The time-dependence of a spectrum is therefore a clear sign of a non-stationary state.

Up to now we have analyzed the Lehmann representation for peaks of  $\delta$ -shape, i.e. with infinitely long lifetimes. Summarizing, we found:

- The positions of the excitation peaks are fixed at the many-body transition energies.
- The spectral weights of the peaks depend on the laser and on the delay  $\tau$  between

pump and probe pulse; peaks can be positive or negative depending on whether the rate of absorption is larger than the rate of stimulated emission or vice-versa.

- If the pump leaves the system in a non-stationary state, the spectral weights oscillate as a function of time. The involved frequencies correspond to the differences of the eigenenergies of the eigenstates occupied in the non-stationary state.
- For non-stationary states, the spectrum can be divided into an equilibrium and an interference contribution. The equilibrium contribution depends neither on time nor on the initial phase differences  $\varphi_j - \varphi_k$ . It depends on the pulse only through the occupations. Phase- and time-dependence of the spectrum enter through the interference term, which depends on the initial phase differences and periodically on time.

In the next section, we will discuss line broadening mechanisms and how the Lehmann representation can help to understand laser-induced lineshape changes. All these concepts will be illustrated in Chapter 4.

### 2.3. Resonance Line Shapes

Up to now we have looked at the positions and the spectral weights of transition peaks. Since we assumed infinite lifetimes of the states, the discussed peaks were of  $\delta$ -shape. Nonetheless, in reality, life times of excitations are finite. Thus, the corresponding transition peaks are not infinitely sharp but have some type of broadening and a specific shape depending on the interaction of the corresponding state with its environment.

For atoms and molecules in the gas-phase the main broadening mechanisms are lifetime, pressure (collision) and Doppler broadening. The minimal possible linewidth is determined by the natural broadening which is the consequence of spontaneous emission. If atoms and molecules are in gas-phase, they also undergo collisions depending on their velocity and the pressure of the gas. These collisions reduce the lifetime of the excited state, leading to pressure broadening. Finite lifetimes caused by spontaneous emission or by collisions produce lines with **Lorentzian** or **Breit-Wigner** shape

$$L(\bar{\omega}) = \frac{\Gamma/2}{\bar{\omega}^2 + \Gamma^2/4}, \quad (2.64)$$

where  $\Gamma$  is the full width at half maximum of  $L(\bar{\omega})$ . Coupled to the Lorentzian line shape



via the Kramers-Kronig relations is the **Rayleigh** shape

$$R(\bar{\omega}) = \frac{\bar{\omega}}{\bar{\omega}^2 + \Gamma^2/4}. \quad (2.65)$$

If the imaginary part of the polarizability tensor  $\alpha_{\mu\nu}(\omega, t_0 + \tau)$  is described by a Lorentzian, the real part is described by a Rayleigh and vice versa.

A different line shape is produced by the Doppler broadening, which is a consequence of particles moving with different velocities. In thermal Doppler broadening, the velocities of the particles follow a Maxwell distribution, which leads to the spectral lines being of **Gaussian** shape

$$G(\bar{\omega}) = \frac{1}{\sigma\sqrt{2\pi}} e^{-\left(\frac{\bar{\omega}}{2\sigma}\right)^2}, \quad (2.66)$$

with the full width at half maximum  $\Gamma = 2\sqrt{2\ln 2}\sigma$ . If lifetime/pressure broadening and Doppler broadening happen at the same time and  $\sigma$  and  $\Gamma$  are of the same order of magnitude, the lineshape is a convolution of Lorentzian and Gaussian, a peak of **Voigt** shape

$$V(\bar{\omega}, \sigma, \Gamma) = \int_{-\infty}^{\infty} d\omega' G(\omega') L(\bar{\omega} - \omega'). \quad (2.67)$$

If a discrete transition is embedded within a flat continuum of possible transitions, the configuration interaction couples both configurations, leading to an auto-ionizing state having contributions from both discrete and continuum states. This phenomenon was investigated by Ugo Fano in the context of the 2s2p state in Helium [148, 167]. He found the related peaks to be of the **Fano** line shape

$$F(\bar{\omega}) = \sigma_0 \frac{(q\Gamma/2 + \bar{\omega})^2}{\bar{\omega}^2 + \Gamma^2/4} \quad (2.68)$$

with the background  $\sigma_0$  and the Fano asymmetry parameter  $q$ , which describes the ratio between the scattering into the discrete state modified by the continuum states and the unperturbed continuum states. The Fano line shape consists of two contributions, one coming from the modified discrete state, the other coming from the continuum. Both contributions interfere with each other with opposite signs on the two sides of the resonance, leading to the Fano line shape being highly asymmetric.

Fano resonances describe interferences between bound and unbound (closed and open) scattering channels. This is a phenomenon, which exists in many areas of physics. In 1927

Wentzel used a similar approach to explain the Auger effect [168], followed by a series of papers by Majorana on the non-radiative recombination process of two electron excited states [169, 170]. Fano's work was finally followed up by Feshbach, who was working on the topic of shape resonances in nuclear physics [171]. After having developed the cloudy crystal ball model of the nucleus [172], he used the same partitioning scheme (known today as Feshbach-Fano partitioning) to develop the theory of the multichannel resonances in the frame of the general nuclear reaction theory for multistep reactions [173]. These resonances today are known as Feshbach-resonances. After Fano realized, that Feshbach's work was an extension of his 1935 paper (that he had considered as closed work [174]), the theory of shape resonances was developed and applied to many processes of association and dissociation [175]. For a more detailed overview about the development of Fano-resonances in different fields of physics, I refer the reader to Ref. [176].

In the last years, caused by the development of ultra-fast spectroscopy techniques, the dynamical properties of line shapes, e.g. Fano resonances have been investigated [141, 142, 143, 146] as well as the modification and control of resonance shapes using laser dressing [95, 105, 139, 140, 144, 145]. Works like [2, 152] describe and interpret the laser-control of Fano-to-Lorentz transitions.

In the following, we discuss, how laser-induced Lorentz-to-Rayleigh transitions can be understood in terms of the generalized Lehmann representation of the excited-state polarizability tensor, which was developed previously. In Chapter 4, we will demonstrate this lineshape-control using the analytically solvable Hydrogen atom. The concept of changing the lineshape by imprinting a phase on the wave function is hereby similar to the case of changing a Fano- into a Lorentzian line [2].

For the following lineshape analysis, we concentrate on isolated peaks only. We denote this by replacing  $\mathfrak{F}$  by  $\sum$ . Comments on the continuum part of the spectrum will be provided afterwards. We again distinguish the three cases described previously. In case (i) the response function reduces to the usual Lehmann representation of the ground state spectrum

$$\Im \alpha_{\mu\mu}[\mathcal{C}](\omega^+) = \sum_m |d_{0m}|^2 L(\omega - \omega_{0m}), \quad (2.69)$$

where all peaks are positive and of Lorentzian lineshape. In case (ii), as mentioned before,

we can find both positive and negative peaks. Again both are of Lorentzian shape:

$$\Im \alpha_{\mu\mu}[\mathcal{E}](\omega^+) = \sum_{\xi < m} |d_{\xi m}|^2 L(\omega - \omega_{\xi m}) - \sum_{\xi > m} |d_{\xi m}|^2 L(\omega + \omega_{\xi m}). \quad (2.70)$$

In case (iii) we divided the spectrum into an equilibrium and an interference term (2.63a). As to be expected, since the equilibrium term is formed by the equilibrium spectra of the involved states, it again only contains Lorentzian peaks. The interesting part is the interference term, which after having applied the broadening is:

$$\begin{aligned} \Im \alpha_{\mu\mu}^{IN}[\mathcal{E}](\omega, t_0 + \tau) = \sum_{j \neq k; m} d_{jm} d_{mk} |\gamma_j \gamma_k| & \left\{ \cos(\Theta_{kj}(\tau)) L(\omega - \omega_{jm}) + \sin(\Theta_{kj}(\tau)) R(\omega - \omega_{jm}) \right. \\ & \left. - \cos(\Theta_{kj}(\tau)) L(\omega + \omega_{jm}) + \sin(\Theta_{kj}(\tau)) R(\omega + \omega_{jm}) \right\} \end{aligned} \quad (2.71)$$

As one can see, the angle  $\Theta_{kj}$  not only modulates the peak's height with time, but it mixes real and imaginary part of the response function, therefore converting Lorentzian line shapes into Rayleigh line shapes and vice versa. A complete spectrum of a non-equilibrium state will therefore contain time-independent positive and negative peaks of Lorentzian shape and some interference terms at the same energies, that oscillate between Lorentzian and Rayleigh shape with a periodicity proportional to the energy-differences of the eigenstates involved.

This demonstrates, how using a pump to imprint an internal phase difference  $\varphi_j - \varphi_k$  onto a state and controlling the delay time  $\tau$  between the pump and probe laser can be used to change a spectrum, converting absorption into emission peaks (and vice versa) as well as changing the overall shape of the lines.

In Chapter 4.1.1 we will use the example of an excited non-stationary state of Hydrogen to illustrate the transformation between Lorentzian and Rayleigh peaks. Furthermore we demonstrate, how to use a laser to control the spectral lineshapes.

Note, that in the discussion above, the lineshape analysis is valid for isolated peaks without contributions from continuum states. If coupling to continuum states is involved, an additional shaping comes into play, coming from the dependence of the matrix elements  $d_{jm}$  on the energy. This is e.g. the case for Fano lineshapes.

## 2.4. Time-Dependent Density Functional Theory for Response Calculations

Time-dependent Density Functional Theory (TDDFT) in the Kohn-Sham approach can be utilized to compute the response of a many-electron system to a perturbation, weak or strong. In the perturbative regime, ideally one wishes to obtain the response functions [(hyper)-polarizabilities, optical and magnetic susceptibilities, ...], since (i) these objects then permit to predict any reaction in the appropriate order, and (ii) experiments typically provide spectra that are directly related to the response functions – e.g. the optical absorption cross section of a gas is proportional to the imaginary part of the dipole-dipole molecular polarizability. In contrast, in the strong-field regime, where perturbative treatments become cumbersome, one normally computes the particular response of the system to the perturbation of interest by directly propagating the TDKS equations in real time.

The vast majority of TDDFT applications have addressed the first-order response of the ground-state system to weak electric fields – which can provide the absorption spectrum, the optically-allowed excitation energies and oscillator strengths, etc. This can be performed by linearizing the TDKS equations in the frequency domain and casting the result into matrix-eigenvalue form (using e.g. Casida’s method [177]), or by propagating the same equations in real time applying a sufficiently weak dipole perturbation. In any case, the response function computed in this manner will be that of the ground state. If we want to analyze a transient absorption spectroscopy (TAS) experiment, the objective is to obtain the response of the excited states that are visited by the system as it is driven by the pump pulse (i.e. the response function of a system out of equilibrium). A generalization of the general linear response formalism to the linear response formalism based on excited states was presented in Section 2.2.

Likewise, TDDFT can be used to compute strong field non-linear photo-electron spectra of atoms and molecules, for example with the method recently presented in [178]. Even though these spectra are also characteristic of the ground state, in Section 2.4.6, we demonstrate, how the methodology can be extended to tackle the pump-probe case (TRPES [83]).

In this subsection, I show, how (TD)DFT can be used to perform TAS and TRPES calculations. To this goal, I first give a brief introduction into DFT and present the

energy functionals, which are used throughout the thesis. I then discuss the concept of TDDFT and present the TDKS equations. To perform TAS calculations, we need access to the dipole-dipole response function. How the dipole-dipole response function can be obtained from the density-density response function, which is accessible through TDDFT is presented in Section 2.4.3 followed by the connection between the many-body and the KS-response function in Section 2.4.4. In Section 2.4.5, I comment on how the density-density response function can be obtained by propagating the TDKS equations in real time after a sufficiently weak dipole perturbation (kick). Finally in Section 2.4.6, I explain how to perform TRPES calculations using the mask method.

### 2.4.1. Static Density Functional Theory

I start this section by giving a brief introduction to Density Functional Theory (DFT) to set the framework to talk about some of the more technical details of the work in this thesis. For a comprehensive introduction to DFT, I refer the reader to works like e.g. [179, 180, 181].

Static Density Functional Theory is based on the Hohenberg-Kohn (HK) theorem [182], which states the possibility to directly and unambiguously correlate the ground-state electronic energy of a many-particle system with its one-body electron density  $n_{gs}(\mathbf{r})$ .

In Section 2.1 we showed that with the help of the adiabatic principle and the Born-Oppenheimer approximation, we can separate the many-particle Hamiltonian into a Hamiltonian for the electronic and a Hamiltonian for the ionic problem. In this work, we are mainly interested in the electronic problem (2.12), but solving the time-dependent Schrödinger equation (TDSE) exactly in three dimensions for more than two electrons is unfeasible [178] and for one-dimensional models, the limit rises to not more than four electrons [183]. One way to cut down on computational expenses is to shift attention from the exact ground-state many-electron wavefunction  $\Psi(\mathbf{r}_i)$  to the much more manageable ground-state one-body electron density  $n_{gs}(\mathbf{r})$ .

In DFT it is shown, that the ground-state energy of a many-particle system can indeed be expressed as a functional of the one-body electronic density, what means that by minimizing this energy it is possible to determine  $n_{gs}(\mathbf{r})$ . Furthermore, the HK theorem [184] proofs a one-to-one correspondence between the external potential and the ground state density. Since the ground state wave function can be obtained from the external po-

tential by solving the Schrödinger equation, this means, that every quantum mechanical observable  $\hat{O}$  is a direct functional of the ground state density  $\hat{O} = \hat{O}[n]$ . Nevertheless, whilst in principal all observables can be obtained from  $n_{gs}(\mathbf{r})$ , in practice the functional dependencies are mostly unknown.

The most important observable in DFT is the ground state energy associated to a system in an external potential. In the Hohenberg-Kohn variational principle one writes the total energy  $E$  for a fixed external potential  $V_{ext}(\mathbf{r})$  as a functional of the density

$$E[n] = \langle \Psi[n] | \hat{T} + V_{ee} | \Psi[n] \rangle + \langle \Psi[n] | V_{ext} | \Psi[n] \rangle = F_{HK}[n] + \int d^3\mathbf{r} V_{ext}(\mathbf{r}) n(\mathbf{r}) \quad (2.72)$$

where we defined the HK functional

$$F_{HK}[n] = \langle \Psi[n] | \hat{T} + V_{ee} | \Psi[n] \rangle, \quad (2.73)$$

which does not depend on the external potential  $V_{ext}(\mathbf{r})$ . The energy (2.72) is now minimized with respect to the density  $n(\mathbf{r})$  to find ground state density and energy of the system. This is most commonly done using the Kohn-Sham (KS) scheme [182] even though orbital-free schemes exist. In KS-DFT, one uses an auxiliary fictitious system of non-interacting electrons that produces the same density as the interacting electrons. This is possible, since  $F_{HK}[n]$  depends exclusively on the density and the proof of the Hohenberg-Kohn theorem does not depend on the interaction of the electrons. Substituting the interacting electrons by a system of non-interacting electrons with the same density is the source of a great computational simplification, since a non-interacting system of electrons can in general be represented by a single Slater determinant formed by a set of “Kohn-Sham” orbitals,  $\varphi_i$  ( $i = 1, \dots, N/2$ ). If not stated otherwise, in this work, we assume a spin-compensated system of  $N$  electrons doubly occupying  $N/2$  spatial orbitals. In this case, the density is

$$n(\mathbf{r}) = 2 \sum_{i=1}^{N/2} |\varphi_i(\mathbf{r})|^2. \quad (2.74)$$

To obtain the KS orbitals  $\varphi_i$ , one splits the Hohenberg-Kohn functional  $F_{HK}$  according to

$$F_{HK}[n] = T_S[n] + E_H[n] + E_{xc}[n] \quad (2.75)$$

where

$$T_S[n] = - \sum_i \langle \varphi_i[n] | \frac{\nabla^2}{2} | \varphi_i[n] \rangle \quad (2.76)$$

is the KS kinetic energy,

$$E_H[n] = \frac{1}{2} \int \int d^3\mathbf{r} d^3\mathbf{r}' \frac{n(\mathbf{r})n(\mathbf{r}')}{|\mathbf{r} - \mathbf{r}'|} \quad (2.77)$$

is the Hartree energy and

$$E_{xc}[n] = F_{HK}[n] - T_S[n] - E_H[n] \quad (2.78)$$

is the exchange correlation energy.

The KS orbitals are then obtained by self-consistently solving the KS equations

$$\left[ -\frac{\nabla^2}{2m} + V_{KS}(\mathbf{r}) \right] \varphi_i(\mathbf{r}) = \epsilon_i \varphi_i(\mathbf{r}) \quad (2.79)$$

together with (2.74) with the KS potential

$$V_{KS}(\mathbf{r}) = V_{ext}(\mathbf{r}) + V_H(\mathbf{r}) + V_{xc}(\mathbf{r}) \quad (2.80)$$

where the Hartree potential  $V_H$  corresponds to a classical electrostatic term

$$V_H[n](\mathbf{r}) = \int d^3r' \frac{n(\mathbf{r}')}{|\mathbf{r}' - \mathbf{r}|}, \quad (2.81)$$

and the exchange-correlation potential  $V_{xc}$  is the functional derivative of the exchange-correlation energy

$$V_{xc}(\mathbf{r}) = \frac{\delta E_{xc}[n(\mathbf{r})]}{\delta n(\mathbf{r})}. \quad (2.82)$$

The exchange correlation energy is a functional of the density and accounts for all the intricate many-electron effects. It is in practice unknown and must be approximated [99, 101]. Finding good approximations for  $E_{xc}[n]$  is an active field of research as well as analyzing the properties of the exact functional. For example in Ref. [185], Helbig *et al.* analyzed the exact KS potential of a stretched Hydrogen molecule by reconstructing the potential from the exact density. In Appendix C, we include an analysis of the description

of tunneling in a many-particle system and its description in DFT, where we compare the description of the situation by a few current functionals to calculations using the exact functional, which we reconstruct from exact calculations.

Many energy functionals are currently in usage. In the next paragraph we present the ones, that are used in this thesis.

#### 2.4.1.1. The Energy Functionals

**L(S)DA** The simplest density functional to approximate the exchange correlation energy (2.78) is the **local (spin) density approximation (L(S)DA)**, where it is assumed, that the density can locally be approximated as homogeneous electron gas. The effects of exchange and correlation are local in character and the exchange correlation energy is simply the integral over all space with the exchange correlation energy density being assumed the same as in a homogeneous electron gas with the same electron density.

$$E_{xc}^{LSDA} [n(\mathbf{r})] = \int d^3\mathbf{r} n(\mathbf{r}) \epsilon_{xc}^{hom}(n(\mathbf{r})) \quad (2.83)$$

To be able to use (2.83),  $\epsilon_{xc}^{hom}$  has to be determined, which is usually split into exchange term  $\epsilon_x$  and correlation part  $\epsilon_c$ :

$$\epsilon_{xc} = \epsilon_x + \epsilon_c. \quad (2.84)$$

The exchange energy is given by the Dirac functional [186]

$$\epsilon_x = -\frac{3}{4} \left( \frac{3}{\pi} \right)^{\frac{1}{3}} n(\mathbf{r}) \quad (2.85)$$

and the correlation part is parametrized with the help of Quantum Monte Carlo simulations. In this thesis, the parametrization of Perdew and Wang [187] is used.

**ADSIC** One of the functionals used in this thesis, is the LDA functional coupled to an **Average Density Self Correction ADSIC**. In self interaction correction schemes, one subtracts from the energy the interaction energy of every electron with itself. One consequence and the reason, why this approach is used so often in this thesis is the yield of the correct asymptotic behaviour of the exchange correlation potential for large distances away from the molecule  $V_{xc}(r) \sim -1/r$  for  $r \rightarrow \infty$ . This leads to better accuracies for the high lying KS bound states close to the ionization threshold. This is particularly



important for the observation of the  $\pi \rightarrow \pi^*$  transition in Ethylene (Section 3.3) but also for the description of excited-state spectra (Section 5).

The first self interaction correction scheme was proposed by Perdew and Zunger [188]. One of its drawbacks is its orbital-dependence. A different, orbital-independent approach is the Krieger-Li-Iafrate (KLI) approach [189] (and others). However, many of the proposed schemes are computationally expensive. A convenient way of combining an orbital-independent self interaction correction with relatively small computational cost is the ADSIC approach introduced in [190]. Here, one assumes that the density  $n_i(\mathbf{r})$  of each electron  $i$  is represented by an equal fraction of the total spin density  $n^{\sigma_i}(\mathbf{r})$  of its respective spin  $\sigma_i$ :  $n_i(\mathbf{r}) = n^{\sigma_i}(\mathbf{r})/N^{\sigma_i}$  where  $N^{\sigma_i}$  is the number of electrons with spin  $\sigma_i$ . In this case, the ADSIC exchange-correlation energy is given by

$$E_{xc}^{ADSIC} [n^\uparrow, n^\downarrow] = E_{xc}^{FHK} [n^\uparrow, n^\downarrow] - NE_H \left[ \frac{n}{N} \right] - N^\uparrow E_{xc} \left[ \frac{n^\uparrow}{N^\uparrow}, 0 \right] - N^\downarrow E_{xc} \left[ 0, \frac{n^\downarrow}{N^\downarrow} \right] \quad (2.86)$$

with the  $E_H$  being the Hartree energy (2.77) and  $E_{xc}^{FHK}$  the exchange correlation energy of the functional  $F_{HK}$ , that is to be corrected. In this thesis we use the ADSIC together with the LDA functional.

**LB94** An obvious first step beyond L(S)DA is the inclusion of terms depending on the density gradient - the generalized gradient approximations (GGAs). One of them is the LB94 functional developed by van Leeuwen and Baerends [191]. Its exchange-correlation potential reads

$$V_{xc}(\mathbf{r}) = -n(\mathbf{r})^{-\frac{1}{3}}\beta \frac{x^2}{1 + 3\beta x \sinh^{-1}(x)} \quad (2.87)$$

with  $x = \frac{|\nabla n(\mathbf{r})|}{n(\mathbf{r})^{\frac{4}{3}}}$  and  $\beta = 0.05$ . Note, that LB94 is not technically an energy functional, but a model for the exchange correlation potential (2.82). Here,  $V_{xc}$  is given explicitly and is not the functional derivative of an energy. Since for potentials, which are not derived from an energy functional, the zero-force theorem is not necessarily fulfilled, this can lead to problems during the time-propagation as for example self-excitation. This has been shown explicitly for e.g. the Becke-Johnson potential [192] in [193]. LB94 has – like the ADSIC functionals – the advantage of being asymptotically correct.

**EXX** Also in use are orbital-dependent functionals, which depend on the KS orbitals. One of them is the Exact Exchange **EXX** functional, where one neglects the correla-

tion term and calculates the exchange energy using the expression for the Hartree-Fock exchange energy employing KS orbitals

$$E[n] = \frac{1}{2} \sum_{i,j}^{occ} \int d\mathbf{r} d\mathbf{r}' \frac{\varphi_i^*(\mathbf{r}) \varphi_j^*(\mathbf{r}') \varphi_j(\mathbf{r}) \varphi_i(\mathbf{r}')}{|\mathbf{r} - \mathbf{r}'|}. \quad (2.88)$$

The exchange correlation potential  $V_{xc}$  is then obtained from the energy by solving the time-dependent optimized effective potentials (TDOEP) equations [194, 195]. Since, this is not an easy task [196], in practice, the TDOEP equations are solved using the time-dependent Krieger-Li-Iafrate (TDKLI) approximation. In [197], EXX in combination with the KLI-TDOEP equations were shown to violate the zero-force theorem. This can again lead to unphysical behaviour like self-excitations. Nevertheless, the authors also argued, that in many practical cases this was not a problem.

#### 2.4.1.2. Pseudopotentials

The strong Coulomb potential in the core region of atoms is hard to describe with real-space codes like `octopus`. Since the KS wave functions are all eigenstates to the same Hamiltonian, they have to be mutually orthogonal, which requires the valence states to be strongly oscillating in the core region. These oscillations are numerically hard to describe. For calculations, where one is not interested in core excitations, one therefore freezes the core electrons and replaces the strong Coulomb potential in the core region by smoother potentials (so-called *pseudo-potentials*) based on a combination of the nucleus and the influence of the core electrons.

The pseudo-potentials used in this thesis were generated with the Troullier-Martins scheme [198] and were used as distributed in the `octopus`-package [101, 102, 103].

#### 2.4.2. Time-Dependent Density Functional Theory \*

As seen in the last Section, DFT [199] establishes a one-to-one correspondence between the ground-state density and the external potential of a many-electron system. This implies that any system property is, in principle, a ground-state density functional. For excited states properties, however, or in order to simulate the behavior of the system in

---

\*The theory presented in this section forms part of [3].

time-dependent external fields, one must use its time-dependent version, TDDFT [99, 200, 201].

In the case of TDDFT, a one-to-one correspondence also exists between the time-dependent densities and potentials. If the real system is irradiated with an external field characterized by a scalar potential  $V(\mathbf{r},t)$  (the extension to vector potentials is also possible), the “time-dependent Kohn-Sham” (TDKS) equations that characterize the evolution of the fictitious system are:

$$i\frac{\partial}{\partial t}\varphi_i(\mathbf{r},t) = -\frac{1}{2}\nabla^2\varphi_i(\mathbf{r},t) + V_{KS}[n](\mathbf{r},t)\varphi_i(\mathbf{r},t), \quad (2.89)$$

$$n(\mathbf{r},t) = 2\sum_{i=1}^{N/2}|\varphi_i(\mathbf{r},t)|^2. \quad (2.90)$$

As in the static case, the time-dependent density  $n(\mathbf{r},t)$  is the central object, and is identical for the real and for the KS systems. The KS potential  $V_{KS}$  is a functional of this density, and is defined as:

$$V_{KS}[n](\mathbf{r},t) = V_0(\mathbf{r}) + V(\mathbf{r},t) + V_H[n](\mathbf{r},t) + V_{xc}[n](\mathbf{r},t), \quad (2.91)$$

where the Hartree potential  $V_H$  is defined as in (2.81) with a time-dependent density  $n(\mathbf{r},t)$ ,  $V_0(\mathbf{r})$  is the static external potential that characterizes the system in its ground state (in a molecule, originated by a set of nuclei), and the “exchange and correlation” potential is  $V_{xc}[n]$ .  $V_{xc}[n]$  is non-local in time and recently much work has been dedicated to characterize its time-dependence [202, 203, 204, 205], but since its time-dependence is in general not known, in practice one mostly works with adiabatic functionals. Here, memory-effects are ignored and at each time, the ground state functional of choice is evaluated with the instantaneous density at this time. In this thesis, all used functionals are adiabatic.

### 2.4.3. Time-Resolved Photoabsorption Spectroscopy - The Density-Density Response

As we have seen in Section 2.2.4, the photoabsorption coefficient of a system can be obtained from the imaginary part of the dipole-dipole polarizability in frequency space. Up to here, we have also learned, that the most important observable in (TD)DFT

is the density and consequently, the most important response function is the density-density response function. In the following, we show how to connect the density-density response to the dipole-dipole response, thus enabling us to use TDDFT to extract the photoresponse of a system from the density-density response function.

The density-density response function describes the response of the electronic density to perturbation in the density. Here, the external perturbation (e.g. the probe pulse) is a scalar potential  $v(\mathbf{r}, t)$ , which is switched on at time  $t'$  and couples to the density operator  $\hat{n}(\mathbf{r}) = \sum_{i=1}^{\infty} \delta(\mathbf{r} - \mathbf{r}_i)$ , where  $\mathbf{r}_i$  is the coordinate of the  $i$ th electron. The coupling is described by the Hamiltonian

$$\hat{H}_1(t) = \int d^3\mathbf{r}' v(\mathbf{r}', t) \hat{n}(\mathbf{r}'). \quad (2.92)$$

The time-dependent density response is given by

$$\delta n(\mathbf{r}, t) = \int dt' \int_{-\infty}^{\infty} d^3\mathbf{r}' \chi_{nn}(\mathbf{r}, \mathbf{r}', t, t') v(\mathbf{r}', t') \quad (2.93)$$

with the **density-density response function** of the (excited state) density matrix  $\hat{\rho}(t_0)$

$$\chi_{nn}(\mathbf{r}, \mathbf{r}', t, t') = -i\theta(t - t') \text{Tr} \{ \hat{\rho}(t_0) [\hat{n}_I(\mathbf{r}, t), \hat{n}_I(\mathbf{r}', t')] \}, \quad (2.94)$$

where  $\hat{n}_I(\mathbf{r}, t)$  is the density operator in the interaction representation (2.28). For weak perturbations we are only interested in the linear density response

$$\delta n(\mathbf{r}, t) \approx n_1(\mathbf{r}, t) = \int dt' \int_{-\infty}^{\infty} d^3\mathbf{r}' \chi_{nn}(\mathbf{r}, \mathbf{r}', t, t') v_1(\mathbf{r}', t') \quad (2.95)$$

Eq. (2.94) and Eq. (2.95) describe a particular case of the general definitions Eq. (2.30) and Eq. (2.29). This can be seen by taking into account that the linear responses to different perturbations can simply be added up and thus the perturbing Hamiltonian (2.92) can be seen as sum of perturbations  $v_1(\mathbf{r}', t') \hat{n}(\mathbf{r}')$  each giving rise to a retarded density response.

In order to connect the density-density response  $\chi_{nn}(\mathbf{r}, \mathbf{r}', t, t')$  to the dipole-dipole polarizability  $\alpha(t, t') = \chi_{\hat{D}, \hat{D}}(t, t')$  we recall Eq. (2.52), which relates the polarization in the

$\mu$ -direction  $p_\mu(t, t')$  with the perturbing electric field in the  $r_\nu$ -direction like

$$p_\mu(t, t') = \sum_\nu \alpha_{\mu\nu}(t, t') E_\nu(t). \quad (2.96)$$

The electronic polarization in  $\mu$ -direction can be obtained from the linear density response  $n_1(\mathbf{r}, t)$  as

$$\begin{aligned} p_\mu(t, t') &= - \int d^3\mathbf{r} r_\mu n_1(\mathbf{r}, t) \\ &= - \int d^3\mathbf{r} \int d^3\mathbf{r}' r_\mu \chi_{nn}(\mathbf{r}, \mathbf{r}', t, t') v_1(\mathbf{r}', t) \end{aligned} \quad (2.97)$$

Here,  $v_1(\mathbf{r}', t)$  is the potential associated to the electric field  $\mathbf{E}(t)$ , which as in Section 2.2.4 is assumed to be monochromatic of frequency  $\omega$ , linearly polarized along the  $r_\nu$ -direction ( $r_\nu$  being one of the Cartesian coordinates  $x, y, z$ ) and of amplitude  $E_0$ .  $v_1(\mathbf{r}, t)$  can then be written as

$$v_1(\mathbf{r}, t) = -q\mathbf{E}(t) \cdot \mathbf{r} = E_0 r_\nu e^{-i\omega t}, \quad (2.98)$$

where we again treated the electric field in dipole-approximation. Inserting Eq. (2.98) into Eq. (2.97) and comparing to Eq. (2.96) leads to the following connection between density-density and dipole-dipole response function

$$\alpha_{\mu\nu}(t, t') = - \int d^3\mathbf{r} d^3\mathbf{r}' r_\mu r'_\nu \chi_{nn}(\mathbf{r}, \mathbf{r}', t, t') \quad (2.99)$$

which in mixed frequency/time space is

$$\alpha_{\mu\nu}(\omega, \tau) = - \int d^3\mathbf{r} d^3\mathbf{r}' r_\mu r'_\nu \chi_{nn}(\mathbf{r}, \mathbf{r}', \omega, \tau). \quad (2.100)$$

with  $\tau = t' - t_0$ . Note again, that while normally  $\alpha_{\mu\nu}(\omega, \tau)$  does not depend on  $\tau$ , the additional dependence on  $\tau$  is caused by the fact, that  $\alpha(t, t') \neq \alpha(t - t')$ . Together with the definition of the average absorption coefficient in terms of the dipole-dipole polarizability (2.54) this connection enables us to obtain the photoresponse of a system from its density-density response, which is easily available in TDDFT.

#### 2.4.4. Kohn-Sham Linear Response Function

In the last section, we established the connection between a small change in the external potential  $\delta v_{ext}(\mathbf{r}, t')$  and the consequent change in the density  $\delta n(\mathbf{r}, t)$  via the many-body density-density response function  $\chi_{nn}(\mathbf{r}, \mathbf{r}', t, t')$

$$\delta n(\mathbf{r}, t) = \int dt' \int_{-\infty}^{\infty} d^3\mathbf{r}' \chi_{nn}(\mathbf{r}, \mathbf{r}', t, t') \delta v_{ext}(\mathbf{r}', t') \quad (2.101)$$

with

$$\chi_{nn}(\mathbf{r}, \mathbf{r}', t, t') = \frac{\delta n(\mathbf{r}, t)}{\delta v_{ext}(\mathbf{r}', t')}. \quad (2.102)$$

In a similar matter, one can define the change of the density due to a change in the Kohn-Sham (KS) potential via the Kohn-Sham density-density response function  $\chi_{nn}^{KS}(\mathbf{r}, \mathbf{r}', t, t')$  like

$$\delta n(\mathbf{r}, t) = \int dt' \int_{-\infty}^{\infty} d^3\mathbf{r}' \chi_{nn}^{KS}(\mathbf{r}, \mathbf{r}', t, t') \delta v_{KS}(\mathbf{r}', t') \quad (2.103)$$

with

$$\chi_{nn}^{KS}(\mathbf{r}, \mathbf{r}', t, t') = \frac{\delta n(\mathbf{r}, t)}{\delta v_{KS}(\mathbf{r}', t')}. \quad (2.104)$$

According to the Runge-Gross theorem, the time-dependent density of a many-body system is reproduced within the TDDFT formalism, which means, that both expressions for the change of density have to be the same. This leads to a Dyson-like equation connecting the many-body and the KS response function, which for a system in its ground state reads

$$\chi_{nn}(\mathbf{r}, \mathbf{r}', \omega) = \chi_{nn}^{KS}(\mathbf{r}, \mathbf{r}', \omega) + \int d\mathbf{r}_1 \int d\mathbf{r}_2 \left( \frac{1}{|\mathbf{r}_1 - \mathbf{r}_2|} + f_{xc}(\mathbf{r}_1, \mathbf{r}_2, \omega) \right) \chi_{nn}(\mathbf{r}_2, \mathbf{r}', \omega) \quad (2.105)$$

with the exchange-correlation kernel

$$f_{xc}(\mathbf{r}, \mathbf{r}', t - t') = \left. \frac{\delta v_{xc}(\mathbf{r}, t)}{\delta n(\mathbf{r}', t')} \right|_{n=n_{GS}}. \quad (2.106)$$

Here, we took advantage of the time-translational invariance of the response function of systems in their ground state to get rid of the second time-dependence and have the response function only depending on the frequency  $\omega$ .

The use of adiabatic functionals can lead to unphysical effects in the description of

photo-excitation spectra as we will demonstrate in the results chapters. This issue has also recently been addressed in Ref. [206].

### 2.4.5. Absorption Spectra from the Time-Evolution

As mentioned before, a common way to obtain optical spectra in TDDFT is by propagating the TDKS equations in real time following the scheme proposed by Yabana and Bertsch [207]. This is the approach used for most calculations in this thesis, since it is straightforward to extend the usual formalism to the situation of excited state spectroscopy like transient absorption spectroscopy (TAS) and time-resolved photoelectron spectroscopy (TRPES). Whilst in the case of TRPES, we use finite probe pulses, in the case of TAS, we probe the system under investigation by applying a delta perturbation, a so-called '**kick**'.

To understand why, we recall the expression for a general linear response  $O_1$  to a perturbation  $F(t)\hat{V}$  (2.31):

$$O_1[\mathcal{E}, F](\omega) = \int_{-\infty}^{\infty} dt' F(t') \chi_{\hat{O}, \hat{V}}[\mathcal{E}](\omega, t').$$

Using as probe a delta perturbation

$$F(t') = \lambda \delta(t - t') \quad (2.107)$$

permits to obtain the response-function directly from the linear response by

$$\chi_{\hat{O}, \hat{V}}[\mathcal{E}](\omega, \tau) = \frac{1}{\lambda} O_1[\mathcal{E}, \lambda \delta_\tau](\omega). \quad (2.108)$$

In our case, this means, that the dynamic polarizability  $\alpha[\mathcal{E}](\omega, \tau)$  needed to obtain the spectrum can be directly obtained from the change of the expectation value of the electronic dipole

$$\delta D[\mathcal{E}, \lambda \delta_\tau](\omega) = - \int d^3\mathbf{r} \delta n(\mathbf{r}, \omega) x \quad (2.109)$$

with the dipole operator (2.51) like

$$\alpha[\mathcal{E}](\omega, \tau) = \frac{1}{\lambda} \delta D[\mathcal{E}, \lambda \delta_\tau](\omega). \quad (2.110)$$

The action of such a delta perturbation applied at instant  $\tau$  on the a system is given as

$$|\Psi(t \rightarrow \tau^+)\rangle = e^{-i\lambda\hat{V}}|\Psi(\tau)\rangle. \quad (2.111)$$

which gives the electrons a coherent velocity field. In the KS scheme, the perturbation has to be applied to each of the KS orbitals leading to

$$\varphi_i(\mathbf{r}, t \rightarrow \tau^+) = e^{i\lambda x} \varphi_i(\mathbf{r}, \tau). \quad (2.112)$$

Note, that whilst in this thesis, we focus on the optical response, by changing the type of perturbation one can also address the magnetic response, the dichroic response, etc. In fact, all linear and higher-order responses can be obtained in terms of a kick or of series of kicks.

#### 2.4.6. Time-Resolved Photoelectron Spectroscopy – The Mask Method <sup>†</sup>

In the last sections, I have shown, how TDDFT can be used to obtain time-resolved absorption spectra. In this section, I present, how TDDFT can be used to obtain time-resolved photoelectron spectra (TRPES). Note again, that whilst the theorems of TDDFT tell us, that a functional that describes the PES in terms of the density exists, in practice, this functional is not known and other ways of obtaining the PES from the KS equations have to be found. The photoelectron spectra presented in this work are produced within TDDFT using the Mask Method [178]. This method is based on a geometrical partitioning and a mixed real- and momentum-space time evolution scheme [208]. In the following, I summarize the main traits of the technique. A complete description can be found in [178]. Furthermore, I demonstrate how it can be straightforwardly applied to the non-equilibrium situation required by pump-probe experiments.

In photoemission processes a light source focused on a sample transfers energy to the system. Depending on the light intensity electrons can absorb one or more photons and escape from the sample due to the photoelectric effect. In experiments, electrons are detected and their momentum is measured. By repeating measurements on similarly prepared samples it is possible to estimate the probability to measure an electron with a given momentum. From a computational point of view, the description of such pro-

---

<sup>†</sup>The theory presented in this chapter forms part of [3].



cesses for complex systems is a challenging problem. The main difficulty arises from the necessity of describing properly electrons in the continuum.

In typical experimental setups, detectors are situated far away from the sample and electrons overcoming the ionization barrier travel a long way before being detected. The distances, that electrons travel are usually orders of magnitude larger than the typical interaction length scales in the sample. During their journey towards the detector, and far away from the parent system, they practically evolve as free particles driven by an external field. The solution of the Schrödinger equation for free electrons in a time dependent external field is known analytically in terms of plane waves known as Volkov states. It therefore seems a waste of resources to solve the Schrödinger equation numerically in the whole space if a considerable part of the wave function can be described analytically.

In order to take advantage of the previous observations we partition the space according to the scheme shown in Figure 2.2 (b). The space is divided into two regions,  $A$  and  $B$ ; the inner region  $A$ , containing the system with enough empty space around, is where electrons are allowed to interact with each other and with the system, and region  $B$ , defined as the complement of  $A$ , is where electrons are non-interacting and freely propagating. Every KS orbital  $\varphi_i(\mathbf{r})$  can be decomposed according to  $\varphi_i(\mathbf{r}) = \varphi_i^A(\mathbf{r}) + \varphi_i^B(\mathbf{r})$ , so that  $\varphi_i^A(\mathbf{r})$  resides mainly in region  $A$  and  $\varphi_i^B(\mathbf{r})$  mainly in region  $B$ .

The geometrical partition is implemented by a smooth mask function  $M(\mathbf{r})$  defined to be one deep in the interior of  $A$  and zero outside (see Figure 2.2 (a)):

$$\varphi_i^A(\mathbf{r}) = M(\mathbf{r})\varphi_i(\mathbf{r}), \quad (2.113)$$

$$\varphi_i^B(\mathbf{r}) = (1 - M(\mathbf{r}))\varphi_i(\mathbf{r}). \quad (2.114)$$

The mask function takes care of the boundary conditions in  $A$  by forcing every function to be zero at the border. In order to give a good description of functions extending over the whole space it is convenient to represent the orbitals  $\varphi_i^B(\mathbf{r})$  in momentum space  $\tilde{\varphi}_i^B(\mathbf{p})$ .

A mixed real and momentum-space time evolution scheme can then be easily derived following the geometrical splitting. Given a set of orbitals at time  $t$  their value at a

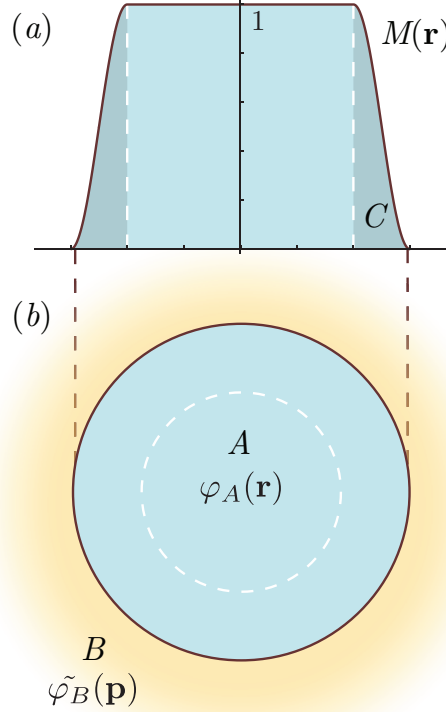


Figure 2.2.: Schematic description of the space partition implemented by the mask method. A mask function (a) is used to implement the spatial partitions (b). In region A (interaction region) the TDKS equations are numerically solved in real space while in B (free propagation region) electrons are evolved analytically as free particles in momentum space. Region C is where  $\varphi_A$  and  $\varphi_B$  overlap. This figure was published as Fig. 1 in our publication [3]. Copyright © 2013 Wiley-VCH Verlag GmbH & Co. KGaA, Weinheim.

successive time  $t + \Delta t$  is provided by

$$\begin{aligned}\varphi_i^A(\mathbf{r}, t + \Delta t) &= M(\mathbf{r})e^{-i\hat{H}\Delta t}\varphi_i^A(\mathbf{r}, t) \\ \tilde{\varphi}_i^B(\mathbf{p}, t + \Delta t) &= e^{-i\frac{(\mathbf{p}-\mathbf{A}(t))^2}{2}\Delta t}\varphi_i^B(\mathbf{p}, t) + \tilde{\varphi}_i^A(\mathbf{p}, t + \Delta t)\end{aligned}\tag{2.115}$$

with  $\hat{H}$  being the effective single-particle TDDFT Hamiltonian,  $\mathbf{A}(t)$  the total external time dependent vector potential (the coupling with the external field is conveniently

expressed in the velocity gauge), and

$$\tilde{\varphi}_i^A(\mathbf{p}, t + \Delta t) = \frac{1}{(2\pi)^{3/2}} \int d\mathbf{r} (1 - M(\mathbf{r})) e^{-i\hat{H}\Delta t} \varphi_i^A(\mathbf{r}, t) e^{i\mathbf{p}\cdot\mathbf{r}}, \quad (2.116)$$

constituting the portion of electrons leaving the system at time  $t + \Delta t$ . At each iteration in the evolution the outgoing components of  $\varphi_i^A(\mathbf{r})$  are suppressed in the interaction region by the multiplication with  $M(\mathbf{r})$  while being collected as plane waves in  $\tilde{\varphi}_i^B(\mathbf{p})$  via  $\tilde{\varphi}_i^A(\mathbf{p})$ . The resulting momentum space wavefunctions are then evolved analytically simply by a phase multiplication.

The advantage of using such an approach resides in the fact that we can conveniently store the wavefunctions on a spatial grid inside  $A$  while treating wavefunctions in  $B$  (and therefore the tails extending to infinity) as free-electrons in momentum space. Moreover the mask function introduces a region  $C$ , where the wavefunctions in  $A$  and  $B$  overlap (see Figure 2.2) and that acts as matching layer. In spite of the fact that, from a theoretical point of view, the matching between inner and outer region could be performed on a single surface, from a numerical point of view, having a whole region to perform the matching is more stable and less influenced by different choices of spatial grids.

From the momentum components of the orbitals in  $B$  it is possible to evaluate the momentum-resolved photoelectron probability distribution as a sum over the occupied orbitals

$$P(\mathbf{p}) \approx \lim_{t \rightarrow \infty} \sum_{i=1}^{occ} |\tilde{\varphi}_i^B(\mathbf{p}, t)|^2, \quad (2.117)$$

the limit  $t \rightarrow \infty$  ensuring that all the ionized components are collected. This scheme is entirely non-perturbative; in a pump-probe setup, it does not assume linearity in either pump or probe. Therefore, it can be applied in the same manner when two pulses are present than with one pulse only, as it was shown in [178]. Like in the case of linear response, where we generalize the usual linear response theory to describe transient absorption spectroscopy (Section 2.2), we can generalize the previous derivation to address transient photoelectron spectroscopy (spin-, angle- and energy-resolved) in practice by employing a pump-probe scheme and performing numerical simulations with two time delayed external pulses. A TRPES map is then generated by performing a computation for each different time delay.

From  $P(\mathbf{p})$  several relevant quantities can be calculated. The energy-resolved photo-

electron probability  $P(E)$ , usually referred to as photoelectron spectrum (PES), can be obtained by integrating  $P(\mathbf{p})$  over solid angles

$$P(E = \mathbf{p}^2/2) = \int_{4\pi} d\Omega_p P(\mathbf{p}). \quad (2.118)$$

The angular- and energy-resolved photoelectron probability  $P(\theta, \phi, E)$ , or photoelectron angular distribution (PAD), can easily be evaluated by expressing  $P(\mathbf{p})$  in polar coordinates with respect to a given azimuth axis.

It is noteworthy that during the evolution defined in (2.115) the part of the density contained in  $A$  transferred to  $B$  is not allowed to return. Clearly, in cases where the external field is strong enough to produce electron orbits crossing the boundary of  $A$  and backscattering to the core the mask method provides a poor approximation. In these cases a bigger region  $A$  or a more refined scheme must be employed [178]. The laser fields employed in this work are weak enough that we can safely assume region  $A$  to always be sufficiently large to contain all the relevant electron trajectories.

## 2.5. Few-Electron Systems and Model-Hamiltonians

In the last Section 2.4, I have talked about how to use Time-Dependent Density Functional Theory (TDDFT) for calculating electronic spectra. But whilst for practical purposes methods like (TD)DFT have to be used, it is instructive to test theories for smaller systems, which can be solved either analytically or numerically exactly. In this thesis, we look at excited state spectra of several model systems (in one or three dimensions) and also use model systems to test our control algorithm. Therefore, in the following, I firstly present the general form of the model Hamiltonians used throughout the thesis.

For the analysis of excited state spectra in the exact case, the concept of Rabi-oscillations assuming a two-level system is used throughout this thesis. Therefore, after having presented the model Hamiltonians, I give a short introduction into the text-book derivation of Rabi oscillations. This concept is then extended to certain cases of three-level systems, which will later on be used to obtain a control laser to control the excitation of electrons from the ground state into a linear combination of excited states in Hydrogen.

### 2.5.1. Model Hamiltonians

The 1D model Hamiltonian of an atom exposed to a time-dependent external potential is given by

$$H(t) = T + V_{ext}(t) + V_{ee}, \quad (2.119)$$

in which the external potential is given by

$$V_{ext}(t) = - \sum_{i=1}^N \frac{C}{\sqrt{\Delta^2 + x_i^2}} + \mathcal{E}(t)x_i \quad (2.120)$$

where  $C$  is the charge of the nucleus and  $N$  the number of electrons in the system. The Coulomb interaction  $1/|x|$  is softened to  $1/\sqrt{\Delta^2 + x^2}$  with the softening parameter  $\Delta$ , which is set to one throughout this thesis. The softening is introduced in order to avoid unphysical results due to the Coulomb potential being too singular in 1D. One of these artefacts is e.g. the infinite ground state energy of the 1D Hydrogen atom [209].

In time-dependent problems, the coupling with the external time-dependent field  $\mathcal{E}(t)$  is expressed in length gauge, and electrons are confined to move along the  $x$  direction only. Finally,

$$T = - \sum_{i=1}^N \frac{1}{2} \frac{\partial^2}{\partial x_i^2} \quad (2.121)$$

is the kinetic energy, and the electron-electron interaction is given by

$$V_{ee} = \sum_{i \neq j} \frac{1}{2} \frac{1}{\sqrt{\Delta^2 + (x_i - x_j)^2}}. \quad (2.122)$$

This model is numerically solvable given the exact mapping discussed in Refs. [183, 210], where it is proved that the many-body problem of  $N$  electrons in one dimension is equivalent to that of one electron in  $N$  dimensions.

In the TDDFT treatment, the external potential is one-dimensional

$$V_{ext,TDDFT} = - \frac{C}{\sqrt{1 + x^2}} + \mathcal{E}(t)x \quad (2.123)$$

and the electron-electron interaction is described through the chosen energy functional.

## 2.5.2. Rabi-Oscillations

First, the general concept of Rabi oscillations in two-level systems is presented. Afterwards, the general concept is extended to the treatment of three-level systems, where the transition between two of the levels is dipole-forbidden.

### 2.5.2.1. Rabi-Oscillations in Two-Level Systems

A Rabi oscillation is a fluctuation behavior of states occupation occurring due to the interaction of an oscillatory optical field in resonance with a two-level system. The derivation of the Rabi oscillation formalism can be found in standard textbooks (e.g. [211, 212]). In the following I give a brief summary of the standard derivation of this formalism and then show, how we extend it to a three-level Hamiltonian.

The standard derivation of the Rabi oscillation formalism assumes a two-level Hamiltonian, whose eigenstates  $|\Phi_a\rangle$  and  $|\Phi_b\rangle$  with the eigenenergies  $\varepsilon_a$  and  $\varepsilon_b$  are coupled by the dipole transition element  $\mu = \mu_{ab} = \mu_{ba}$ . The most general wave function in this system may be written as  $|\Psi(t)\rangle = a(t)e^{-i\varepsilon_a t}|\Phi_a\rangle + b(t)e^{-i\varepsilon_b t}|\Phi_b\rangle$  with the constraint  $|a(t)|^2 + |b(t)|^2 = 1$ . One applies a single-frequency optical field  $\varepsilon_1 \cos(\omega t)$  and observes the expansion coefficients  $a(t)$  and  $b(t)$ :

$$\dot{a}(t) = i\frac{\mu\varepsilon_1}{2} \left( e^{+i(\omega-\omega_{ba})t} + e^{-i(\omega+\omega_{ba})t} \right) b(t) \quad (2.124a)$$

$$\dot{b}(t) = i\frac{\mu\varepsilon_1}{2} \left( e^{-i(\omega-\omega_{ba})t} + e^{+i(\omega+\omega_{ba})t} \right) a(t), \quad (2.124b)$$

where  $\omega_{ba} = \varepsilon_b - \varepsilon_a$ . To continue, one assumes the laser frequency  $\omega$  to be close to the transition energy  $\omega_{ba}$ , i.e. the detuning  $\Delta = \omega - \omega_{ba}$  to be small in comparison to the transition energy:  $\Delta \ll \omega_{ba}$ . One then invokes the rotating wave approximation (RWA), which states, that if  $\exp(-i(\omega - \omega_{ba}))$  is slowly varying while  $\exp(-i(\omega + \omega_{ba}))$  is rapidly oscillating,  $\exp(-i(\omega + \omega_{ba}))$  integrates to approximately zero and can be ignored. Choosing the initial conditions  $|a(0)|^2 = 1$  and  $|b(0)|^2 = 0$ , one finds for the expansion coefficients

$$a(t) = e^{+\frac{i}{2}\Delta t} \left( \cos(\Omega t/2) - i\frac{\Delta}{\Omega} \sin(\Omega t/2) \right) \quad (2.125)$$

$$b(t) = e^{-\frac{i}{2}\Delta t} \left( \frac{\mu\varepsilon}{\Omega} \right) (i \sin(\Omega t/2)) \quad (2.126)$$

with the Rabi frequency

$$\Omega = \sqrt{\Delta^2 + (\mu\varepsilon)^2} = \sqrt{\Delta^2 + \bar{\Omega}^2}, \quad (2.127)$$

which for the resonant case  $\Delta = 0$  reduces to

$$a(t) = \cos(\bar{\Omega}t/2) \quad (2.128)$$

$$b(t) = i \sin(\bar{\Omega}t/2). \quad (2.129)$$

In the resonant case, one can additionally show, that if the envelope function of the laser is time-dependent, i.e.  $\varepsilon = \varepsilon(t)$ , the expansion coefficients are of the form

$$a(t) = \cos\left(\int_0^t \frac{\bar{\Omega}(t')dt'}{2}\right) \quad (2.130)$$

$$b(t) = i \sin\left(\int_0^t \frac{\bar{\Omega}(t')dt'}{2}\right), \quad (2.131)$$

which indicates, that for the resonant case the population transfer depends only on the integral  $\int_0^t \bar{\Omega}(t')dt'$  and not on the specific form of  $\bar{\Omega}(t)$ . This is called the **pulse area theorem**.

Note the differences between resonant and detuned Rabi oscillations. In the resonant case  $\Delta = 0$ , the Rabi frequency is  $\bar{\Omega}$  and the population is completely transferred from state  $\Phi_a$  to  $\Phi_b$  and back. In the detuned case, the Rabi frequency is modified by the detuning to  $\sqrt{\bar{\Omega}^2 + \Delta^2}$  and the population is not completely transferred to  $\Phi_b$ . The maximum population transferred to  $\Phi_b$  reduces to  $\bar{\Omega}/\sqrt{\bar{\Omega}^2 + \Delta^2}$ .

### 2.5.2.2. Rabi-like Oscillations in Three-Level Systems

Here, we extend the previous text book discussion to a three-level Hamiltonian with eigenstates  $|\Phi_a\rangle$ ,  $|\Phi_b\rangle$  and  $|\Phi_c\rangle$  and the corresponding eigenenergies  $\varepsilon_a$ ,  $\varepsilon_b$  and  $\varepsilon_c$ . We define the transition energies  $\omega_{ab} = \varepsilon_b - \varepsilon_a$ ,  $\omega_{bc} = \varepsilon_c - \varepsilon_b$  and  $\omega_{ac} = \varepsilon_c - \varepsilon_a$ . The most general wave function of this system can be written as

$$|\Psi(t)\rangle = a(t)e^{-i\varepsilon_a t}|\Phi_a\rangle + b(t)e^{-i\varepsilon_b t}|\Phi_b\rangle + c(t)e^{-i\varepsilon_c t}|\Phi_c\rangle, \quad (2.132)$$

with the constraint  $|a(t)|^2 + |b(t)|^2 + |c(t)|^2 = 1$ . If this system is coupled via its dipole moments to an optical field

$$\mathcal{E}(t) = \varepsilon_1 \cos(\omega_1 t + \varphi_1) + \varepsilon_2 \cos(\omega_2 t + \varphi_2), \quad (2.133)$$

the time-dependent Schrödinger equation in matrix form is

$$i \frac{d}{dt} \begin{pmatrix} a(t)e^{-i\varepsilon_a t} \\ b(t)e^{-i\varepsilon_b t} \\ c(t)e^{-i\varepsilon_c t} \end{pmatrix} = \begin{pmatrix} \varepsilon_a & -\mu_{ab}\mathcal{E}(t) & -\mu_{ac}\mathcal{E}(t) \\ -\mu_{ba}\mathcal{E}(t) & \varepsilon_b & -\mu_{bc}\mathcal{E}(t) \\ -\mu_{ca}\mathcal{E}(t) & -\mu_{cb}\mathcal{E}(t) & \varepsilon_c \end{pmatrix}. \quad (2.134)$$

We take  $\mu_{ab} = \mu_{ba}$  and  $\mu_{ac} = \mu_{ca}$  and assume, that the transition between  $|\Phi_b\rangle$  and  $|\Phi_c\rangle$  is dipole forbidden, i.e.  $\mu_{bc} = \mu_{cb} = 0$ . This leads to the following set of differential equations for the expansion coefficients:

$$\begin{aligned} \dot{a}(t) &= i \frac{\mu_{ab}}{2} \left( \varepsilon_1 \left( e^{i(\omega_1 - \omega_{ba})t + i\varphi_1} + e^{-i(\omega_1 + \omega_{ba})t - i\varphi_1} \right) + \varepsilon_2 \left( e^{i(\omega_2 - \omega_{ba})t + i\varphi_2} + e^{-i(\omega_2 + \omega_{ba})t - i\varphi_2} \right) \right) b(t) \\ &\quad + i \frac{\mu_{ac}}{2} \left( \varepsilon_1 \left( e^{i(\omega_1 - \omega_{ca})t + i\varphi_1} + e^{-i(\omega_1 + \omega_{ca})t - i\varphi_1} \right) + \varepsilon_2 \left( e^{i(\omega_2 - \omega_{ca})t + i\varphi_2} + e^{-i(\omega_2 + \omega_{ca})t - i\varphi_2} \right) \right) c(t) \\ \dot{b}(t) &= i \frac{\mu_{ab}}{2} \left( \varepsilon_1 \left( e^{i(\omega_1 + \omega_{ba})t + i\varphi_1} + e^{-i(\omega_1 - \omega_{ba})t - i\varphi_1} \right) + \varepsilon_2 \left( e^{i(\omega_2 + \omega_{ba})t + i\varphi_2} + e^{-i(\omega_2 - \omega_{ba})t - i\varphi_2} \right) \right) a(t) \\ \dot{c}(t) &= i \frac{\mu_{ac}}{2} \left( \varepsilon_1 \left( e^{i(\omega_1 + \omega_{ca})t + i\varphi_1} + e^{-i(\omega_1 - \omega_{ca})t - i\varphi_1} \right) + \varepsilon_2 \left( e^{i(\omega_2 + \omega_{ca})t + i\varphi_2} + e^{-i(\omega_2 - \omega_{ca})t - i\varphi_2} \right) \right) a(t) \end{aligned}$$

If each laser is in resonance with one of the transitions, i.e.  $\omega_1 = \omega_{ba}$  and  $\omega_2 = \omega_{ca}$ , we can apply the rotating wave approximation to the terms combining  $\omega_1$  with  $\omega_{ba}$  and the ones combining  $\omega_2$  with  $\omega_{ca}$  analogue to the two-level case. This casts the differential equations into the shape:

$$\dot{a}(t) = i \frac{\mu_{ab}}{2} \left( \varepsilon_1 e^{i\varphi_1} + \varepsilon_2 \left( e^{-i(\omega_1 - \omega_2)t + i\varphi_2} + e^{-i(\omega_1 + \omega_2)t - i\varphi_2} \right) \right) b(t) \quad (2.136a)$$

$$+ i \frac{\mu_{ac}}{2} \left( \varepsilon_1 \left( e^{i(\omega_1 - \omega_2)t + i\varphi_1} + e^{-i(\omega_1 + \omega_2)t - i\varphi_1} \right) + \varepsilon_2 e^{i\varphi_2} \right) c(t),$$

$$\dot{b}(t) = i \frac{\mu_{ab}}{2} \left( \varepsilon_1 e^{-i\varphi_1} + \varepsilon_2 \left( e^{i(\omega_1 + \omega_2)t + i\varphi_2} + e^{i(\omega_1 - \omega_2)t - i\varphi_2} \right) \right) a(t), \quad (2.136b)$$

$$\dot{c}(t) = i \frac{\mu_{ac}}{2} \left( \varepsilon_1 \left( e^{i(\omega_1 + \omega_2)t + i\varphi_1} + e^{-i(\omega_1 - \omega_2)t - i\varphi_1} \right) + \varepsilon_2 e^{-i\varphi_2} \right) a(t). \quad (2.136c)$$



To continue, we apply the rotating wave approximation a second time. This time, we assume, that the laser frequencies are sufficiently well separated in energy:

$$|\omega_1 + \omega_2| \gg 0 \quad (2.137a)$$

$$|\omega_1 - \omega_2| \gg 0. \quad (2.137b)$$

With this approximation, Eqs. (2.136) become

$$\dot{a}(t) = i\frac{\mu_{ab}}{2}\varepsilon_1 e^{i\varphi_1} b(t) + i\frac{\mu_{ac}}{2}\varepsilon_2 e^{i\varphi_2} c(t) \quad (2.138a)$$

$$\dot{b}(t) = i\frac{\mu_{ab}}{2}\varepsilon_1 e^{-i\varphi_1} a(t) \quad (2.138b)$$

$$\dot{c}(t) = i\frac{\mu_{ac}}{2}\varepsilon_2 e^{-i\varphi_2} a(t). \quad (2.138c)$$

Choosing the initial conditions  $a(0) = 1$ ,  $b(0) = c(0) = 0$ , Eqs. (2.138) yield the solution

$$a(t) = \cos(\bar{\Omega}/2t) \quad (2.139a)$$

$$b(t) = \frac{\mu_{ab}\varepsilon_1}{\sqrt{(\mu_{ab}\varepsilon_1)^2 + (\mu_{ac}\varepsilon_2)^2}} e^{-i(\varphi_1 - \pi)} \sin(\bar{\Omega}/2t) \quad (2.139b)$$

$$c(t) = \frac{\mu_{ac}\varepsilon_2}{\sqrt{(\mu_{ab}\varepsilon_1)^2 + (\mu_{ac}\varepsilon_2)^2}} e^{-i(\varphi_2 - \pi)} \sin(\bar{\Omega}/2t) \quad (2.139c)$$

with the Rabi-frequency

$$\bar{\Omega} = \sqrt{(\mu_{ab}\varepsilon_1)^2 + (\mu_{ac}\varepsilon_2)^2}. \quad (2.140)$$

There are three main conclusions from this solution.

- I The Rabi-frequency of the three-level Hamiltonian is the Pythagorean mean of the Rabi-frequencies of the single transitions:  $\bar{\Omega} = \sqrt{\bar{\Omega}_{ab}^2 + \bar{\Omega}_{ac}^2}$ . Consequently, it is larger than each of the single frequencies.
- II The maximum populations of the excited states depend only on the ratio of the Rabi-frequencies belonging to the respective transitions  $\frac{|b(t)|^2}{|c(t)|^2} = \frac{\bar{\Omega}_{ab}^2}{\bar{\Omega}_{ac}^2}$ .
- III The relative phases of the expansion coefficients depend on the phases of the applied lasers.

Finally, one finds, that also in the three-level case, the pulse area theorem holds true.

## 2.6. Quantum Optimal Control Theory

In this thesis we are not only interested in the analysis, but also in the control of spectroscopic properties. To achieve this goal, we employ Quantum Optimal Control Theory (Quantum-OCT).

The measurement and control of ultrafast processes are inherently intertwined. In fact, quantum optimal control theory [108, 109] (Quantum-OCT) can be viewed as the *inverse* of theoretical spectroscopy: rather than attempting to predict the reaction of a quantum system to a perturbation, it attempts to find the perturbation that induces a given reaction in a given quantum system. It is the quantum version, first developed in the 80s [110, 111, 112], of a more general mathematical framework, *control theory* [113, 114], which is commonly applied in engineering, for example to design trajectories for satellites and space probes [109]. This quantum version of control was needed given the fast advances in experimental quantum control – or *coherent control of quantum systems*, as it is sometimes called.

The experimental control of quantum systems was born in the field of photo-chemistry: the goal was to achieve the selective destruction or creation of bonds by means of suitably tailored laser fields. It was therefore a consequence of the raise of the field of *femtochemistry*. Numerous techniques were invented in a short period of time, such as the control of quantum interference proposed by Brumer and Shapiro (also called *coherent control scheme*) [115, 116, 117], the “pump-dump” control proposed by Tannor and Rice [118, 119] (where the probe pulse not only probes, but in fact partially “dumps” the excited state wave-packet on the ground state), stimulated Raman adiabatic passage [120], wave-packet interferometry [121], etc.

However, the most successful technique – since it can be considered in fact a generalization of all the previous ones – has been found to be the adaptive feedback control (AFC) first proposed by Judson and Rabitz [122] and first realized in 1997 [123]. Using AFC, ground-breaking results were achieved in the control of chemical reactions [124], and in many related experiments such as the control of the efficiency of photosynthesis processes [125]. Even the photo-isomerization of the retinal molecule in rhodopsin proteins (a process that is crucial e.g. for vision in higher organisms) was optimized [126].

All these advances in experimental quantum control require a theoretical counterpart, provided by Quantum-OCT. Quantum-OCT is concerned with studying the optimal

Hamiltonian (in practice, a portion of the Hamiltonian, such as the temporal profile of the coupling of an atom or molecule to a laser pulse) that induces a target system behaviour: it attempts to answer questions such as what is that optimal shape, is there only one or are there various solutions, what is the most efficient computational algorithm in order to obtain the solution, what is the stability of the solution, etc.

### 2.6.1. General Aspects of Quantum Optimal Control Theory

Let us consider a quantum mechanical system governed by Schrödinger's equation during the time interval  $[0, T]$ :

$$i\frac{\partial\Psi}{\partial t}(x,t) = \hat{H}[u,t]\Psi(x,t), \quad (2.141a)$$

$$\Psi(x,0) = \Psi_0(x), \quad (2.141b)$$

where  $x$  is the full set of quantum coordinates, and  $u$  is the *control*, an external potential applied to the system. Typically, one distinguishes between two types of representations for  $u$ : it can either be a real valued continuous function defined in time or a set of parameters that determine the precise shape of the control function. Throughout this thesis, the latter option is used exclusively. The specification of  $u$ , together with an initial value condition,  $\Psi(0) = \Psi_0$  determines the full evolution of the system,  $\Psi[u]$ , via the propagation of Schrödinger's equation.

The behaviour of the system must then be measured by defining a “target functional”  $F$ , whose value is high if the system evolves according to our goal, and small otherwise. In many cases, it is split into two parts,  $F[\Psi, u] = J_1[\Psi] + J_2[u]$ , so that  $J_1$  only depends on the state of the system, and  $J_2$ , called the “penalty”, depends explicitly on the control  $u$ . Regarding  $J_1$ , it may have two functional forms:

- It may depend on the full evolution of the system during the time interval  $[0, T]$ . We may write this as  $J_1[\Psi] = J_1^{[0, T]}[\Psi]$ , where the  $J_1^{[0, T]}[\Psi]$  functional admits continuous functional derivatives, in particular  $\frac{\delta J_1^{[0, T]}}{\delta \Psi^*(x, t)}$  is continuous at  $t = T$ .
- $J_1$  may only depend on the state of the system at the end of the propagation:  $J_1[\Psi] = J_1^T[\Psi(T)]$ .

Of course,  $J_1$  can be a combination of the two options, i.e.:

$$J_1[\Psi] = J_1^{[0,T]}[\Psi] + J_1^T[\Psi(T)]. \quad (2.142)$$

Often, the functionals are defined through the expectation value of an observable  $\hat{O}$ , i.e.:

$$J_1^T[\Psi(T)] = \langle \Psi(T) | \hat{O} | \Psi(T) \rangle. \quad (2.143)$$

The mathematical problem is then reduced to the problem of maximizing a real-valued function  $G$ :

$$G[u] = F[\Psi[u], u]. \quad (2.144)$$

Therefore, one needs an optimization algorithm to find the maximum (or maxima) of  $G$ . Two broad families can be distinguished: gradient-free procedures, that only require some means to compute the value of  $G$  given a control input  $u$ , and gradient-based procedures, that also require the computation of the gradient of  $G$  with respect to  $u$ . For our work, we have mostly used gradient-free algorithms (all the examples shown in this thesis are based on them); however we have also tried the gradient-based ones. For completeness, I display here the equation for the gradient that Quantum-OCT provides. It is

$$\nabla_u G[u] = \nabla_u F[\Psi, u] \Big|_{\Psi=\Psi[u]} + 2\Im \int_0^T dt \langle \chi[u](t) | \nabla_u \hat{H}[u, t] | \Psi[u](t) \rangle \quad (2.145a)$$

if the control is parametrized and

$$\frac{\delta G}{\delta u(t)} = \frac{\delta F[\Psi, u]}{\delta u(t)} \Big|_{\Psi=\Psi[u]} + 2\Im \langle \chi[u](t) | \hat{D} | \Psi[u](t) \rangle \quad (2.145b)$$

if the control is given as a continuous function of time. Here,  $\hat{D}$  is the coupling of  $u(t)$  to the system, i.e. the time-dependent Hamiltonian is  $\hat{H}[u, t] = \hat{H}_0 + u(t)\hat{D}$ . For a detailed derivation of Eqs. (2.145) I refer the reader to Refs. [111, 213, 214, 215]. Note that a new “wave function”,  $\chi[u]$ , has been introduced; it is given by the solution of:

$$i \frac{\partial \chi[u]}{\partial t}(x, t) = \hat{H}^\dagger[u, t] \chi[u](x, t) - i \frac{\delta J_1^{[0,T]}}{\delta \Psi^*[u](x, t)}, \quad (2.146a)$$

$$\chi[u](x, T) = \frac{\delta J_1^T}{\delta \Psi^*[u](x, T)}. \quad (2.146b)$$

This is similar to the original Schrödinger's equation (2.141), except: (i) It may be inhomogeneous, if  $J_1^{[0,T]}$  is not zero (i.e. if the target is time-dependent) and (ii) The initial condition is given at the final time  $t = T$ , which implies it must be propagated *backwards*. The computation of the gradient or functional derivative of  $G$ , therefore, requires  $\Psi[u]$  and  $\chi[u]$ , which are obtained by first propagating Eq. (2.141a) forwards, and then Eq. (2.146a) backwards. The maxima of  $G$  are found at the critical points  $\nabla_u G[u] = 0$ .

Note, that these are the Quantum-OCT equations based on the linear Schrödinger equation. If one uses gradient-based Quantum-OCT in combination with the non-linear KS equations, the Quantum-OCT equations have to be adapted accordingly. However, since in this thesis only gradient free algorithms are used, I refer the reader to [153] for the derivation and the full description of the correct TDDFT-Quantum-OCT equations.

Depending on the representation of the control, different optimization strategies are used. For gradient-based optimization strategies, where the control is parametrized, one can e.g. use conjugate gradient algorithms like the Broyden-Fletcher-Goldfarb-Shanno (BFGS) variant [216]. If the control is represented directly in real time, a number of algorithms have been developed directly in the field of Quantum-OCT. These algorithms –if applicable– can provide very fast convergence. Examples are the Krotov method [217] and the monotonically convergent techniques proposed by Zhu and collaborators [218, 219].

If the gradient of the control is not available, one uses gradient-free optimization strategies. This is the case in this thesis. In these cases, one can use “evolutionary” or “genetic” algorithms, which are specifically designed for large, typically discrete search spaces [220, 221]. For moderate search spaces, classic choices are the simplex-downhill algorithm by Nelder and Mead [222] or the newer NEWUOA algorithm by Powell [223]. The optimization strategy used for the optimization of spectra in this thesis is based on the simplex-downhill algorithm. For a more detailed description of it, see appendix A.

Finally, if the problem is small and analytically solvable, one can even perform “Quantum-OCT by hand” and can write down the optimal pulse analytically (possibly after having made a few approximations). This is the case in the part about optimal control of Hydrogen. In Section 4.2.1 we write down the analytical shape of the control field based on the derivation of the Rabi-like oscillations in three-level systems in Section 2.5.2.2.

A Quantum-OCT formulation is constructed on top of a given model for the system

process under study. In this thesis we study and optimize the absorption spectra of atoms and molecules using either analytically solvable model Hamiltonians or obtaining the spectra by solving the time-dependent Kohn-Sham equations (TDKS). In either case, we are interested in controlling the spectra with the help of laser pulses, i.e. the control function  $u(t)$  is a laser field  $\mathcal{E}(t)$  (in our case in dipole-representation), that couples to the system via the dipole-operator. In our optimization algorithm, the control function is implemented in a parametrized representation. It is a natural choice to expand the control field in a basis set and to establish the coefficients of this expansion as control parameters:

$$\mathcal{E}(t) = \sum_{i=1}^N c_i g_i(t) \quad (2.147)$$

where  $N$  is the dimension of the optimization (“search”) space and  $g_n(t)$  are orthonormal over the optimization period

$$\int_0^T dt g_n(t) g_m(t) = \delta_{nm}. \quad (2.148)$$

Typical choices for the basis sets are the sine basis

$$g_n(t) = \sqrt{\frac{2}{T}} \sin\left(\frac{\pi}{T} n t\right) \quad n = 1, \dots, N \quad (2.149a)$$

or the normal Fourier basis

$$g_n(t) = \begin{cases} \sqrt{\frac{2}{T}} \sin\left(\frac{2\pi}{T} n t\right) & n = 1, \dots, \frac{N}{2}, \\ \sqrt{\frac{2}{T}} \cos\left(\frac{2\pi}{T} \left(n - \frac{N}{2}\right) t\right) & n = \left(\frac{N}{2} + 1\right), \dots, N. \end{cases} \quad (2.149b)$$

Both have the advantage, that spectral constraints can be automatically enforced: the maximum frequency is given by  $N$  and if we do not include the zero-frequency mode, both sets fulfill the condition  $\int_0^T dt \mathcal{E}(t) = 0$ , which follows from Maxwell’s equations for a freely propagating pulse in the electric dipole approximation [224]. In this thesis, a sine basis is used for all optimizations.

### 2.6.2. Derivation of the Quantum-OCT Equations for the Optimization of Response Functions

We now apply the general theory presented above, to derive the equations for the computation of the gradient of a target functional designed to optimize the response of a system. The *gedanken* setup is the following: for a certain time interval  $[0, T]$  a quantum system is driven by a pump pulse  $\mathcal{E}$  whose precise shape can be manipulated; we wish to design such shape in order to make the (linear) response of the system to some later perturbation *optimal* in some given way.

This setup is consistent with the non-overlapping regime described above; the Hamiltonian that governs the system, once that the pump has passed ( $t \geq T$ ) has the form:

$$\hat{H}(t) = \mathcal{H} + F(t)\hat{V}. \quad (2.150)$$

If, at time  $t = T$ , the system has been driven into the state  $|\Psi(T)\rangle$ , the response function for a perturbation at later times is given by:

$$\chi_{\hat{O}, \hat{V}}(t, t') = -i\theta(t - t')\langle\Psi(T)| [\hat{O}_I(t), \hat{V}_I(t')] |\Psi(T)\rangle. \quad (2.151)$$

The first-order response of the system would then be given by:

$$O_1[\mathcal{E}, F](t) = \int_T^t dt' F(t') \chi_{\hat{O}, \hat{V}}(t, t'). \quad (2.152)$$

In order to simplify the discussion, let us consider a particular form for the perturbation: a sudden one at the end of the pump  $F(t') = \delta(t' - T)$ . Therefore:

$$O_1[\mathcal{E}, \delta_T](t) = \chi_{\hat{O}, \hat{V}}(t, T). \quad (2.153)$$

We may now define a target: for example, we may be interested in enhancing the reaction of the system at a given frequency, i.e.  $O_1[\mathcal{E}, \delta_T](\omega) = \int_T^\infty dt' e^{-i\omega t'} O_1(t')$ . By making use of the previous equations, it can be easily seen that the problem fits into the framework discussed in the previous section, i.e. the target functional is given by the expectation value of some operator:

$$J_1^T[\Psi(T)] = \langle\Psi(T)| -i \int_T^\infty dt' e^{-i\omega t'} \left[ e^{i(t'-T)\mathcal{H}} \hat{O} e^{-i(t'-T)\mathcal{H}}, \hat{V} \right] |\Psi(T)\rangle \quad (2.154)$$

The equations for the gradient are therefore Eqs. (2.145); that must be completed with the equations of motion for the co-state, Eq. (2.146a), and, in particular, with its boundary condition at time  $t = T$ , which is the only one that in fact depends on the definition of the target operator:

$$|\chi(T)\rangle = -i \int_T^\infty dt' e^{-i\omega t'} \left[ e^{i(t'-T)\mathcal{H}} \hat{O} e^{-i(t'-T)\mathcal{H}}, \hat{V} \right] |\Psi(T)\rangle. \quad (2.155)$$

Similar formulas can be obtained for more general definitions of the target functional in terms of the response  $O_1(\omega)$ , and for more general probe functions. In all cases the computational difficulties associated to the computation of this boundary condition are also similar, and are considerable. By inspecting the previous formula, it can be learnt that various time-propagations of the wave functions, forward and backwards, are required. These difficulties are even larger if the scheme is formulated within TDDFT – in the previous derivation we have used the exact many-electron wave functions. In consequence, we decided to employ, for this type of optimization, gradient-free algorithms, such as the one that we describe in next section.

### 2.6.3. Derivation of a Gradient-Free Algorithm for Quantum Optimal Control Theory

In this thesis the goal is to maximize the absorption of light in a certain energy range by means of exciting a system with a laser. This idea falls into the optimization category that we have just described. Here, we describe, a general gradient-free procedure to optimize spectra – in particular, the maximization of absorption.

First, we define the target functional  $F[\Psi[u], u]$ . For a general optimization of a spectrum,  $F$  is an arbitrary functional of the average absorption coefficient  $\bar{\sigma}(\omega, T + \tau)$  (2.54) and of the control laser  $\mathcal{E}(t)$  and so is the real-valued function  $G$ :

$$G(\mathcal{E}) = F[\bar{\sigma}[\mathcal{E}], \mathcal{E}]. \quad (2.156)$$

$F$ , respectively  $G$  have to be chosen in a such a way, that their value will be maximal for the desired type of spectrum. In order to maximize the absorption of light, we employ two different definitions of  $G(\mathcal{E})$ : (A) We compute the integral over the spectrum in a certain energy interval  $[E_{min}, E_{max}]$  after the excitation of the system with the control



laser field  $\mathcal{E}$  and (B) like before but we add a penalty for ionization:

$$G^A(\mathcal{E}) = \int_{E_{min}}^{E_{max}} \bar{\sigma}[\mathcal{E}](E) dE, \quad (2.157a)$$

$$G^B(\mathcal{E}) = \int_{E_{min}}^{E_{max}} \bar{\sigma}[\mathcal{E}](E) \exp\left(-\gamma \frac{N_0 - N_T[\mathcal{E}]}{N_0}\right) dE. \quad (2.157b)$$

where  $N_0$  and  $N_T$  are the number of electrons in the system at the beginning and the end of the control pulse and  $\gamma$  is the penalty for ionization.

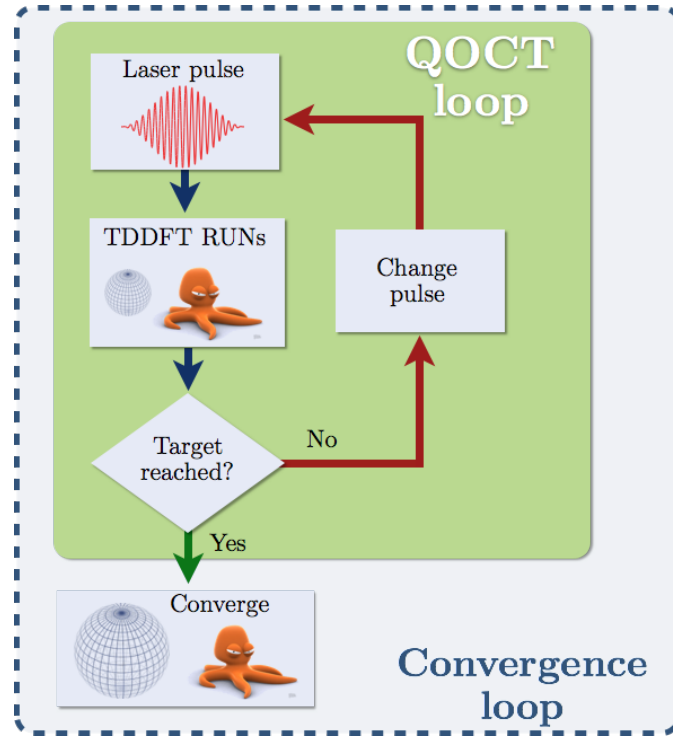


Figure 2.3.: Gradient-free optimization procedure to optimize the response-function of an excited-state system using the real-time, real-space TDDFT code `octopus`.

Next, one chooses a representation of the control field: pump duration, carrier frequencies, polarizations, envelope function and – since we describe pump-probe experiments – the delay  $\tau$  between the end of the pump and the probe pulse (which can be positive or negative). One then decides, which of these parameters should be optimized and which ones should be kept fixed. The control pulse is then defined as a function of the

optimization parameters

$$\mathcal{E} = \mathcal{E}(c_1, c_2, \dots, c_N) \quad (2.158)$$

in an  $N$ -dimensional parameter space and the initial parameters are chosen.

For this kind of optimizations we work with gradient-free algorithms like the Downhill-Simplex algorithm, described in appendix A. Having defined the control parameter and the laser parametrization, we can start the optimization circle.

Each optimization step consists of two steps. In the first step, the pump pulse is generated and the system is evolved under its influence until the probe time  $T_P + \tau$ . The evolution is stopped. In the second step, the absorption is calculated by probing the system with a delta perturbation. To this end,  $(n+1)$  copies of the propagation are created ( $n$  being the dimensionality of the system). In each dimension, a kick is applied (see Section 2.4.5 for how to obtain an excited-state spectrum from a time-dependent calculation) and the system evolved for the “spectrum time”  $T_S$  afterwards. From these  $(n+1)$  time-propagations, the excited-state spectrum  $\bar{\sigma}(\omega, \tau)$  is calculated and the control function  $G(\mathcal{E})$  is evaluated.  $G(\mathcal{E})$  is then fed back into the optimization algorithm, which creates a new set of parameters to form a new control pulse. The general procedure is illustrated in Fig. 2.3.

Note, that in order to obtain the average absorption coefficient, the full-frequency dependent polarizability tensor has to be known. Therefore,  $(n+1)$  time-propagations have to be performed for the “spectrum time”  $T_S$  - one for each kick-direction and the  $(n+1)$ -th for the reference calculation. This makes this scheme computationally rather expensive. Whilst these calculations are feasible for small systems, a future development of faster computers and better parallelization techniques will be needed to tackle larger problems. Appendix B contains further information about the more technical details of the optimization.

## 2.7. The Colour Perception of the Human Eye

In this thesis, we analyze optical spectra in the context of their perception by us - human beings. We argue, that by controlling the spectrum of a system, one can control its colour. In this context, one has to understand, how the light, that is perceived by the human retina is translated into human colour perception. This question is addressed in

the following.

In 1802 Thomas Young proposed the existence of three different types of photoreceptors in the eye [225]. The perception of light from these three receptors should enable the human being to see all the different colours, that it is able to see. His theory was further developed by Hermann von Helmholtz and became known as **Young-Helmholtz trichromatic theory**. The existence of three different kinds of cones was proven in the 20th century by Gunnar Svaetichin [226] and their existence in the human eye finally proven in 1983.

According to the Young-Helmholtz trichromatic theory, any colour perceived by the human eye can be described by only three parameters, the **tristimulus values**. Each tristimulus value describes the perception of one of a set of three colour-matching functions (which span the complete colour space). A set of three linearly independent colour-matching functions is called **observer**.

The first two observers and therefore the first quantitative link between physical light and the physiological experience of light was defined in 1931 by the International Commission on Illumination (CIE). The spanned colour spaces carry the names CIE 1931 RGB colour space and CIE 1931 XYZ colour space. The observer belonging to the CIE 1931 XYZ colour space is called **CIE standard observer** and describes the colour perception of an average human eye when illuminated from an angle smaller than 2 degrees. A newer version, the CIE 1964 colour space deals with illumination from angles above 4 degrees.

The CIE's colour matching functions  $\bar{x}(\lambda)$ ,  $\bar{y}(\lambda)$  and  $\bar{z}(\lambda)$ , which form the standard observer are shown in the left part of Figure 2.4. The tristimulus values for a colour with a spectral power distribution  $I(\lambda)$  are obtained from the standard observer according to

$$X = \int_{380nm}^{780nm} I(\lambda) \bar{x}(\lambda), \quad (2.159a)$$

$$Y = \int_{380nm}^{780nm} I(\lambda) \bar{y}(\lambda), \quad (2.159b)$$

$$Z = \int_{380nm}^{780nm} I(\lambda) \bar{z}(\lambda). \quad (2.159c)$$

A full diagram containing all visible colours is a three-dimensional object. Nevertheless, in practice, colours are often displayed as objects in a two-dimensional space. This is due

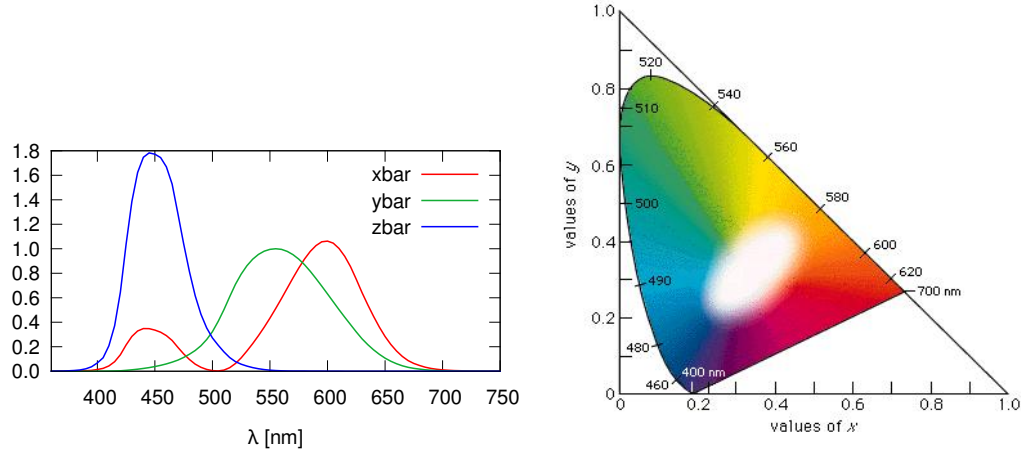


Figure 2.4.: (left) The CIE standard observer colour matching functions. (right) The CIE 1931 chromaticity diagram (taken from the Encyclopedia Britannica (<http://global.britannica.com/science/tristimulus-system>)).

to the fact, that the description of colours is usually divided into two aspects: brightness and chromaticity. The CIE XYZ space was designed in a way, that the Y parameter is a measure for the brightness, while the two derived quantities  $x$  and  $y$

$$x = \frac{X}{X + Y + Z}, \quad (2.160a)$$

$$y = \frac{Y}{X + Y + Z}, \quad (2.160b)$$

$$z = \frac{Z}{X + Y + Z}. \quad (2.160c)$$

characterize the chromaticity, which is then displayed in a so-called chromaticity diagram. The CIE 1931 chromaticity diagram is shown in the right part of Figure 2.4. The derived colour space is called CIE xyY colour space and is widely used to specify colours in practice.

### 3. Simulating Pump-Probe Photo-Electron and Absorption Spectroscopy on the Attosecond Time-Scale with Time-Dependent Density-Functional Theory <sup>‡</sup>

#### Contents

<b>3.1. One-dimensional Model Helium . . . . .</b>	<b>77</b>
<b>3.2. Helium Atom in 3D . . . . .</b>	<b>82</b>
3.2.1. Transient Absorption Spectroscopy . . . . .	82
3.2.2. Time-Resolved Photo-Electron Spectroscopy . . . . .	85
<b>3.3. Ethylene Molecule . . . . .</b>	<b>88</b>
3.3.1. Transient Absorption Spectroscopy . . . . .	88
3.3.2. Time-Resolved Photo-Electron Spectroscopy . . . . .	89
<b>3.4. Conclusions . . . . .</b>	<b>93</b>

Pump-probe experiments are the preferred technique to study the dynamical behaviour of atoms and molecules: the dynamics triggered by the pump pulse can be monitored by the time-dependent reaction of the system to the probe pulse, a reaction that can be measured in terms of, for example, the absorption of the pulse intensity, or of the emission of electrons [227].

A wealth of possibilities exists, depending on the frequencies, durations and intensities

---

<sup>‡</sup>The results presented in this chapter were published in [3].

of the two pulses. A common set-up in attosecond physics employs an XUV attosecond pulse and a relatively more intense, longer (few femtoseconds) NIR or visible pulse used for its generation. Combining two XUV attosecond pulses is in principle possible (and has been theoretically analysed [68]), but unfortunately the low outputs of current XUV attosecond pulses lead to much too weak signals. Another choice to make is the final observable, i.e. what kind of system reaction is to be measured as a function of the time delay. In this work we focus on two common choices. One is time-resolved photo-electron spectroscopy (TRPES) where one observes the emission of electrons (their energies, angular distribution, or total yield) from the pumped system due to the probe pulse. The other is transient absorption spectroscopy (TAS), where one observes the optical absorption of the probe signal.

Both TAS and TRPES have recently been demonstrated in the attosecond regime [1, 85, 89, 90, 91, 92]. The goal of this work is to study TAS and TRPES at the attosecond time scale going beyond the Single-Active Electron (SAE) approximation. Indeed, it would be desirable to analyze these processes with a non-perturbative theory (since at least one of the pulses is usually very intense), which at the same time is capable of going beyond the SAE approximation and accounting for many-electron interaction effects. This last fact is relevant since the attosecond time resolution obtained in this type of experiments is able to unveil the fast dynamical electron-electron interaction effects. The SAE, which essentially assumes that only one electron actively responds to the laser pulse, has been successfully used to interpret many strong-field processes. However, its range of validity is limited, and roughly speaking it is expected to fail whenever the energies of multielectron excitations become comparable to the laser frequencies or the single electron excitations [98].

Time-Dependent Density Functional Theory (TDDFT) in principle meets all requirements: it may be used non-perturbatively, includes the electron-electron interaction and can handle out-of-equilibrium situations. It has been routinely used in the past decades to study the electron dynamics in condensed matter *in equilibrium*. By this we mean that, usually, one computes the linear or non-linear response properties of systems in the ground state (or at thermal equilibrium). In pump-probe experiments, however, one must compute the response of a system that is being driven out of equilibrium by an initial pulse. In Section 2.2 we have demonstrated how the general linear response theory can be extended to describe TAS and in Section 2.4 we have shown how both TAS and

TRPES can be combined with TDDFT. The discussed theory was implemented in the `octopus` code [100, 101, 102, 103] and here we present some applications.

In order to simplify the illustration of the results, the Born Oppenheimer approximation in combination with a clamped ion approximation has been used in the calculations for the molecular case. Further inclusion of the ionic motion could be done at the semi-classical level with Ehrenfest dynamics [101, 228] – already implemented in the code – and without any essential modification to the theory presented.

### 3.1. One-dimensional Model Helium

As first example we study the absorption spectrum of an excited one-dimensional soft-Coulomb Helium atom. This is an exactly solvable model that provides a useful benchmark to test different approximations. We will first discuss the exact solution, and later apply TDDFT. A more realistic 3D model will be presented in the next section.

The 1D model of the Helium atom is defined as given in (2.119) in Chapter 2.5 with an atomic charge of  $C = 2$  and two electrons  $N = 2$ . The wave functions and other necessary functions are represented on a real space regular grid; a squared (linear for one-dimensional TDDFT) box of size  $L = 200$  a.u. and spacing  $\Delta x = 0.2$  a.u. has been employed in all the calculations.

In order to illustrate how an external field can modify the optical properties of a system in Figure 3.1 we show a scan of the non-equilibrium absorption spectrum generated by a 45 cycle  $\sin^2$  envelope pulse with intensity  $I = 5.26 \times 10^{11}$  W/cm<sup>2</sup> at different angular frequencies  $0.51 \text{ a.u.} \leq \omega_P \leq 0.59 \text{ a.u.}$ . The plot displays  $\Im[\alpha[\mathcal{E}, \tau](\omega, \omega_P)]$ , choosing the time of the kick  $\tau$  (see Section 2.4.5) right at the end of the pump pulse.

It can be seen how the absorption around the first excitation frequency 0.533 a.u. is strongly diminished when the frequency of the pump resonates with that frequency. In that situation, an absorption peak also appears around the excitation frequency corresponding to the transition from the first to the second excited state, in our case at 0.076 a.u.. This behavior is a direct consequence of the fact that the laser is pumping the system to the first excited state and this process is more efficient for a field tuned with the excitation energy. The absorption spectrum is therefore a mixture of the one corresponding to the unperturbed ground state and that of the first excited state.

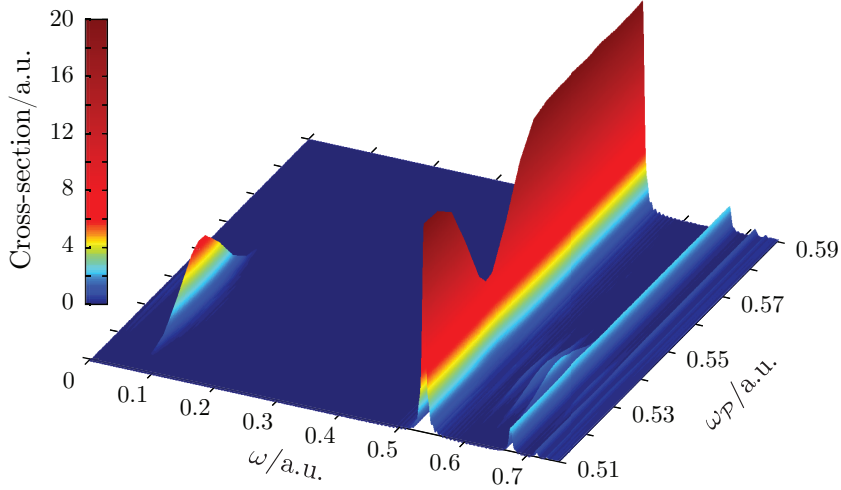


Figure 3.1.: Out of equilibrium absorption spectrum as function of the pump laser frequency for one-dimensional Helium. The system is driven out of equilibrium by 45 cycle  $\sin^2$  envelope laser pulses of intensity  $I = 5.26 \times 10^{11}$  W/cm<sup>2</sup>, at different carrier frequencies and then probed right after. Maximal response is observed for frequencies close to the first optical transition  $\omega_P = 0.533$  a.u..

In order to analyze this point further, a cut at the resonant frequency is displayed in the lower (blue) curves of Figure 3.2. The filled curve represents the spectrum obtained from the system in its ground state while the solid line corresponds to the spectra of the system excited by a laser pulse with a frequency resonant with the first optical transition and probed after the perturbation. By direct comparison of the two spectra it is easy to discriminate the peaks associated with the ground-state absorption from the ones characterizing the absorption from the excited state. In particular, the peaks related to the ground-state absorption are located at the energies  $\omega_{0 \rightarrow 1} = \epsilon_1 - \epsilon_0 = 0.533$  a.u. corresponding to the transition from the ground ( $\epsilon_0 = -2.238$  a.u.) to the first excited state ( $\epsilon_1 = -1.705$ ) and  $\omega_{0 \rightarrow 3} = \epsilon_3 - \epsilon_0 = 0.672$  a.u. corresponding to the third excited state ( $\epsilon_3 = -1.566$  a.u.) – the direct excitation of the second excited state is forbidden by symmetry. The solid curves show fingerprints of the population of the first excited state, namely the peaks corresponding to transitions from that first excited state to others: in



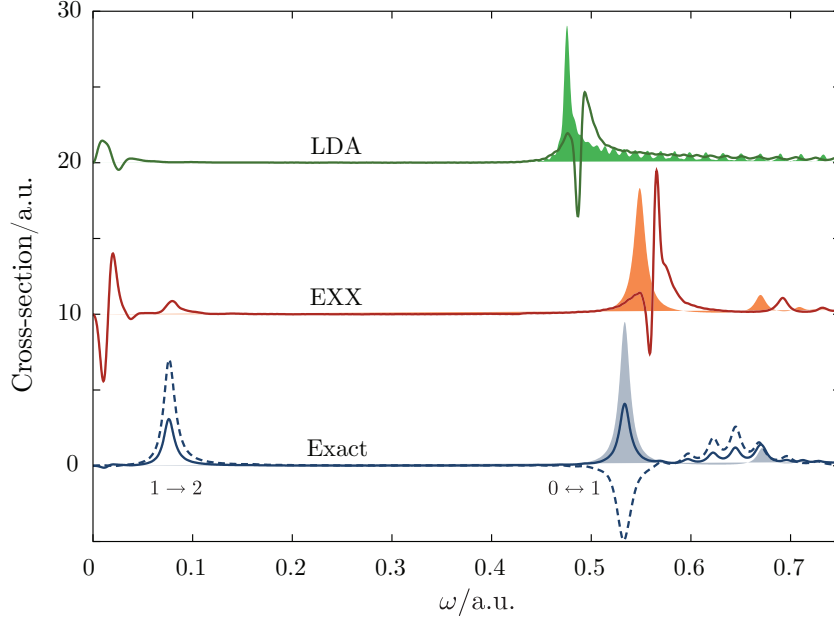


Figure 3.2.: Comparison of absorption spectra calculated in different approximations for a one-dimensional Helium model. The filled curves are the spectra for the unperturbed systems while the solid lines are the spectra of the system excited by a laser as in Figure 3.1 resonant with the first allowed optical transition: exact time-dependent Schrödinger equation  $\omega_P = 0.533$  a.u. (in blue), EXX  $\omega_P = 0.549$  a.u. (in red), and LDA  $\omega_P = 0.475$  a.u. (in green). The dashed blue line is the absorption of the system perturbed by a 180 cycle laser and probed at  $t = 30.62$  fs, where the population on the excited state is maximal. The lines have been shifted by a vertical constant to facilitate the comparison between results.

particular, the peak appearing at the low energy  $\omega_{1 \rightarrow 2} = \epsilon_2 - \epsilon_1 = 0.076$  a.u. is associated with the transition from the first excited state  $\epsilon_1$  to the second one  $\epsilon_2 = -1.629$  a.u..

These spectra contain information that is not contained in the equilibrium ones. For example, let us consider the spectra that would be produced by each single eigenstate, given by the state-dependent dynamical polarizabilities, which may be written in the sum-over-states form as:

$$\alpha^{(i)}(\omega) = \sum_{j \neq i} \left[ \frac{|\langle \Psi_i | \hat{D} | \Psi_j \rangle|^2}{\omega + (\epsilon_j - \epsilon_i) + i0^+} - \frac{|\langle \Psi_i | \hat{D} | \Psi_j \rangle|^2}{\omega - (\epsilon_j - \epsilon_i) + i0^+} \right].$$

The poles of this function provide us with the eigenvalue differences  $\epsilon_j - \epsilon_i$ ; if this value is positive, the corresponding term is associated with a photon-absorption process; if it is negative, with a stimulated emission term. The weight associated with each one of these poles provide us with the dipole coupling matrix elements  $\langle \Psi_i | \hat{D} | \Psi_j \rangle$ .

During the time evolution, the wavefunction can be expanded on the basis of eigenstates of the unperturbed system  $\Psi(t) = \sum_i \gamma_i(t) \Psi_i$ . When the system is probed at a certain time  $t$ , the resulting spectrum can be thought as a linear combination of the spectra produced by each single eigenstate plus interference terms. An analysis of the transient spectrum may therefore provide information about the mixing weights  $\gamma_i$ , and about excitation energies and dipole couplings between excited states – information that is absent in equilibrium ground-state linear response.

In our case, we find by direct projection of the time-dependent wave function onto the eigenstates, that the system after the pulse is composed mainly of the ground and the first excited state with weights,  $|\gamma_0|^2 = |\langle \Psi_0 | \Psi(t) \rangle|^2 = 0.7120$  and  $|\gamma_1|^2 = |\langle \Psi_1 | \Psi(t) \rangle|^2 = 0.2876$ . The same information can be recovered by comparing the perturbed and the unperturbed spectrum at  $\omega_{0 \rightarrow 1}$ . At this energy we only have the contribution coming from  $\Psi_0 \rightarrow \Psi_1$  and its inverse  $\Psi_1 \rightarrow \Psi_0$ . The peak height of the perturbed spectrum after the laser pulse  $h_t$  is therefore a combination of the heights associated with the ground  $h_0$  and the excited  $h_1$  states:  $h_t = |\gamma_0|^2 h_0 + |\gamma_1|^2 h_1$ . At this energy  $h_0 = -h_1$  due to the nature of the transition  $1 \rightarrow 0$  the ratio  $\alpha = h_t/h_0 = |\gamma_0|^2 - |\gamma_1|^2 = 0.4258$  thus gives direct information on the difference of the mixing weights. Complementing this information with a two-level system assumption  $|\gamma_0|^2 + |\gamma_1|^2 = 1$  we obtain  $|\gamma_0|^2 = (1 + \alpha)/2 = 0.7129$  and  $|\gamma_1|^2 = (1 - \alpha)/2 = 0.2871$  in good agreement with the results calculated by direct projection of the wavefunction.

In Figure 3.3 we display the population weights for two different laser pulses. The red lines correspond to the same laser pulse as in Figure 3.2 while the blue lines pertain to a four times longer laser with the same parameters (intensity, envelope shape and carrier frequency) and 180 optical cycles. For both lasers the populations of both the ground and first excited state at each time almost sum to one, indicating an essential two-level dynamics. In the case of the long pulse we observe a maximum (minimum) of the population over the excited (ground) state at  $t = 30.62$  fs. This behavior can be understood in terms of Rabi oscillations (see Section 2.5.2).

A Rabi oscillation is a fluctuation behavior of states occupation occurring due to the

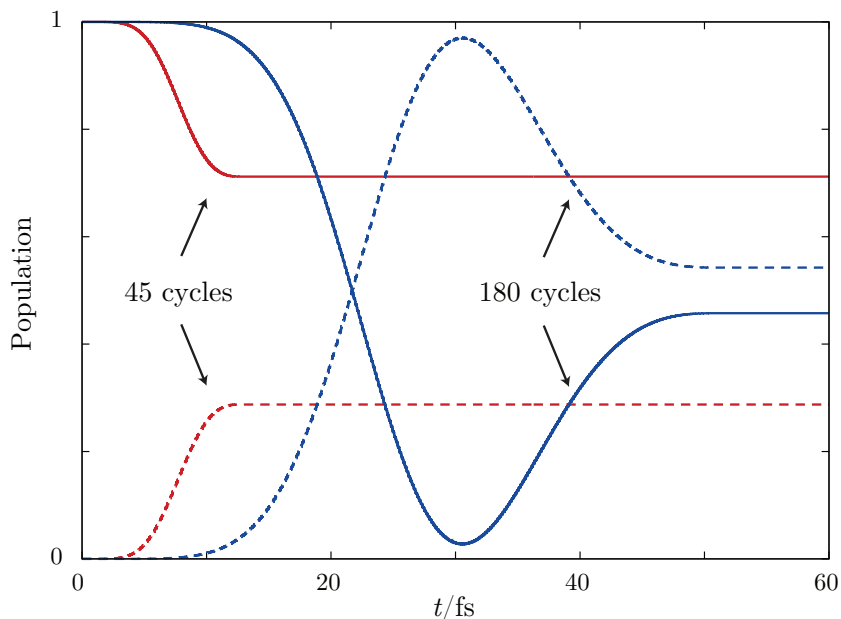


Figure 3.3.: Exact population on the ground  $|\gamma_0(t)|^2 = |\langle \Psi_0 | \Psi(t) \rangle|^2$  (solid lines) and first excited  $|\gamma_1(t)|^2 = |\langle \Psi_1 | \Psi(t) \rangle|^2$  (dashed lines) states as a function of time for different laser pulses. In red a 45 cycles pulse with parameters as in Figure 3.2, and in blue a longer 180 cycles pulse with the same parameters.

interaction of an oscillatory optical field in resonance with a two-level system. The occupation probability alternates with the Rabi frequency  $\Omega(t) = f(t)\mu_{0 \rightarrow 1}$ , where  $\mu_{0 \rightarrow 1}$  is the dipole transition matrix element between the states and  $f(t)$  is the electric field envelope. Extremal points of the populations should be located at times where the pulse area  $\Theta(t) = \int_{-\infty}^t d\tau f(\tau)\mu_{0 \rightarrow 1}$  is an integer multiple of  $\pi$ ,  $\Theta(t) = n\pi$ . With the numerically calculated matrix element  $\mu_{0 \rightarrow 1} = 1.11$  a.u. the first maximal population of the excited state is expected at  $t = 30.65$  fs, in good agreement with what is observed. The absorption spectrum at this time, as shown in Figure 3.2 (dashed blue line), displays a considerable enhancement at  $\omega_{1 \rightarrow 2}$  and a negative emission peak at  $\omega_{0 \rightarrow 1}$  as expected from a pure excited state.

It is interesting to study the same model with TDDFT instead of with an exact treatment in order to address the performance of available (mainly static) xc-functionals. In Figure 3.2 we display results obtained with TDDFT, employing two different exchange-correlation (xc) functional approximations: exact exchange [229] (EXX) in red, and one-

dimensional local density approximation [230] (LDA) in green. The calculations were performed in the adiabatic approximation using the same parameters as in the exact case. The laser frequency was tuned to match the first optical transition appearing at:  $\omega_P = 0.549$  a.u. for EXX, and  $\omega_P = 0.475$  a.u. for LDA.

The unperturbed spectrum (solid curve) provided by EXX is in good agreement with the exact calculation, and the perturbed one qualitatively reproduces the exact result. In particular the new peak appearing at low energy associated with the transition  $1 \rightarrow 2$  is well represented. In contrast LDA is only capable of reproducing one peak both for the perturbed and unperturbed cases. This is due to the known problem of asymptotic exponential decay of the functional that in this one-dimensional example supports only a single bound excited state.

A common feature of both approximations is constituted by the presence of negative values in the perturbed spectra. This can be tracked down to the lack of memory in the adiabatic xc-functional approximation [231]. The lack or wrong memory dependence in the functional results in slightly displaced absorption and emission peaks associated with the same transition. This fact, analyzed in the light of Eq. (3.1), results, at the transition energy, in a sum of two Lorentzian curves with different sign and slightly different centers. This explains why we get two inverted peaks where we should have only a single one going from positive to negative strength as we populate the excited state – as shown by the exact (blue) curves in Figure 3.2.

## 3.2. Helium Atom in 3D

In this section we study the real Helium atom. We employed the EXX functional and discretized TDDFT equations on a spherical box of radius  $R = 14$  a.u., spacing  $\Delta x = 0.4$  a.u. and absorbing boundaries 2 a.u. wide.

### 3.2.1. Transient Absorption Spectroscopy

We begin by investigating the changes in absorption of He under the influence of an external UV laser field driving the system with the frequency of the first dipole-allowed excitation. To this end we used a 45 cycle  $\sin^2$  laser pulse in velocity gauge with carrier  $\omega_P = 0.79$  a.u. resonant with the  $1s^2 \rightarrow 1s2p$  transition, of intensity  $I = 2.6 \times 10^{12}$  W/cm<sup>2</sup>

polarized along the  $x$ -axis. In Figure 3.4 we show a comparison of the absorption spec-

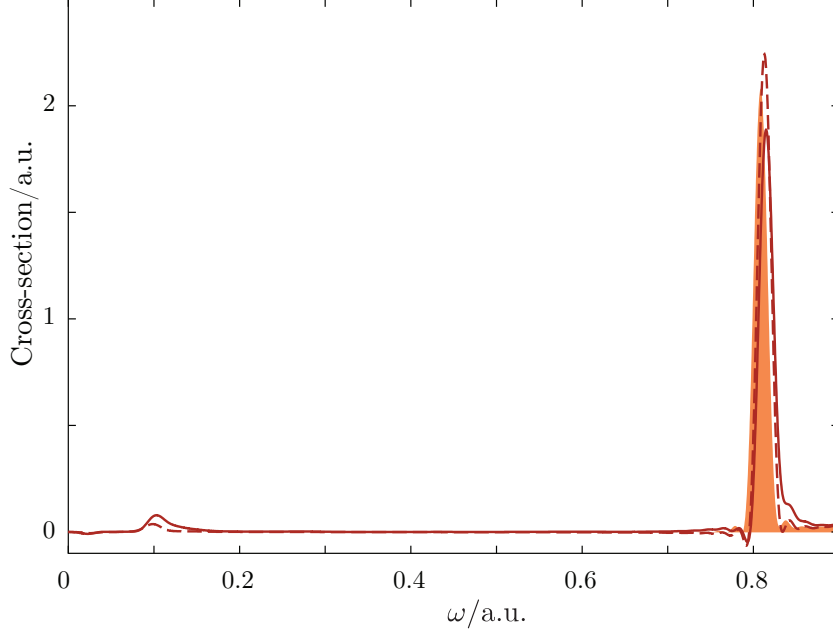


Figure 3.4.: Comparison of the absorption spectra of unperturbed (filled curve) and perturbed He atom probed at  $\tau = 5.32$  fs (solid line) and after the end of the pulse  $\tau = 8.68$  fs (dashed line). The spectrum range is below the ionization threshold. The atom is excited by a 45 cycle  $\sin^2$  envelope laser pulse polarized along the  $x$ -axis with carrier  $\omega_P = 0.79$  a.u. resonant with the first optical transition, intensity  $I = 2.6 \times 10^{12}$  W/cm<sup>2</sup>.

trum for the unperturbed atom (filled curve) and the perturbed one probed with a delta perturbation (i) during the excitation at  $\tau = 5.32$  fs (solid line) and (ii) right after the pump pulse at  $\tau = 8.68$  fs (dashed line). The comparison presents many traits similar to the ones discussed in Section 3.1 for the one-dimensional Helium model. In particular, fingerprints of the population of the first excited state can be observed in the appearance of a peak in the gap at  $\omega_{2p \rightarrow 3s} = 0.10$  a.u. associated with the transition  $1s2p \rightarrow 1s3s$ . The second peak, associated with the transition  $1s^2 \rightarrow 1s2p$ , presents height changes correlated with the former one. We also obtain the small artifacts, such as the energy shifts and the negative values attributed to the xc-kernel memory dependence discussed previously which hinder a population analysis similar to what performed for exact 1D He model. Additional details on the excitation process can be acquired by expanding

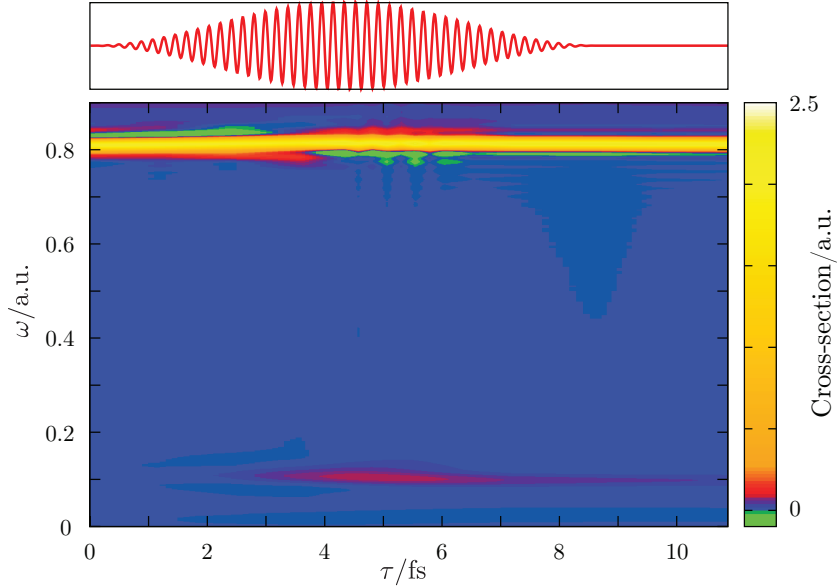


Figure 3.5.: Helium transient absorption spectrum scan for different time delays  $\tau$ . The pump laser pictured in the upper panel is the same as in Figure 3.4.

the time dimension of the absorption spectrum. In Figure 3.5 the time resolved absorption spectrum (TAS) map is displayed. The map was produced by probing the system at different time delays. As the delay is increased we observe the build-up of the peak associated with the state being pumped by the laser pulse at  $\omega_{2p \rightarrow 3s}$ . This changes are reflected in the oscillations of the ground state first optical peak at  $\omega_{1s \rightarrow 2p}$ . In TDDFT the knowledge of the wavefunction is lost in favor of the density, which does not allow us to do a population analysis based on simple wave function projection. For this reason a population analysis, that would require a projection of wavefunctions is not a simple task. The transient absorption spectrum, on the other hand, is an explicit density functional, and its computation with TDDFT may help us to understand the evolution of the state populations. The peak appearing in the gap presents a maximum at  $\tau = 5.39$  fs that emerges before the end of the pump pulse ( $\tau = 8.68$  fs). This peak is associated only with the transition from the  $1s2p \rightarrow 1s3s$  and therefore its height is proportional to the  $2p$  excited state population. The oscillation can then be interpreted in terms of Rabi physics as discussed in Section 3.1.

## 3.2.2. Time-Resolved Photo-Electron Spectroscopy

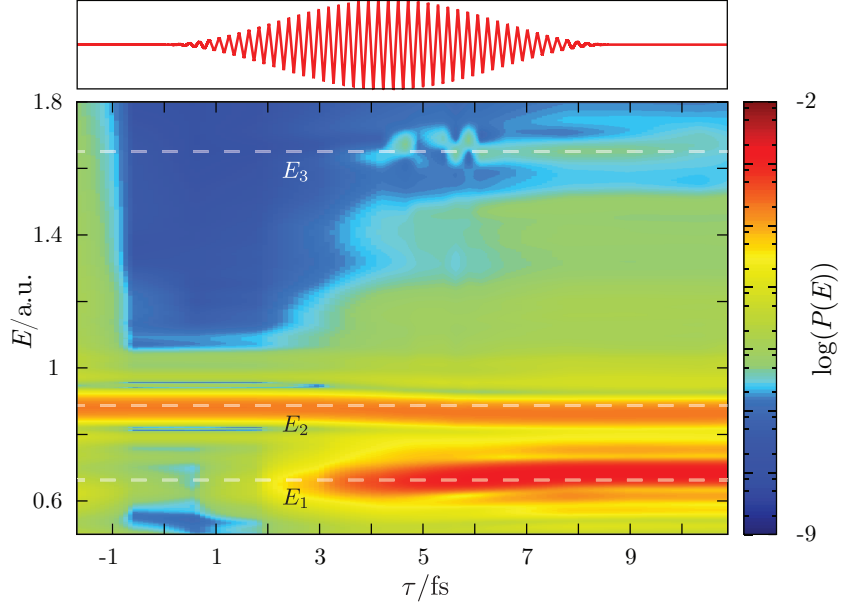


Figure 3.6.: Helium transient photoelectron spectrum in logarithmic scale. The pump laser (upper panel) is the same as in Figure 3.4 and the probe is a 40 cycles trapezoidal laser pulse with 8 cycles ramp,  $\omega_p = 1.8$  a.u.,  $I = 5.4 \times 10^9$  W/cm<sup>2</sup> aligned with the pump pulse.

Further insight can be achieved investigating the photoemission properties of the system. In Figure 3.6 we show the TRPES map, as calculated in a pump-probe set up. Photoelectrons are calculated with the technique outlined in Section 2.4.6. The pump pulse is the same as the one employed for TAS. The probe is a 40 cycles trapezoidal laser pulse (8 cycles ramp) with carrier frequency  $\omega_p = 1.8$  a.u., intensity  $I = 5.4 \times 10^9$  W/cm<sup>2</sup>, polarized along the  $x$ -axis and is weak enough to discard non-linear effects. We performed a scan for different time delays, measuring each delay as the difference from the probe center to the beginning of the pump. Negative delays correspond to the situation where the probe precedes the pump. Moreover, in order to include all the relevant trajectories a spherical box of  $R = 30$  a.u. was employed, and photoelectrons were recorded only during the up-time of the probe pulse.

The TRPES map in Figure 3.6 shows three main features at  $E_1 = 0.66$  a.u.,  $E_2 = 0.88$  a.u. and  $E_3 = 1.67$  a.u.. In our case the probe pulse is weak, and photoelectrons

escaping the system undergo photoelectric-effect energy conservation. A bound electron can absorb a single photon and escape from the atom with a maximum kinetic energy  $E = \omega_p - I_P$ , where  $\omega_p$  is the probe carrier frequency and  $I_P$  is the field-free ionization energy. The ionization potential can be evaluated in DFT as the negative energy of the highest occupied KS orbital (HOMO)  $I_P = \epsilon_{2s} = 0.92$  a.u. [232]. Thus the peak appearing at  $E_2$  is energetically compatible with photoelectrons emitted from the  $2s$  level:  $E_2 = \omega_p - I_P$ . Consistently, this peak is the only one appearing at negative delays where the pulses do not overlap. Moreover, the peak strength is weakly varying with the delay while slightly shifting towards lower values around 3 fs in accordance with TAS findings. At about the same delay time the peak at  $E_3$  begins to emerge. This peak corresponds to emission from the pump-excited  $2p$  state  $E_3 = \omega_p + \omega_p - I_P$ . It is a process where the atom, initially in the ground state, absorbs a photon from the pump and gets excited to the  $2p$  bound state. The subsequent absorption of a probe photon frees the electron into the continuum. The peak at  $E_1$  is understood in terms of pump photons only:  $E_3 = 2\omega_p - I_P$ . The ionization mechanism shares the first step with the  $E_3$  process, namely a  $2s \rightarrow 2p$  excitation produced by the absorption of a  $\omega_p$  photon. In the second step the electron is directly excited to a continuum state by the absorption of a second  $\omega_p$  photon. In the linear regime, the direct photoionization cross-section decays exponentially with energy [233]. For this reason and due to the disparity in intensity between pump and probe this ionization channel is by far the most favorable one.

In direct photoemission processes, the photoelectron angular distribution (PAD) contains information about the electronic configuration of the ionized state [234]. In order to support the energetic arguments PADS  $P(\theta, \phi, E)$  at  $\tau = 8.99$  fs are presented in Figure 3.7 (a), (b), (d) together with cuts on TRPES map at  $\tau = 0$  fs and  $\tau = 8.99$  fs (b). For each energy marked in Figure 3.7 (c) we perform spherical cuts of the photoemission probability on energy shells at  $E = E_1, E_2, E_3$ . Each cut is then plotted in polar coordinates with  $\theta$  being the angle from the  $z$ -axis and  $\phi$  the angle in the  $xy$ -plane measured from the  $x$ -axis. Intersection of the lasers polarization axis with the sphere are marked with a white cross.

Figure 3.7 shows clearly that photoelectrons at  $E_1$  (a) and  $E_3$  (d) have similar nature compared to  $E_2$  (b), in agreement with the energy analysis. Electrons emerging with a kinetic energy of  $E_2$  are emitted from a  $2s$  state, and symmetry of the orbital is imprinted in the photoelectrons angular distribution. In order to understand the PAD features it



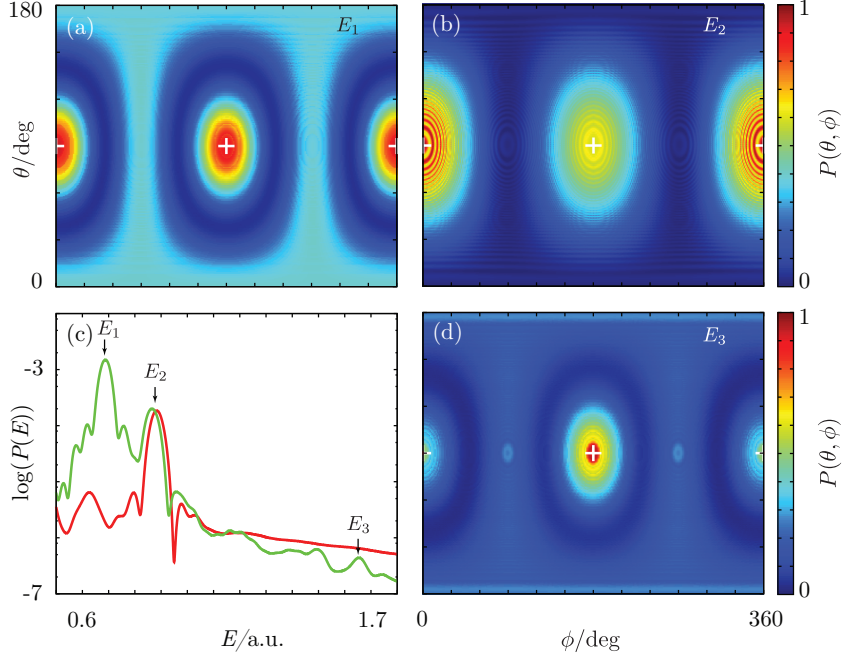


Figure 3.7.: Energy- and angular-resolved photoelectron spectra for Helium at fixed delay  $\tau = 8.99$  fs. Panel (c) displays a logarithmic scale PES  $P(E)$  comparison at fixed delays  $\tau = -1.69$  fs (red) and  $\tau = 8.99$  fs (green). The other panels depict normalized PADs  $P(\theta, \phi, E)$  with polar coordinates referred to axis  $z$  at fixed delay  $\tau = 8.99$  fs and energy: (a)  $E_1 = 0.66$  a.u., (b)  $E_2 = 0.88$  a.u., and (d)  $E_3 = 1.67$  a.u.. White crosses mark the intersection between the probe polarization axis and the cutting sphere.

must be taken into account that  $2s$  electrons are perturbed by a laser with a specific polarization direction that breaks the rotational symmetry. The laser transfers maximal kinetic energy along directions parallel to the polarization and minimal along the perpendicular plane and, if non-linear effects can be discarded, it induces a geometrical factor of the form  $|\mathbf{A} \cdot \mathbf{p}|$  where  $\mathbf{A}$  is the polarization direction and  $\mathbf{p}$  the electron momentum. For this reason electrons emitted along  $\phi = 90^\circ$ , and  $270^\circ$  are strongly suppressed, and panel (b) is compatible with the spherical symmetry of a  $2s$  state.

In panel (a) electrons are excited to a  $p$  state and then ejected into the continuum by the absorption of two pump photons. The PAD displays marked emission maxima for the direction aligned with the laser polarization (indicated by white crosses). The extension

in  $\theta$  is narrower compared with the  $2s$  emission in panel (b), which is consistent with the ionization from a  $p_x$  orbital. Of the three degenerate  $p$  orbitals the  $p_x$  is the one producing the strongest response. Signatures of  $p_y$  and  $p_z$  response can be identified in the non vanishing PAD on the  $yz$ -plane around  $\phi = 90^\circ$  and  $270^\circ$ . Such perpendicular response indicates a degree of non-linearity induced by the pump. Similar considerations hold for panel (b) where the  $p$  state excited by the pump is probed with  $\omega_p$ . As before the emission is mainly from a  $p_x$  state.

### 3.3. Ethylene Molecule

In this section we extend our calculations to the treatment of the Ethylene molecule ( $C_2H_4$ ) and show how these techniques permit to study the time-dependence of molecular electronic states. In particular we report on the clear observation of a strong  $\pi \rightarrow \pi^*$  transition. In order to have a good description of states close to the ionization threshold we employed the asymptotically correct LB94 xc-functional in the adiabatic approximation [191]. We choose the molecular plane to be in the  $xy$ -plane with carbon atoms at coordinates  $(\pm 1.26517, 0, 0)$  a.u. and hydrogens at  $(\pm 2.33230, 1.75518, 0)$  a.u. and  $(\pm 2.33230, -1.75518, 0)$  a.u.. The ion positions are held fixed during the time evolution. Norm-conserving Trouiller-Martin pseudopotentials (see Section 2.4.1.2) are employed to describe the core electrons of Carbon. Moreover TDDFT equations are numerically integrated on a spherical grid with spacing  $\Delta x = 0.3$  a.u., radius  $R = 16$  a.u. and 2 a.u. wide absorbing boundaries.

#### 3.3.1. Transient Absorption Spectroscopy

We perturb the system with a 15 cycles (3 cycles ramp) trapezoidal laser pulse with carrier frequency  $\omega_p = 0.297$  a.u. and intensity  $I = 1.38 \times 10^{11}$  W/cm<sup>2</sup> polarized in the direction of the  $x$ -axis. The laser frequency and the polarization direction are suited to excite mainly the molecular  $\pi \rightarrow \pi^*$  transition. The absorption spectrum of the excited molecule probed after the pulse (see Figure 3.8) shows the emergence of a peak associated with the population of the  $\pi^*$  state. Optical transitions from this excited state to high lying bound states occur at energies lower than the HOMO-LUMO gap as illustrated by the scheme in Figure 3.8. Effects of the lack of memory in our xc-potential can be observed in the shifts of the peaks with respect to the known excitations of the

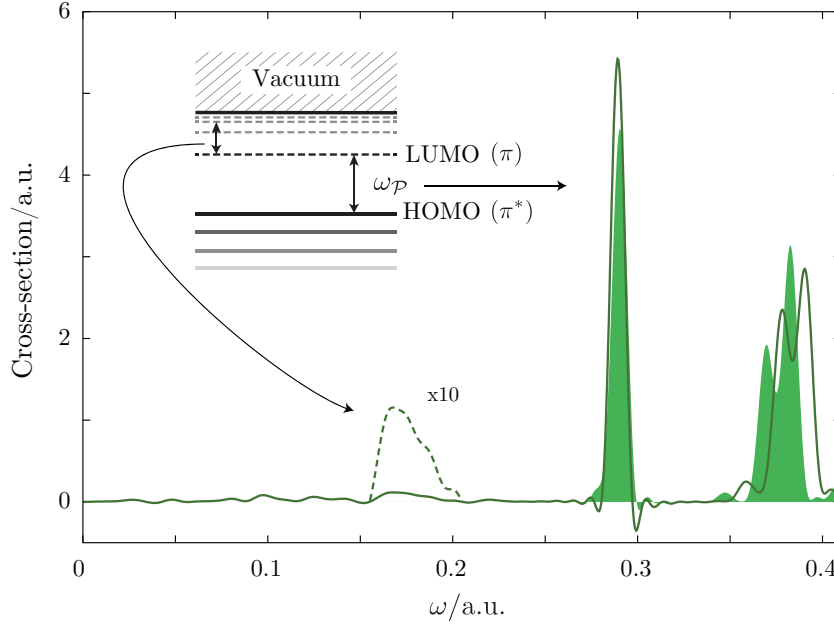


Figure 3.8.: Comparison of the absorption spectra of unperturbed (filled curve) and perturbed (solid line) Ethylene molecule below the ionization threshold. The molecule is excited by a 45 cycle  $\sin^2$  envelope laser pulse polarized along the  $x$ -axis with carrier frequency  $\omega_P = 0.297$  a.u. of intensity  $I = 1.38 \times 10^{11}$  W/cm<sup>2</sup>.

unperturbed system. The characteristic excitations of a many-body system should not depend on the perturbation, unless we are in a strong light-matter coupling regime.

The build up of the transient spectrum as a function of time is shown in Figure 3.9. In comparison with the case of He discussed in Section 3.2 the TAS map does not display any maxima during the pump time lapse due to the envelope area not having crossed  $\pi$  by the end of the pulse. A pulse with larger area would reveal the first Rabi oscillation.

### 3.3.2. Time-Resolved Photo-Electron Spectroscopy

The TRPES map is presented in Figure 3.10. Calculations were performed in a box of radius  $R = 30$  a.u. and the probe pulse is equal to the one used for the Helium atom in Section 3.2, namely a 40 cycles (8 cycles ramp) trapezoidal pump at  $\omega_p = 1.8$  a.u. and  $I = 5.4 \times 10^9$  W/cm<sup>2</sup>, but polarized along the  $z$ -axis. The choice of the polarization

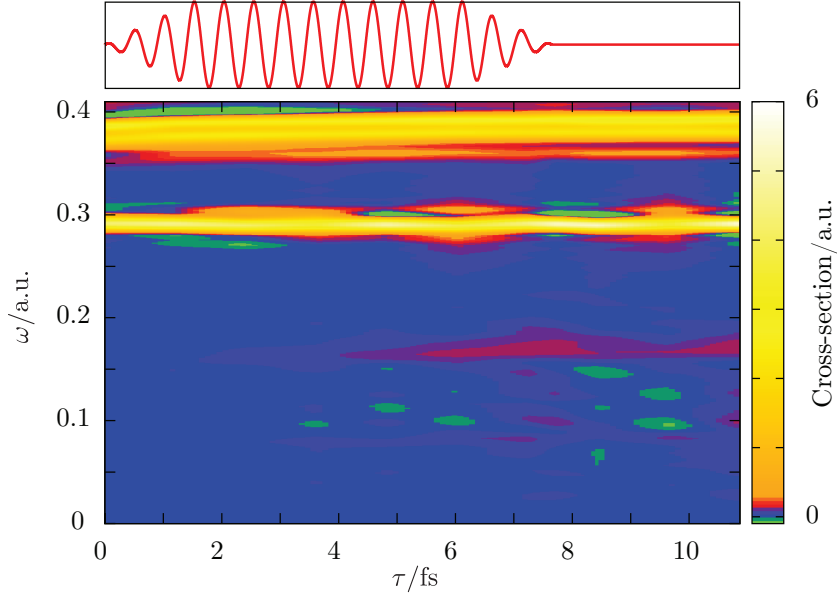


Figure 3.9.: TAS of the Ethylene molecule. The pump laser pictured in the upper panel is the same as in Figure 3.4.

direction is important since, as we shall show, the spectra may reveal geometrical features that depend on it.

The TRPES displays a behavior similar to the one discussed in Section 3.2. A set of constant crests can be observed in the energy range between 0.8 a.u. and 1.5 a.u.. These are the peaks associated with electrons residing in the ground-state and ejected by the probe pulse. In particular the peak at  $E_2 = 1.37$  a.u. corresponds to the emission from the  $\pi$  HOMO  $E_2 = \omega_p - \epsilon_\pi$ , with  $\epsilon_\pi = 0.43$  a.u.. The  $\pi$  orbital is localized on the Carbon atoms with two density lobes lying in the  $xz$ -plane and nodes in the  $xy$ -plane (refer to Figure 3.11 (a) for geometrical visualization). A probe laser orientation along  $y$  should suppress electrons on  $xy$ -plane perpendicular to its polarization and therefore the PAD  $P(\theta, \phi, E_2)$  in Figure 3.11 (c) for  $\theta = 0^\circ$  is diminished also due to geometrical reasons. The signature of a  $\pi$  symmetry can be clearly observed in the oscillations with  $\phi$  presenting maxima at  $\phi = 90^\circ$  and  $270^\circ$  along the plane perpendicular to  $x$  that indicates a concentration along the  $C - C$  bond axis, and minima for  $\phi = 0^\circ$  and  $360^\circ$  consistent with a depletion in the direction of each carbon atom.

Separated by a probe photon  $\omega_p$  at  $E_3 = \omega_p + \omega_p - \epsilon_\pi = 1.67$  a.u. we find photoelectrons

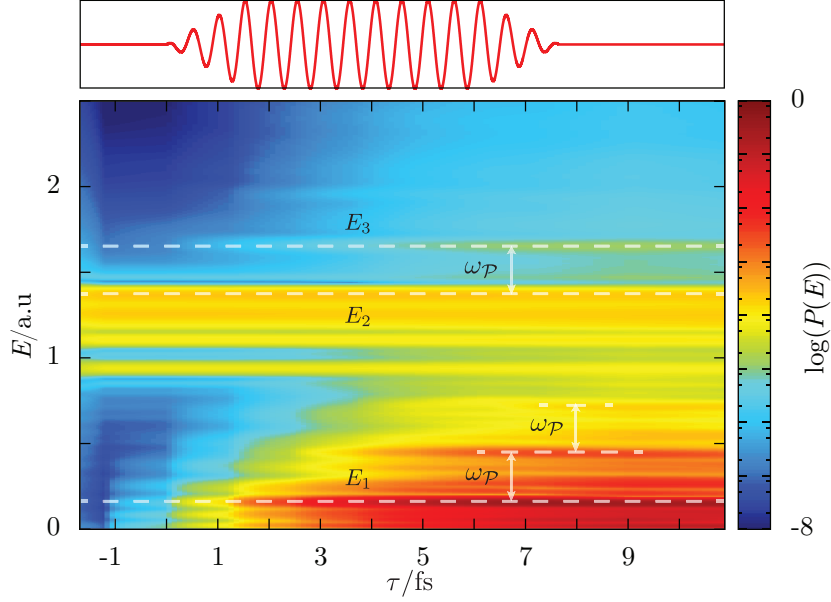


Figure 3.10.: Logarithmic scale TRPES for  $C_2H_4$ . The molecule is probed at different delays with a 40 cycles trapezoidal laser pulse with 8 cycles ramp,  $\omega_p = 1.8$  a.u. and  $I = 5.4 \times 10^9$  W/cm<sup>2</sup> polarized along the  $z$ -axis perpendicular to the pump. The pump laser (upper panel) is the same as in Figure 3.9.

ejected from the  $\pi^*$  state. The intensity of the peak steadily increases in time accordingly to what is observed with TAS. Compared with  $\pi$ , the  $\pi^*$  orbital presents additional nodes on the plane perpendicular to the molecular bond and a field polarized along  $z$  is sensible to this kind of geometry. The PAD  $P(\theta, \phi, E_3)$  in Figure 3.11 (e) displays strong suppression of electrons along the  $yz$ -plane at  $\phi = 90^\circ$  and  $270^\circ$  and therefore presents a clear manifestation of photoemission from a  $\pi^*$  state.

Slow electrons ejected at  $E_1 = 2\omega_p - \epsilon_\pi = 0.16$  a.u. gradually increase and become the predominant ionization channel. The emergence in time of multi-photon peaks separated by  $\omega_p$  indicates that the pump is strong enough to trigger non-linear effects. These electrons are ejected after the simultaneous absorption of pump photons. Electrons at  $E_1$  reach the continuum with an  $\omega_p$  photon after the molecule has been excited to a  $\pi^*$  state by another  $\omega_p$  photon. PAD should therefore carry again signs of  $\pi^*$  symmetry. It must be noted, that in this case,  $\pi^*$  electrons are *probed* with the pump itself, and therefore the laser polarization is along  $x$ . As already discussed in the previous section,

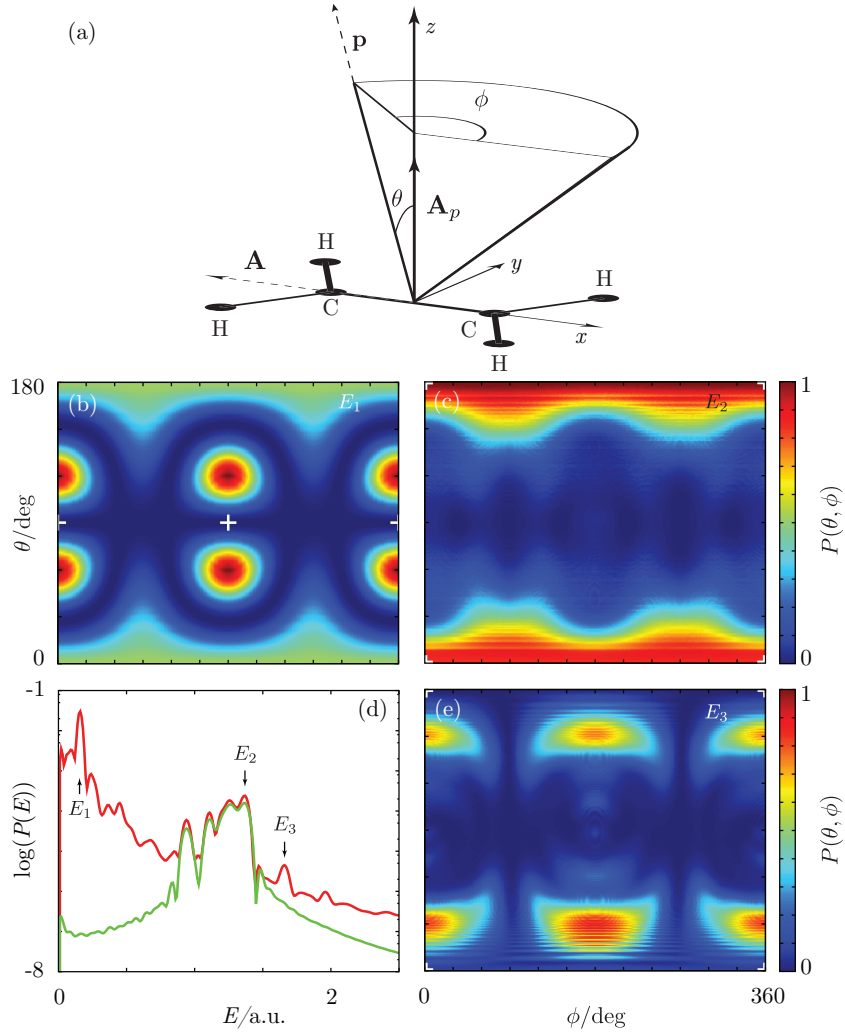


Figure 3.11.: Angular- and energy-resolved photoelectron spectra for  $C_2H_4$  at two fixed delay times. Panel (a) shows the geometry of the process:  $\mathbf{p}$  indicates the photoelectron direction,  $\mathbf{A}$  is the pump polarization vector, and  $\mathbf{A}_p$  the probe one. Panel (d) shows the logarithmic scale PES  $P(E)$  for  $\tau = -1.69$  fs (red) and  $\tau = 3.63$  fs (green). The other panels depict normalized PADs  $P(\theta, \phi, E)$  at  $\tau = 3.63$  fs and energies marked in (d): (b)  $E_1 = 0.16$  a.u., (c)  $E_2 = 1.37$  a.u. and (e)  $E_3 = 1.67$  a.u.. White marks indicate the position of the probe polarization vector (c), (e) (at the corners) and the pump one (b) on the sphere.

the laser polarization carries a geometrical factor of the form  $\mathbf{A} \cdot \mathbf{p}$  with  $\mathbf{A} = A\mathbf{x}$ , that introduces a suppression along the  $yz$ -plane ( $\phi = 90^\circ, 270^\circ$ ). Unfortunately, this plane is precisely where the  $\pi^*$  photoemission minima should lie. For this reason PAD  $P(\theta, \phi, E_3)$  in Figure 3.11 (b) is not suited to clearly discern a  $\pi$  from a  $\pi^*$  symmetry, and the suppression for  $\theta = 0^\circ$  along the  $xy$ -plane is compatible with both structures.

### 3.4. Conclusions

In this chapter we studied the problem of describing ultrafast (attosecond scale) time-resolved absorption and photoemission in finite systems with TDDFT. After having presented the theory and discussed its implementation in Sections 2.2 and 2.4.6, we demonstrated that TDDFT can be successfully employed in the task of describing the dynamics of electronic excited states in atoms and molecules. We illustrated this with three applications: the one-dimensional Helium model, the three-dimensional Helium atom and the Ethylene molecule.

We studied the one-dimensional Helium atom perturbed by an external time dependent field exactly, by solving the time-dependent Schrödinger equation. We showed how it is possible to recover information about state populations through a comparison of the perturbed and unperturbed absorption cross-sections, and that the population evolution in time can be described in terms of Rabi physics. We then performed TDDFT calculations on the same model, and we may conclude that the results obtained with the EXX potential are in good agreement with the exact solution, although small artifacts appear due to the incorrect description of the functional memory dependence.

Furthermore we investigated the Helium atom in a more realistic three-dimensional treatment using the EXX functional. We performed resonant pump-probe calculations monitoring both absorption and photoemission properties of the excited atom. TAS turned out to be a sensible tool to monitor the build-up of the excited state, allowing us to observe Rabi oscillations as a function of the time delay between pump and probe. TRPES also allowed the characterization of the excitation process in time. However, due to a dominant ionization channel associated with sequential two (pump) photons absorption, the information about the excited state population was less apparent. Nonetheless the PAD, being an observable sensitive to the geometrical arrangement of the ionized state, is a useful tool to discern the nature of each photoelectron peak. As a final example we

considered the case of the Ethylene molecule, to study the time evolution of a  $\pi \rightarrow \pi^*$  transition. The PAD for ejected electrons offered clear evidence that the states taking part in the process were indeed of  $\pi$  and  $\pi^*$  nature.

The theoretical framework that we have developed is a useful tool to understand and control non-equilibrium electronic dynamical processes in nanostructures and extended systems. New emergent properties of matter in the strong-coupling regime could appear that might give rise to new technological developments. Furthermore, monitoring electron and ion dynamics provides fundamental insights into structure (i.e. time-resolved crystallography) and chemical processes in biology and materials science (e.g. for energy applications). There is plenty of room for new and fascinating discoveries about the behavior of matter under out-of-equilibrium conditions.

Still, from the fundamental point of view, there is a clear need for the development of non-adiabatic exchange and correlation functionals able to provide a reliable description of non-equilibrium processes and strong light-matter interaction. Clearly, the methods presented here will automatically benefit from any theoretical advance in this direction. Conversely, the developers of new functionals may take into account the correct description of pump-probe experiments as a useful quality test.



## 4. Control of Optical Properties – The Case of the Hydrogen Atom

### Contents

<b>4.1. Excited State Spectroscopy . . . . .</b>	<b>96</b>
4.1.1. Converting Lorentzians Into Rayleigh Resonances and Viceversa	99
4.1.2. Convergence Tests . . . . .	102
4.1.3. Transient Absorption Spectroscopy and the Change of Colour	104
<b>4.2. Control . . . . .</b>	<b>108</b>
4.2.1. Equations of Control . . . . .	109
4.2.2. Numerical Example . . . . .	113
<b>4.3. Summary and Conclusion . . . . .</b>	<b>114</b>

In the previous chapter, we showed how to simulate pump-probe photoelectron and absorption spectroscopy on the attosecond time scale with the help of TDDFT and pointed out some aspects of how the extra degrees of freedom (pump-pulse duration, intensity, frequency and delay-time), that are absent in a conventional steady-state experiment, provide additional information about the electronic structure and dynamics of a system.

In this chapter we take a more detailed look at the origin of spectral excited-state features. We particularly pay close attention to the shape of the absorption/emission peaks. The idea is to first understand the effect of electronic excitations on the spectrum of a species and with this knowledge be able to manipulate its spectral properties. Applying this knowledge to the visible range, one possible application is to selectively change and control the colour of molecular systems. In this chapter we present the concept and demonstrate calculations for the analytically solvable Hydrogen. We start with a detailed analysis of the features of excited-state spectra and the changes in the spectrum, that can

be obtained by a laser excitation and continue to discuss the topic of laser control. As an application we finally show how we tailor a pulse to manipulate the colour of Hydrogen. In the next chapter we continue with the topic of control and show how to use TDDFT to control spectral properties of molecules in the visible.

## 4.1. Excited State Spectroscopy

In Section 2.2.5 we have developed the generalized Lehmann representation of the polarizability tensor  $\alpha_{\mu\nu}[\mathcal{E}](\omega, \tau)$  of an arbitrary excited-state and in Section 2.3 introduced the concept of states with finite life times and the resulting line shapes. For an excited state spectrum where each peak is subjected to Lorentzian broadening, we found the diagonal elements of the polarizability tensor to be

$$\alpha_{\mu\mu}[\mathcal{E}](\omega, t_0 + \tau) = \sum_{jkm} d_{jm}^\mu d_{mk}^\mu |\gamma_j| |\gamma_k| \left\{ \frac{e^{i\Theta_{kj}(\tau)} (\omega + \omega_{jm} - i\frac{\Gamma}{2})}{(\omega + \omega_{jm})^2 + \frac{\Gamma^2}{4}} - \frac{e^{-i\Theta_{kj}(\tau)} (\omega - \omega_{jm} - i\frac{\Gamma}{2})}{(\omega - \omega_{jm})^2 + \frac{\Gamma^2}{4}} \right\} \quad (4.1)$$

with the dipole-matrix elements

$$d_{jm}^\mu = \langle \Phi_j | \hat{D}_\mu | \Phi_m \rangle, \quad (4.2)$$

and the time-dependent phase

$$\Theta_{kj}(\tau) = \varphi_j - \varphi_k - \omega_{kj}\tau, \quad (4.3)$$

where  $\{\varphi_i\}$  are the phases of the expansion coefficients  $\{\gamma_i\}$  of the wave function at time  $t_0$  at the end of the pump in the eigenbasis of the time-independent Hamiltonian  $\hat{\mathcal{H}}$

$$|\Psi(t_0)\rangle = \sum_{j=1}^{\infty} \gamma_j |\Phi_j\rangle = |\gamma_j| e^{i\varphi_j} |\Phi_j\rangle, \quad \hat{\mathcal{H}} |\Phi_j\rangle = \varepsilon_j |\Phi_j\rangle \quad (4.4)$$

and where

$$\omega_{kj} = \varepsilon_j - \varepsilon_k, \quad (4.5)$$

$$\tau = t - t_0. \quad (4.6)$$

We found, that based on the polarizability tensor (4.1), the average absorption coefficient takes the form

$$\begin{aligned} \bar{\sigma}(\omega, t_0 + \tau) = \frac{4\pi\omega}{3c} \sum_{\mu j k m} d_{jm}^\mu d_{mk}^\mu |\gamma_j| |\gamma_k| \{ \cos(\Theta_{kj}) L(\omega - \omega_{jm}) + \sin(\Theta_{kj}) R(\omega - \omega_{jm}) \\ - \cos(\Theta_{kj}) L(\omega + \omega_{jm}) + \sin(\Theta_{kj}) R(\omega + \omega_{jm}) \} \end{aligned} \quad (4.7)$$

which can be divided into its time- and phase-independent equilibrium contributions:

$$\bar{\sigma}^{EQ}[\mathcal{E}](\omega^+) = \frac{4\pi\omega}{3c} \sum_{\mu, j} |\gamma_j|^2 \left\{ \sum_{j < m} |d_{jm}^\mu|^2 L(\omega - \omega_{jm}) - \sum_{j > m} |d_{jm}^\mu|^2 L(\omega + \omega_{jm}) \right\}, \quad (4.8)$$

and its interference terms:

$$\begin{aligned} \bar{\sigma}^{IN}[\mathcal{E}](\omega, t_0 + \tau) = \sum_{j \neq k; m} d_{jm}^\mu d_{mk}^\mu |\gamma_j \gamma_k| \{ \cos(\Theta_{kj}(\tau)) L(\omega - \omega_{jm}) + \sin(\Theta_{kj}(\tau)) R(\omega - \omega_{jm}) \\ - \cos(\Theta_{kj}(\tau)) L(\omega + \omega_{jm}) + \sin(\Theta_{kj}(\tau)) R(\omega + \omega_{jm}) \} , \end{aligned} \quad (4.9)$$

where the Rayleigh line shape is defined as

$$R(\bar{\omega}) = \frac{\bar{\omega}}{\bar{\omega}^2 + \Gamma^2/4} \quad (4.10)$$

and the Lorentzian line shape is defined as

$$L(\bar{\omega}) = \frac{\Gamma/2}{\bar{\omega}^2 + \Gamma^2/4}. \quad (4.11)$$

Recalling the main conclusions of this analysis, we found that

- The positions of the excitation peaks are fixed at the many-body transition energies.

- The spectral weights of the peaks depend on the laser and on the delay  $\tau$  between pump and probe pulse; peaks can be positive or negative depending on whether the rate of absorption is larger than the rate of stimulated emission or vice-versa.
- If the pump leaves the system in a non-stationary state, the spectral weights oscillate as a function of time. The involved frequencies correspond to the differences of the eigenenergies of the eigenstates occupied in the non-stationary state.
- For stationary states, the imaginary part of the polarizability tensor consists of peaks with Lorentzian shape, while the real part consists of peaks with Rayleigh shape.
- For non-stationary states, the spectrum can be divided into an equilibrium and an interference contribution. The equilibrium contribution is time-independent and its line shapes are always Lorentzians. In the interference part, the phase  $\Theta(\tau)$  mixes real and imaginary parts of the polarizability tensor, resulting in a spectrum, where peak shapes are a combination of Lorentzians and Rayleigh shapes. Since  $\Theta(\tau)$  is periodic in  $\tau$ , so is the average absorption coefficient.
- The shape of the terms in the interference term is governed by the laser through the initial phases  $\{\varphi\}_i$  and through the delay.
- If continuum states are involved in the process, an additional influence on the lineshapes can appear.

In the following we demonstrate these conclusions using the example of Hydrogen, which is analytically solvable and compare the analytic solutions to a numerical treatment using the real-space code `octopus`. This enables us to address the issue of numerical convergence when dealing with excited states. As example state, we will use a state, that is a linear combination of  $|2p_z\rangle$  and  $|3p_z\rangle$  state:

$$\begin{aligned} |\Psi_T\rangle &= e^{i\varphi_{2p_z}} \sqrt{\alpha} |2p_z\rangle + \sqrt{1-\alpha} e^{i\varphi_{3p_z}} |3p_z\rangle \\ &= \sqrt{\alpha} |2p_z\rangle + \sqrt{1-\alpha} e^{i\varphi_{32}} |3p_z\rangle \end{aligned} \quad (4.12)$$

with fixed  $\alpha = 0.4$  and variable  $\varphi$ , i.e.

$$\gamma_i = \begin{cases} \sqrt{0.4} & i = 2p_z \\ \sqrt{0.6} e^{i\varphi_{32}} & i = 3p_z \\ 0 & \text{else} \end{cases} \quad (4.13)$$

First we demonstrate the change from Lorentzian to Rayleigh peaks for the analytic solution. We then compare analytic and numerical treatment and discuss the issue of convergence. For the numerical solution, we proceed to show a 2D-spectrum of  $\Psi_T$  in dependence of the delay  $\tau$  demonstrating the oscillating behaviour of the spectrum. Finally, we show how these oscillations translate to a periodic change of colour.

#### 4.1.1. Converting Lorentzians Into Rayleigh Resonances and Viceversa <sup>§</sup>

First we demonstrate the influence of the phase  $\varphi_{32}$  on the shape of the spectral peaks. For this, we use the average absorption (4.7) obtained from the generalized Lehmann representation of the polarizability tensor together with analytically obtained dipole-transition matrix elements and eigenenergies. In this subsection we are not explicitly interested in the time-dependence, therefore we set the delay  $\tau = 0$ , assuming the probe laser to come directly at the end of the pump. This results in the phase  $\Theta_{kj} = \varphi_j - \varphi_k$ . We denote this by writing  $\bar{\sigma}(\omega, t_0 + \tau) = \bar{\sigma}(\omega, \Theta)$ . Note, that we do so in order to focus attention on the phase without taking care of the question about its origin. Later on, we will discuss, how this phase is a function of the pump laser and how it changes with the delay  $\tau$ . For  $\Psi_T$  as defined in Eq. (4.12), the equilibrium contribution to the spectrum is:

$$\bar{\sigma}^{EQ}(\omega) = 0.4\bar{\sigma}_{2p}(\omega) + 0.6\bar{\sigma}_{3p}(\omega), \quad (4.14)$$

and the interference term:

$$\begin{aligned} \bar{\sigma}^{IN}(\omega, \Theta) = 0.4 \cdot 0.6 \cdot \frac{4\pi\omega}{3c} & \left[ \sum_m d_{2p,m} d_{m,3p} \left\{ \cos \varphi_{32} L(\omega - \omega_{3p,m}) + \sin \varphi_{32} R(\omega - \omega_{3p,m}) \right. \right. \\ & \left. \left. - \cos \varphi_{32} L(\omega - \omega_{3p,m}) + \sin \varphi_{32} R(\omega - \omega_{3p,m}) \right\} \right. \\ & + \sum_m d_{2p,m} d_{m,3p} \left\{ \cos \varphi_{32} L(\omega - \omega_{2p,m}) - \sin \varphi_{32} R(\omega - \omega_{2p,m}) \right. \\ & \left. \left. - \cos \varphi_{32} L(\omega - \omega_{2p,m}) - \sin \varphi_{32} R(\omega - \omega_{2p,m}) \right\} \right]. \end{aligned} \quad (4.15)$$

Note the change in the sign of the Rayleigh terms in both sums.

<sup>§</sup>The results presented in this section form part of [235].

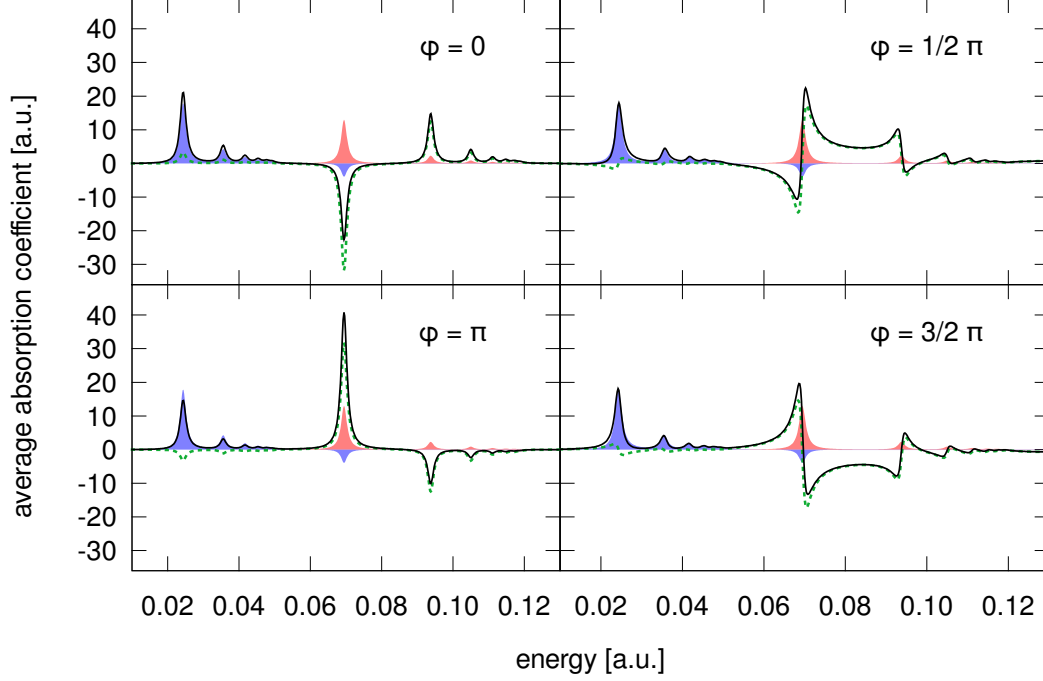


Figure 4.1.: Absorption coefficient  $\bar{\sigma}(\omega)$  of the the state  $\Psi_T = \sqrt{0.4}|2p_z\rangle + \sqrt{0.6}e^{i\varphi}|3p_z\rangle$  for  $\varphi = 0, 1/2\pi, \pi$  and  $3/2\pi$ . The total spectrum (black line) is the sum of the two phase-independent terms  $0.4\bar{\sigma}_{2p_z}$  (red shaded) and  $0.6\bar{\sigma}_{3p_z}$  (blue shaded) coming from the excited state spectra of the respective states multiplied by the absolute values of their expansion coefficients squared plus the phase-dependent interference term  $\bar{\sigma}^{IN}(\omega, \Theta)$  (green dashed line), which is responsible for the change of the spectrum with the delay time  $\tau$ .

Fig. 4.1 shows the different contributions and the resulting complete spectrum for the phases  $\varphi_{32} = 0, 1/2\pi, \pi$  and  $3/2\pi$ , which are the cases, where the interference term is either of purely Lorentzian ( $\varphi_{32} = 0$  and  $\pi$ ) or of purely Rayleigh shape ( $\varphi_{32} = 1/2\pi$  and  $3/2\pi$ ). The shaded areas show the weighted stationary-state contributions (red shows  $\bar{\sigma}_{2p}$ , blue shows  $\bar{\sigma}_{3p}$ ), the dotted line shows the interference terms and the solid line the final absorption coefficient. The energy range shown includes the transitions from  $n = 2$  to all higher states and from  $n = 3$  to all higher states and to  $n = 2$ . Transitions to the ground state lie outside of the shown region.

As can be seen from Eq. (4.7), interference terms require the existence of eigenstates  $\Phi_m$

which are dipole-coupled to both  $\Phi_{2p}$  and  $\Phi_{3p}$ . This is the case for s- and d-orbitals. This means, that for example for Hydrogen in a linear combination of the states  $\Phi_{2s}$  and  $\Phi_{4f}$ , all the interference terms are zero. Let us look a bit closer at the structure of the interference terms. We start with the interference term at the energy  $\omega_{23}$ : It has contributions from terms with  $m = 2s$ ,  $m = 3s$  and  $m = 3d$ . All contributions have different prefactors and the contribution of the 2s-state has the opposite sign of the contributions of the 3s and 3d states. For the other peaks, one can wonder, why the interference terms are so much smaller at energies  $\omega_{3n}$  than their counterparts at the energies  $\omega_{2n}$ . Looking at Eq. (4.15), one sees, that in fact, the height of the interference peaks of the response function is the same for each set of peaks  $\omega_{2n}$  and  $\omega_{3n}$  with the same state  $n$ . The difference comes purely from the factor  $\frac{4\pi\omega}{3c}$ . Furthermore it is interesting to note, that the sign of the Rayleigh contributions is opposite in these pairs of peaks. This variation in the amplitude of the interference terms has the following consequences for the change of the overall spectrum:

At the transition energies  $\omega_{3n}$  the spectrum has positive contributions from  $\bar{\sigma}_{3p_z}$  and contributions from the interference terms, but since the interference terms are much smaller than  $\bar{\sigma}_{3p_z}$ , the spectrum changes only slightly for different  $\varphi$ 's. This is different for the peaks at energies  $\omega_{2n}$ . Here, the photoabsorption spectrum has positive, phase-independent contributions from  $\bar{\sigma}_{2p_z}(\omega)$ , but the contributions from the interference terms are much larger and dominate the spectrum leading to a strong dependence of the spectrum in this energy range on the phase  $\varphi_{23}$ . For  $\varphi_{32} = 0$  and  $\varphi_{32} = \pi$ ,  $\cos \varphi_{32} = 1$  and  $\sin \varphi_{32} = 0$ , therefore  $\bar{\sigma}^{IN}(\omega, \Theta)$  only contains Lorentzian peaks and consequently the whole spectrum only contains Lorentzians. Nevertheless,  $\bar{\sigma}^{IN}(\omega, \Theta)$  changes sign between  $\varphi_{32} = 0$  and  $\varphi_{32} = \pi$ , switching the sign of all peaks  $\omega_{2n}$ . This is a demonstration of, how the manipulation of the internal phase  $\varphi$  can lead to a switch from gain to loss regime and vice versa. Finally, for  $\varphi_{32} = 1/2\pi$  and  $\varphi_{32} = 3/2\pi$ , the interference spectrum contains purely Rayleigh shaped peaks. Together with the small contributions from the stationary-state contributions, the final spectrum consists of slightly asymmetric Rayleigh peaks, again with different signs for  $\varphi_{32} = 1/2\pi$  and  $\varphi_{32} = 3/2\pi$ . We can therefore not only change peaks from emission to absorption peaks, we can also manipulate their resonance shape.

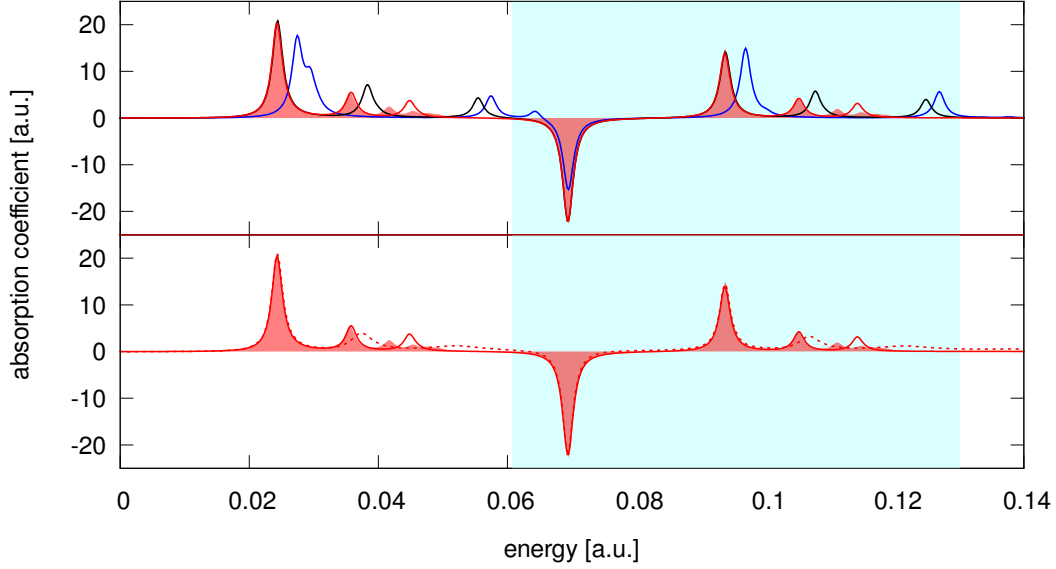


Figure 4.2.: Average photoabsorption coefficient  $\bar{\sigma}$  of  $|\Psi_T\rangle = \sqrt{0.4}|2p_z\rangle + \sqrt{0.6}|3p_z\rangle$  of Hydrogen. Analytic result including states up to  $n = 9$  (shaded) in comparison to (top) numerical results (solid lines) obtained through the generalized Lehmann representation with numerically obtained eigenenergies and dipole matrix elements for boxes with radii  $r = 30$  (blue),  $r = 45$  (black) and  $r = 60$  a.u. (red) and to (bottom) numerical results obtained through the generalized Lehmann representation (solid line) and through time-propagation (dashed), both in a box with  $r = 60$  a.u.. The shaded blue area indicates the visible range of the spectrum (350 nm - 750 nm).

#### 4.1.2. Convergence Tests

Whilst in the case of Hydrogen many calculations can be done analytically, this is not true for general systems, where results have to be obtained numerically. Even some time-dependent calculations of Hydrogen have to be done analytically due to many excited states being involved. To put our work on a general equal footing, in the following we make the transition from analytic results to numerical simulations. It is therefore important to look at the numerical accuracy, that can be achieved. The main complication of calculations, that involve excited states, is the need of an increased basis set. If one uses



codes which employ orbital basis sets, one has to use more basis functions. In contrast, if one uses a real space grid, one has to take into account, that excited states are more delocalized than the ground state, and increase the size of the simulation box.

Figure 4.2 shows a comparison of the average photoabsorption coefficient  $\bar{\sigma}$  of the test state  $|\Psi_T\rangle$ , once obtained analytically, once obtained numerically. The exact solution was obtained from the generalized Lehmann representation with analytic eigenenergies and dipole matrix elements, including states with main quantum number up to  $n = 9$ , corresponding to a basis set of 285 states. In the upper panel we show a comparison of the analytic solution with results, that were obtained using the generalized Lehmann representation in combination with eigenenergies and dipole matrix elements for the first 100 states ( $\approx n = 6$ ) in a spherical simulation box with radii  $r = 30$  a.u.,  $r = 45$  a.u. and  $r = 60$  a.u.. As comparison, a calculation of the ground state density converges with  $r = 10$  a.u.. Here, two effects can be seen, one due to the number of states used, one due to the size of the simulation box.

The first effect is the smaller set of basis functions (100 states for the numerical calculation in comparison to 285 states for the analytic calculation). Since only states with main quantum number  $n \leq 6$  are included in the numerical calculation, transitions to higher peaks do not appear in the numerically obtained spectrum, whilst they are present in the analytically obtained spectrum.

The second effect is due the size of the simulation box. If a state does not fit freely into the box, it is squeezed and its energy increases. Since the effect is stronger for higher lying states, in general peaks, that are effected by the box, get shifted to higher energies with smaller box sizes. Let's look at which box size is needed to correctly describe the shown transitions. In a box of radius  $r = 30$  a.u. the states with main quantum number  $n = 2$  and  $n = 3$  are described correctly, whilst states with  $n \geq 4$  are not. Therefore the transition peak  $2 \rightarrow 3$  is located at the correct energy. whilst all peaks describing transitions to states with  $n \geq 4$  are shifted upwards. In a box of radius  $r = 45$  a.u., states with  $n$  up to 4 are described correctly, so the  $n = 4$  peaks  $2 \rightarrow 4$  and  $3 \rightarrow 4$  are located at the correct positions and the heights are reproduced. Finally, a box with radius  $r = 60$  a.u. describes peaks including states up to  $n = 5$  correctly in position and height, whilst any transition including states with main quantum number  $n \geq 6$  is not described correctly any more for radii smaller than 60 a.u.. Unfortunately, this is roughly the computational limit for 3D calculations. Since our goal is to correctly

describe spectral properties in the visible and the whole Balmer series of transitions from  $n = 2$  lies in the visible, we in principle have to correctly describe orbitals with arbitrarily high main quantum numbers, which is obviously not possible. Nevertheless, as one can see in Figure 4.2, transitions to states with  $n = 6$  have already very small peaks in comparison to peaks involving only lower lying orbitals. Therefore we content ourselves with a box size of radius  $r = 60$  a.u., knowing that we can correctly describe the spectrum of peaks with main quantum number  $n$  up to 5. Nevertheless, we still include states with  $n$  up to 6 in our calculations. States with higher quantum numbers are not included in the basis set.

Finally we compare the results obtained numerically through the Lehmann representation in a box of  $r = 60$  a.u. with the average absorption coefficient obtained from a time-dependent propagation in the same box with absorbing boundary conditions. Absorbing boundaries of width  $w = 20$  a.u. were used. The result is shown in the bottom panel of Figure 4.2. Due to the absorbing boundaries, we can only describe peaks including states with  $n$  up to 4. Similar to the results obtained with the help of the Lehmann representation for a box of  $r = 45$  a.u., peaks that include transitions to states with  $n = 5$  or higher are not reproduced exactly, but are slightly shifted. This leads to the conclusion, that the time-propagation due to the absorbing boundaries gives worse results for higher states than the Lehmann representation.

In the rest of this chapter, we will therefore present results, that were obtained using the generalized Lehmann representation in combination with numerically obtained eigenenergies and dipole-matrix-elements in a box with radius  $r = 60$  a.u., including the first 100 eigenstates.

#### 4.1.3. Transient Absorption Spectroscopy and the Change of Colour

In the previous section, we analyzed the effect of the phase  $\varphi_{23}$  on the spectral weights and the shape of the photoabsorption spectrum. In this context, we considered  $\varphi_{23}$  to be fixed and did not care about its origin. Here, we show, how, by taking into account the dependence of this phase on the delay  $\tau$  between pump and probe, one can obtain a time-resolved spectrum of an excited non-stationary state. We also show, how the periodicity of the time-dependent phase shows up in the spectrum and the associated colour. As before, we look at the test state  $|\Psi_T\rangle$  as defined in Eq. (4.12), but now with fixed  $\varphi_{32} = 0$ . The time-dependence of the angle  $\Theta_{32}(\tau)$  then enters through the delay

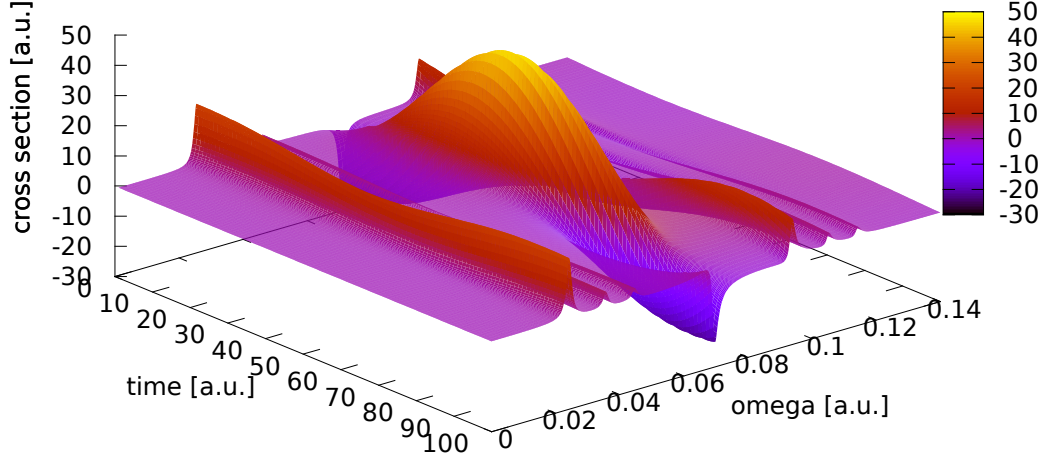


Figure 4.3.: Time-resolved spectrum of the  $\sqrt{0.4}|2p_z\rangle + \sqrt{0.6}|3p_z\rangle$  of Hydrogen. Because the phases of the  $|2p\rangle$  and  $|3p\rangle$  states evolve with different velocities, the spectral weights of each of the peaks changes with time, leading to a time-dependent spectrum with a periodicity of  $T = \frac{2\pi}{\varepsilon_{2p} - \varepsilon_{3p}} \approx 91 a.u.$ . The first 100 eigenstates were included, continuum contributions neglected.

$\tau$  like  $\Theta_{32}(\tau) = \omega_{32}\tau$ . Figure 4.3 shows the time-resolved spectrum  $\bar{\sigma}(\omega, \tau)$  of  $|\Psi_T\rangle$ . Since the eigenenergies of  $|2p_z\rangle$  and  $|3p_z\rangle$  are different, the phase  $\Theta_{32}(\tau)$  evolves with the frequency  $\omega_{32}$ . At  $\tau = 0$ ,  $\tau = \frac{\pi}{2\omega_{32}}$ ,  $\tau = \frac{\pi}{\omega_{32}}$  and  $\tau = \frac{3\pi}{2\omega_{32}}$ , the spectra of  $\varphi_{32} = 0$ ,  $\varphi_{32} = 1/2\pi$ ,  $\varphi_{32} = \pi$  and  $\varphi = 3/2\pi$ , that were discussed in Section 4.1.1 are reproduced. One sees the strong changes of  $\bar{\sigma}$  in the energy range  $\omega > 0.06$  Ha, while the spectrum remains almost unchanged for  $\omega < 0.06$  Ha. The spectrum is periodic with  $T = \frac{2\pi}{\omega_{32}} \approx 91$  a.u..

Finally we address, which effect the change of the spectrum has on the colour of a system, translating the time-dependent spectra of the  $\sqrt{0.4}|2p_z\rangle + \sqrt{0.6}|3p_z\rangle$  state in Hydrogen, which is shown in Figure 4.3 into a chromaticity diagram. For this we assume a thin medium, so that changes in the medium due to the propagation through the medium can be neglected. Furthermore we neglect the contribution of the emission peaks to

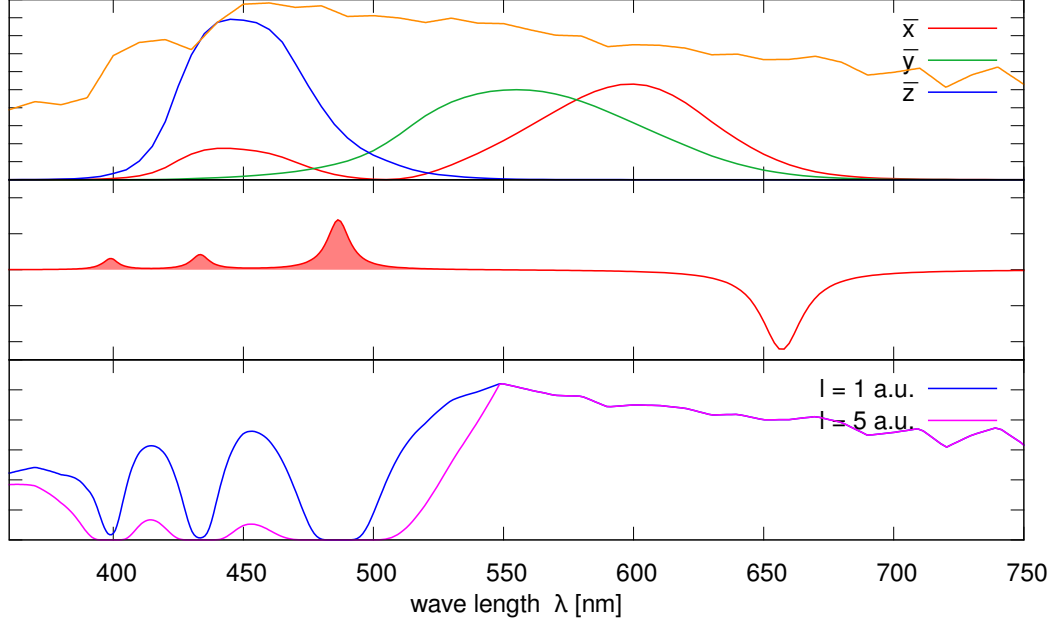


Figure 4.4.: (top) CIE 1931 colour matching functions  $\bar{x}$ ,  $\bar{y}$  and  $\bar{z}$  and the spectral power distribution of the sun (orange). (center) Average absorption coefficient of  $|\Psi_T\rangle = \sqrt{0.4}|2p_z\rangle + \sqrt{0.6}|3p_z\rangle$  (solid) and the part taken into account in the calculation of the colour (shaded). (bottom) Power distribution of sun light after having passed through a gas of atoms in the state  $|\Psi_T\rangle$  with a pathlength of  $l = 1$  a.u. (blue) and  $l = 5$  a.u. (pink).

the colour, treating them as energy windows, where the light can propagate unaffectedly. These assumptions enable us to use the Beer-Lambert law, which describes the power distribution  $I(\omega)$  of a light source after having propagated through a medium of density  $N$  for the length  $l$

$$I(\lambda, l) = I_0(\lambda) e^{-i\sigma(\lambda)lN}. \quad (4.16)$$

The resulting power distribution is then matched with a set of matching functions, which describe the sensitivity of the human eye to different wave lengths. The resulting so-called tristimulus values (e.g. the RGB-values) then characterize the colour perceived by the human eye and can be presented as a point in a chromaticity diagram. For a more detailed description of how to convert spectra into colours, see Section 2.7.

Figure 4.4 demonstrates the procedure using the example of the spectrum of  $\sqrt{0.4}|2p_z\rangle +$

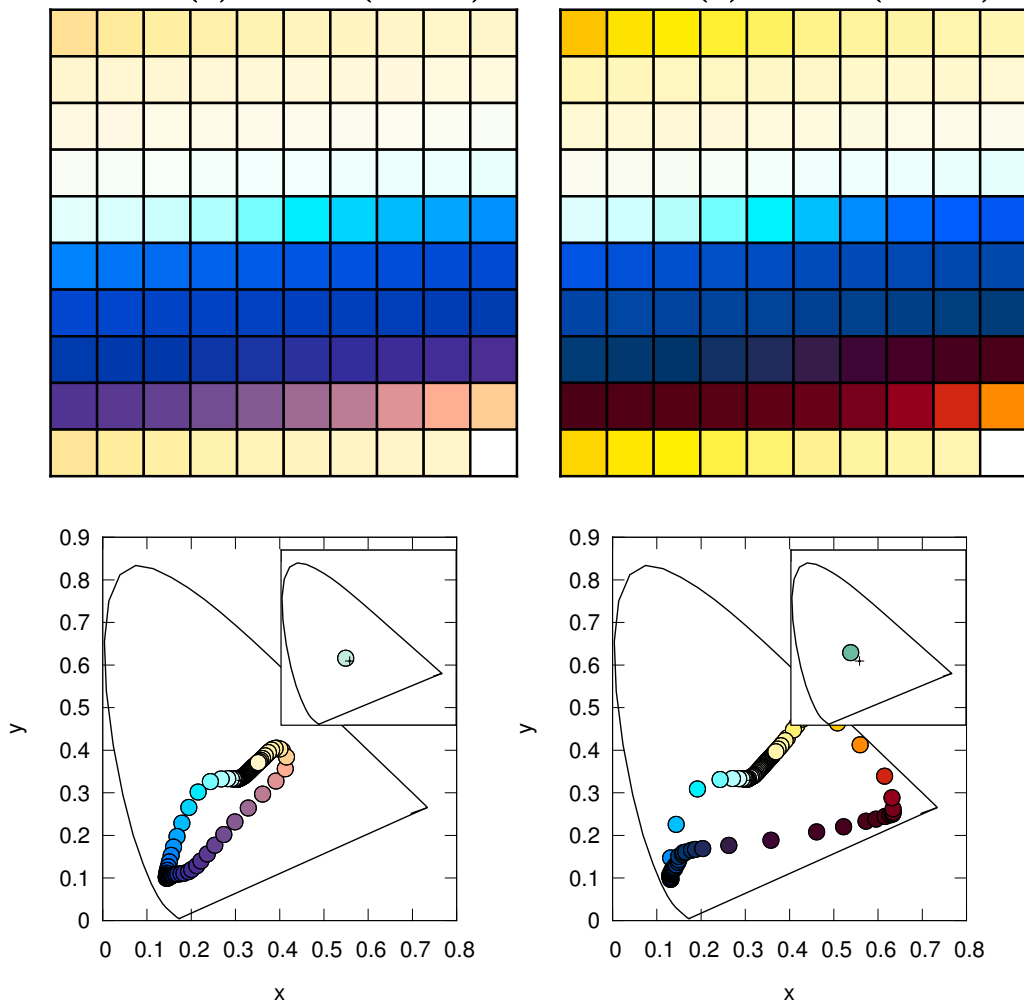


Figure 4.5.: (top): Colour associated to the time-dependent spectrum of the  $\sqrt{0.4}|2p_z\rangle + \sqrt{0.6}|3p_z\rangle$  state of Hydrogen for a path in the gas of length  $l = 1$  a.u. (left) and of  $l = 5$  a.u. (right). From left to right, from top to bottom each square shows the colour at a time  $\Delta t = 1.01$  a.u. later than the previous one. (bottom) The colours above shown in a chromaticity diagram, illustrating the periodic changes in colour with time. (inset) Time-averaged colours.

$\sqrt{0.6}|3p_z\rangle$ . The middle panel shows its average absorption coefficient. We neglect the emission part, treating it as a window, where light can pass without being effected by the medium. The bottom panel shows  $I(\omega, l)$  for two different propagation lengths  $l$ , if the

radiation source is the sun, the spectral power distribution of which is shown in the upper panel. These exponentials are folded with the colourmatching functions (shown in the upper panel) to obtain the tristimulus values  $X_l = \int d\lambda \bar{x}(\lambda) I(\lambda, l)$ ,  $Y_l = \int d\lambda \bar{y}(\lambda) I(\lambda, l)$  and  $Z_l = \int d\lambda \bar{z}(\lambda) I(\lambda, l)$ , which are then converted into  $x = \frac{X}{X+Y+Z}$  and  $y = \frac{Y}{X+Y+Z}$  and form a point in the chromaticity diagram. By converting the time-dependent absorption coefficient of Hydrogen shown in Figure 4.3 into a colour at each delay  $\tau$ , we can translate the time-dependent absorption coefficient into a time-dependent colour, forming a colour-trajectory in the chromaticity diagram. Figure 4.5 shows in the two bottom panels these colour-trajectories for the two pathlengths  $l = 1$  a.u. and  $l = 5$  a.u., where the colour was calculated for times  $n\Delta t$  with  $\Delta t = 1.01$  a.u.. It is interesting to see, how the periodicity of the spectrum is reflected in the fact, that the trajectories form a closed path in the chromaticity diagram. The upper two panels show again the single colours at each  $t$ .

Whilst it is interesting and instructive to discuss time-dependent colours, one has to take into account, that calculations as the one above describe samples, where all atoms/molecules are in the same phase. This is usually not the case for macroscopic samples. For realistic macroscopic samples, one should take the time-average of the average absorption coefficient Eq. (4.7), leading to a time-averaged average absorption coefficient

$$\bar{\sigma}(\omega) = |\gamma_{2p_z}| \bar{\sigma}_{2p_z}(\omega) + |\gamma_{3p_z}| \bar{\sigma}_{3p_z}(\omega), \quad (4.17)$$

which is the weighted sum of the stationary state spectra of the involved states. Note, that here, the interference terms disappear. The resulting time-averaged colours are shown in Figure 4.5 as inset.

## 4.2. Control ¶

In the previous section, we have taken a detailed look at excited state spectral properties of Hydrogen. We have discussed the spectral weights and the shape of the spectral peaks in detail and shown how these properties translate into a time-dependent spectrum and the associate colour. We have therefore discussed extensively the probe part of a pump-probe experiment. But what about the pump part? Imagine, we want to design a system with specific properties. The previous section has told us, how a state looks like, that

---

¶The results presented in this section form part of [235].

has specific properties. But how do we get our system – here Hydrogen – into this state? This is the topic of this section. We ask the question of how to design a laser, that brings our system from the ground state into an excited state of our choice. As before, we look at the test (or here target) state  $|\Psi_T\rangle$  as defined in Eq. (4.12). The task is therefore to bring Hydrogen from its ground state  $|1s\rangle$  into a linear combination of  $|2p_z\rangle$  and  $|3p_z\rangle$ . Since here, we have reduced the dimensionality of the problem by including only the  $|1s\rangle$ ,  $|2p_z\rangle$  and  $|3p_z\rangle$  states and since  $|2p_z\rangle$  and  $|3p_z\rangle$  are of the same symmetry and therefore in dipole-approximation decoupled, we do not have to apply the general theory of control, but can indeed solve the problem analytically. To this goal, we have in Section 2.5.2.2 developed a Rabi-like formulation of the behaviour of the expansion coefficients under the influence of a laser, that is resonant with both transition energies  $\omega_{21}$  and  $\omega_{31}$ . In the following we extend the results of Section 2.5.2.2 to demonstrate full control of the excitation of a Hydrogen-like atom from an eigenstate into a linear combination of this eigenstate plus two other eigenstates, both dipole coupled to the first, but without dipole allowed transition among them. First, we point out the general procedure, then we show numerical simulations.

### 4.2.1. Equations of Control

#### 4.2.1.1. Time-independent Envelope Functions

As in Section 2.5.2.2 we assume, that our system is described by a three-level Hamiltonian with eigenstates  $|\Phi_a\rangle$ ,  $|\Phi_b\rangle$  and  $|\Phi_c\rangle$ , the corresponding eigenenergies  $\varepsilon_a$ ,  $\varepsilon_b$  and  $\varepsilon_c$  and the transition frequencies  $\omega_{jk} = \varepsilon_k - \varepsilon_j$ . In this Hilbert-space, any time-dependent wave function can be written as

$$|\Psi(t)\rangle = a(t)e^{-i\varepsilon_a t}|\Phi_a\rangle + b(t)e^{-i\varepsilon_b t}|\Phi_b\rangle + c(t)e^{-i\varepsilon_c t}|\Phi_c\rangle \quad (4.18)$$

with the constraint  $|a(t)|^2 + |b(t)|^2 + |c(t)|^2 = 1$ . We found, that if we couple this system to an optical field

$$\mathcal{E}(t) = \varepsilon_1 \cos(\omega_{ba}t + \varphi_1) + \varepsilon_2 \cos(\omega_{ca}t + \varphi_2), \quad (4.19)$$

the time-evolution of the coefficients is

$$a(t) = \cos(\bar{\Omega}/2t), \quad (4.20a)$$

$$b(t) = \frac{\mu_{ab}\varepsilon_1}{\sqrt{(\mu_{ab}\varepsilon_1)^2 + (\mu_{ac}\varepsilon_2)^2}} e^{-i(\varphi_1 - \pi)} \sin(\bar{\Omega}/2t), \quad (4.20b)$$

$$c(t) = \frac{\mu_{ac}\varepsilon_2}{\sqrt{(\mu_{ab}\varepsilon_1)^2 + (\mu_{ac}\varepsilon_2)^2}} e^{-i(\varphi_2 - \pi)} \sin(\bar{\Omega}/2t). \quad (4.20c)$$

with the Rabi-frequency

$$\bar{\Omega} = \sqrt{(\mu_{ab}\varepsilon_1)^2 + (\mu_{ac}\varepsilon_2)^2}. \quad (4.21)$$

We define the target state

$$|\Psi_T\rangle = |\alpha|e^{-i\varphi_\alpha}|\Phi_a\rangle + |\beta|e^{-i\varphi_\beta}|\Phi_b\rangle + |\gamma|e^{-i\varphi_\gamma}|\Phi_c\rangle \quad (4.22)$$

with the constraint  $|\alpha|^2 + |\beta|^2 + |\gamma|^2 = 1$ . Since the overall phase of a wave function has no physical meaning, we can recast  $|\Psi_T\rangle$  into

$$\begin{aligned} |\Psi_T\rangle &= |\alpha||\Phi_a\rangle + |\beta|e^{-i(\varphi_\beta - \varphi_\alpha)}|\Phi_b\rangle + |\gamma|e^{-i(\varphi_\gamma - \varphi_\alpha)}|\Phi_c\rangle \\ &= |\alpha||\Phi_a\rangle + |\beta|e^{-i\tilde{\varphi}_\beta}|\Phi_b\rangle + |\gamma|e^{-i\tilde{\varphi}_\gamma}|\Phi_c\rangle \end{aligned} \quad (4.23)$$

A similar recast can be done for the time-dependent expansion coefficients (2.139) of the wave function under laser-influence, resulting in:

$$\begin{aligned} |\Psi(t)\rangle &= \cos(\bar{\Omega}/2t)|\Phi_a\rangle \\ &+ \frac{\mu_{ab}\varepsilon_1}{\sqrt{(\mu_{ab}\varepsilon_1)^2 + (\mu_{ac}\varepsilon_2)^2}} \sin(\bar{\Omega}/2t) e^{-i(\varphi_1 - \pi + \omega_{ba}t)}|\Phi_b\rangle \\ &+ \frac{\mu_{ac}\varepsilon_2}{\sqrt{(\mu_{ab}\varepsilon_1)^2 + (\mu_{ac}\varepsilon_2)^2}} \sin(\bar{\Omega}/2t) e^{-i(\varphi_2 - \pi + \omega_{ca}t)}|\Phi_c\rangle. \end{aligned} \quad (4.24)$$

Our goal is to find a laser pulse, that drives our system from the state  $|\Psi(t=0)\rangle = |\Phi_a\rangle$  into the target state  $|\Psi_T\rangle$  within the time  $T$ .

$$|\langle\Psi(T)|\Psi_T\rangle|^2 = 1. \quad (4.25)$$

Whilst here we focus on a laser with constants  $\varepsilon_1$  and  $\varepsilon_2$ , we can relief the constraint of



constants  $\varepsilon_1$  and  $\varepsilon_2$  and work with envelope functions by making use of the pulse area theorem.

Setting the wave function under laser influence at  $t = T$  equal to the target function Eq. (4.22) leads to two sets of equations: one connecting the envelope functions  $\varepsilon_1$  and  $\varepsilon_2$  to the populations  $|\alpha|^2$ ,  $|\beta|^2$  and  $|\gamma|^2$

$$|\alpha| = \cos(\bar{\Omega}/2T) \quad (4.26a)$$

$$|\beta| = \frac{\mu_{ab}\varepsilon_1}{\sqrt{(\mu_{ab}\varepsilon_1)^2 + (\mu_{ac}\varepsilon_2)^2}} \sin(\bar{\Omega}/2T) \quad (4.26b)$$

$$|\gamma| = \frac{\mu_{ac}\varepsilon_2}{\sqrt{(\mu_{ab}\varepsilon_1)^2 + (\mu_{ac}\varepsilon_2)^2}} \sin(\bar{\Omega}/2T), \quad (4.26c)$$

and the other one connecting the laser phases to the relative phases  $\tilde{\varphi}_\beta$  and  $\tilde{\varphi}_\gamma$  of the wave function

$$\tilde{\varphi}_\beta = \varphi_1 - \pi + \omega_{ba}T \quad (4.27a)$$

$$\tilde{\varphi}_\gamma = \varphi_2 - \pi + \omega_{ca}T. \quad (4.27b)$$

Solving these sets, we find

$$\varepsilon_1 = \frac{2}{T} \frac{\arccos(|\alpha|)}{\sin(\arccos(|\alpha|))} \frac{|\beta|}{\mu_{ab}} \quad (4.28a)$$

$$\varepsilon_2 = \frac{2}{T} \frac{\arccos(|\alpha|)}{\sin(\arccos(|\alpha|))} \frac{|\gamma|}{\mu_{ac}} \quad (4.28b)$$

and

$$\varphi_1 = \tilde{\varphi}_\beta + \pi - \omega_{ba}T \quad (4.29a)$$

$$\varphi_2 = \tilde{\varphi}_\gamma + \pi - \omega_{ca}T. \quad (4.29b)$$

An example of a constant-envelope laser, that achieves the required transition is therefore given by

$$\mathcal{E}(t) = \frac{2}{T} \frac{\arccos(|\alpha|)}{\sin(\arccos(|\alpha|))} \left( \frac{|\beta|}{\mu_{ab}} \cos(\omega_{ab}(t-T) + \tilde{\varphi}_\beta + \pi) + \frac{|\gamma|}{\mu_{ac}} \cos(\omega_{ac}(t-T) + \tilde{\varphi}_\gamma + \pi) \right). \quad (4.30)$$

Note, that in addition to the set  $\{\varepsilon_1, \varepsilon_2\}$ , also all other sets  $\{(2n+1)\varepsilon_1, (2n+1)\varepsilon_2\}$

fulfill the equations above. These solutions represent lasers, where the evolution of the coefficients covers  $(n+1)$  complete Rabi cycles within the time  $T$ .

#### 4.2.1.2. Time-dependent Envelope Functions

In practice, one is often interested in time-dependent envelope functions. For these cases, we have to adapt the amplitude of the laser according to the pulse area theorem in a way, that the laser envelope covers the same area. In the following, we will use a  $\sin^2$  envelope with period  $2T$  and Eq. (4.28) is modified to

$$\tilde{\varepsilon}_1(t) = \frac{4}{T} \frac{\arccos(|\alpha|)}{\sin(\arccos(|\alpha|))} \frac{|\beta|}{\mu_{ab}} \sin^2\left(\pi \frac{t}{T}\right) \quad (4.31a)$$

$$= 2\varepsilon_1 \sin^2\left(\pi \frac{t}{T}\right)$$

$$\tilde{\varepsilon}_2(t) = \frac{4}{T} \frac{\arccos(|\alpha|)}{\sin(\arccos(|\alpha|))} \frac{|\gamma|}{\mu_{ac}} \sin^2\left(\pi \frac{t}{T}\right) \quad (4.31b)$$

$$= 2\varepsilon_2 \sin^2\left(\pi \frac{t}{T}\right)$$

and the time-dependent Rabi-frequency is

$$\tilde{\Omega}(t) = \sqrt{(\mu_{ab}\tilde{\varepsilon}_1(t))^2 + (\mu_{ac}\tilde{\varepsilon}_2(t))^2} = 2\bar{\Omega} \sin^2\left(\pi \frac{t}{T}\right) \quad (4.32)$$

The populations finally result to

$$a(t) = \cos\left(\frac{\int_0^t \tilde{\Omega}(t') dt'}{2}\right), \quad (4.33a)$$

$$b(t) = \frac{\mu_{ab}\varepsilon_1}{\sqrt{(\mu_{ab}\varepsilon_1)^2 + (\mu_{ac}\varepsilon_2)^2}} e^{-i(\varphi_1 - \pi)} \sin\left(\frac{\int_0^t \tilde{\Omega}(t') dt'}{2}\right), \quad (4.33b)$$

$$c(t) = \frac{\mu_{ac}\varepsilon_2}{\sqrt{(\mu_{ab}\varepsilon_1)^2 + (\mu_{ac}\varepsilon_2)^2}} e^{-i(\varphi_2 - \pi)} \sin\left(\frac{\int_0^t \tilde{\Omega}(t') dt'}{2}\right). \quad (4.33c)$$

with the integral

$$\int_0^t \frac{\tilde{\Omega}(t') dt'}{2} = \left(\frac{1}{2}t - \frac{T}{4\pi} \sin\left(2\pi \frac{t}{T}\right)\right) \bar{\Omega}. \quad (4.34)$$

### 4.2.2. Numerical Example

As an example for the presented control of a three-level system, we show numerical simulations of the excitation of an electron in a Hydrogen atom from the groundstate  $|\Phi_a\rangle = |1s\rangle$  to an excited state, which is a linear combination of  $|\Phi_b\rangle = |2p_z\rangle$  and  $|\Phi_c\rangle = |3p_z\rangle$ . As before, the target state is defined as

$$|\Psi_T\rangle = \sqrt{0.4}|2p_z\rangle + \sqrt{0.6}|3p_z\rangle. \quad (4.35)$$

The control time is set to  $T = 3200$  a.u.. We apply a  $\sin^2$ -envelope pulse. Assuming, that there is no coupling to other states, we can write down the shape of the control pulse analytically. In accordance with Eq. (4.30) and the time-dependent modifications Eq. (4.31), the control pulse is

$$\mathcal{E}(t) = \frac{2\pi}{T} \left( \frac{\sqrt{0.4}}{\mu_{1s \rightarrow 2p}} \cos(\omega_{1s \rightarrow 2p}(t - T) + \pi) + \frac{\sqrt{0.6}}{\mu_{1s \rightarrow 3p}} \cos(\omega_{1s \rightarrow 3p}(t - T) + \pi) \right) \sin^2 \left( \pi \frac{t}{T} \right). \quad (4.36)$$

Calculations were performed using the octopus code [101]. The wave functions are represented on a real-space regular grid. A spherical simulation box of radius  $r = 60$  a.u. (see Section 4.1.2), a spacing of  $\Delta x = 0.435$  a.u. and absorbing boundaries of a width of 20 a.u. were employed. To align the atomic orbitals a small electric field in z-direction was applied during the ground state calculation. The relevant dipole-matrix elements in this configuration are  $\mu_{1s \rightarrow 2p} = 0.725$  a.u. and  $\mu_{1s \rightarrow 3p} = 0.283$  a.u.. Figure 4.6 shows the time-evolution of the populations  $|a(t)|^2$ ,  $|b(t)|^2$  and  $|c(t)|^2$  of the states  $|\Phi_{1s}\rangle$ ,  $|\Phi_{2p_z}\rangle$  and  $|\Phi_{3p_z}\rangle$  respectively. The numerical values (solid lines) follow closely the analytic model (4.33) (dashed lines). A frequency analysis of the additional oscillations shows, that they are due to the rotating wave approximation in the derivation of the Rabi formula. The small deviation in the final populations from the analytic prediction comes from the charge transfer into the  $|\Phi_{3d}\rangle$  orbitals (not shown). Coupling to these orbitals was neglected in the three-level approximation. The charge transfer to the  $|\Phi_{3d}\rangle$  nonetheless is less than 4% , in total we achieve a charge transfer into the desired wave function  $|\Psi_T\rangle$  of 96%. The bottom panel of Figure 4.6 shows the time-evolution of the phase  $\varphi_{3p} - \varphi_{2p}$ . After some switching-on time, we see the periodic variations with a period of  $\frac{2\pi}{\varepsilon_{3p} - \varepsilon_{2p}} \approx 90$  a.u.. As desired at  $T = 3200$  a.u. the phase difference is zero.

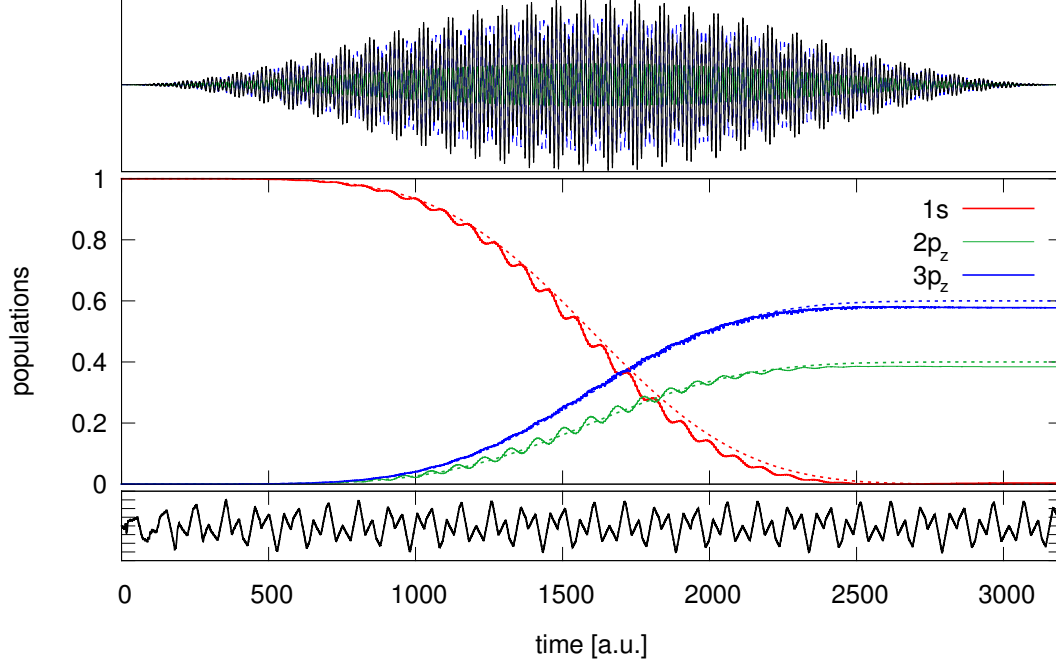


Figure 4.6.: Time-evolution of the populations of the  $1s$ –,  $2p_z$ – and  $3p_z$ – state. Dashed lines show the analytic model, solid lines the numerical results. The total pump-laser (upper panel, black) has two carrier-frequencies, one resonant to the transition  $|\Phi_{1s}\rangle \rightarrow |\Phi_{2p}\rangle$  (green), the other resonant to the transition  $|\Phi_{1s}\rangle \rightarrow |\Phi_{3p}\rangle$  (blue). The bottom panel shows the phase difference  $\varphi_{3p} - \varphi_{2p}$ .

### 4.3. Summary and Conclusion

In this chapter we took a detailed look at the origin and the control of spectral excited-state features in the non-overlapping regime using the example of excited states in Hydrogen.

First we carefully analyzed general features of excited-state spectra. Using a general Lehmann representation of the response function, we discussed the principle differences between spectra obtained from (i) the ground state, (ii) stationary states and (iii) non-stationary states. We found that whilst the peak positions are fixed through the many-body transition frequencies, the heights of the transition peaks as well as their shape depend on the expansion coefficients of the wave functions. The main conclusions are

the following. Ground state spectra are always non-negative and have only Lorentzian-shaped peaks. Stationary-state spectral peaks are still Lorentzian shaped, but can be positive or negative, depending on the size of the transition dipole-matrix elements of the states involved in the process. Both ground and stationary-state spectra are independent of time, i.e. stationary state spectra are independent of the delay between pump and probe. Finally, the contributions to the spectrum of a non-stationary state can be divided into (i) stationary contributions, which are the stationary spectra from the respective states scaled by their population and (ii) interference terms. The stationary contributions are of Lorentzian shape and time-independent, while the interference terms are time-dependent (i.e. depend on the delay between pump and probe) and oscillate with a frequency proportional to the energy-difference of the involved states. Their shape oscillates between Lorentzian and Rayleigh shape.

This strong dependence of the spectrum on the expansion coefficients is also reflected in the colour that would be perceived by the human eye when illuminating a macroscopic coherent sample of atoms/molecules with light. The time-dependence of the spectrum of a non-stationary state is periodic in time and leads to a time-dependent periodic change of colour. The time-dependent colour, if shown in a chromaticity diagram, forms a closed trajectory. Nonetheless, one has to take into account that in a macroscopic sample, not all molecules are in the same state at the same time. Therefore, one has to take the time-average of the spectrum, which leads to a spectrum that only contains stationary contributions.

After having analyzed the features of excited state spectra, we focused on the part of control. We showed that a Rabi-like formalism can be formulated for three-level systems, where the excited states are not dipole-coupled. This formalism can be used to derive a laser-pulse that excites an electron from its ground state into a non-stationary state, which is a linear combination of two non-dipole-coupled eigenstates. We found that whilst the envelope of the control-laser is responsible for controlling the populations of the involved states, the relative phases of the involved states are governed by the phase of the laser pulse.

We showed that the developed model is valid for the case of Hydrogen, when exciting the electron from the ground state into a linear combination of the  $|2p_z\rangle$  and the  $|3p_z\rangle$  state. Using the analytically derived pulse, we can achieve an overlap of 96 %. A population analysis shows that the missing few per cent are due to the fact that the

3-level assumption is not 100 per cent accurate and that some population is transferred to other dipole-coupled states. Nevertheless, we conclude that it is a viable assumption and provides a good model for the control of Hydrogen.

On the technical aspects, we found that due to the stronger delocalization of excited states, particular care has to be taken of numerical convergence when dealing with excited state spectra. In the context of simulations using real-space grids, this mainly means that the box has to be adjusted to the extension of the states. We found that, depending on which part of the spectrum one is interested in and the involved transitions, numerical convergence can be difficult. Nevertheless, if one is interested in transitions from the ground state, transitions to very highly excited states are mostly not very strong and one can confine oneself to the description of a few excited states.

## 5. Control of Optical Properties – Many-Electron Systems

### Contents

<b>5.1. Approach I: Direct Optimization . . . . .</b>	<b>118</b>
5.1.1. One-dimensional Model Hydrogen . . . . .	119
5.1.2. One-dimensional Helium . . . . .	122
5.1.3. One-dimensional Singly-Ionized Beryllium . . . . .	128
5.1.4. Methane . . . . .	129
<b>5.2. Approach II: Spectrum of an Excited Kohn-Sham Orbital . .</b>	<b>138</b>
<b>5.3. Summary and Conclusions . . . . .</b>	<b>143</b>

In the previous chapter, we have analyzed the properties of excited state spectra using the example of exactly solvable Hydrogen and have demonstrated a way to control its spectral properties by laser excitation. In this chapter we move beyond one-electron systems, and demonstrate the optimization of the absorption in the visible of a set of atoms and molecules using TDDFT. In the following we present two different approaches to tackle this problem. In the first approach, we define a target function that characterizes the absorption of radiation in the visible, and perform a direct optimization of the absorption by finding a laser pulse that maximizes this target. In the second approach we focus on an excited state with the desired absorption properties, and attempt to find a laser that excites the system from its ground state into this target state.

## 5.1. Approach I: Direct Optimization

Here, we use the downhill-simplex algorithm (also called Nelder-Mead or amoeba algorithm, for a description see Appendix A) to optimize a laser pulse to make a system, that is transparent in its ground state, absorb as much light as possible. To this goal we employ two different control target functions:

$$\varepsilon_{\tau}^A[\mathcal{E}] = \int_{E_{min}}^{E_{max}} \bar{\sigma}_{\tau}[\mathcal{E}](E) dE, \quad (5.1a)$$

$$\varepsilon_{\tau}^B[\mathcal{E}] = \int_{E_{min}}^{E_{max}} \bar{\sigma}_{\tau}[\mathcal{E}](E) \exp\left(-\gamma \frac{N_0 - N_{T_P}[\mathcal{E}]}{N_0}\right) dE. \quad (5.1b)$$

where  $\bar{\sigma}_{\tau}[\mathcal{E}](E)$  [in the following we will call it just  $\bar{\sigma}(E)$ ] is the average absorption coefficient of the system at a given time delay  $\tau$  after the pump pulse  $\mathcal{E}(t)$ , and  $E_{min}$  and  $E_{max}$  define the optimization region (OR) - the energy range, where the absorption is optimized. In the second target function we have introduced an exponential factor that depends on  $N_0$  and  $N_{T_P}$ , the number of electrons in the system at the beginning and the end of the pump pulse, respectively. The reason to introduce this factor is to avoid ionization, i.e. we wish to lead the system to a state with the desired absorption properties, but keeping the ionization probability low. The term  $\exp\left(-\gamma \frac{N_0 - N_{T_P}[\mathcal{E}]}{N_0}\right)$  inflicts a penalty, whose strength can be modulated by  $\gamma$ , to pump pulses that produce strong system ionization. Note that ionization is characterized in our calculations with the help of absorbing boundary conditions: Electrons are considered ionized as soon as they are absorbed by the boundaries. In practice, one can also combine the two target functions: one may start optimizations using  $\varepsilon_{\tau}^A[\mathcal{E}]$ , and later continue with  $\varepsilon_{\tau}^B[\mathcal{E}]$ , restarting from the previous optimum.

To test the algorithm, we start with a broader energy range and in later examples reduce the optimization region to the visible. We chose to work with the simplex-downhill algorithm because it is gradient free. The general procedure is explained in Section 2.6.3, a more detailed description of the computational details is given in Appendix B. We choose to work with a parametrized representation of the pump laser, with a sine basis. The pump duration  $T_P$  and the polarization are fixed, as well as the delay  $\tau$  between the end of the pump and the beginning of the probe pulse. We exclusively work in the non-overlapping regime, where the system is probed after the end of the pump pulse (i.e.



$\tau \geq 0$ ). Firstly, we present optimizations, where the pump frequencies were chosen as the frequencies of standard commercially available laser systems, later we show results with carrier frequencies adjusted to the resonance frequencies of our system. As optimization parameters we take only the expansion coefficients of the laser in the sine basis. The calculations are started with a set of initial coefficients  $\{c_i^0\} \in \mathbb{R}$ , that are then iterated, creating at each step  $m$  a pump laser:

$$\mathcal{E}_m(t) = \sum_i c_i^m \sin(\omega_i t) \Theta(t) \Theta(T_{\mathcal{P}} - t) \quad (5.2)$$

The downhill-simplex algorithm varies the laser coefficients  $\{c_i\}^m$  in order to maximize  $\varepsilon_\tau$ , keeping the laser polarization, the carrier frequencies and the phases fixed. As explained in Section 2.6.3, each computation of  $\varepsilon_\tau$  consists of two steps. In the first step, the system is evolved under the influence of the pump pulse  $\mathcal{E}_m(t)$  for the time  $T_{\mathcal{P}}$ . In the second step, the absorption after a given delay time  $\tau$  is calculated from a time-evolution as described in Section 2.4.5: The system is probed with a delta perturbation at the time  $T_{\mathcal{P}} + \tau$  and then evolved for the “spectrum time”  $T_S$  afterwards. Finally,  $\varepsilon_\tau[\mathcal{E}_m]$  is calculated from the average absorption coefficient  $\bar{\sigma}(\omega, \tau)$  (2.54).

To obtain the full polarizability tensor, the time evolution after the perturbation has to be performed four times, once for each polarization direction of the probe and a fourth time for the reference time evolution without perturbation. Performing time evolutions is computationally expensive and in our setup, the required resources scale linearly with a factor of four in  $T_S$  and scale to the power of three in the radius of the box. Therefore, during the optimization, we keep  $T_S$  and the box size as small as possible. At the end of the optimization, the average polarization under the influence of the optimal pump laser is converged with respect to the box size and the system is propagated for a longer time  $T_S$  to obtain a more detailed spectrum.

### 5.1.1. One-dimensional Model Hydrogen

As first test case for the algorithm, we studied the optimization of a 1D soft-Coulomb Hydrogen atom. The 1D model of Hydrogen is defined by the Hamiltonian (2.119) in Chapter 2.5 with an atomic charge of  $C = 1$  and one electron  $N = 1$ . The numerical parameters can be found in Table 5.1. After the optimization, we checked the convergence of the spectrum with respect to the box size and found the optimization box to be

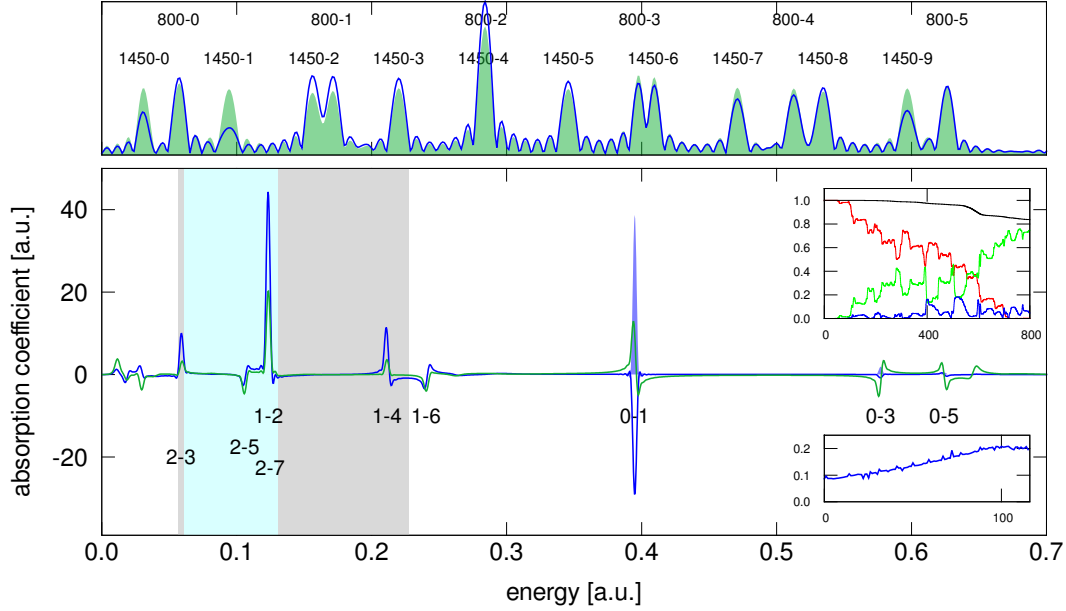


Figure 5.1.: Optimization of the one-dimensional soft-Coulomb Hydrogen atom. (Top) Comparison of initial (green) and optimized pump laser (Fourier transforms). Peaks are labeled by their basis wave length and the number  $n$  of their harmonic  $2n + 1$ . (Bottom) Ground state (shaded) and excited state (solid lines) spectra. Results for the initial pump laser are shown in green, results for the optimized pump laser (after 100 iterations) are shown in blue. The numbers label the transitions. The grey shaded box marks the optimization area, the blue shaded one the visible range of the spectrum (350 nm - 750 nm). (Top inset) Populations of the ground state (red), the first excited state (green) and the second excited state (blue) under the influence of the pump pulse. The black line shows the number of electrons in the system. (Lower Inset) The function  $\varepsilon^A$  as a function of the number of iterations.

sufficiently large. The search space was constructed from the two wave lengths  $\lambda = 800$  nm and  $\lambda = 1450$  nm and their first nine odd harmonics. Wave lengths of 800 nm and 1450 nm can be obtained e.g. with a Ti:Sapphire (800 nm) and a diode laser (1450 nm). All initial coefficients were set to  $c_i^0 = 0.005$ . The optimization region covers the energy range between 200 nm and 800 nm.

Figure 5.1 shows the ground state spectrum of the 1D model Hydrogen in comparison to

## 5.1. APPROACH I: DIRECT OPTIMIZATION

system	$\Delta x$	$r$		$w$		$dt$	$T_{\mathcal{P}}$	$\tau$	$T_S$	
		opt	conv	opt	conv				opt	conv
H, He, Be	0.2	50	100	20	70	0.025	800	50	450	1450
CH <sub>4</sub>	0.3	15	30	5	15	0.04	800	0	250	1000
CH <sub>4</sub> <sup>2+</sup>	0.3	15	30	5	15	0.04	600	0	250	1000

Table 5.1.: Numerical parameters: spacing  $\Delta x$ , radius  $r$ , absorbing boundary width  $w$ , time step  $dt$ , pump pulse duration  $T_{\mathcal{P}}$ , delay  $\tau$  and spectrum time  $T_S$ , both during the optimization (opt) and for the fully converged calculations (conv). All values are given in a.u..

the excited-state spectrum after excitation by the initial guess pump-pulse  $\mathcal{E}_0(t)$  and after excitation by the optimized pump-pulse  $\mathcal{E}_{100}(t)$  after 100 iterations. The bottom inset shows the evolution of the control function  $\varepsilon^A$  with the number of iterations. The initial pulse is actually, by chance, a rather good guess: While the ground state spectrum of the atom is completely flat in the optimization region, the initial-guess pump pulse  $\mathcal{E}_0(t)$  creates features there. The value of  $\varepsilon^A$  obtained with it is around 0.1. The inset shows a steady enhancement of  $\varepsilon^A$  up to a value of about 0.2, where the enhancement starts to flatten. This result could be further enhanced by restarting the optimization using the optimized laser coefficients as initial guess for a new optimization (see comments on the convergence of the downhill-simplex algorithm in appendix A). Nevertheless, since this is just a test-case for the algorithm, we stopped the optimization at this point.

A comparison of the excited state spectra at the beginning and at the end of the optimization shows, that the algorithm further enhances the peaks, that appeared under the influence of the initial pump pulse. Its effect is mostly to excite the system from its ground state ( $\epsilon_0 = -0.670$  a.u.) into its first excited state ( $\epsilon_1 = -0.275$  a.u.), creating peaks at  $\omega_{1 \rightarrow 2} = 0.123$  a.u. and  $\omega_{1 \rightarrow 4} = 0.211$  a.u. in the optimization region (the transition from 1 to 3 is dipole forbidden) and into the second excited state ( $\epsilon_2 = 0.151$  a.u.), creating peaks at  $\omega_{2 \rightarrow 3} = 0.059$  a.u. and  $\omega_{2 \rightarrow 5} = 0.106$  a.u..

The disappearance of the ground state peaks indicates, that the laser completely depopulates the ground state. A population analysis (which is shown for the improved laser  $\mathcal{E}_{100}$  in the bottom inset of Figure 5.1) confirms this suspicion. The algorithm optimizes the pump pulse to transfer most of the population ( $\approx 75\%$ ) from the ground state into the first excited state, while the second excited state is also slightly populated ( $\approx 5\%$ ). About 16% of the electrons are ionized and the rest is distributed evenly across the re-

maining states. In comparison the initial pump pulse  $\mathcal{E}_0$  only transfers about 21% into the first excited state (which is the most desirable to obtain features in the optimization region), while the transfer into the second excited state is almost the same. It is noteworthy, that a relatively small change in the pump pulse (see the Fourier transform of the laser in the top panel) can have such a strong effect on the population transfer.

### 5.1.2. One-dimensional Helium <sup>||</sup>

As second example, we study the one-dimensional soft-Coulomb Helium atom. One-dimensional Helium is interesting, because it is still exactly solvable and can be used to compare the exact solution to the solution obtained with TDDFT. The 1D model of the Helium atom is defined as given in (2.119) in Chapter 2.5 with an atomic charge of  $C = 2$  and two electrons  $N = 2$ . In the TDDFT treatment, the external potential is given by (2.123) and the electron-electron interaction is described through the adiabatic exact exchange functional (EXX, as described in Section 2.4.1.1). In the following, this case will be named TDEXX description. The numerical parameters are the same as in the case of Hydrogen (see Table 5.1) and also the carrier frequencies and initial coefficients are the same. The optimization region lies between 200 and 800 nm.

Figure 5.2 shows a comparison of exact and TDEXX optimization. The first thing to notice is the difference of the spectra already at the level of the ground state spectrum. Taking this into account, it does not surprise that the systems show different excited-state responses under the influence of the same initial pump pulse. Both systems (exact and TDEXX) gain features in the optimization region under the influence of the initial pump laser, but to a different extend. While in the exact case, the system reacts strongly to  $\mathcal{E}_0$  reaching an  $\varepsilon_{\tau,exact}^{A,0}$  of approximately 0.090,  $\varepsilon_{\tau,TDEXX}^{A,0} = 0.006$  is about an order of magnitude smaller. This trend continues throughout the whole optimization: both models enhance  $\varepsilon_{\tau}^A$ , but while the exact treatment reaches an  $\varepsilon_{\tau,exact}^{A,100}$  of about 0.11 after the first 100 iterations,  $\varepsilon_{\tau,TDEXX}^{A,100}$  is only 0.013. This difference is clearly visible in the excited state spectra. While the exact model under the influence of the pump gains a broad feature in the optimization region (consisting in fact of several peaks), the TDEXX model only grows a shallow peak, which almost disappears in the bottom panel, which shows the results fully converged with respect to the simulation box size.

---

<sup>||</sup>The results presented in this section form part of [235].

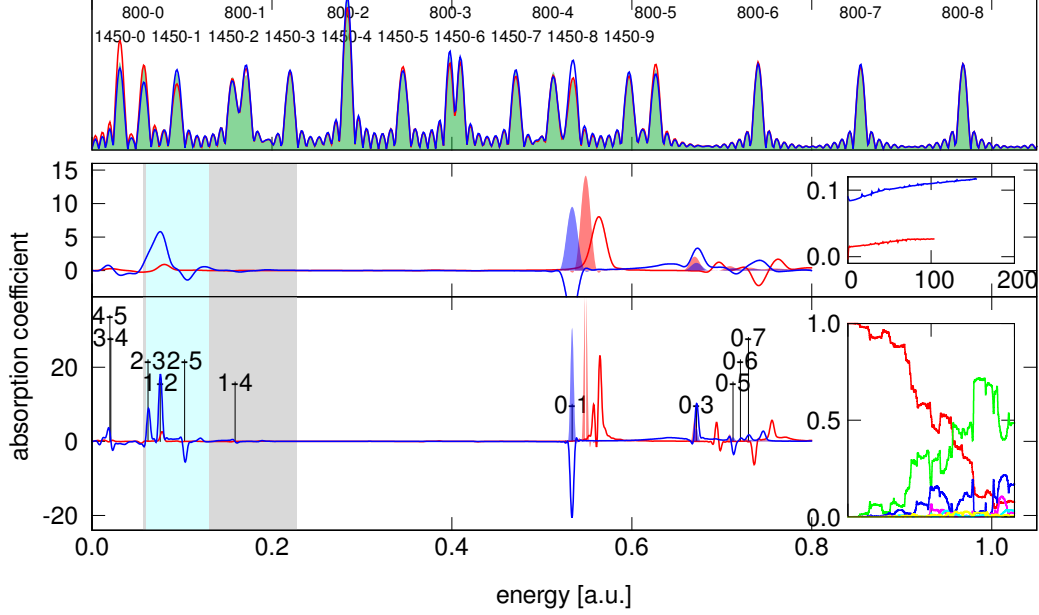


Figure 5.2.: (Middle and bottom) Ground state (shaded) and excited state (solid lines) spectra of one-dimensional Helium in a box of (middle)  $r = 50$  a.u. and (bottom)  $r = 100$  a.u.. In the bottom panel, the excited state transitions of the exact calculations are indicated. (Top) Comparison of initial (green) and optimized pump laser (Fourier transforms). Peaks are labeled by their basis wave length and the number  $n$  of their harmonic  $2n + 1$ . (Inset, middle) The control function  $\varepsilon^A$  as a function of the number of iterations. (Inset, bottom)  $|\langle \Psi(t) | \Psi_i \rangle|^2$  of the exact time propagation under the influence of the optimized pump pulse for the (red) ground state, (green) first excited state, (blue) second excited state, (pink) third excited state and (turquoise) fourth excited state. In all panels, results obtained by exact propagation are shown in blue, results obtained by (TD)DFT using the adiabatic spin-polarized exact exchange functional are shown in red. The grey shaded box marks the optimization area, the blue shaded one the visible range of the spectrum (350 nm - 750 nm).

In the exact case, the laser transfers the population from the ground state ( $\epsilon_0 = -2.238$  a.u.) into the first excited state ( $\epsilon_1 = -1.705$ ) with the help of the 13th carrier frequency (the 9th higher harmonic of  $\lambda = 1450$  nm) at  $\omega_{P13} = 0.534$  a.u.. Due to this population transfer, the peak at  $\omega_{0 \rightarrow 1} = 0.533$  a.u. turns from positive to negative and peaks com-

ing from the first excited state ( $\omega_{1\rightarrow 2} = 0.076$  a.u. and  $\omega_{1\rightarrow 4} = 0.159$  a.u.) arise in the excited-state spectrum, where the peak at  $\omega_{1\rightarrow 2}$  is located in the visible part of the energy range. At the same time, population is transferred into the second excited state ( $\epsilon_2 = -1.629$  a.u.), leading to e.g. the peaks at  $\omega_{2\rightarrow 3} = 0.062$  a.u. and  $\omega_{2\rightarrow 5} = 0.103$  a.u.. Note, that the numbering of the peaks is according to their appearance in the ground state spectrum, i.e. states, that are not dipole coupled to the ground state (e.g. triplet states) are not discussed.

The bottom inset of Figure 5.2 shows the time evolution of the populations  $|\langle \Psi(t) | \Psi_i \rangle|^2$  during the radiation by the pump  $\mathcal{E}_{100}(t)$ . The population analysis confirms, that the laser depopulates the ground state and transfers population into the excited states. At the end of the pump pulse only  $\approx 8\%$  of the electrons remain in the ground state, the rest has been transferred into higher excited states. About half of the electrons have been excited into the first excited state, and about a fifth into the second excited state. Also the third and fourth excited state are populated. This population of excited states explains the appearance of the peaks in the excited state spectrum.

The strong difference between the exact and the TDEXX case might be due to two effects. Firstly, it is known, that the real-time description of resonance processes is subject to an error if TDDFT is used with adiabatic functionals [231, 236] and the consequences for calculations using coherent control schemes were pointed out for example in Ref. [237, 238]. Secondly, the search space formed by the carrier frequencies of the pump pulse includes a frequency that is almost exactly resonant to the transition from the ground state to the first excited state in the exact case, but not so close to resonance in the TDEXX picture. Assuming a Rabi-like picture, this detuning between the transition energy and the driving frequency would lead to a smaller population transfer. While the small peak of the TDEXX spectrum is at roughly the position of the  $\omega_{1\rightarrow 2}$ -transition-peak, it does not seem to be strongly populated. The population analysis of the exact calculation suggests that the excitation of the higher states is a subsequent process after the excitation to the first excited state. Therefore, if this is not strongly populated, no subsequent excitation of higher states can occur. This might explain the lack of higher excitation peaks in the TDEXX spectrum.

To clarify this aspect, we repeated the TDEXX optimization with an adapted search space, in which the laser component at  $\omega = \omega_8^{1450}$  was replaced by a component with the same initial intensity at  $\omega = 0.549$  a.u., which is in resonance with the TDEXX

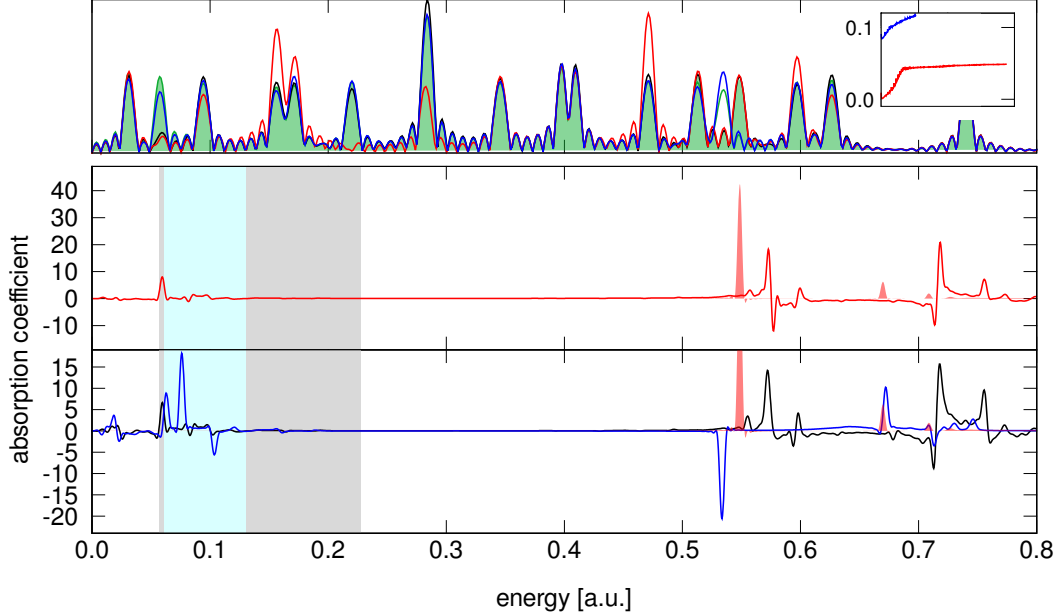


Figure 5.3.: (Middle and bottom) Ground state (shaded) and excited state (solid lines) spectra of one-dimensional Helium in a box of  $r = 100$  a.u.. (Middle) Spectrum optimized with the adapted search space using TDEXX after 550 iterations. Features in the visible have emerged. (Bottom) Optimized spectra after 100 iterations: Comparison of the exact optimization (blue) with the TDEXX optimization in the adapted search space (black). (Top) Optimization lasers in energy space: (shaded green) adapted initial laser and (green line) original initial laser as well as optimized laser with TDEXX after 100 iterations and (red) 550 iterations. (Inset) Target function  $\varepsilon^A$  for the adapted TDEXX optimization (red) and original exact optimization (blue).

transition from the ground to the first excited state. The results are shown in Figure 5.3. The middle panel shows the optimized spectrum after 550 iterations. In contrast to the optimization with the previous search space, features in the visible emerge. The bottom panel shows a comparison between the optimization in the exact case with the previous search space and the optimization in the TDEXX case with the adopted search space. One notices, that similar features arise, but still the  $1 \rightarrow 2$  peak of the exact case seems to be missing. There is, however, one peak arising in the TDEXX case at the same position as the exact  $2 \rightarrow 3$  peak, which could in fact be the shifted  $1 \rightarrow 2$

transition. Unfortunately, one cannot do a real population analysis with TDDFT (since we do not have access to the real many-electron state and its projections), and therefore this question remains unsolved. Nevertheless, one can conclude that a better performance of the exact optimization can be obtained once the search space is chosen more wisely, including the right frequencies.

Finally, we draw attention to the fact, that again, one can observe the artefacts of TDDFT spectroscopy as already pointed out in Chapter 3. While the peaks of the exact spectrum are independent of the ionization, this is not true in the TDEXX-case. With increasing ionization, the peaks are shifted to higher energies (compare the ground state and the excited state spectrum in Figure 5.2). To avoid these artefacts as much as possible, attention should be paid to keep the ionization of the system as small as possible.

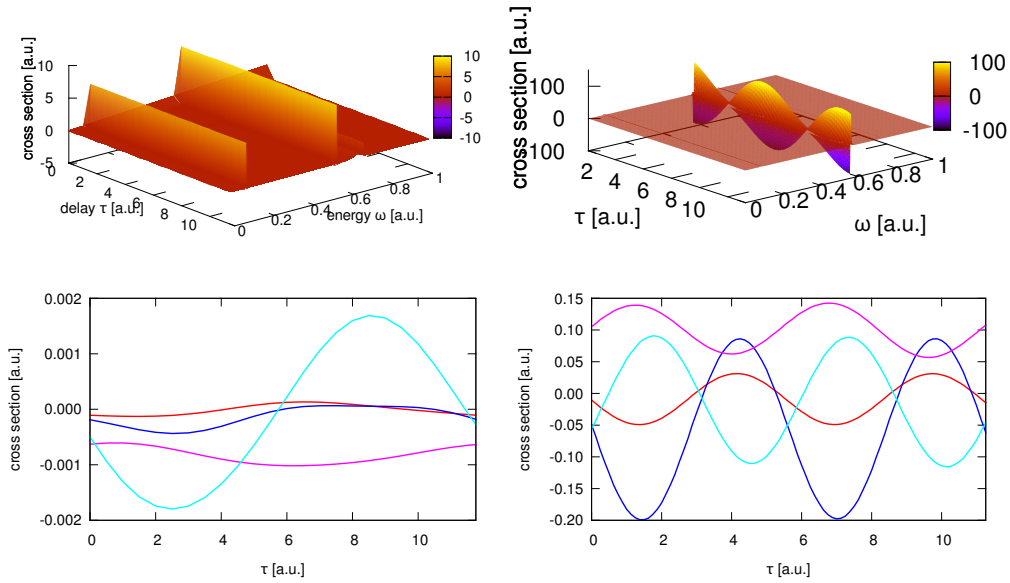


Figure 5.4.: (Top) Transient Absorption Spectrum of Helium after the excitation with a 45 cycle  $\sin^2$  laser pulse of intensity  $I = 5.26 \cdot 10^{11} \text{ W cm}^{-2}$  with a carrier frequency resonant to the excitation energy from the ground state to the first excited state for (left) exact and (right) adiabatic EXX description. (Bottom) Time-evolution of the cross section tensor at selected energies  $E_n = 0.2$  (red),  $0.4$  (blue),  $0.6$  (purple)  $0.8$  (turquoise) a.u. for (left) exact and (right) adiabatic EXX description. In the exact case, the curve at  $0.6$  a.u. is offset for clarity. In all cases, the time interval  $T = 2\pi/\epsilon_1 - \epsilon_0$  is shown.



To wrap up the comparison between exact and TDEXX formalism, we compare the dependence of the excited-state spectrum on the delay  $\tau$  in exact and TDEXX calculations. Figure 5.4 shows in the top panels the TAS of He in the exact description (left) and TDEXX formalism (right). The systems were excited by a 45 cycle  $\sin^2$  laser pulse resonant with the excitation energy from the ground state into the first excited state. In both cases, the laser excites the system into a linear combination of ground state and first excited state, resulting in a peak at  $\omega = 0.076$  a.u., which corresponds to the transition from the first to the second excited state. Note, that the excited state spectra at a delay of  $\tau = 0$  were already shown in Figure 3.2 and discussed in Chapter 3. Comparing the two figures, one notes, that here, the features in the very low energy region are missing. This is due to the usage of absorbing boundary conditions.

As previously discussed, a system in a linear combination of ground state and first excited state should have spectral components, which oscillate with the period time  $T = \frac{2\pi}{\epsilon_1 - \epsilon_0}$ , which is 11.76 a.u. in the exact case and 11.26 a.u. in TDEXX. However, in the exact case, a time-dependence of the spectrum is hardly visible due to scaling effects. Therefore, in the bottom panels of Figure 5.4 we display a time-analysis of the spectrum, where we record the cross section in dependence of the delay at a number of energies  $E_n = 0.2, 0.4, 0.6$  and  $0.8$  a.u.. The exact case is shown in the left bottom panel. The figure shows the time window corresponding to the period time 11.76 a.u.. As expected, the values oscillate with the predicted period time.

We now compare this to the TDEXX case. Here, the oscillations in the spectrum with the delay time are clearly visible. Nevertheless, performing the same analysis as in the exact case, one finds, that the values of the cross section vector in the TDEXX case do not oscillate with the expected periodicity of  $T_{TDEXX} = 11.26$  a.u., but twice as fast (see bottom right panel). We conclude, that the TDEXX description seems to have a similar structure to the exact case, in the sense, that the energy difference of the involved states is reflected in the periodicity of the oscillations of the spectrum. Nonetheless, there are major differences in the behaviour, which is reflected in the factor of two in the periodicity. We again point out, that the observed lineshapes are also different and the lineshapes occurring in the TDEXX description could e.g. be the result of two peaks of Lorentzian/Rayleigh shapes, which are shifted in energy.

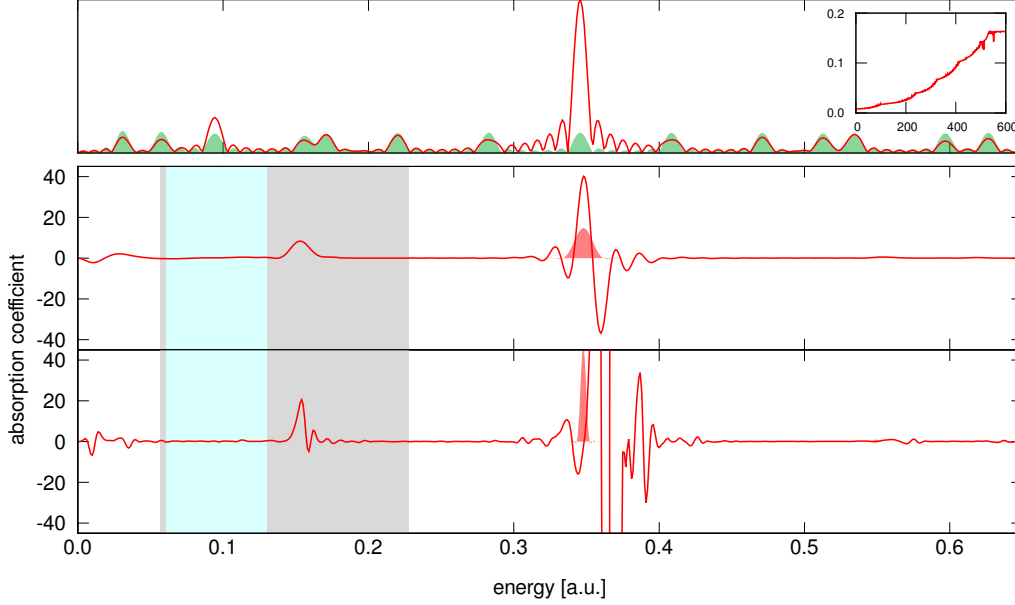


Figure 5.5.: (Middle and bottom) Ground state (shaded) and excited state (solid lines) spectra of one-dimensional singly-ionized Beryllium in a box of (middle)  $r = 50$  a.u. and (bottom)  $r = 100$  a.u. (Top) Comparison of initial (green) and optimized pump pulse (Fourier transforms). Peaks are labeled by their basis wave length and the number  $n$  of their harmonic  $2n + 1$ . (Inset) The target function  $\varepsilon_{\tau}^{A,m}$  as a function of the iteration number  $m$ . The grey shaded box marks the optimization area, the blue shaded one the visible range of the spectrum (350 nm - 750 nm).

### 5.1.3. One-dimensional Singly-Ionized Beryllium

Our final single-atom test system is one-dimensional singly-ionized Beryllium, which is calculated with TDDFT using the adiabatic local density approximation (ALDA). The optimization parameters (box and times) are defined as before (see Table 5.1). The carrier frequency search space is the same as before, except that we discarded  $\omega_2^{800nm}$  and  $\omega_3^{800nm}$  for being too close to  $\omega_4^{1450nm}$  and  $\omega_6^{1450}$ . The optimization region lies between 200 and 800 nm.

Figure 5.5 shows spectrum and laser of the best result after about 550 iterations. The algorithm clearly enhances the amplitude of the 8th carrier frequency (the 5th harmonic

of  $\lambda = 1450$  nm)  $\omega_{p8} = 0.3457$  a.u., that is in resonance with the ground state excitation  $\omega_{0 \rightarrow 1} = 0.346$  a.u.. Nevertheless, it is not clear, which transition belongs to the peak, that appears in the optimization region. It lies at around 0.15 a.u. but the lowest excitation from the first excited state, judging by the energy differences in the ground state spectrum, should be at around 0.2 a.u. The peak is not a spurious numerical feature, which we discarded by repeating the calculations with very well converged parameters. The most likely explanation is that this peak is due to a transition  $\omega_{1 \rightarrow m}$ , where  $\omega_{0 \rightarrow m}$  is dipole-forbidden, and therefore does not appear in the ground state absorption spectrum. This example is a good illustration of how a general search algorithm like the one we employ can find routes to the solution that are not obvious, or are even hidden, in a simple system analysis.

#### 5.1.4. Methane

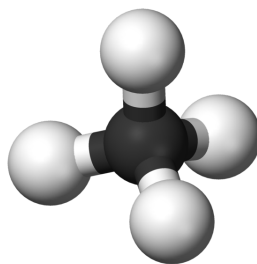


Figure 5.6.: Structure of Methane: A Carbon atom tetrahedrally surrounded by four Hydrogen atoms. Taken from <https://commons.wikimedia.org/wiki/File:Methane-3D-balls.png>.

Finally, we applied our scheme to molecules. Since the optimizations involve many time-propagations, we had to choose a relatively small molecule due to the restriction of computational resources. We chose Methane, which consists of one Carbon atom tetrahedrally surrounded by four Hydrogens (see Fig. 5.6) with a binding length of  $CH = 2.054132$  a.u.. It has eight valence electrons.

The optimizations of neutral  $\text{CH}_4$  were carried out in a reduced version of the previous carrier frequency search space used for the case of Beryllium, where – in order to keep computational times as small as possible – only the lowest nine frequencies were kept. As before, the optimizations were carried out in a small box and after the optimization the

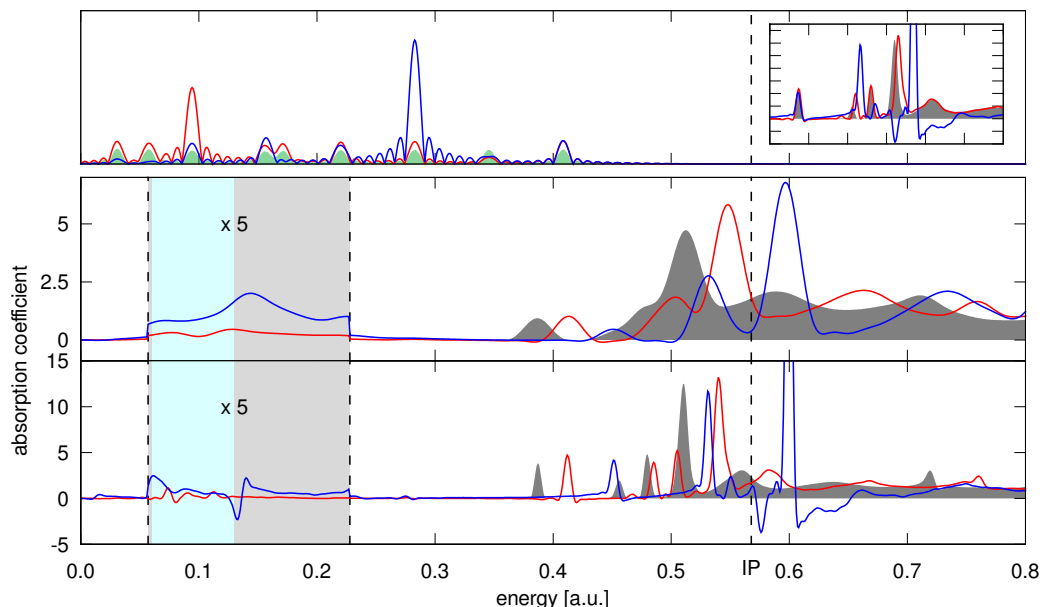


Figure 5.7.: (Middle and bottom) Ground state (shaded) and excited state (solid lines) spectra of Methane ( $\text{CH}_4$ ) in a box of (middle)  $r = 15$  a.u. and (bottom)  $r = 30$  a.u. for two different laser pulses. The grey shaded box marks the optimization area, the blue shaded one the visible range of the spectrum (350 nm - 750 nm). The spectra within the optimization area are shown enhanced by a factor of 5. (Top) Comparison of initial (green) and optimized lasers (Fourier transforms). Peaks are labeled by their basis wave length and the number  $n$  of their harmonic  $2n + 1$ . (Inset) The spectra shifted to lower energies to coincide with the ground state spectrum.

calculations were converged with respect to the box size. The parameters can be found in Table 5.1. The employed functional was the adiabatic LB94 functional due to its good description of higher lying states and the optimization region covered the energy range between 200 and 800 nm.

The use of a 3D model further increases the required computational resources. In particular the calculations scale cubically with the simulation box radius, which makes it unfeasible – with the current numerical implementation and resources – to reach a radius like the ones used for 1D calculations. Unfortunately, the use of small boxes leads to the artificial interaction of the electrons with the box boundaries. This effect results, in

our calculation, in the appearance of spurious peaks in the absorption spectrum that are due to “box states”, i.e. bound states that are due to the confinement in the simulation region. These unwanted errors can be alleviated with the use of absorbing boundary conditions, but even in this case the box needs to be sufficiently large. In practice, we found a good compromise using spherical boxes with a 15 a.u. radius, which includes a 5 a.u. absorbing region. This is the “small box” that we used for the optimization runs; later the optimal pulse was checked with a “large box” twice as large.

Furthermore, in order to discourage the algorithm from exciting too many electrons into the continuum, we modified the target function  $\varepsilon_\tau^A$  to include an exponential “penalty” for ionization, leading to the definition of  $\varepsilon_\tau^B$ :

$$\varepsilon_\tau^B = \varepsilon_\tau^A \exp\left(-\gamma \frac{N_0 - N_{Tp}}{N_0}\right) \quad (5.3)$$

Here,  $N_0$  is the number of electrons of the system at time zero and  $N_{Tp}$  is the number of electrons left in the system after the pump. The parameter  $\gamma$  controls the strength of the penalty. Figure 5.7 shows a comparison between the average absorption coefficients  $\bar{\sigma}_\tau^{12}(E)$  (red) in the 12th iteration step and  $\bar{\sigma}_\tau^{66}(E)$  (blue) in the 66th iteration step of the same optimization. A comparison of the spectra in the small and the big box shows, that the obtained features in the optimization region persist. We note, that both spectra are shifted with respect to the ground state spectrum:  $\bar{\sigma}_\tau^{12}(E)$  by about 0.03 a.u.,  $\bar{\sigma}_\tau^{66}(E)$  by about 0.07 a.u.. This is due to ionization, which is not completely suppressed by the algorithm. The ionization in the case of  $\bar{\sigma}_\tau^{12}(E)$  is about 0.1 electrons, whereas the ionization in the case of  $\bar{\sigma}_\tau^{66}(E)$  is 0.35 electrons. The inset of the top panel shows the converged spectra, offset by these shifts. One sees, that the weight of the first peak is almost not affected by the laser, while the weights of the higher lying peaks change and some of them become negative.

Since the optimization of  $\text{CH}_4$  was smaller than what we had hoped for, we started working with its doubly-ionized version  $\text{CH}_4^{2+}$ .  $\text{CH}_4^{2+}$  has two main advantages over neutral Methane: (i) it has two fewer electrons and therefore requires about a quarter less computational time, and (ii) it has more unoccupied bound states. The number of bound states is important, since we want the excited state spectrum to have peaks coming from transitions into bound states, not into the continuum. Also it is obviously more difficult to ionize the cation.

The previous results were obtained with a search space, constructed from carrier frequencies that are high harmonics of standard commercially available laser systems, such as the ones we used for the 1D models presented in the previous sections. Nonetheless, those results obtained for 1D Hydrogen and Beryllium suggest, that it might be important to include resonant laser frequencies in the search space. For the optimization of  $\text{CH}_4^{2+}$ , we therefore tailored the carrier frequencies included in the search space to resonances of the molecule. The excited state resonant frequencies were obtained from resonances in the ground state spectrum of  $\text{CH}_4^{2+}$ .

\*\* Here, we present two of these optimizations. For the first search space, the idea was to find two eigenstates with energies  $\epsilon_h$  and  $\epsilon_l$ , that differ by an energy in the visible:  $0.057 \text{ a.u.} \leq \epsilon_h - \epsilon_l \leq 0.139 \text{ a.u.}$ . By exciting the system into the lower state  $\epsilon_l$  (“basis state”) one might obtain transition peaks in the visible due to the transition into the higher one. This fact is not guaranteed since the transition might not be dipole allowed – a possibility that we cannot know beforehand by simply performing linear response TDDFT calculations. The energy of the eigenstates with respect to the ground state  $\epsilon_0$  is extracted from the ground state spectrum of  $\text{CH}_4^{2+}$ , which is shown in Figure 5.8. The peaks are numbered for reference and we refer to them by  $\epsilon_n$ , with  $n$  being the peak number in the ground state spectrum.

The ground state spectrum shows, that the first possible basis state is  $\epsilon_3$ . The energy difference between  $\epsilon_3 = 0.690 \text{ a.u.}$  and  $\epsilon_4 = 0.816 \text{ a.u.}$  is  $\omega_{3 \rightarrow 4} = 0.126 \text{ a.u.}$  and lies – with 362 nm – at the red end of the visible spectrum. Also  $\epsilon_4$  provides a transition in the visible range – into  $\epsilon_5 = 0.938 \text{ a.u.}$  with  $\omega_{4 \rightarrow 5} = 0.122 \text{ a.u.} = 373 \text{ nm}$ . Starting from  $\epsilon_5$ , states even have more than one transition in the visible. We therefore choose a carrier frequency search space, that allows the construction of a pump pulse, that excites electrons from the ground state into  $\epsilon_3$  and higher lying states either directly or by successive excitations.

The first search space includes carrier frequencies, that are resonant to the ground state excitation energies  $\epsilon_n$  or to excited state excitations  $\epsilon_m - \epsilon_n$ . To avoid ionization, all carrier frequencies are smaller than  $\epsilon_7 = 1.0 \text{ a.u.}$ . The second carrier frequency search space was designed using the ionization potential  $I_P$  of the system (which according to Koopman’s theorem is equal to minus the energy  $\epsilon_H$  of the highest occupied KS orbital  $\varphi_H$ ) and the energy differences  $I_P - \epsilon_n$ . One carrier frequency is resonant with  $-\epsilon_H$ ,

---

\*\*The results presented in the following for doubly-ionized Methane form part of [235].

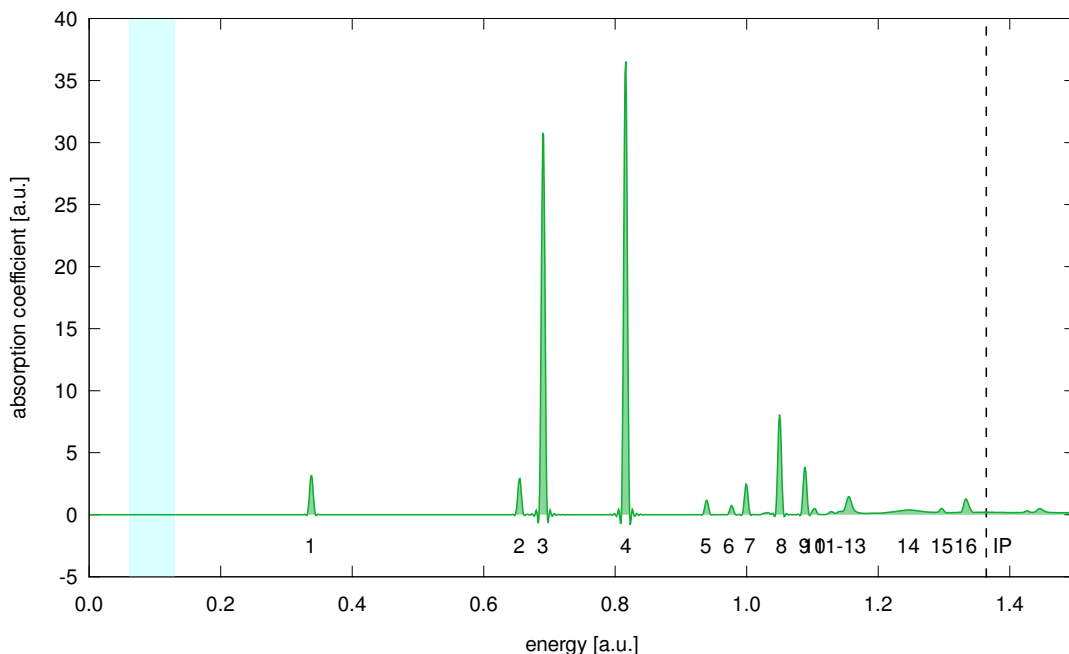


Figure 5.8.: Ground state spectrum of doubly-ionized Methane  $\text{CH}_4^{2+}$ . Peaks are numbered for later reference. The blue area marks the visible range of the spectrum (350 nm - 750 nm).

all other frequencies are resonant with excitations from the target excited states ( $\epsilon_3$  to  $\epsilon_8$ ) to the continuum limit. The idea is to excite an electron into a state close to the ionization threshold and from there deexcite it into one of the target states. The laser frequencies, that were included in the search spaces and the corresponding resonances are summarized in Tab. 5.2.

In both optimizations, box, time-step, delay and spectrum time were the same as for neutral  $\text{CH}_4$  (see Table 5.1). The pump duration was reduced by 200 a.u. to 600 a.u. (14.5 fs). The initial coefficients were  $c_i^I \approx 0.001$  for all  $i \neq 6$  and  $c_6^I = 0.005$  and  $c_i^{II} \approx 0.001$  for all  $i$ . The employed functional was ADSIC LDA (see Chapter 2.4.1.1) because of its accurate description of the higher lying states. The optimization region was reduced to the interval between 328 and 750 nm. The obtained pump pulses  $\mathcal{E}^I$  and  $\mathcal{E}^{II}$ , the associated excited-state spectra and the resulting colours are shown in Figure 5.9. It can be seen that both search spaces include optimal lasers that cause the molecule to lose its transparency and absorb in the visible. These new absorption features found by

Search Space I									
$\omega_1^I$	$\omega_2^I$	$\omega_3^I$	$\omega_4^I$	$\omega_5^I$	$\omega_6^I$	$\omega_7^I$	$\omega_8^I$	$\omega_9^I$	$\omega_{10}^I$
0.122	0.248	0.345	0.479	0.601	0.654	0.690	0.816	0.938	1.000
$\epsilon_4 - \epsilon_5$	$\epsilon_3 - \epsilon_5$	$\epsilon_1 / \epsilon_1 - \epsilon_3$	$\epsilon_1 - \epsilon_4$	$\epsilon_1 - \epsilon_5$	$\epsilon_2$	$\epsilon_3$	$\epsilon_4$	$\epsilon_5$	$\epsilon_7$

Search Space II						
$\omega_1^{II}$	$\omega_2^{II}$	$\omega_3^{II}$	$\omega_4^{II}$	$\omega_5^{II}$	$\omega_6^{II}$	$\omega_7^{II}$
0.311	0.364	0.386	0.426	0.548	0.674	1.364
$\epsilon_3 - I_P$	$\epsilon_4 - I_P$	$\epsilon_5 - I_P$	$\epsilon_6 - I_P$	$\epsilon_7 - I_P$	$\epsilon_8 - I_P$	$I_P$

Table 5.2.: Laser frequencies (in a.u.) and the corresponding resonances of the search spaces of the optimization of  $\text{CH}_4^{2+}$ . Nomenclature as in Figure 5.8,  $\epsilon_H$  is minus the energy of the highest occupied KS state.  $\omega_3^I$  is the average of  $\epsilon_1 = 0.337$  a.u. and  $\epsilon_3 - \epsilon_1 = 0.353$  a.u.. Since the frequencies are broadened by the finite pulse duration,  $\omega_3^I$  covers both resonances.

the algorithm making use of a small simulation box persist when repeating the calculation with a larger, fully converged box radius. We may therefore conclude that the proposed algorithm is a viable option to find pump laser pulse that excite systems into visible light absorbing states, also when considering realistic 3D molecular first principle descriptions, and not only 1D models. The scalability of TDDFT permits to foresee the extension of the technique to larger systems. Nonetheless, the need for larger search spaces for more complex molecules and the resulting increase of the number of iteration steps needed pose challenges on the computational feasibility.

These challenges can partially be faced by intelligent design of the search space, i.e. by careful selection of the carrier frequencies included in the search space. In order to be able to design more appropriate search spaces, a detailed understanding of the underlying dynamics would be useful. This has two benefits: (i) By analyzing the dynamics, one can obtain deeper insight into how laser excitations are described within the TDDFT formalism. (ii) An identification of the laser components, that are the main driving forces in the optimization, allows us to put forward a two-step optimization process. In the first one, a broader search space could be used for a pre-optimization to find the important frequencies in the optimization. In a second step, one could then discard the frequencies without effect and further optimize the pulse in a smaller search space, leading to faster convergence. Alternatively one could use the cleaned pulse as an initial guess for a more costly gradient-based algorithm, which would be expected to show faster convergence



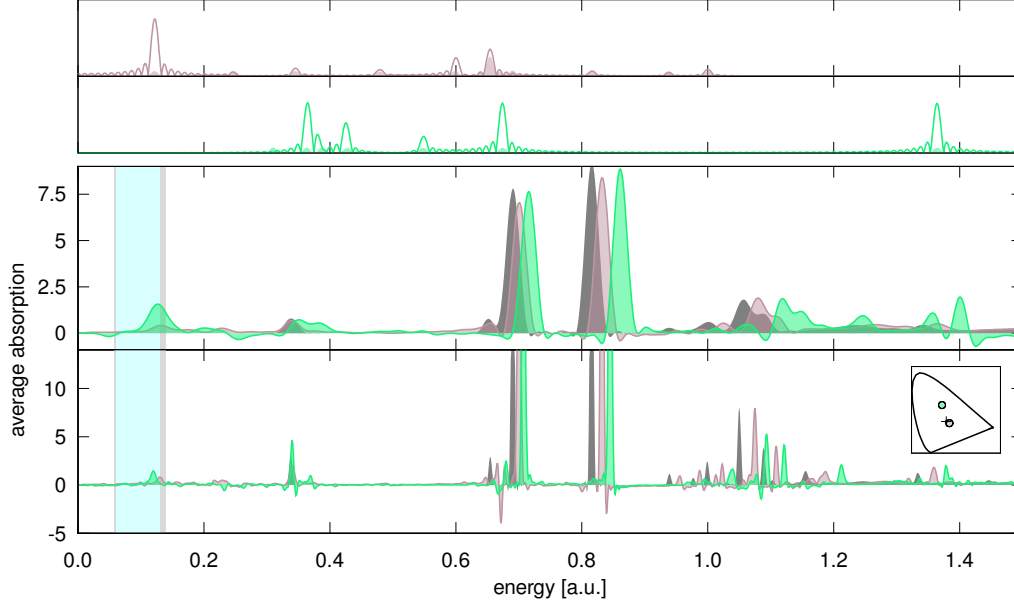


Figure 5.9.: (Middle and bottom) Ground state (dark grey) and excited state spectra of doubly-ionized Methane ( $\text{CH}_4^{2+}$ ) in a box of (middle)  $r = 15$  a.u. and (bottom)  $r = 30$  a.u. for two different pump pulses  $\mathcal{E}^I$  (brown) and  $\mathcal{E}^{II}$  (green). The grey shaded box marks the optimization area, the blue shaded one the visible range of the spectrum (350 nm - 750 nm). (Top) Comparison of initial (shaded) and optimized (solid lines) pump pulses (Fourier transforms). (Inset) Chromaticity diagram with colours obtained by excitation of the system by the pump pulses.

since the initial guess is already close to an optimal solution. This scheme has recently been proven useful in the optimization of quantum gates [239].

In either scenario, the first step is to identify the components of the control laser, that play the main role in the obtained excitation. One can think of several possible approaches to this analysis: (a) One solves the response equations using e.g. Casida's scheme and obtains the many-body excitations in a basis of KS particle-hole excitations. One determines the time-dependent occupations of the KS ground state orbitals and tries to correlate the change in occupation with the many-body excitations. One checks against the excited state spectrum to confirm the analysis. (b) One uses TAS and its analysis as

described in Chapter 3 to analyse the time-dependent excitation of the many-body states. (c) One selectively exposes the system to the single frequency components of the control laser (and some combinations) and calculates the resulting excited state spectra. These spectra can then be compared to the excited state spectrum created by the full pump and to the many-body excitation energies obtained from the ground state spectrum (as described before).

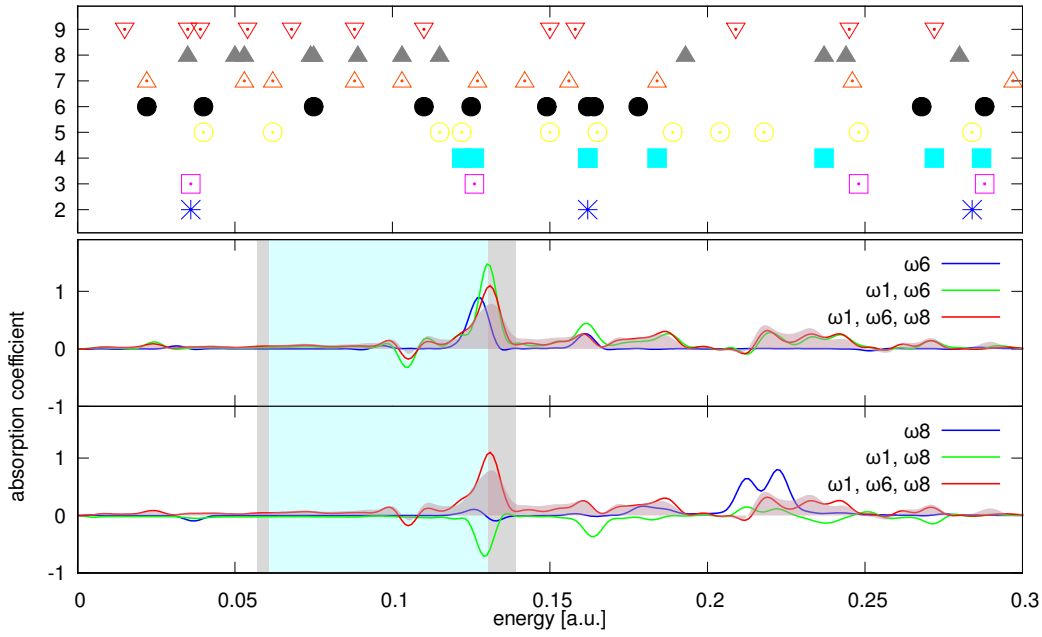


Figure 5.10.: (Middle and bottom) Laser spectra obtained by exposure of  $\text{CH}_4^{2+}$  to selected frequency components of the pump pulse  $\mathcal{E}^I$ . The shaded line shows the spectrum obtained by the full pulse. (top) Many-body excitation energies obtained through analysis of the ground state spectrum. The x axis denotes the excitation energy, the y axis the excited state, from where the excitation takes place.

In the following, we opt for (c), demonstrating the procedure using the example of the optimized pump  $\mathcal{E}^I$  obtained in the first search space. Figure 5.10 shows in the top panel the many-body excitation energies, which were obtained from the ground state spectrum through calculating the energy differences between the ground state peaks. Each row represents the possible transitions between the corresponding peak (e.g. the row labeled

'2' belongs to the second peak of the spectrum) and the others (higher and lower ones), i.e. the  $n$ -th row depicts the transition energies  $\omega_{n \rightarrow m}$ . Transitions from the first excited state lie outside of the energy range shown .

We want to compare these many-body excitation energies to the peaks obtained in the spectrum by selectively exposing the system to the single frequency components of the pump. From this we hope to be able to reconstruct the excitations triggered in the system by the single frequency components. Furthermore, we want to identify the main driving frequencies of the multi-step excitation, that leads to the optimized excited state spectrum. We start this analysis by exposing the system to each of the pump frequencies  $\{\omega_i\}_{i=1,\dots,10}$  alone. We find, that out of the eight frequencies, there are only two, that are able to excite the system, leading to a change in the spectrum in comparison to the ground state spectrum. These are the frequencies  $\omega_6^I = 0.654$  a.u., which corresponds to the excitation from the ground state into the second excited state  $= \epsilon_2$  and  $\omega_8^I = 0.816$  a.u., which corresponds to an excitation from the ground state into the fourth excited state  $= \epsilon_4$  (see Tab. 5.2). Figure 5.10 shows the resulting spectra (blue lines). Here, we focus on the analysis of the frequency  $\omega_6^I$ , which is shown in the middle panel. The analysis of  $\omega_8^I$ , which is shown in the bottom panel can be done in a similar way.

Figure 5.10 shows a comparison of the full excited state spectrum (obtained through excitation with the full control laser  $\mathcal{E}^I$ ) in shaded with the spectrum obtained by the exposure to the single frequency component  $\omega_6^I$ . One sees, that this single frequency causes a peak similar to the main peak of the full spectrum. This is surprising at first sight, since  $\omega_6^I$  is the resonance frequency to excite the system from its ground state into its second excited state and as shown in the top panel, the second excited state (labeled '2', depicted in blue crosses) should not have any peaks at this energy. This shows, that calculating the energy differences of the ground state peaks can only lead to a rough analysis of the excitation energies between excited states: There might be transitions to peaks, which do not show up in the ground state spectrum (since their excitation from the ground state might be dipole-forbidden) and others, where the transition between the excited states is dipole-forbidden.

To extract the important frequency components of  $\mathcal{E}^I$  and get further insight into the dynamics of the excitation, we now combine  $\omega_6^I$  with a second carrier frequency to look for subsequent excitations. Again, only a few of the frequencies show effect, namely  $\omega_1$  and  $\omega_3$ , but since the changes due to  $\omega_3^I$  are minor, we do not analyze this combination

further but concentrate on the combination with  $\omega_1^I$ . Note, that the same holds true for the case, where we analyze the combinations with the carrier frequency  $\omega_8^I$  (shown in the bottom panel). By combining  $\omega_6^I$  with the laser component at  $\omega_1^I = 0.122$  a.u. (green spectrum) we are able to reconstruct already most of the features in the depicted energy range and to create an absorption peak in the visible, which is even slightly higher than the one created by the full pump  $\mathcal{E}^I$ . This is partially “corrected” by adding the component at  $\omega_8^I$ , which modifies the main peak in the visible in the direction of the one obtained by  $\mathcal{E}^I$ . As can be seen in the figure, this combination of the three frequency components at  $\omega_1^I$ ,  $\omega_6^I$  and  $\omega_8^I$  almost completely reproduces the spectrum obtained in the energy range  $[0.0-0.3]$  a.u..

By exposing the system to combinations of the frequency components of the pump pulse, we were therefore able to identify the main driving frequencies of the multi-step excitation. A possible application of this knowledge would be to start a new optimization in a search space consisting of only these three frequencies. As a side effect of this analysis we even found a pulse, that produces a higher absorption in the visible than the optimized one – the one, that only consists of the components at  $\omega_6^I$  and  $\omega_1^I$ . Therefore, one would expect the algorithm to follow this path in future iterations, diminishing the frequency component at  $\omega_8^I$ .

## 5.2. Approach II: Spectrum of an Excited Kohn-Sham Orbital

As we have seen in the last section, the optimizations obtained with our first approach are not very impressive. We have found that the choice of the optimization space is crucial to obtain good results; unfortunately, the identification of a good search space is not easy. One could in principle choose a very large search space hoping that it contains the right region, but then the optimizations become prohibitive: the number of optimization steps grows super-linearly with the search space dimension. Each of these steps requires one time evolution under the influence of the pump pulse and four time evolutions to obtain the spectrum after the excitation. In the following, we present a different approach, that cuts back on the required computational resources by getting rid of the time evolution after the laser. In this approach, the optimization is divided into two steps: In the first step, we analyse the ground state spectrum for promising excited many-body states,

and in the second step we look for a laser pump pulse that drives the system, at least approximately, into these excited states. The procedure is the following:

- I First, we perform an analysis of the ground state absorption spectrum, which can be computed with the real-time propagation technique, or with the Casida equations. One can then identify states that (1) are strongly dipole-coupled to the ground state, and (2) are separated energetically to other excited states in the visible range, so that their absorption spectrum is likely to contain features in that range.
- II We then analyze the excited state in terms of the Casida *ansatz* for the excited states [177]:

$$|\Psi_I\rangle \approx \sum_{ij\sigma} c_{ij\sigma} \hat{a}_{j\sigma}^\dagger \hat{a}_{i\sigma} |\Phi_0\rangle, \quad (5.4)$$

where  $\Psi_0$  is the ground state KS determinant, and  $\hat{a}_{j\sigma}^\dagger \hat{a}_{i\sigma}$  is a creation-annihilation operator pair that substitutes the occupied  $i\sigma$  KS orbital by the unoccupied  $j\sigma$  orbital ( $i$  and  $j$  run over the spatial orbitals, and  $\sigma$  is the spin index). The coefficients  $c_{ij\sigma}$  are obtained from the solution of the Casida equations. The resulting states are approximations to the true excited many-particle states.

- III We are interested in those excited states that are composed primarily of one dominant single-particle excitation, i.e. those for which the previous linear combination of determinants is dominated by only one of them. Note, however, that we are considering spin-restricted calculations, and therefore, even pure “single-particle” excitations are in fact necessarily composed of two Slater determinants, i.e.:

$$|\Psi_I\rangle = \frac{1}{\sqrt{2}} \left[ \hat{a}_{j\uparrow}^\dagger \hat{a}_{i\uparrow} + \hat{a}_{j\downarrow}^\dagger \hat{a}_{i\downarrow} \right] |\Psi_0\rangle. \quad (5.5)$$

- IV Once we have identified interesting excited states according to those criteria, we construct the Kohn-Sham determinants that approximate them, by substituting the corresponding occupied by unoccupied orbitals. We then compute the excited state spectra of these approximate excited states to confirm that they have good response properties in the visible (a fact that is not guaranteed, since the excited state to excited state transitions could be dipole-forbidden). In this manner, we select the excited state with the spectrum, that is most convenient for our purpose, e.g. that has the largest absorption in the visible.

- V This will be the target state for step two: we use an optimal control algorithm to

find a pump pulse that excites the system from its ground state into this target state.

Note that, in the spin-restricted setup that we are using, the simple swap of an occupied by an unoccupied orbital results in fact in a *double* excitation, that cannot be used to approximate the excited states that we are targeting. As mentioned above, these are necessarily composed of two Slater determinants, with unoccupied KS orbitals of opposite spins. We want, however, to use only one Slater determinant, and in order to do so, we employ the following further approximation: we swap the occupied state  $i$  by a linear combination, with equal weights, of  $i$  and the unoccupied state  $j$ . The resulting KS determinant has the same density as the single particle excitation composed of the two Slater determinants.

In the following, we demonstrate the procedure using the example of the Methane molecule as described before. In order to be able to perform the Casida analysis, we return to the neutral Methane. This is necessary, because due to the three-fold degeneracy of the KS HOMO, one has to use fractional occupations for the cation in order to converge the ground state density, and our implementation of the Casida method does not allow for fractional occupation numbers. The calculations were performed in a spherical box of radius  $r = 45$  a.u. with 15 a.u. absorbing boundaries and a spacing of 0.3 a.u.. Again, the LDA functional in combination with ADSIC was used.

The ground state spectrum of Methane using the LDA-ADSIC functional is shown in Figure 5.11. One candidate for a target state is the first excited state  $\epsilon_1 = 0.379$  a.u. From here, there might be interesting transitions to  $\epsilon_3 = 0.458$  a.u.,  $\epsilon_4 = 0.471$  a.u.,  $\epsilon_5 = 0.491$  a.u. and  $\epsilon_6 = 0.496$  a.u.. With excitation energies between  $\omega_{1 \rightarrow 3} = 0.079$  a.u. ( $= 577$  nm) and  $\omega_{1 \rightarrow 6} = 0.117$  a.u. ( $= 389$  nm) all of them lie in the desired energy range. An analysis of the Casida excitations furthermore reveals, that there are more transitions in this energy range, which do not appear in the ground state spectrum, because their excitation from the ground state is dipole-forbidden. Nonetheless, they might contribute to the excited state spectra. Also interesting as target state are the second excited state  $\epsilon_2 = 0.425$  a.u. and the third excited state  $\epsilon_3$ . From both, excitations in the visible can be found. Analyzing  $\epsilon_1$ , we find that it is three-fold degenerate and contains contributions from the KS excitations  $\varphi_2 \rightarrow \varphi_5$ ,  $\varphi_3 \rightarrow \varphi_5$  and  $\varphi_4 \rightarrow \varphi_5$  ( $\varphi_i$  being the involved KS orbitals). By applying a small electric field during the ground state calculation, one can align the KS orbitals in such a way, that one of the three versions of  $\epsilon_1$  belongs to a

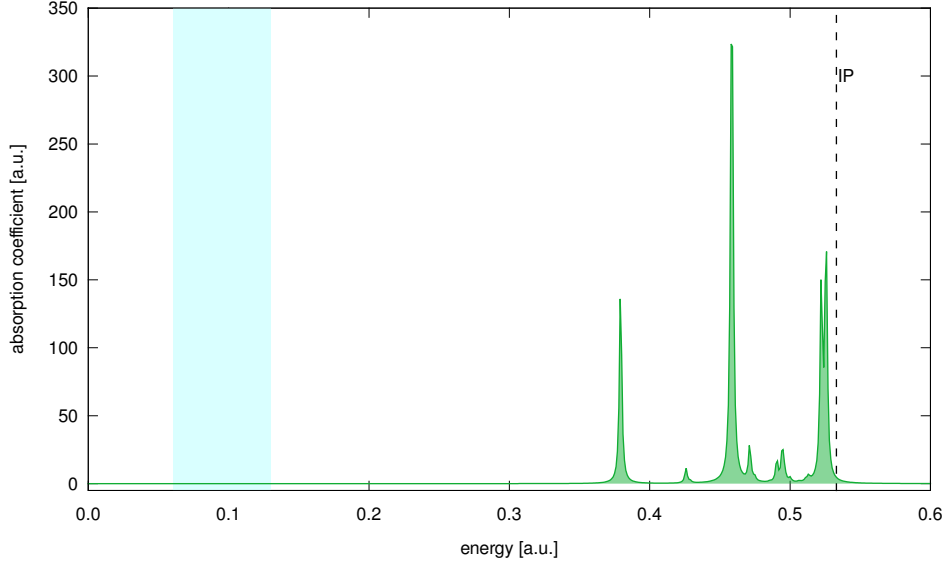


Figure 5.11.: Ground state spectrum of Methane using the LDA-ADSIC functional.

single KS excitation, e.g. consists to almost 100 % of the excitation  $\varphi_4 \rightarrow \varphi_5$ . This transition is then used for two different excitations. In the first, we transform the 4th KS orbital  $\varphi_4$  into  $\varphi_5$ . This can be interpreted as a double-excitation from the HOMO into the LUMO. Accordingly, half of this transformation, i.e. transforming  $\varphi_4$  into a linear combination of  $\varphi_4$  and  $\varphi_5$  with equal weights:  $\varphi_4 \rightarrow 1/\sqrt{2}(\varphi_4 + \varphi_5)$  results in the same density as exciting a single electron from the HOMO into the LUMO and can therefore be interpreted as such.

In the same way, we find that  $\epsilon_2$  (which belongs to the HOMO  $\rightarrow$  LUMO+1 transition) consists in transforming two of the degenerate KS orbitals  $\varphi_2$ ,  $\varphi_3$  and  $\varphi_4$  into linear combinations of themselves with one of the also degenerate KS orbitals  $\varphi_6$ ,  $\varphi_7$  and  $\varphi_8$ , e.g. at the same time transforming  $\varphi_3 \rightarrow 1/\sqrt{2}(\varphi_3 + \varphi_8)$  and  $\varphi_4 \rightarrow 1/\sqrt{2}(\varphi_4 - \varphi_7)$ . This forms the third excitation, that we perform. After the transformations are made, the spectra of the so-created excited-states are calculated. They are shown in Figure 5.12 in the bottom panel while the top panel shows the many-body excitation energies as obtained from the ground state spectrum (energy differences to higher and lower lying states are depicted). The excited-state spectra confirm, that all three excitations lead to strong absorption in the visible. We also see, that both - the peaks of the single and of the

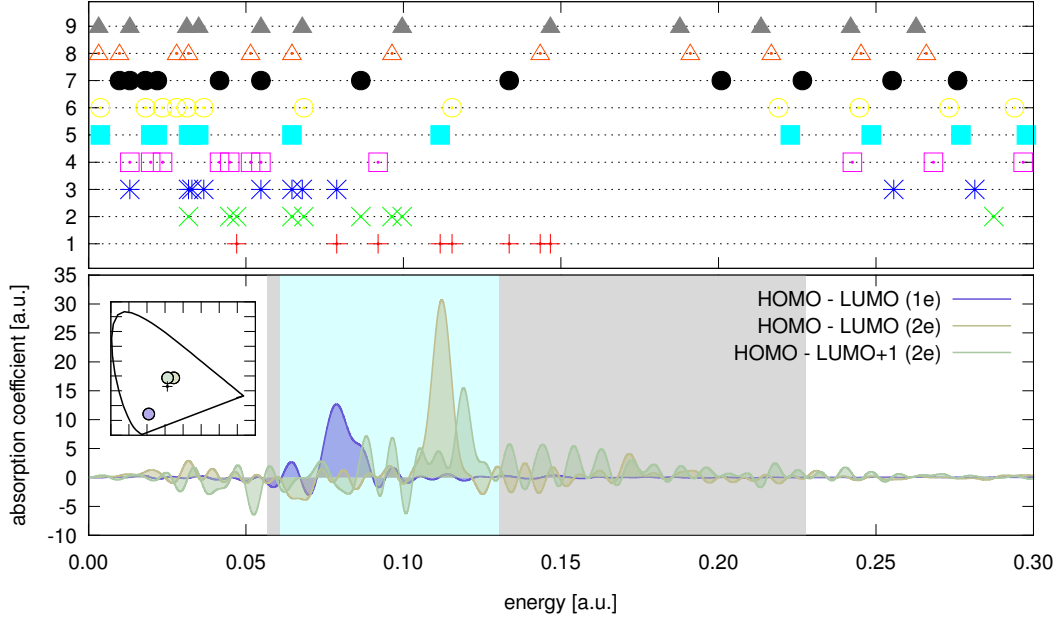


Figure 5.12.: (Bottom) Excited-state spectra of CH<sub>4</sub> according to scheme II and (inset) the chromaticity diagram with the resulting colours. (Top) Many-body excitation energies of CH<sub>4</sub> obtained through calculating the energy differences of the ground state spectrum. The x axis denotes the excitation energy, the y axis is the excited state, from where the excitation takes place.

double excitation from the HOMO into the LUMO (HOMO-LUMO (1e) and HOMO-LUMO (2e)) are at energies, where  $\epsilon_1$  should have peaks according to the frequency analysis shown in the top panel. The case of the HOMO  $\rightarrow$  LUMO+1 excitation is not clear though. The new peak in the spectrum is at an energy, where only  $\epsilon_1$  should have peaks.

In the second step, we would now have to find a laser, that excites the system into the state, that we put it into manually. This could be done using a quantum optimal control algorithm. Unfortunately, there was not enough time to finish the quantum optimal control calculations for this thesis. However, I did some test runs, where I exposed the system to pulses with carrier frequencies around the many-body resonance frequency. Particularly in this system, due to the degeneracy of the KS-HOMO, it was important to chose the laser polarization in accordance to the orientation of the KS-orbitals. These



test runs were done in a very small box, so the results are not necessarily reproducible in a bigger box neither. What I found during these optimizations, was, that for the system in question, it was necessary to dynamically “retune” the carrier frequency during the exposure to the pump. For the small system I was able to achieve a considerable excitation using this retuning technique. Together with the known problem of achieving full excited state populations using standard approximate adiabatic xc-functionals of TDDFT, this could give first hints to the necessity of combining Quantum-OCT with chirped pulses to obtain a satisfying excitation into higher states in the TDDFT formalism.

### 5.3. Summary and Conclusions

In this chapter, we have presented two ways of optimizing the absorption in the visible region and how they can be used in combination with TDDFT. In the first approach, we define a target function – the integral over the visible region of the excited-state absorption spectrum – and optimize the coefficients of a pump pulse, which was given as linear combination of components with different carrier frequencies (the search space) to maximize the target function, which was calculated from the excited state spectrum after a certain delay time. The coefficients were the only components that were varied; phases, duration and polarization of the pump as well as the delay between pump and probe were kept fixed during the optimization. The algorithm was tested for a one-dimensional Hydrogen model, which was solved exactly, one-dimensional Helium, which was used to compare exact and TDEXX treatment and for singly-ionized Beryllium, which was only treated within the TD-ALDA framework. The carrier frequencies included in the search space belonged to the wavelengths  $\lambda = 800$  nm and  $\lambda = 1450$  nm, two standard laser wave lengths and their higher harmonics.

We found that this search space was appropriate for both Hydrogen and Helium in the exact treatment. In both cases, the search space included the transition energy from the ground state into the first excited state and the algorithm was able to take advantage of this resonance to excite electrons into excited states and create absorption peaks in the visible. In the case of Helium, even subsequent excitation into higher excited states took place, further improving the absorption in the target region. In comparison, the TDEXX optimization of Helium did not lead to satisfying results. We found that this was due to different ground-state excitation energies of the exact model and the TDEXX treatment.

While in the exact case, the resonance between the ground state and the first excited state was included in the search space that was not true for the TDEXX case, where a resonant excitation into the first excited state was not possible. This demonstrates the importance of an appropriate design of the search space. When we adapted the search space by replacing the exact excitation energy by its TDEXX equivalent, we found that an excitation was achieved, creating features in the visible, which were shifted with respect to the exact ones. We found that it was hard to tell, if the emerging peaks came from subsequent excitations or were just shifted with respect to the exact ones, since TDDFT does not allow for a real population analysis.

The importance of resonances in the design of the search space also becomes clear in the case of singly-ionized Beryllium in TDALDA treatment. Here, the optimization algorithm clearly enhances the amplitude of the laser frequency belonging to the resonant excitation of the first excited state from the ground state. This leads to the creation of a peak in the optimization region with unknown origin. From this example, we also learn that the ground state spectrum can only give us a few possible excited-state excitation peaks. Not all excited-state transitions that we can calculate based on the ground state spectrum will be allowed and not all allowed excited-state transitions are deducible from the ground state spectrum.

We also analyzed the time-dependence of a non-stationary state spectrum in TDDFT, using the example of Helium, which was excited into a linear combination of ground state and first excited state. We found that in this linear combination, the TDEXX oscillations in the spectrum were related to the many-body excitation energy as one would expect. Nonetheless, the oscillations were twice as fast as the predicted ones. Analyzing this behaviour in TDDFT is the goal for future work.

We then moved on to Methane and doubly-ionized Methane, which is more convenient for computational purposes due to it having two fewer electrons (and therefore being computationally less expensive) and also because it has more unoccupied, bound states. We learned that the chosen search space was not suitable for Methane. Furthermore, we found that the algorithm favours the excitation of box states, leading to a large, but unfortunately unphysical absorption in the optimization region. We found that this problem can partially be solved by introducing absorbing boundaries and an exponential penalty factor for ionization. For doubly-ionized Methane, we designed two search spaces taking into account its resonances. The first search space was based on subsequent

excitation, the second one on excitation of states close to the ionization threshold and subsequent stimulated relaxation into the lower excited target states. We found that both approaches enable us to construct pump lasers, which do improve the absorption in the visible. Furthermore we found that an analysis of the involved excitations can yield some insight into the dynamics of excitation, but exactly identifying the mechanisms is difficult.

Regarding the technical aspect, we found that whilst this optimization scheme in principle works, it requires vast computational resources due to its multiple time propagations. An intelligent design of the search space can cut down on the resources needed, but is hard to do in practice since the ground state spectrum does not provide any information on whether inter-excited-state transitions are allowed or not. The second approach developed cuts down on computational resources within the optimization by splitting the optimization into two steps. In the first step, a KS excited state with desirable features is identified. For neutral Methane, we were able to find three interesting KS excited states. In the second step, a laser is found that excites the system from the ground state into this KS excited state. To this end, efficient quantum optimal control algorithms can be used. Finding these pulses is the goal for future work.



## 6. Conclusions and Outlook

---

*“I gotta stop somewhere - I’ll leave you something to imagine.”*

*Richard Feynman - Symphony of Science*

---

In this thesis, I studied how to analyze and control transient spectra using exactly solvable model systems and first principles real-time time-dependent density functional theory. Normally, TDDFT is used for the description of the response of systems in their ground state. Here, I showed how TDDFT can be used to study time-resolved pump-probe experiments in an excited state and assessed the possibility of combining TDDFT with Quantum Optimal Control Theory in order to tailor pump pulses for enhancing (or reducing) some given features of the probe absorption. This provides a tool for the interpretation of fast evolving attosecond time-resolved spectroscopic experiments and a method to design control experiments.

In the first part, I studied the problem of describing ultrafast (attosecond scale) time-resolved absorption and photoemission in finite systems with TDDFT. I demonstrated, that TDDFT can be successfully employed to describe the dynamics of electronic excited states in atoms and molecules. I illustrated this with three applications: the one-dimensional Helium model, the three-dimensional Helium atom and the Ethylene molecule. Using a one-dimensional Helium model, I showed how in the exact case, it is possible to recover information about state populations through a comparison of perturbed and unperturbed absorption cross-sections, and that the population evolution in time can be described in terms of Rabi physics. From the TDDFT calculations of the same system, one may conclude that the results obtained with the adiabatic EXX potential are in good agreement with the exact solution, although small artifacts appear

due to the incorrect description of the functional memory dependence.

Using the same functional, I investigated the Helium atom in a more realistic three-dimensional treatment, where I performed resonant pump-probe calculations monitoring both absorption and photoemission properties of the excited atom. TAS turned out to be a sensible tool to monitor the build-up of the excited state. TRPES also allowed the characterization of the excitation process in time. However, due to a dominant ionization channel associated with sequential two (pump) photon absorption, the information about the excited state population was less apparent. Nonetheless, the TRPES is rich in information; for example it can be angularly resolved in order to obtain the photoelectron angular distribution (PAD), which is sensitive to the geometrical arrangement of the ionized state, and is a useful tool to discern the nature of each photoelectron peak. Finally, I found that for the case of the Ethylene molecule, the PAD for ejected electrons was able to provide clear evidence of the occurrence of a  $\pi \rightarrow \pi^*$  transition and to study its time evolution.

In addition to numerical modeling a theoretical understanding of the described processes would be useful. Therefore, in the second part I took a detailed look at the origin and the control of spectral excited-state features in the non-overlapping regime using the example of Hydrogen. First I carefully analyzed general features of excited-state spectra. Using a general Lehmann representation of the response function, I analyzed the main differences between spectra obtained from (i) the ground state, (ii) stationary states and (iii) non-stationary states. I found that whilst in all cases the peak positions are fixed at the many-body transition frequencies, the heights of the transition peaks as well as their shape depend on the state, i.e. they depend on the expansion coefficients of the wave functions in the eigenbasis. If there are no continuum contributions, ground state and excited stationary state spectra have only Lorentzian-shaped peaks: positive ones in the ground state case, and both positive and negative ones in the excited state case. Furthermore, the peaks are time-independent. For the non-stationary states I found that their spectra can be divided into (i) stationary contributions, which are the stationary spectra from the respective states scaled by their population, and (ii) interference terms. The stationary contributions have Lorentzian shape and are time-independent, while the interference terms are responsible for the time-dependence of the spectrum. They oscillate with a frequency proportional to the energy-difference of the involved states and their shape oscillates between Lorentzian and Rayleigh type.

---

The time-dependence of the spectrum would be reflected in the color, perceived by the human eye when illuminating a macroscopic coherent sample with light. Its periodicity leads to a time-dependent periodic change of color. This “time-dependent color”, if shown in a chromaticity diagram, forms a closed trajectory. Nonetheless, one has to take into account, that in a realistic macroscopic sample, not all molecules are in the same state at the same time. Therefore, one has to take the time-average of the spectrum, which leads to a spectrum, that only contains stationary contributions. Also, the human eye is not able to capture such fast oscillations, and therefore the resulting impression would also reflect the time average.

In the third part, I used Quantum Optimal Control Theory to optimize excited state spectra. I took three different approaches, one based on analytical models, the other two based on TDDFT. The first one is a viable option for systems whose behaviour can be, after some assumptions, modeled with few-level models, therefore allowing to understand the optimization processes analytically. For these cases, given a certain dipole-coupling structure, one can use the theory of Rabi oscillations to describe the excitation of a system into a non-stationary state. I performed the necessary derivations for a three-level system, but it can easily be adapted to include more levels. For a three-level system, I showed how to use the Rabi-description to derive a laser-pulse, that excites an electron from its ground state into a non-stationary target state. I found that whilst the envelope of the control-laser is responsible for controlling the populations of the involved states, their relative phases are governed by the phase of the laser pulse. I showed, that this model is valid for the excitation of Hydrogen from its ground state into a linear combination of the  $|2p_z\rangle$  and the  $|3p_z\rangle$  state and was able to obtain an overlap of 96% with the target state, where the missing few per cent were due to the coupling to states outside of the three-level assumption. I concluded that the proposed model provides a good description of the control of Hydrogen.

I also analyzed the time-dependence of a non-stationary state spectrum in TDDFT, using the example of Helium, which was excited into a linear combination of ground state and first excited state. I found that, in this linear combination, the TDDFT oscillations in the spectrum were related to the many-body excitation energy as one would expect. Nonetheless, the oscillations were twice as fast as the predicted ones. Analyzing this behaviour in TDDFT is the goal for future work. In this context, investigating the existence of a Lehmann representation of the TDDFT response function of an excited state

(and if it exists, deriving it) would be helpful. I then presented two ways of combining Quantum-OCT with TDDFT to optimize excited state spectra. In the first approach, I used a gradient-free quantum optimal control algorithm to maximize the integral over the visible region of the excited-state absorption spectrum. The laser was expanded in a sinusoidal basis set and its expansion coefficients taken as control parameters while phases, duration and polarization were kept fixed. The choice for a gradient-free algorithm was motivated by the heavy computational demands found when attempting gradient-based ones; I also derived the Quantum Optimal Control equations that provide the gradient for this type of optimization, but concluded that the resulting scheme was not computationally viable.

The gradient-free algorithm was tested for a one-dimensional Hydrogen model, which was solved exactly, one-dimensional Helium, which was used to compare exact and TDDFT treatment and for singly-ionized Beryllium, which was only treated within the TDDFT framework. It was then used to assess the feasibility of optimizing a poly-atomic molecule using the examples of neutral and doubly-ionized Methane. I found that a search space consisting of frequencies of two standard laboratory lasers and their higher harmonics was appropriate for the exact models, since it included the excitation energy from the ground state into the first excited state in both cases and the algorithm was able to take advantage of this resonance to excite the system and create absorption peaks in the visible. In the case of Helium, even subsequent excitation into higher energy states took place, further improving the absorption in the target region.

In comparison, the TDDFT optimization of Helium did not lead to satisfying results due to different ground-state excitation energies of the exact model and the TDEXX treatment. While in the exact case the resonance between ground state and first excited state was included in the search space, that was not true for the TDEXX case, where a resonant excitation into the first excited state was not possible. This demonstrates the importance of an appropriate design of the search space. When I adapted the search space by replacing the exact excitation energy by its TDEXX equivalent, I found that an excitation was achieved, creating features in the visible, which were shifted with respect to the exact ones. The attempt to ascertain the reason for this shift was hampered however by one significant deficiency of TDDFT: it does not permit a real population analysis (as the true many-body wave functions are not accessible). Due to this fact, it was not possible to tell if the emerging peaks were due to subsequent excitations, or were



---

just the original peaks, but shifted due to the TDDFT functional approximation error.

The importance of resonances in the design of the search space also became clear in the case of singly-ionized Beryllium in TD-ALDA treatment. Here, the optimization algorithm clearly enhanced the amplitude of the laser frequency belonging to the resonant excitation of the first excited state from the ground state. This leads to the creation of a peak in the optimization region, although of unknown origin. This example demonstrates that the ground state spectrum can only give us a few possible excited-state excitation peaks. Not all excited-state transitions that one can calculate based on the ground state spectrum will be allowed and not all allowed excited-state transitions are deducible from the ground state spectrum.

I then moved on to Methane and doubly-ionized Methane. Since the optimization of Methane with the previously chosen search space failed, for doubly-ionized Methane I designed two search spaces based on its resonances. The first search space was based on subsequent excitation, the second one on a combination of excitation and stimulated relaxation. I found that both search spaces included pump pulses that lead to absorption in the visible. Furthermore I found that an analysis of the involved excitations can yield some insight into the dynamics of excitation. A cleaning of the pulse in terms of its frequency components can help to learn more about the involved dynamics, but exactly identifying the mechanisms is cumbersome. Perhaps the main computational challenge of the technique used for these optimizations was the necessity of a large simulation box in real space. The high intensity fields, in combination with the choice of the target, favours the excitation of “box states” (i.e. excitations that appear due to the existence of a finite simulation box), leading to a large, but unfortunately unphysical absorption in the optimization region. The partial solution to this problem was found to be the introduction of absorbing boundaries, and the inclusion to an exponential penalty factor for ionization in the definition of the target. I conclude that while the optimization scheme in principle works, it nevertheless requires vast computational resources due to its necessity of multiple time propagations. An intelligent design of the search space can cut down on the resources needed, but is hard to do in practice since the ground state spectrum does not provide any information on whether inter-excited-state transitions are allowed or not.

The second approach developed cuts down on computational resources within the optimization by splitting the optimization into two steps. In the first step, a KS excited state

with desirable features is identified. For neutral Methane, for example, three interesting KS excited states could be identified. In the second step, a laser is found, that excites the system from the ground state into this KS excited state. To achieve this goal, efficient quantum optimal control algorithms could be used. Finding these pulses should be done in the near future based on the finding of the present PhD thesis.

The theoretical and computational framework developed here is a useful tool to understand and to control non-equilibrium electronic dynamical processes.

First, we created a toolbox for simulating pump-probe experiments with the help of first principle real-time real-space time-dependent density functional theory by implementing TRPES and TAS into the `octopus` code. Creating these kind of toolboxes enables us to simulate experiments on the computer. New emergent properties of matter in the strong-coupling regime could appear that might give rise to new technological developments. Furthermore, monitoring electron and ion-dynamics provides fundamental insights into structure (i.e. time-resolved crystallography) and chemical processes in biology and materials science (e.g. for energy applications). There is plenty of room for new and fascinating discoveries about the behavior of matter under out-of-equilibrium conditions.

But being able to simulate does not necessarily mean understanding if the tools to interpret the findings are missing. A microscopical understanding of the underlying processes is therefore required – or at least useful. Thus, I analysed the general properties of non-equilibrium excited-state spectra using a modified Lehmann representation, where I analysed positions and shapes of the spectral peaks. This analysis in addition to providing understanding of the structure of excited-state spectra, also helps to understand the possibilities and restrictions to the control possible, for example the fact, that in the non-overlapping regime, the positions of the resonances are an inherent property of the system and therefore controllable only through the weights of the peaks. Having a detailed understanding of the time-dependence of excited-state spectra can also be used to investigate properties of excited-state spectra in a TDDFT description and help to identify shortcomings of current adiabatic exchange and correlation functionals, e.g. could we show, that in the current implementation, excited state spectra exhibit incorrect shapes and an incorrect time-dependence. Further work in this direction is required and could be combined with the search for a KS excited state response function (or solving the question about its existence). Both the implemented pump-probe toolbox as well as

---

the analysis of the excited state spectral properties were then combined with Quantum-OCT (analytical and numerical) to control and modify excited-state spectra of atoms and molecules for a given purpose. I illustrated the concept with optimizing a system to absorb as much light as possible in a given range of the spectrum, e.g. in the visible, turning a previously transparent sample opaque.

Whilst I could show, that the developed optimization algorithm in principle works and that TDDFT is a suitable candidate to describe out-of-equilibrium spectroscopy experiments and solve the related control-questions, I could also identify fundamental caveats that need to be addressed in the future. From the computational perspective, it became obvious that the computational requirements are too big to tackle large molecules and systems. Therefore, schemes to reduce the model complexity and smarter system representations are needed. Much work has already been done to improve the speed of TRPES calculations using massive parallelization strategies, but a similar development for TAS (and consequently for the control of absorption properties) is still missing. More importantly, from the fundamental point of view, TDDFT is still in clear need of more precise non-adiabatic exchange and correlation functionals, capable of providing a reliable description of non-equilibrium processes and strong light-matter interaction. Clearly, the methods presented here will automatically benefit from any theoretical advance in this direction. This is particularly apparent in the part of the thesis about control, where a correct description of resonant excitation is necessary. On the other hand, performing Quantum-OCT on the resonant excitation of states could provide deeper insight into the failures of current functionals. Finding pulses, that do achieve a sufficient excitation by “tracking” the TDDFT resonances could give insights into the time-dependence of the TDDFT energy levels. Conversely, the developers of new functionals may take into account the correct description of pump-probe experiments as a useful quality test.



## A. The Downhill-Simplex Algorithm

The downhill-simplex algorithm, also known as Nelder-Mead or amoeba algorithm is a gradient-free optimization method proposed by John Nelder and Roger Mead in 1965 [222]. It is based on a simplex, the simplest volume in a N-dimensional parameter space, which is spanned by N+1 points. Examples include a line-segment in one dimension, a triangle on a plane, a tetrahedron in a three-dimensional space and so on. Given a continuous function  $y = f(x_1, \dots, x_N)$ , the goal is to find the minimum  $y^m$  and its corresponding position  $\mathbf{x}^m$  using **reflection**, **contraction**, **compression** and **expansion**. One starts the algorithm by choosing N+1 starting points  $\mathbf{x}^1, \mathbf{x}^2, \dots, \mathbf{x}^{N+1}$ . Then one follows the following scheme (The different operations are illustrated in Figure A.1):

I **Ordering**: Evaluate  $f(\mathbf{x}^i)$  and order them according to the values of their vertices

$$f(\mathbf{x}^1) \leq f(\mathbf{x}^2) \leq \dots \leq f(\mathbf{x}^{n+1}) \quad (\text{A.1})$$

II **Reflection**: Calculate the mirror center

$$\mathbf{x}^s = \frac{1}{N} \sum_{i \neq \max} \mathbf{x}^i \quad (\text{A.2})$$

from all points but the worst  $\mathbf{x}^{\max}$ . Reflect  $\mathbf{x}^{\max}$  at the mirror center using the reflection coefficient  $\alpha$

$$\mathbf{x}^r = \mathbf{x}^s - \alpha(\mathbf{x}^{\max} - \mathbf{x}^s) \quad (\text{A.3})$$

If  $f(\mathbf{x}^1) \leq f(\mathbf{x}^r) \leq f(\mathbf{x}^n)$ , i.e. the reflected point is better than the second worst, but not better than the best, replace the worst point  $\mathbf{x}^{n+1}$  by the reflected point  $\mathbf{x}^r$  and go back to step 1.

If  $f(\mathbf{x}^r) \leq f(\mathbf{x}^1)$ , i.e.  $\mathbf{x}^r$  is the best point so far, go to step 2. If the reflected point is not better than the second worst, contract (go to step 4).

III **Expansion**: If the  $\mathbf{x}_r$  is the new minimum, one expects to find interesting points

in this direction, therefore one makes a bigger step in the reflection direction, using the expansion coefficient  $\gamma$ :

$$\mathbf{x}^e = \mathbf{x}^s - \gamma(\mathbf{x}^{n+1} - \mathbf{x}^s). \quad (\text{A.4})$$

Replace the worst point  $\mathbf{x}^{n+1}$  by whichever is better,  $\mathbf{x}^e$  or  $\mathbf{x}^r$  and go back to step 1.

- IV **Contraction:** If the reflected point is not better than the second worst, one expects to be able to find a better value inside the simplex. Therefore compute the contracted point  $\mathbf{x}^c$  using the contraction/compression coefficient

$$\mathbf{x}^c = \mathbf{x}^s + \beta(\mathbf{x}^{n+1} - \mathbf{x}^s) \quad (\text{A.5})$$

If  $f(\mathbf{x}^c) \leq f(\mathbf{x}^{n+1})$ , i.e. the contracted point is better than the worst point, replace the worst point by  $\mathbf{x}^c$  and go back to step 1. Otherwise continue at step 5.

- V **Reduction:** For all but the best point  $\mathbf{x}^1$ , replace the point by its reduced version

$$\mathbf{x}^i = \mathbf{x}^1 + \beta(\mathbf{x}^i - \mathbf{x}^1). \quad (\text{A.6})$$

Go back to step 1.

The reduction handles the case, that contracting away from the largest point increases  $f$ . Since this should not happen close to a non-singular minimum, one contracts towards the lowest point, hoping to find a simpler landscape.

Usually the parameters are chosen as  $\alpha = 1$ ,  $\beta = 1/2$  and  $\gamma = 2$ , which are the parameters suggested by Nelder and Mead and which they showed gave the best results for a set of test cases [222].

**Local Minima:** As with many optimization algorithms, there is the danger of converging into a local minimum. There are several approaches to dealing with this problem, all of them centered around stopping the algorithm at some point and at this point, starting from the best value  $\mathbf{x}^1$  at this point, construct a new initial simplex and restart the algorithm. When to stop the algorithm (if after a fixed set of steps or randomly) and how to create the new initial simplex varies between the approaches.

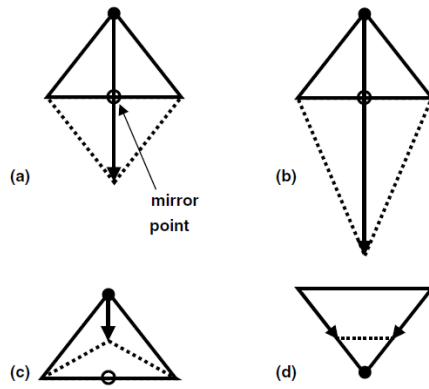


Figure A.1.: The four methods used in the Downhill-Simplex algorithm. (a) Reflection, (b) expansion, (c) contraction, and (d) compression. Taken from [4].





## B. The Optimization Procedure - Scheme 1

The implementation of the optimization algorithm was done in Python, using the scientific libraries `scipy` and `numpy`. The reason to use python, is that it is easy to program and that there is a huge variety of predefined libraries, that can easily be included.

The ones needed are `numpy`, `scipy`, `subprocess`, `os`, `shutil`, `linecache`, `pickle` (and `amoeba` or `fmin` from the `scipy` library (see B.4).

As pointed out in Section 2.6.3 and Section 5.1, the algorithm optimizes one of the two target functionals

$$\varepsilon_{\tau}^A[\mathcal{E}] = \int_{E_{min}}^{E_{max}} \bar{\sigma}_{\tau}[\mathcal{E}](E) dE, \quad (\text{B.1a})$$

$$\varepsilon_{\tau}^B[\mathcal{E}] = \int_{E_{min}}^{E_{max}} \bar{\sigma}_{\tau}[\mathcal{E}](E) \exp\left(-\gamma \frac{N_0 - N_{T_{\mathcal{P}}}[\mathcal{E}]}{N_0}\right) dE, \quad (\text{B.1b})$$

where  $\bar{\sigma}_{\tau}[\mathcal{E}](E)$  is the average absorption coefficient of the system at a given time delay  $\tau$  after the pump pulse  $\mathcal{E}(t)$  and  $E_{min}$  and  $E_{max}$  define the optimization region – the energy range, where the absorption is optimized.  $N_0$  and  $N_{T_{\mathcal{P}}}$  are the number of electrons in the system at the beginning and the end of the pump pulse, so that the term  $\exp\left(-\gamma \frac{N_0 - N_{T_{\mathcal{P}}}[\mathcal{E}]}{N_0}\right)$  inflicts a punishment of strength  $\gamma$  on the system due to ionization.

The control pulse is defined in a parametrized representation, the optimization parameters are the expansion coefficients of the laser in the sine basis.

$$\mathcal{E}_m(t) = \sum_i c_i^m \sin(\omega_i t) \Theta(t) \Theta(T_{\mathcal{P}} - t) \quad (\text{B.2})$$

Pump duration  $T_{\mathcal{P}}$  and polarization (depending on the symmetry of the system) are fixed, as well as the delay  $\tau$  between the end of the pump and the probe pulse. We

exclusively work in the non-overlapping regime, where the system is probed after the end of the pump pulse (i.e.  $\tau \geq 0$ ).

Each optimization iteration consists of two steps. In the first step, the system is evolved under the influence of the pump pulse  $\mathcal{E}_m(t)$  for the time  $T_P$ . In the second step, the absorption after a given delay time  $\tau$  is calculated by obtaining the absorption spectrum from a time-evolution as described in Section 2.4.5: The system is probed with a delta perturbation at the time  $T_P + \tau$  and the system is evolved for the “spectrum time”  $T_S$  afterwards. Finally,  $\varepsilon_\tau[\mathcal{E}_m]$  is calculated from the average absorption coefficient  $\bar{\sigma}(\omega, \tau)$  (2.54).

At the end of the optimization, the average polarization under the influence of the optimal pump laser is converged with respect to the box size and the system is propagated for a longer time  $T_S$  to obtain a more detailed spectrum.

The main part of the program is the definition of two classes - the octopus and the optimization class and a few functions. The octopus class includes everything, that has to do with `octopus` and is different for each system, the optimization class defines everything else and is the same for all optimizations, it basically constitutes the wrapper around everything.

## B.1. The Octopus Class

The octopus class has the attributes shown in Table B.1, a constructor, a routine to write input files, several run routings (`run`, `run_gs`, `run_laser`, `run_response`) and finally a routine to calculate the spectrum. Each of the run routines consists in linking or copying the necessary files (see Section B.5), creating the necessary input files and running the main run routine, which runs the specified executable on the specified number of nodes. The `calculate_spectrum` routine runs the octopus utility to obtain the cross section vectors for each of the kick directions and calculates the average absorption from them.

## B.2. The Optimization Class

The optimization class has the attributes shown in Table B.2, a constructor, and a call routine, which takes as input a set of laser coefficients – the optimization parameters

parallel	Path of the octopus executable (parallel)
runmode	Serial or parallel executable
spectrum	Path of the oct-propagation_spectrum executable
ncore	Number of cores to use for parallel calculations
np	Number of nodes to use for parallel calculations
lasertime	$T_{\mathcal{P}}$
spectime	$T_{\mathcal{S}}$
dt	time step
laserfrequencies	frequencies of laser
machine	cluster, where it is running
dim	number of dimensions

Table B.1.: Attributes of the octopus clase.

octopus	an instance of the octopus class mentioned above
$E_{min}$	lower boundary of the optimization window
$E_{max}$	upper boundary of the optimization window
nelectrons	number of electrons in the system $N_0$
gamma	punishment $\gamma$
iter	number of iteration, where the run started from (for restarting purposes)

Table B.2.: Attributes of the optimization clase.

at that iteration. The call routine takes the laser coefficients, sets the right links and then runs one after the other the run routine of the octopus class: laser propagation (`run_laser`), the necessary  $(n+1)$  time evolutions after the kick, the octopus tool, that obtains the cross section vectors and a function combining the cross section vectors to obtain the average absorption coefficient (all together combined in the `run_response` routine). Finally, it uses another function `get_epsilon` to obtain  $\varepsilon$  (either A or B), which it returns to the main program.

### B.3. The Main Program

The main program knits everything together in the following order

- I reads laser frequencies from *laserfrequencies.dat*, which contains a list of all the laser frequencies included in the search space
- II reads octopus class attributes (see Table B.1) from *optimizationparameters.dat*
- III initializes octopus class
- IV reads iteration file: does it restart (if so from which iteration) or start from scratch
- V if it starts from scratch: reads the initial coefficients file (containing a list of all the initial coefficients in the same order like the laser frequencies) and feeds them into the minimization algorithm (`fmin` or `amoeba`). Otherwise: restarts
- VI waits for convergence

### B.4. Implementation of the Simplex-Downhill - Amoeba or `fmin`

The easiest way to implement the minimization is by taking the `fmin` routine as it is included in the `scipy` package. A disadvantage of this solution is, that the `fmin` routine does not seem to include a restart option. Therefore, I took an implementation of the Simplex-Downhill algorithm, that is provided in the GPAW package (<https://wiki.fysik.dtu.dk/gpaw>) and adapted it using the `pickle` package to enable restarting. The implementation of a restart option was necessary for the bigger systems, since they were calculated on clusters, where the maximal run time was limited.

## B.5. General Comments on the Implementation

Performing time evolutions is computationally expensive. Several things have to be taken into account: The computational time scales linearly in the simulation time. If one wants to optimize resources, one can calculate the time evolution under influence of the laser, stop and save the result and then fork the calculation into the  $(n+1)$  calculations needed for the response. Nonetheless, one has to restrict the time  $T_{\mathcal{P}}$  of the laser influence. Even more important is the time needed for the response, since this calculation has to be done  $(n+1)$  times. But here, one can at least take advantage of the fact, that these  $(n+1)$  calculations are independent of each other and are therefore perfectly suitable for parallelization.

Memory and computational time scale to the power of three in the radius of the box. This can be partially compensated by using the code in parallel. Nevertheless, a price for the communication has to be paid. For an overview about the scaling of the `octopus` code see Ref. [103].

Depending on the network communication of the cluster, writing data can take considerable amounts of time. To save on this time, (i) output and restart files should only be written at the end of each run and (ii) a multipoles-dummy file can be used, which has the correct header (kick strength, kick time, etc). Instead of writing the multipoles file, during the pump time  $T_{\mathcal{P}}$ , one can use this file as a dummy, which is then copied into the folders, where the response calculations are performed. This can be done, because the time-evolution of the dipole moment during the pump pulse has no influence on the response.

When using the Downhill-Simplex algorithm, the simplex has to be generated at the beginning, i.e. if one has  $m$  laser frequencies,  $m$  initial evaluations have to be performed. This has to be taken into account, if the time available is limited and no proper restart options are available (e.g. because one uses the `fmin` algorithm, which does not provide a restart option).



## C. Many-Body Tunneling in Exact and Density Functional Theory

### C.1. Introduction

In this thesis we have seen some examples of failures of current state-of-the-art approximations to the exchange and correlation energy or potential functional. These failures prompted us to study these limitations from a different perspective, namely from the point of view of the correct description of tunneling. Since this study departs from the main research line of the thesis, we describe it in this separate appendix.

Here, we analyze tunneling in many-particle systems (two, three and four electrons), first exactly, and then using DFT. The goal is to study how interacting electrons tunnel through a barrier from a donor to an acceptor. First, we will look at exactly solvable model Hamiltonians. We will analyze how the resonance conditions for tunneling differ in a fully-interacting system from a system in which the electrons on the donor and the acceptor do not interact among them. To this goal, we compare the exact tunneling points to the ones obtained by simply aligning the ionization potential of the donor with the electron affinity of the acceptor. We then develop a scheme to correct the resonances predicted by this simple alignment to get the exact resonances, by making use only of the densities of the subsystems. This scheme is developed for two electrons and extended to three and four electrons.

We then approach the problem with DFT. We first show that DFT, using the LDA functional, is not able to predict the tunneling behaviour in an interacting two-electron system, and neither is LDA-SIC or spin-polarized LDA. Only the spin-polarized LDA-SIC is able to predict the correct density, but unfortunately the spin-resolved density is not correct. We also compare the exact KS-potential (which is obtained from inverting the exact solution) to the different potentials in LDA, LDA-SIC etc. Finally, the procedure is

analyzed in terms of the KS eigenenergies: these must fulfill some conditions to correctly describe tunneling.

Section C.2 presents the model systems to be studied; Sections C.3 and C.4 present the exact and DFT calculations, respectively.

## C.2. A Simple Donor-Acceptor Many-Body Model

Tunneling is often treated in the framework of non-interacting particles. The goal of this appendix is to analyze the influence of the interaction and to predict the necessary conditions for interacting electrons to tunnel through a barrier from a donor to an acceptor. To this end, we solve the many-body Schrödinger equation for a system of  $N$  electrons in one dimension. We compare calculations for a fully interacting system with those of a system in which the interaction between electrons at the donor with electrons at the acceptor is switched off. The corresponding Hamiltonians read

$$\hat{H}^{(1,2)} = \hat{T} + \hat{V}_{ext} + \hat{V}_{ee}^{(1,2)}, \quad (\text{C.1})$$

where,  $\hat{T} = \sum_{j=1}^N -\partial^2/\partial x_j^2$  denotes the one-dimensional kinetic energy and

$$\hat{V}_{ext} = \sum_{j=1}^N V_{ext}(x_j) \quad (\text{C.2})$$

is the external potential. This external potential is shown in Fig C.1. It describes a system of donor (D) and acceptor (A), separated by a barrier (B). The potential  $V_A$  of the acceptor is fixed to zero, while the potential  $V_D$  of the donor can be varied. This system mimics a tunneling setup, where the potential of the donor can be varied by applying a gate voltage.  $V_B$  is the barrier height, for which we use two different values in the calculations: case (I) (high-barrier case), for well separated subsystems, and case (II) (low-barrier case), where the subsystems coupling is stronger. In both cases, since we want to focus on tunneling from one bound system to another, the vacuum potential  $V_V$  is large in comparison to all other potentials, and is for computational purposes set to infinity.

The Hamiltonians  $\hat{H}^{(1)}$  and  $\hat{H}^{(2)}$  differ in the form of the electron-electron interaction,  $\hat{V}_{ee}^{(1)}$  or  $\hat{V}_{ee}^{(2)}$ . We will label the corresponding wave-functions, densities, etc, with (1) or



(2) only whenever necessary.

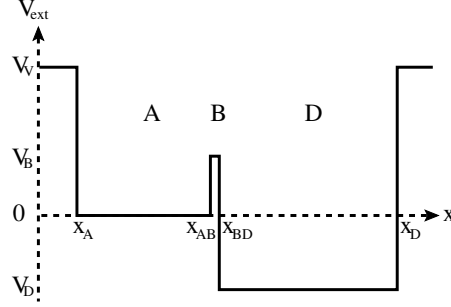


Figure C.1.: The external potential  $V_{ext}(x)$  is a double well potential surrounded by vacuum of the energy  $V_V$ . The right well is located between  $x_{BD}$  and  $x_D$  and serves as donor (D). Its potential is  $V_D$  and can be varied. The left well is located between  $x_A$  and  $x_{AB}$  and serves as electron acceptor (A). Its potential is fixed to zero for all calculations. Donor and acceptor are separated by a barrier of variable height  $V_B$ , which is fixed to two different heights.

The precise definition of the electron-electron interaction potentials is as follows:

$$\hat{V}_{ee}^{(1)} = \sum_{j,k,j < k} \frac{1}{\sqrt{(x_j - x_k)^2 + 1}} \quad (\text{C.3})$$

describes a softened Coulomb interaction and

$$\hat{V}_{ee}^{(2)} = \sum_{j,k,j < k} \left( \frac{\theta(x_j - x_{BD})\theta(x_k - x_{BD})}{\sqrt{(x_j - x_k)^2 + 1}} + \frac{\theta(-x_j + x_{AB})\theta(-x_k + x_{AB})}{\sqrt{(x_j - x_k)^2 + 1}} \right),$$

a truncated softened Coulomb interaction, where electrons, that are localized in different subsystems do not interact with each other. Therefore,

$$\Delta \hat{V}_{ee} = \hat{V}_{ee}^{(1)} - \hat{V}_{ee}^{(2)} \quad (\text{C.4})$$

describes the intersystem interaction between electrons on the donor with electrons on the acceptor. The Schrödinger equation can be solved exactly either as the Hamiltonian of one electron in  $N$  dimensions in the external potential  $\hat{V}_{ext} + \hat{V}_{ee}$  [210] or in second quantization with the help of a Jordan-Wigner transformation. The contributions to the

Hamiltonian (C.1) in second quantization read

$$\begin{aligned}\hat{T} = & -\frac{1}{2\Delta x^2} \sum_{l,\sigma} (\hat{c}_{l,\sigma}^\dagger \hat{c}_{l+1,\sigma} + \hat{c}_{l+1,\sigma}^\dagger \hat{c}_{l,\sigma}) \\ & + \frac{1}{\Delta x^2} \sum_{l,\sigma} \hat{n}_{l,\sigma},\end{aligned}\tag{C.5a}$$

$$\hat{V}_{ee}^{(1)} = \sum_{l,m,\sigma,\sigma'} \frac{\hat{c}_{l,\sigma}^\dagger \hat{c}_{m,\sigma'}^\dagger \hat{c}_{m,\sigma'} \hat{c}_{l,\sigma}}{2\sqrt{(l\Delta x - m\Delta x)^2 + 1}},\tag{C.5b}$$

$$\hat{V}_{ext} = \sum_{l,\sigma} V_{ext}(l) \hat{n}_{l,\sigma},\tag{C.5c}$$

where we use a second-order finite-difference scheme for the kinetic energy. In all cases  $\Delta x$  denotes the spacing between the sites.

To study the conditions for electrons to tunnel from donor to acceptor through a barrier, we have to define a tunneling measure. The most natural object to look at is the transferred charge; one possibility to measure it is to simply integrate the number of electrons  $N_A$  on the acceptor

$$N_A = \sum_{\sigma_i} \int_{x_A}^{x_{AB}} dx_1 \dots dx_N |\Psi(x_1\sigma_1, x_2\sigma_2, \dots, x_N\sigma_N)|^2\tag{C.6}$$

as a function of the donor potential  $V_D$ , where  $\Psi(x_1\sigma_1, x_2\sigma_2, \dots, x_N\sigma_N)$  is the ground-state wave-function.

### C.3. Exact calculations

We perform exact many-body ground-state calculations for  $N = 2, 3$  and 4 electrons. The calculations for 2 electrons are done using the real-space finite-difference code octopus [101, 102, 103], whereas for 3 and 4 electrons we treated the system in a basis constructed in second quantization. Since the computational effort for calculations with  $N$  electrons on  $N_S$  points in space grows as  $(2N_S)^N$ , we can obtain a better spatial resolution for 2 electrons, while for more than 2 electrons we restricted our calculations to a 6 points lattice.

For the two-electron calculations, the complete system has a length of  $L = 36$  a.u. and

is divided into an acceptor region (A) of width  $d_A = 15$  a.u., a donor region (D) of width  $d_D = 20$  a.u., and finally a barrier of width  $d_B = 1$  a.u.. The grid spacing is  $\Delta x = 0.2$  a.u. for all calculations. In the high-barrier case (I) the barrier height is  $V_B = 100$  a.u., whereas in the low-barrier case (II) the barrier height is  $V_B = 0.3$  a.u..

For three and four electrons, the complete system has a length of  $L = 2.4$  a.u., which we represent as a six-point lattice. To be as close as possible to the two-electron calculations, we choose an asymmetric setup, where 3 of the 6 points belong to the donor ( $L_D = 1.2$  a.u.), 2 points belong to the acceptor ( $L_A = 0.8$  a.u.) and the barrier is located on a single point ( $L_B = 0.4$  a.u.). The grid spacing is  $\Delta x = 0.4$  a.u.. Since a stronger confinement of the electrons implies higher energies, we also adapted the barrier height  $V_B$ : In the high-barrier case (I) the barrier potential is  $V_B = 2000$  a.u. and in the low-barrier case (II) it is  $V_B = 100$  a.u.

For each barrier height  $V_B$  we vary the donor potential  $V_D$  while keeping the acceptor potential  $V_A$  fixed to zero. We scan 1000 different donor potentials  $V_D$ , starting from a potential for which all electrons are located on the donor and ending at a potential for which all electrons are located on the acceptor. For two electrons we choose  $-0.3$  a.u.  $< V_D < 0.3$  a.u., while we choose  $-6.0$  a.u.  $< V_D < 11.0$  a.u. for three and four electrons. For each setup we calculate the exact  $N$ -electron ground-state wave function  $\Psi(x_1\sigma_1, \dots, x_N\sigma_N)$ , for both model electron-electron interactions  $\hat{V}_{ee}^{(1,2)}$ , and extract the number of electrons on the acceptor  $N_A^{(1,2)}$  according to Eq. (C.6).

Panel a) of Fig. C.2 shows the number of electrons on the acceptor  $N_A$  as a function of  $V_D$  for a system with two electrons for both electronic interactions  $\hat{V}_{ee}^{(1,2)}$  for the high-barrier case (I). For small donor potentials  $V_D$ , both electrons are localized on the donor. If we increase  $V_D$ , first one electron, and then the other one tunnels to the acceptor. This increases  $N_A$  from zero to one, and then to two. Panel c) describes the same situation for the low-barrier case (II). The behaviour differs clearly in the abruptness of the tunneling: in case (I) the increase of electrons on the acceptor follows an almost perfect step function, leading to an integer number of electrons in each subsystem for any given gate voltage  $V_D$ . In contrast, in case (II), the increase is broadened, leading to fractional charges on donor and acceptor for a small window of donor potentials. As Fig. C.2 shows, the transfer of charge takes place at particular gate voltages, which define the tunneling points. While in the high-barrier case (I), the tunneling points are clearly defined due to the mentioned sudden transfer of electrons, for lower barriers one must

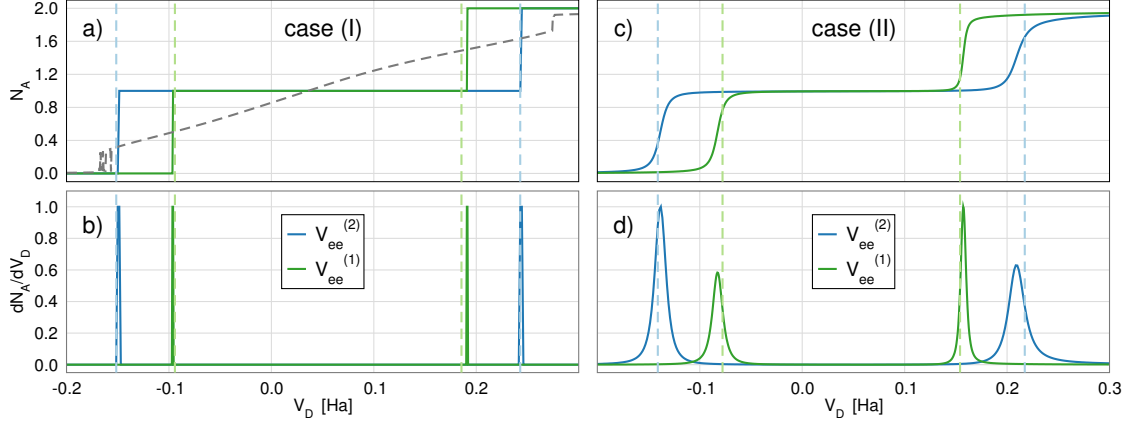


Figure C.2.: (Top) The number of electrons on the acceptor  $N_A$  as a function of the donor potential  $V_D$  for the case of  $N = 2$  for the truncated electron-electron interaction  $\hat{V}_{ee}^{(2)}$  (C.4), and for the full electron-electron interaction  $\hat{V}_{ee}^{(1)}$  (C.3). Panels a) and b) display to the high-barrier case, and c) and d) display the low-barrier case. For comparison a) shows in grey the result as obtained by DFT calculations using the LDA functional. (Bottom) The derivatives of the number of electrons on the acceptor with respect to the donor potential  $dN_A/dV_D$  normalized to its maximum. The tunneling points are identified by the local maxima of  $dN_A/dV_D$ . The vertical lines show the predicted tunneling points, in blue for the IP-EA prediction (C.11), and in green for the predictions corrected with the Hartree interaction  $C_H$  (C.18).

define a tunneling point as a local maximum of the first derivative of the charge on the acceptor  $N_A$  with respect to the donor potential  $V_D$ :

$$TP = \max_{\text{local}} \frac{dN_A}{dV_D}. \quad (\text{C.7})$$

For better visualization, we normalize this derivative to its global maximum in the lower panels of Fig. C.2. Note, that different peak heights result from different peak widths due to the broadening plus the fact, that exactly one electron tunnels at each tunneling point, i.e.  $\int_{TP} dV_D dN_A/dV_D = 1$ . The derivative as a function of the donor potential is shown in panel b) for the high-barrier case (I) and in panel d) for the low-barrier case (II), i.e. they are shown directly below the respective densities. Results for both electronic interactions  $V_{ee}^{(1,2)}$  are shown together. One sees, that the tunneling points for the full interaction  $\hat{V}_{ee}^{(1)}$  are shifted towards zero with respect to the truncated interaction  $\hat{V}_{ee}^{(2)}$ .

In general, a system of  $N$  electrons exhibits  $N$  tunneling points. In the following we will show how these tunneling points can be predicted performing calculations on the isolated subsystems, both for the truncated interaction  $\hat{V}_{ee}^{(2)}$ , and more importantly for the full electron-electron interaction  $\hat{V}_{ee}^{(1)}$ .

### C.3.1. Tunneling Points From Ionization Potential and Electron Affinity

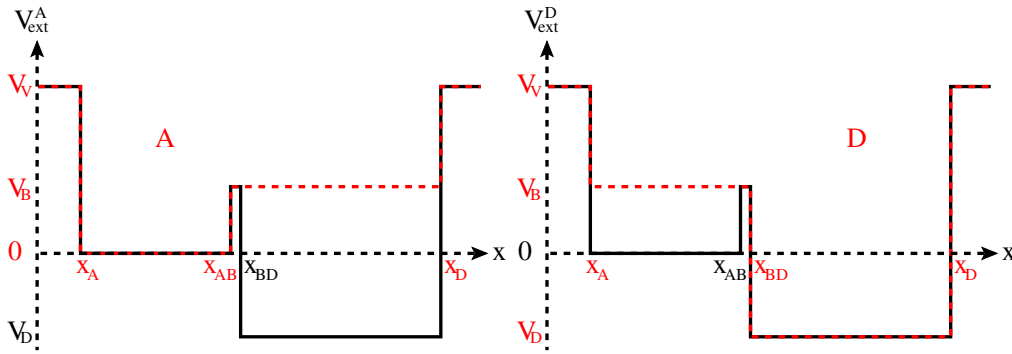


Figure C.3.: The external potentials of the isolated subsystems (dashed red). These were used to calculate the ionization potentials, the electron affinities and the wave functions of the isolated subsystems. On the left we show the potential  $V_{ext}^A(x)$  of the isolated acceptor, on right side we display the potential  $V_{ext}^D(x)$  of the isolated donor. For comparison  $V_{ext}(x)$  of the combined system is shown underlying in black.

By just looking at the isolated acceptor and donor system, one may expect tunneling to occur when the ionization potential of the donor and the electron affinity of the acceptor align. In fact, for non-interacting electrons the tunneling points coincide with the alignment of the one-particle energy levels. In order to define the energy levels for the subsystems, we split the complete system into two isolated subsystems, whose external potentials are given in Fig. C.3.

The ionization potential  $IP$  and the electron affinity  $EA$  of a general system with  $N$  electrons read

$$IP(N) = E(N) - E(N - 1), \quad (C.8a)$$

$$EA(N) = E(N + 1) - E(N). \quad (C.8b)$$

## APPENDIX C. MANY-BODY TUNNELING IN EXACT AND DENSITY FUNCTIONAL THEORY

---

Changing the donor potential  $V_D$  has only a small effect on the wave function, unless we cross a tunneling point. We, therefore, approximate the energy on the donor by

$$E_D(N, V_D) \approx E_D^0(N) + NV_D. \quad (\text{C.9})$$

with  $E_D^0(N)$  being the energy on the donor at  $V_D = 0$ , i.e. we neglect the change in the wave function. For the case of an infinitely high barrier Eq. (C.9) is exact. Since the potential of the acceptor is fixed to zero for all calculations, i.e.  $E_A = E_A^{(0)}$ , we can now align the ionization potential of the donor,  $IP_D$ , and the electron affinity of the acceptor,  $EA_A$ , by adjusting  $V_D$  and changing the total energy of the  $N$  electrons on the donor by  $N \times V_D$ . For a system with  $N$  electrons in total, being divided into  $M$  on the acceptor and  $N - M$  on the donor, aligning  $IP_D$  and  $EA_A$  leads to the condition

$$\text{TP}_M : IP_D(N - M) \stackrel{!}{=} EA_A(M) \quad (\text{C.10})$$

for the  $M$ -th tunneling point, which leads to the following alignment condition for the donor potential  $V_D$

$$\begin{aligned} V_D(\text{TP}_M) \stackrel{!}{=} & E_A^0(M + 1) + E_D^0(N - M - 1) \\ & - [E_A^0(M) + E_D^0(N - M)]. \end{aligned} \quad (\text{C.11})$$

This allows us to estimate the tunneling points of the combined system from the knowledge of properties of the isolated subsystems. In the following we refer to this as the IP-EA approach. Note, that the interwell interaction  $\Delta\hat{V}_{ee}$  does not affect the energies  $E_A(N)$  and  $E_D^0(N)$ .

For  $N = 2$  electrons, we find two tunneling points, which in this IP-EA approach are predicted by

$$V_D(\text{TP}_0) \stackrel{!}{=} E_A^0(1) + E_D^0(1) - E_D^0(2), \quad (\text{C.12a})$$

$$V_D(\text{TP}_1) \stackrel{!}{=} E_A^0(2) - E_A^0(1) - E_D^0(1). \quad (\text{C.12b})$$

$V_D(\text{TP}_0)$  and  $V_D(\text{TP}_1)$  for two electrons are shown in Fig. C.2 as dashed blue lines. They almost exactly reproduce the tunneling points of the Hamiltonian  $\hat{H}^{(2)}$ , where electrons from different subsystems do not interact. One can now start from this IP-EA approach, and find the necessary corrections to predict the tunneling points for the full Hamiltonian

$\hat{H}^{(1)}$ .

### C.3.2. Energy Corrections

In the following we present a scheme to include the electron interaction  $\Delta\hat{V}_{ee}$  between donor and acceptor in order to compute the  $TP^{(1)}$  of the fully interacting Hamiltonian. The interaction between  $M$  electrons on the acceptor with  $N - M$  electrons on the donor can be calculated by constructing an approximate many-body ground-state wave-function  $\Psi(x_1\sigma_1, \dots, x_N\sigma_N; V_D)$  of the fully interacting Hamiltonian  $\hat{H}^{(1)}$  for the respective donor potential  $V_D$ , as an antisymmetric product wave function from the  $(N - M)$ -electron wave function of the donor and the  $M$ -electron wave function of the acceptor. The so-constructed  $\Psi(x_1\sigma_1, \dots, x_N\sigma_N; V_D)$  approximates the ground-state wave-function of  $\hat{H}^{(1)}$  in the range of  $V_D(TP_{M-1}) < V_D < V_D(TP_M)$ , which is the range of  $V_D$ , where  $M$  electrons are localized on the acceptor and  $N - M$  are localized on the donor. Having approximated the wave function of the fully-interacting system, we can calculate the expectation value of the electronic intersystem interaction

$$V(M, N - M) = \langle \Psi(x_1\sigma_1, \dots, x_N\sigma_N; V_D) | \Delta\hat{V}_{ee} | \Psi(x_1\sigma_1, \dots, x_N\sigma_N; V_D) \rangle, \quad (\text{C.13})$$

and use it to correct the prediction of the tunneling points for the fully interacting Hamiltonian, which yields

$$\begin{aligned} V_D(TP_M) &\stackrel{!}{=} E_A^0(M + 1) + E_D^0(N - M - 1) \\ &\quad + V(M + 1, N - M - 1) \\ &\quad - [E_A^0(M) + E_D^0(N - M) + V(M, N - M)]. \end{aligned} \quad (\text{C.14})$$

For our two-electron case, this results in

$$V_D(TP_0) \stackrel{!}{=} E_A^0(1) + E_D^0(1) - E_D^0(2) + V(1, 1), \quad (\text{C.15a})$$

$$V_D(TP_1) \stackrel{!}{=} E_A^0(2) - E_A^0(1) - E_D^0(1) - V(1, 1). \quad (\text{C.15b})$$

Note, that  $\Delta\hat{V}_{ee}$  can be seen as a perturbation to the Hamiltonian  $\hat{H}^{(2)}$ . Therefore, (C.13) is the first-order correction to the total energy of  $\hat{H}^{(2)}$ .

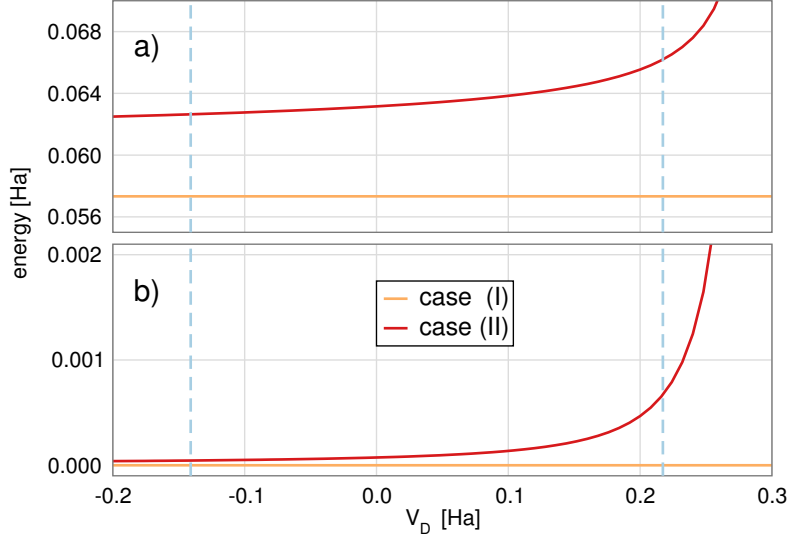


Figure C.4.: a) Hartree correction (C.18) and b) exchange correction (C.19) for high-barrier case (I) (orange) and low-barrier case (II) (red). The vertical dashed blue lines show the tunneling points of case (II) as predicted by the IP-EA approach. They mark the donor potentials  $V_D$ , where in the naive correction scheme the energy corrections to predict the tunneling points of the fully interacting system would be calculated. For the high-barrier case (I), the corrections can be calculated at any point. The strong increase of the energy corrections of case (II) is due to the break-down of our wave function approximation, which is caused by the delocalization of the donor wave-function  $\varphi_D$  for donor-potentials  $V_D$  which are at the order of the barrier height  $V_B$ .

For two electrons and a spin-independent Hamiltonian, the ground state is a singlet wave function. For the range of  $V_D$  where one electron is on the donor and one electron is on the acceptor, the wave function of the complete system can be approximated by

$$\Psi(x_1\sigma_1, x_2\sigma_2) = \frac{1}{\sqrt{4(k^2 + 1)}} [|\uparrow\downarrow\rangle - |\downarrow\uparrow\rangle] \times [\varphi_A(x_1)\varphi_D(x_2) + \varphi_D(x_1)\varphi_A(x_2)] \quad (\text{C.16})$$

where  $\varphi_D(x)$  and  $\varphi_A(x)$  are the normalized spatial parts of the single-electron wave functions of donor and acceptor, respectively, and  $k := |\int dx \varphi_D(x)\varphi_A(x)|$  is the overlap between them, which depends on  $V_B$  and  $V_D$ . To get the interaction energy between electrons which are localized in different subsystems, we evaluate (C.13) with the ap-



proximate wave-function (C.16). This leads to

$$V(1,1) = \langle \Psi(x_1\sigma_1, x_2\sigma_2) | \Delta \hat{V}_{ee} | \Psi(x_1\sigma_1, x_2\sigma_2) \rangle = \frac{C_H}{k^2 + 1} + \frac{C_X}{k^2 + 1}, \quad (\text{C.17})$$

with

$$C_H = \iint dx dx' \frac{\varphi_D(x)\varphi_D(x)\varphi_A(x')\varphi_A(x')}{\sqrt{(x-x')^2 + 1}} = \iint dx dx' \frac{n_D(x)n_A(x')}{\sqrt{(x-x')^2 + 1}} \quad (\text{C.18})$$

describing the Hartree interaction between the electron on the donor with the electron on the acceptor and

$$C_X = \iint dx dx' \frac{\varphi_A(x')\varphi_D(x')\varphi_A(x)\varphi_D(x)}{\sqrt{(x-x')^2 + 1}} \quad (\text{C.19})$$

describing the exchange.

The fact that our subsystems are well separated even in the low barrier case implies that the overlap  $k$  is small. For the high barrier case (I)  $k = 0$  for all  $V_D$ , while for the low-barrier case (II)  $k < 0.04$  for all values of  $V_D < TP_1^{(2)}$ . In consequence, the normalization prefactor is close to 1 and the dependence of the corrections on  $V_D$  via the normalization prefactor is negligible in the intervals where the approximation is valid. Hence, the prefactor can be neglected.

The first-order Hartree correction as a function of  $V_D$  for case (I) and case (II) is shown in panel a) of Fig. C.4, while panel b) shows the first order exchange correction. The exchange correction for the high-barrier case (I) is zero on the scale of the plot. In the high-barrier case (I) the Hartree and exchange interactions are independent of the donor potential  $V_D$ , because the wave function is the same for all  $TP_0 < V_D < TP_1$  due to the very high barrier. In contrast in the low-barrier case (II) the change of the donor potential  $V_D$  results in a change of the effective barrier height which is seen by the electron on the donor. The larger  $V_D$  the smaller is the effective barrier height and the more density penetrates into and through the barrier. Therefore, the electronic densities in the two systems approach each other, resulting in an increase of the energies. In consequence, for small barriers, where the change of the donor wave function due to the change in  $V_D$  is not negligible, it is not clear at which values of  $V_D$  the energy correction  $C_H + C_X$  should be evaluated.

A naive approach would to evaluate the energy corrections for each  $TP_M^{(1)}$  using the correction energies that are obtained at the tunneling points predicted by the IP-EA approximation. Even though this appears intuitive, it leads to incorrect results. As it can be seen in panels a) and c) of Fig. C.2, the truncated Hamiltonian  $\hat{H}^{(2)}$  produces a plateau with electron-electron distribution (1, 1), that is longer than the plateau of the fully interacting Hamiltonian  $\hat{H}^{(1)}$ . The tunneling points  $TP_M^{(2)}$  of  $\hat{H}^{(2)}$ , where we would evaluate the corrections  $V(1,1, V_D)$  are located in a region, where the fully interacting electron distribution is (0, 2) for  $TP_0$  and (2, 0) for  $TP_1$ . Therefore, the naive approach evaluates the energy correction in a region of  $V_D$ , where the approximate wave-function  $\Psi(x_1\sigma_1, x_2\sigma_2)$  (C.16) is not valid. For a high enough barrier this does not make a big difference, since the single-electron wave-function  $\varphi_D$  is not sensitive to changes in the potential  $V_D$ . It is a problem for barriers that are low in comparison to  $V_D$ . This can be seen in Fig. C.4. Here, the IP-EA approach predicts a first tunneling point, that is shifted so far, that for the single well calculation, the electron is not bound in the donor subsystem anymore. This delocalization in the subsystem calculation leads to a fast increase in Hartree and exchange correction, as can be seen for  $V_D > 0.1$  a.u.. This makes this naive approach rather unreliable.

A possible alternative is to evaluate the corrections at  $V_D = 0$ . Even though this method has in principle the same drawback, it has the advantage, that it evaluates the energy corrections for the same potential, where the energies  $E_D(1), \dots E_D(N)$  are calculated. Therefore, the energy correction scheme breaks down at the same point, where the calculation of the energies  $E_D(1), \dots E_D(N)$  does and no further uncertainties are added.

We now compare the size of Hartree and exchange corrections and their significance for the correction of the tunneling points.  $C_H$  describes the Hartree interaction between electrons on the donor with electrons on the acceptor. It is a classical electrostatic energy, that depends only on the densities and does not require any wave function overlap. In contrast, the exchange energy is small for small overlaps  $k$ , and zero if the subsystem wave-functions do not overlap at all. Therefore we expect the exchange correction to be small in comparison to the Hartree correction, which does not require any wave function overlap. This is confirmed by our calculations: it is on average about two orders of magnitude smaller, and therefore it can be neglected. The Hartree corrected predictions for the tunneling points of the fully interacting Hamiltonian  $\hat{H}^{(1)}$  are shown in Fig. C.2 as green dashed lines. We see that Hartree correcting the IP-EA predicted

tunneling points  $TP_M^{(2)}$  already gives a good agreement with the true tunneling points of the fully interacting Hamiltonian. We also note, that the Hartree interaction overcorrects the predictions. This could in principle be compensated by extending the perturbation approach to higher orders.

### C.3.3. Three and Four Electrons

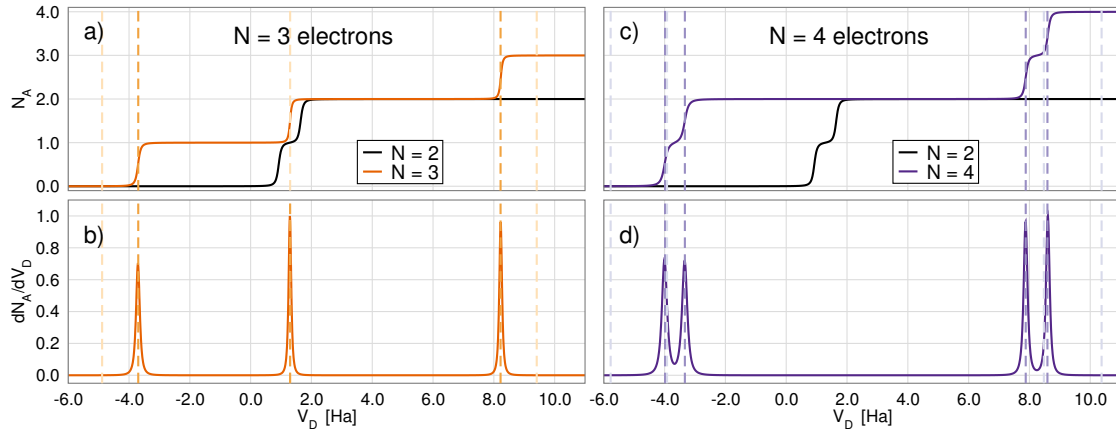


Figure C.5.: (Top) Number of electrons on the acceptor  $N_A$  as a function of the donor potential  $V_D$  in the low-barrier case (II) for a)  $N = 3$  (dark orange) and b)  $N = 4$  (dark violet) electrons. For comparison the case of  $N = 2$  electrons is shown in black. A system of  $N$  electrons exhibits  $N$  tunneling points. The behaviour of three and four electrons is qualitatively similar as the one of two electrons. (Bottom) The derivate  $dN_A/dV_D$  as a function of the donor potential for c)  $N = 3$  and d)  $N = 4$ . In each panel, the predicted tunneling points are shown as dashed vertical lines. The light orange (violet) dashed line shows the IP-EA predicted tunneling points, the slightly darker orange (violet) dashed line the Hartree corrected predictions.

Fig. C.5 shows in the top panels a) and c) the number of electrons on the acceptor  $N_A$  for three (orange) and four (violet) electrons for the low-barrier case (II). The behaviour of two electrons (black) is shown for comparison. A system with  $N$  electrons exhibits  $N$  tunneling points, but except for that, the functional line shape is similar to the one of the two electrons system, which was analyzed in detail before. It is interesting to note the differences of the plateau widths for the cases of three and four electrons. For closed shell systems, the tunneling points appear in pairs of two, whereas the ones in open shell

system appear isolated.

This can be explained already at the level of non-interacting electrons. For very narrow wells, the energy-levels of non-interacting electrons are far apart in energy. Therefore, the level spacing is bigger than the energy splitting due to the electron-electron interaction of electrons in the same spatial non-interacting energy level. The difference of the IP of a system with  $2n$  electrons and the same system with  $2n - 1$  electrons is much smaller than the difference between the IP of the system with  $2n - 1$  and the IP of the system with  $2n - 2$  electrons, i.e.

$$|IP(2n) - IP(2n - 1)| \ll |IP(2n - 1) - IP(2n - 2)|, \quad (\text{C.20a})$$

and analogous for EA

$$|EA(2n) - EA(2n + 1)| \ll |EA(2n + 1) - EA(2n + 2)|. \quad (\text{C.20b})$$

Basically, IP and EA always appear in pairs. This pair structure is inherited by the tunneling points. The difference between open-shell and closed shell calculations is that for the closed-shell calculations, two tunneling points in a row either keep IP and EA in the same pair or both IP as well as EA change the pair. If both stay in the same pair, the tunneling points are close together, if both change, i.e. new energy levels are involved on both donor and acceptor, and then the tunneling points are further apart. In contrast, for the open-shell calculations, for every tunneling point either IP or EA changes from one pair to the next, but never both. For the closed-shell calculations, the width of the plateaus with odd numbers of electrons in the subsystems is mainly governed by the Coulomb interaction of electrons, that would sit in the same one-particle level, the width of the plateaus with even numbers of electrons is mainly governed by the energy level spacing. For completely non-interacting electrons, the odd plateaus vanish, whereas the even ones persist. In contrast, for open-shell calculations, the level spacing plays a role in all of the plateau lengths: even in the case of non-interacting electrons, all plateaus persist.

Furthermore, the tunneling points of three electrons seem to lie in the middle of the odd plateaus of the closed-shell calculations. This is due to symmetry of donor and acceptor. For a completely symmetric setup, the tunneling points of three electrons would in fact lie exactly in the middle.

We now apply our correction scheme for the tunneling points of the fully interacting Hamiltonian  $\hat{H}^{(1)}$  to the three and four electron calculations. The bottom panels of Fig. C.5 show the derivatives  $dN_A/dV_D$  of the interacting number of electrons on the acceptor  $N_A^{(1)}$  for three (b) and four (d) electrons. The vertical dashed lines show the exact tunneling points. The light lines show the IP-EA predictions, the darker lines the tunneling points, that were corrected with our derived scheme. We see, that also for three and four electrons our correction scheme gives a good agreement with the exact tunneling points. Again, we see, that the scheme slightly overcorrects the energies.

#### C.3.4. Lineshape of Electronic Transport

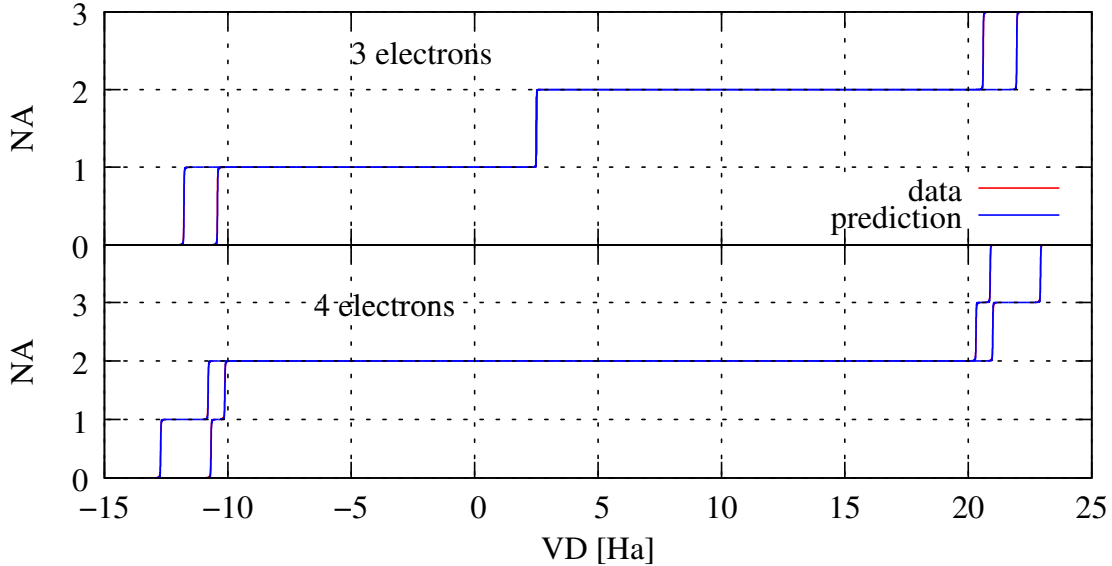


Figure C.6.: Tunneling of (top) three and (bottom) four electrons in a 9-site model. The figure shows the numerical data in comparison with our model, both for the full and the truncated interaction. In both cases, our model reproduces the numerical results on the shown scale. Figs. C.7 and C.8 show zooms into the relevant regions for three and four electrons respectively.

The tunneling behaviour can be characterized by two things: the tunneling point, i.e. the gate voltage at which electrons tunnel, and the functional shape of the number of electrons on the acceptor  $N_A$  as a function of the donor potential  $V_D$ . In the last sections, we have discussed the voltage, in the following we would like to find a simple

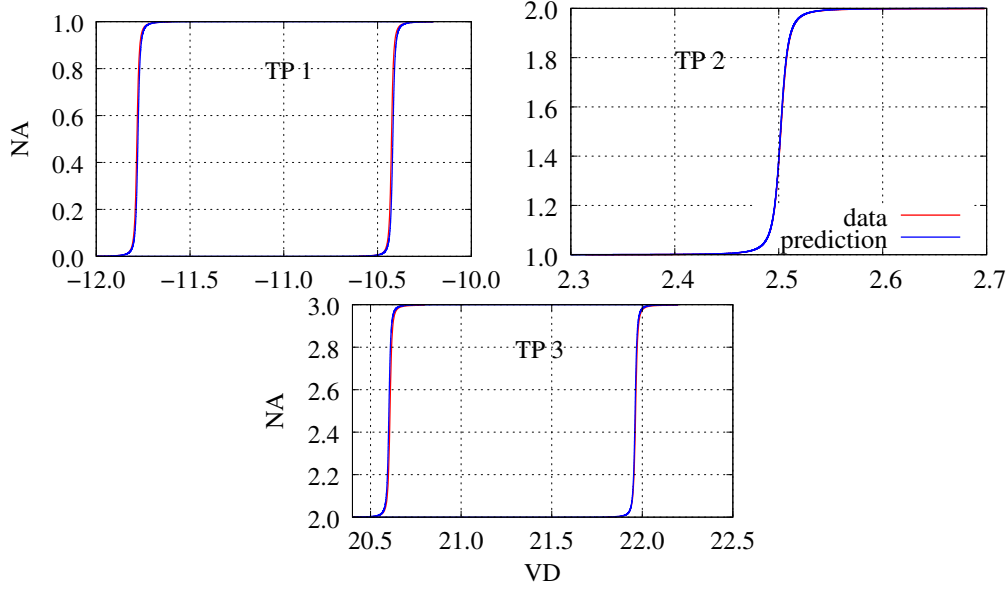


Figure C.7.: Comparison of the tunneling behaviour predicted by our model and the corresponding numerical data for an asymmetric double-well potential with three electrons (zoom into the regions of the different tunneling points).

mathematical model in order to give an analytical expression for the shape.

To this end, we assume, that the tunneling process can be described by two energy levels: one on the donor and one on the acceptor, coupled to each other by a coupling term  $\tau$ . This situation is described mathematically by the two-level Hamiltonian

$$\hat{H} = \begin{pmatrix} 0 & \tau \\ \tau & V_D \end{pmatrix}. \quad (\text{C.21})$$

Here, the on-site potential at the acceptor is zero, the on-site potential of the donor is  $V_D$  and is assumed to be variable as in the previous calculations. The coupling of the two sub-systems is given by  $\tau$ , which mimics a higher or lower barrier.

The Hamiltonian (C.21) yields the energy eigenvalues

$$\varepsilon_{1/2} = \frac{1}{2}V_D \pm \frac{1}{2}\sqrt{V_D^2 + 4\tau^2}, \quad (\text{C.22})$$

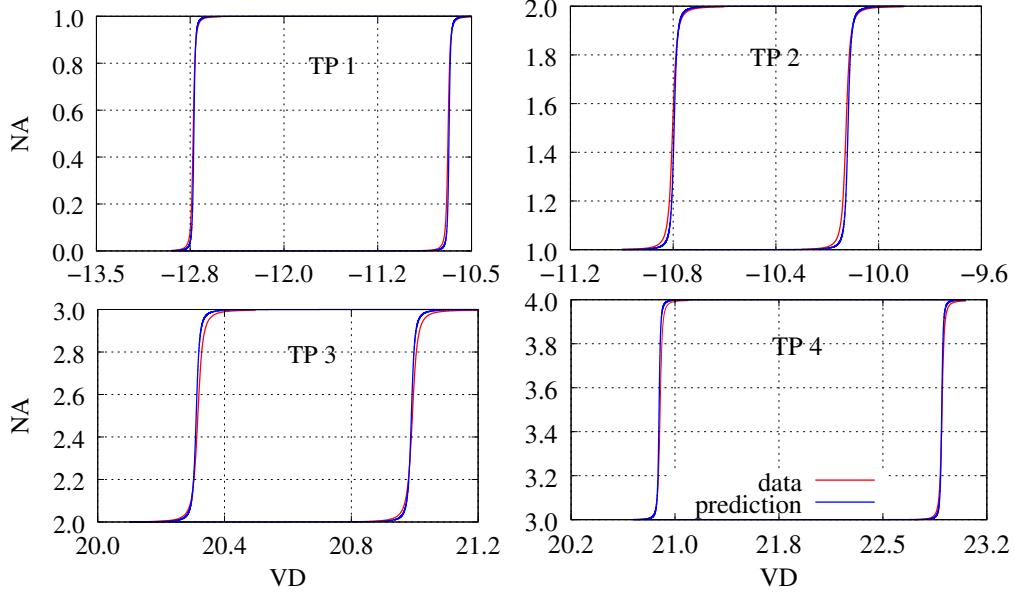


Figure C.8.: Comparison of the tunneling behaviour predicted by our model and the corresponding numerical data for an asymmetric double-well potential with four electrons (zoom into the regions of the different tunneling points).

and the corresponding eigenvectors

$$\Psi_{1/2} = \frac{1}{A_{1/2}} \begin{pmatrix} \frac{-V_D \mp \sqrt{V_D^2 + 4\tau^2}}{2\tau} \\ 1 \end{pmatrix} \quad (\text{C.23})$$

with the normalization factor

$$A_{1/2} = \sqrt{1 \mp \frac{V_D^2 + 4\tau^2}{4\tau^2}}. \quad (\text{C.24})$$

Since we are interested in the number of electrons on the acceptor, we calculate the respective electronic densities

$$n_1 = \frac{1}{2} \begin{pmatrix} 1 + \frac{V_D}{\sqrt{V_D^2 + 4\tau^2}} \\ 1 - \frac{V_D}{\sqrt{V_D^2 + 4\tau^2}} \end{pmatrix} \quad (\text{C.25a})$$

and of the excited state

$$n_2 = \frac{1}{2} \left( \frac{1 - \frac{V_D}{\sqrt{V_D^2 + 4\tau^2}}}{1 + \frac{V_D}{\sqrt{V_D^2 + 4\tau^2}}} \right), \quad (\text{C.25b})$$

where

$$N_A(V_D) = \frac{1}{2} \left( 1 + \frac{V_D}{\sqrt{V_D^2 + 4\tau^2}} \right). \quad (\text{C.26})$$

gives us the number of electrons on the acceptor for the ground state in dependence of the coupling term  $\tau$ .

Since we have a step for each tunneling point and one tunneling point per electron in the system, taking into account that we have to place the steps at the right points  $TP_m$ , we find for general overall shape of  $N_A$

$$N_A(V_D) = \frac{N}{2} + \frac{1}{2} \sum_{m=0}^{N-1} \left( \frac{V_D - TP_m}{\sqrt{(V_D - TP_m)^2 + 4\tau_m^2}} \right). \quad (\text{C.27})$$

One sees, that the functional shape of the number of electron on the acceptor is governed by the coupling element  $\tau$ . This coupling  $\tau$  is the energy splitting between the many-body energy levels at the tunneling point. In 1961, Herring used the continuity equation in combination with a two-term expansion of the wavefunction to obtain this energy splitting for the case of a single particle in a symmetric double-well potential as [240]:

$$\tau = \left[ \varphi \frac{d\varphi}{dx} \right]_{x_0} \quad \varphi = \varphi_A = \varphi_D \quad (\text{C.28})$$

This formula was adapted by Rastelli to asymmetric double-well potentials [241]:

$$\tau = \frac{1}{2} \left[ \varphi_A \frac{d\varphi_D}{dx} - \varphi_D \frac{d\varphi_A}{dx} \right]_{x_0}. \quad (\text{C.29})$$

Both of these cases are for single particle tunneling. To find an approximation to the energy splitting in the many-electron case, we define an auxiliary “excess-electron wave function”. To this goal, we define the “excess-electron density” of the N-th electron on



donor/acceptor:

$$\rho_{excess,D/A}^N(x) = \rho_{D/A}^N(x) - \rho_{D/A}^{N-1}(x) \quad (\text{C.30})$$

Since we are interested in this quantity only at  $x_0$  under the barrier, where it is always positive, we can define the “excess-electron wave-function” at  $x_0$ :

$$\varphi_{excess,D/A}^N(x_0) = \sqrt{\rho_{excess,D/A}^N(x_0)} \quad (\text{C.31})$$

which can be used together with the Rastelli formula (C.29). Figure C.6 shows the results for a 9-site model, with a spacing of  $\Delta x = 0.2$  and four sites on the donor, three sites on the acceptor and two sites for the barrier, Figs. C.7 and C.8 show zooms of the results. As we see, the agreement between the numerical simulations and the predictions using Rastelli’s formula in combination with our “excess-electron wave function” is rather good. To further improve the results, we also implemented a second order correction. This requires a correction of densities and wavefunctions. One possibility is to recalculate the subsystem densities with an additional Hartree potential coming from the other subsystem. We found, that this gives vanishingly small contributions to the tunneling point corrections and does not change the lineshape noticeably.

## C.4. Tunneling in Density-Functional Theory

We now compare the exact calculations for two electrons to calculations using DFT with different functionals. Firstly, we show that for two electrons in an asymmetric double-well potential, LDA and LDA-ADSIC do not reproduce the correct tunneling behaviour, but instead predict a continuous charge transfer from one well into the other. We then show, that the spin-polarized LDA-SIC using the Perdew-Zunger scheme (LDA-PZSIC) has multiple solutions and one of them does reproduce the correct density in the two-electron case. Unfortunately, this comes with the price of an incorrect spin density. We then analyze, how to use the LDA-PZSIC spin-resolved potentials to construct a KS-potential, that reproduces the correct spin-densities and analyze, how tunneling in DFT can be understood in terms of the KS eigenenergies.

#### C.4.1. Tunneling with Different Functionals

Figure C.9 shows the number of electrons on the acceptor  $N_A$  as a function of the donor-potential  $V_D$ . The red line shows the exact many-body tunneling behaviour, the other lines the behaviour with different DFT functionals. One sees that neither LDA, nor LDA-ADSIC reproduce the step-like charge transfer from the donor to the acceptor, but instead predict a continuous behaviour. Furthermore, one finds, that LDA-SIC in the Perdew-Zunger scheme has multiple solutions. If one chooses the one with minimal energy, it reproduces the step-like behaviour of the exact calculations as shown in Figure C.9.

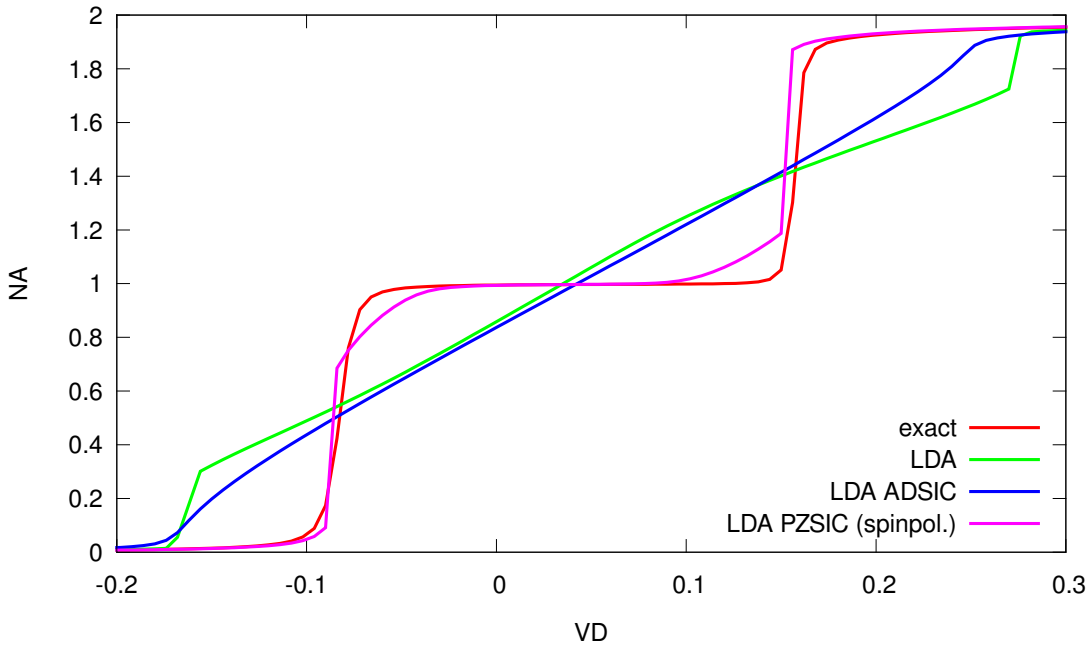


Figure C.9.: Number of electrons on the acceptor as a function of donor potential  $V_D$  for two electrons in an asymmetric double-well potential. The red line indicates the exact many-body solution, the other lines DFT solutions with different functionals: LDA (green), LDA-ADSIC (blue) and spin-polarized LDA-PZSIC (pink). The spin-polarized LDA-PZSIC solution has multiple solutions. If one chooses the one with minimal energy, it exhibits a step-like behaviour like the exact solution.

Nevertheless, even though, the total density is reproduced well, the spin-resolved density is not. If we had the exact functional, the density would be correct for a closed-shell

calculation, with both electrons occupying the same orbital. This leads to the question, if we can use the correct behaviour with respect to the overall density of the spin-polarized LDA-PZSIC calculations to construct the correct spin-unpolarized KS potential.

### C.4.2. Constructing the Exact KS Potential for Tunneling

As a first step, we compare the exact KS potential with the spin-resolved potentials of the spin-polarized LDA-PZSIC calculations. The exact KS potential can be obtained from the exact density through inversion [185]:

$$v_{KS}(\mathbf{r}) = \frac{1}{2} \frac{\nabla^2 \sqrt{n(\mathbf{r})}}{\sqrt{n(\mathbf{r})}} + \epsilon_1 \quad (\text{C.32})$$

Fig. C.10 shows the exact KS-potential on the left, the spin-resolved KS-potentials in the middle and the LDA potential on the right, each together with their respective ground-state densities. The top row shows the situation, where both electrons sit on the donor, the middle row shows the situation where one electrons sits on the donor and the other one on the acceptor and the bottom row shows the situation, where both electrons sit on the acceptor.

In the exact case (left column), the first thing, that jumps into one's eye, is the peak in the KS-potential, which forms between the two densities. This is the well-known peak, that is necessary to keep the two electrons apart [185]. If we now compare this peak structure to the spin-dependent KS-potentials in the case of the spin-polarized LDA-PZSIC calculation (center column), we find, that the two spin-dependent KS-potentials seem to form a similar structure between the two of them. As a comparison, the KS-potential of the LDA calculations (shown in the right column) is completely different from the exact one in all three cases. In the following, we would like to use the two spin-polarized PZSIC KS potentials to construct a new KS potential, which reproduces the correct density without the need of breaking the spin-symmetry. In order to do so, we follow the steps:

- I Perform a spin-polarized calculation using the LDA-PZSIC functional.
- II Combine the two spin-resolved KS-potentials plus possible modifications to a new KS potential  $V_{\text{eff}}$ .
- III Assuming, that  $V_{\text{eff}}$  is the correct KS-potential, solve the Schrödinger equation for

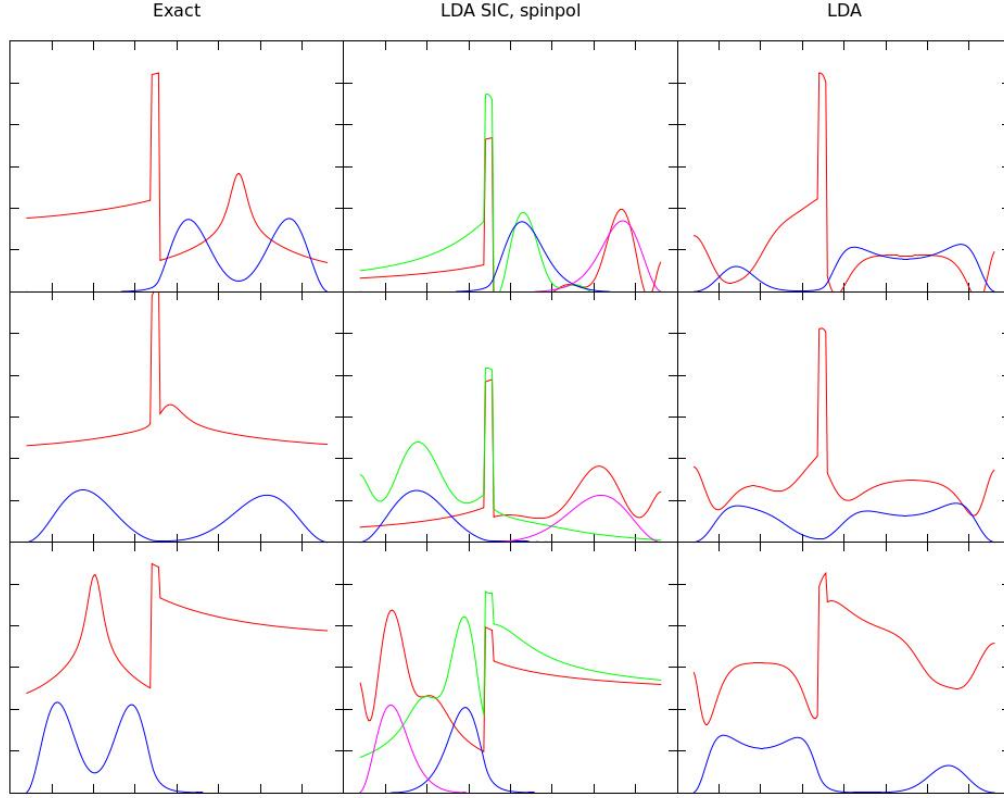


Figure C.10.: KS potentials  $v_{KS}$  and the respective ground-state densities for exact, spin-polarized LDA-PZSIC and LDA calculations. The top row shows the situation where both electrons are on the donor, the middle one, the one, where one is on the donor, one has already tunneled to the acceptor and the bottom row shows the situation where both electrons have tunneled to the acceptor. The left column shows the exact  $V_{KS}$  (red) with its respective density (blue), the middle one the spin-polarized LDA-SIC potentials (red and green) with their respective spin-densities (blue and pink) and the right column finally shows the LDA potential (red) with its density in blue. Note, that the offsets of the potentials are arbitrary and have no physical meaning.

independent particles in the potential  $V_{\text{eff}}$  to get the non-interacting wave functions.

- IV Occupy the non-interacting wave functions with two electrons and calculate the resulting density. This density should then reproduce the correct density and because

we are not performing spin-polarized calculations, the correct spin-densities.

The difficult step is to design a recipe to construct  $V_{\text{eff}}$ . First, we take the minimum of the two spin-polarized potentials  $V_{\uparrow}$  and  $V_{\downarrow}$  in order to take advantage of the before-mentioned peak, that is formed between both. If we compare the resulting potential with the exact one, we find, that the offset between the wells is wrong and that, whilst it has a bit of a peak in the region between the two peaks in the electronic density, the peak is not high enough. We therefore recall [185], where the exact KS-potential for two electrons in a double-well potential in the stretched limit was found to be

$$V_{KS} = V_{ext} + S_{11} + P_{11}$$

with the external potential  $V_{ext}$ , the step-like structure

$$S_{11} = \frac{I_1 n_1 + I_2 n_2}{n_1 + n_2}, \quad (\text{C.33})$$

and the peak-like structure

$$P_{11} = \frac{(\sqrt{n_1} d_x \sqrt{n_2} - \sqrt{n_2} d_x \sqrt{n_1})^2}{2(n_1 + n_2)^2}. \quad (\text{C.34})$$

It is therefore only natural to add these structures by using the spin-polarized densities with  $n_1 = n_{\uparrow}$  and  $n_2 = n_{\downarrow}$ . Thus, we construct our potential  $V_{\text{eff}}$  as

$$\begin{aligned} V_{\text{eff}} &= \min(V_{\uparrow}, V_{\downarrow}) + S_{\uparrow\downarrow} + P_{\uparrow\downarrow} \\ &= \min(V_{\uparrow}, V_{\downarrow}) + \frac{I_{\uparrow} n_{\uparrow} + I_{\downarrow} n_{\downarrow}}{n_{\uparrow} + n_{\downarrow}} + \frac{(\sqrt{n_{\uparrow}} d_x \sqrt{n_{\downarrow}} - \sqrt{n_{\downarrow}} d_x \sqrt{n_{\uparrow}})^2}{2(n_{\uparrow} + n_{\downarrow})^2} \\ &= \min(V_{\uparrow}, V_{\downarrow}) - \frac{\varepsilon_{\uparrow} n_{\uparrow} + \varepsilon_{\downarrow} n_{\downarrow}}{n_{\uparrow} + n_{\downarrow}} + \frac{(\sqrt{n_{\uparrow}} d_x \sqrt{n_{\downarrow}} - \sqrt{n_{\downarrow}} d_x \sqrt{n_{\uparrow}})^2}{2(n_{\uparrow} + n_{\downarrow})^2} \end{aligned} \quad (\text{C.35})$$

where  $I = -\varepsilon$ , because the orbitals in question are the HOMO orbitals.

Applying this scheme, we find that the so-constructed KS-potential  $V_{\text{eff}}$  indeed displays a Coulomb blockade plateau, even though it is not wide enough: Figure C.11 shows the number of electrons on the acceptor  $N_A$  as a function of the donor potential  $V_D$  in the exact case, as obtained by spin-polarized LDA-PZSIC, confining the solution to the

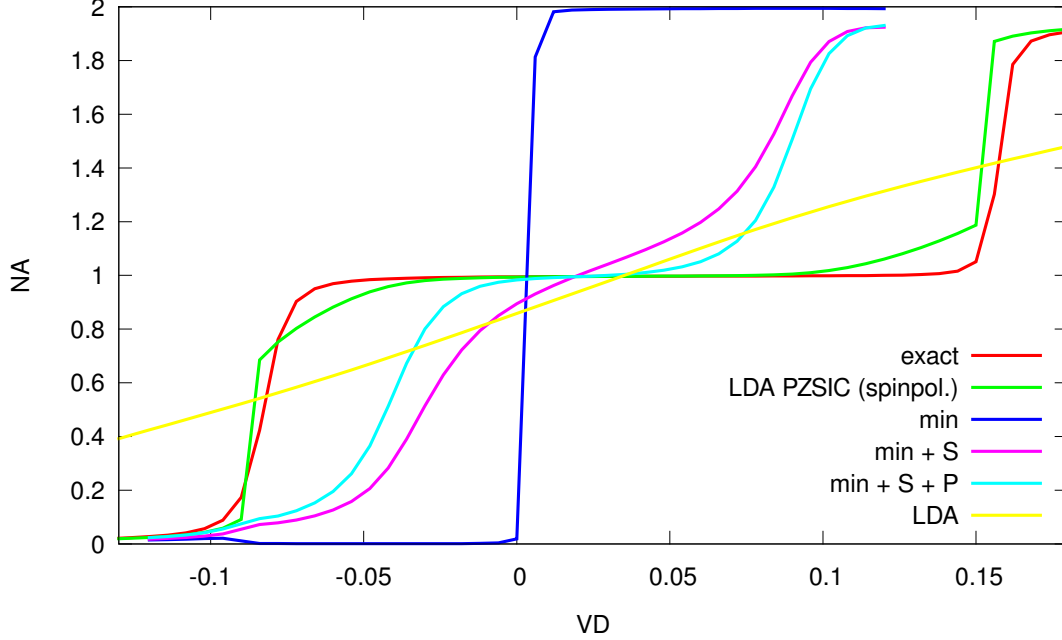


Figure C.11.: Number of electrons on the acceptor  $N_A$  in dependence of the donor potential  $V_D$  for the exact case, as obtained with the wrong spin-symmetry with spin-polarized LDA-PZSIC, with our proposed scheme with the correct spin-symmetry using  $V_{\text{eff}}^{(i)} = \min(V_{\uparrow}, V_{\downarrow})$ ,  $V_{\text{eff}}^{(ii)} = \min(V_{\uparrow}, V_{\downarrow}) + S_{\uparrow\downarrow}$  and  $V_{\text{eff}}^{(iii)} = \min(V_{\uparrow}, V_{\downarrow}) + S_{\uparrow\downarrow} + P_{\uparrow\downarrow}$ .  $V_{\text{eff}}^{(i)}$  does not produce a plateau,  $V_{\text{eff}}^{(ii)}$  produces first hints of a plateau in the center and  $V_{\text{eff}}^{(iii)}$  produces a plateau, even though it is still too narrow. LDA is shown for comparison.

branch with minimal energy and using our developed scheme using (i)  $V_{\text{eff}}^{(i)} = \min(V_{\uparrow}, V_{\downarrow})$ , (ii)  $V_{\text{eff}}^{(ii)} = \min(V_{\uparrow}, V_{\downarrow}) + S_{\uparrow\downarrow}$  and (iii)  $V_{\text{eff}}^{(iii)} = \min(V_{\uparrow}, V_{\downarrow}) + S_{\uparrow\downarrow} + P_{\uparrow\downarrow}$ . One sees that just taking the minimum of the potentials is not enough. We need to add the step structure  $S_{\uparrow\downarrow}$  to get a bend in the  $N_A$  curve. Finally, by additionally adding the peak  $P_{\uparrow\downarrow}$ , we obtain a real plateau, even though it is too narrow.

But what is happening here? How can we explain, what step and peak do? And how can we relate this to the results, that we know about many-particle tunneling? The answer lies in the KS-eigenvalues.

### C.4.3. Eigenenergies - Exact vs. DFT

In many-particle tunneling, we know that tunneling points are situated at avoided crossings between energy levels that have spatially different electronic densities. The tunneling point energy is determined by the avoided crossing, and the energy splitting at the avoided crossing defines the curvature of the tunneling curve at this point.

We wish to determine if this relationship between avoided crossings and tunneling points is reproduced at the DFT level. The answer can be found in Figure C.12, which shows the KS eigenvalues as a function of the donor potential  $V_D$  for the different constructed potentials, in comparison to the eigenvalues of the exact KS potential, which was obtained by inversion using Eq. (C.32). In contrast to the many-body eigenenergies, which have

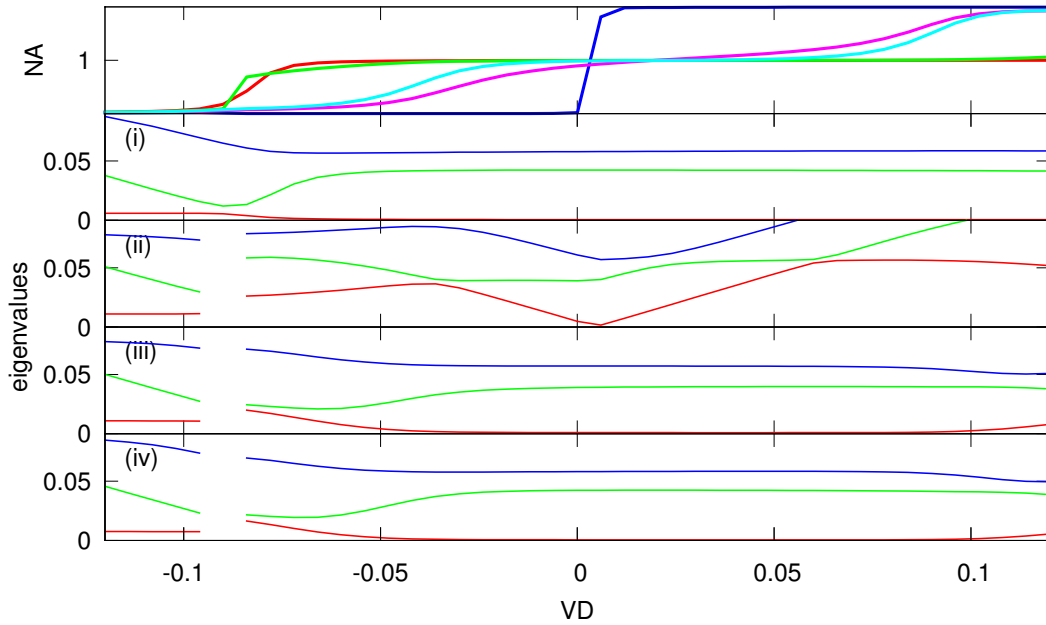


Figure C.12.: (top) Number of electrons on the acceptor  $NA$  as a function of the donor potential  $VD$  (as in Fig. C.11) and (i) - (iv) the corresponding KS eigenvalues: (i) exact KS, (ii)  $V_{\text{eff}}^{(i)} = \min(V_{\uparrow}, V_{\downarrow})$ , (iii)  $V_{\text{eff}}^{(ii)} = \min(V_{\uparrow}, V_{\downarrow}) + S_{\uparrow\downarrow}$  and (iv)  $V_{\text{eff}}^{(iii)} = \min(V_{\uparrow}, V_{\downarrow}) + S_{\uparrow\downarrow} + P_{\uparrow\downarrow}$ . Eigenvalues are plotted as differences to the lowest eigenvalue.

avoided crossings at the tunneling points, the two lowest eigenvalues of the exact KS

potential are (almost) degenerate for the whole length of the plateau. This can be understood as follows. In the KS case, both electrons occupy a single orbital. In the Coulomb blockade plateau region, this one-particle orbital is spread over both wells. From the many-body calculations, we know, that this is the case only at the many-body tunneling points with (almost) degenerate orbitals. Therefore, the KS potential has to mimic this situation over the whole plateau length. This is very well illustrated in panel (ii) of Fig. C.12, which shows the eigenvalues of the potential  $V_{\text{eff}}^{(i)} = \min(V_{\uparrow}, V_{\downarrow})$ . Here, the two lowest eigenvalues are very close in energy only at a single donor potential  $V_D$ , which is precisely the only point, where one electron is on the donor and one on the acceptor (see blue line in the top panel).

The job of step and peak is to create this near degeneracy by closing the gap between the first and the second KS-eigenvalue. The main work is done by the step: In panel (iii) (which corresponds to the pink line in the top panel) the two lowest eigenvalues are close in energy over a certain energy range already. If we now also add the peak (panel (iv)), the difference between the eigenvalues is decreased even more and the Coulomb plateau (bright blue line in top panel) becomes even wider.

It is worth noting, that for LDA (not shown), the (near) degeneracy between first and second eigenenergy is present during the whole time of constant charge transfer; LDA's problem is purely the delocalization of the eigenstates.

## C.5. Summary

In this appendix, we have analyzed tunneling in many-particle systems (in practice two, three and four particles), first exactly, then from a DFT point of view. First, we have looked at exactly solvable model Hamiltonians. Here, we analyzed how the resonance conditions for tunneling differ in a fully-interacting system from a system, where donor and acceptor do not interact. We found, that aligning the ionization potential of the donor with the electron affinity of the acceptor predicts the tunneling points of a Hamiltonian, where electrons on the donor do not interact with the electrons on the acceptor. We then developed a scheme to correct the resonances predicted by this alignment to get the fully-interacting resonances, based on only the densities of the subsystems. Being able to neglect the exchange interaction, we learned that we can construct a correction scheme for the tunneling points in the case of interacting subsystems, where the correction only



depends on the respective subsystem densities. This scheme is therefore easily applicable to any DFT or Hartree-Fock calculation. Finally, we analyzed the tunneling line shapes. We found, that we can adapt the formula developed by Herring for single particles in symmetric wells and adapted by Rastelli for single particles in asymmetric double wells to many particles by defining an excess-density wave function.

We then proceeded to look at the DFT description of many-particle tunneling. We showed, that DFT using the LDA or the LDA-ADSIC functionals is not able to correctly predict the tunneling behaviour in an interacting two-electron system. Only the spin-polarized LDA-SIC approximation using the Perdew-Zunger scheme is able to predict the correct density, but does so by using incorrect spin-densities. We then compared the exact KS-potential, which was obtained from inverting the exact solution, to the different potentials in LDA, LDA-SIC, etc. We then found that one can use the spin-polarized, self-interaction corrected potentials to obtain a solution with the correct spin-resolved densities.

Finally, we found, that while in many-body tunneling, the many-particle energy levels show avoided crossings at the tunneling points, in the DFT case, the first and second eigenvalues are degenerate over the whole Coulomb-blockade plateau. This is one necessary condition for the KS eigenvalues in order to produce the correct description of the Coulomb-plateau in the description of tunneling.



## Bibliography

- [1] E. Goulielmakis, Z.-H. Loh, A. Wirth, R. Santra, N. Rohringer, V. S. Yakovlev, S. Zherebtsov, T. Pfeifer, A. M. Azzeer, M. F. Kling, S. R. Leone, and F. Krausz, “Real-time observation of valence electron motion,” *Nature*, vol. 466, pp. 739–743, Aug. 2010.
- [2] C. Ott, A. Kaldun, P. Raith, K. Meyer, M. Laux, J. Evers, C. H. Keitel, C. H. Greene, and T. Pfeifer, “Lorentz meets fano in spectral line shapes: A universal phase and its laser control,” *Science*, vol. 340, no. 6133, pp. 716–720, 2013.
- [3] U. De Giovannini, G. Brunetto, A. Castro, J. Walkenhorst, and A. Rubio, “Simulating pump-probe photoelectron and absorption spectroscopy on the attosecond timescale with time-dependent density functional theory,” *ChemPhysChem*, vol. 14, no. 7, pp. 1363–1376, 2013.
- [4] D. M. Quinten, *A Practical Guide to Optical Metrology for Thin Films*. Wiley-VCH Verlag GmbH & Co. KGaA, October 2012.
- [5] F. Krausz and M. Ivanov, “Attosecond physics,” *Rev. Mod. Phys.*, vol. 81, pp. 163–234, Feb 2009.
- [6] A. Siegman, *Lasers*. University Science Books, Mill Valley, 1986.
- [7] R. Boyd, *Nonlinear Optics, 2nd Edition*. Academic, New York, 2003.
- [8] W. Kruer, *The Physics of Laser-Plasma Interactions*. Westview, Boulder, 2003.
- [9] P. Abbamonte, K. D. Finkelstein, M. D. Collins, and S. M. Gruner, “Imaging density disturbances in water with a 41.3-attosecond time resolution,” *Phys. Rev. Lett.*, vol. 92, p. 237401, Jun 2004.
- [10] P. Wernet, D. Nordlund, U. Bergmann, M. Cavalleri, M. Odelius, H. Ogasawara, L. Näslund, T. Hirsch, L. Ojam  e, P. Glatzel, L. Pettersson, and A. Nilsson,

- “The structure of the first coordination shell in liquid water,” *Science*, vol. 14, pp. 995–999, 2004.
- [11] M. DiDomenico, “Small-signal analysis of internal (coupling-type) modulation of lasers,” *Journal of Applied Physics*, vol. 35, no. 10, pp. 2870–2876, 1964.
- [12] T. Brabec, C. Spielmann, and F. Krausz, “Mode locking in solitary lasers,” *Opt. Lett.*, vol. 16, pp. 1961–1963, Dec 1991.
- [13] G. Steinmeyer, D. H. Sutter, L. Gallmann, N. Matuschek, and U. Keller, “Frontiers in ultrashort pulse generation: Pushing the limits in linear and nonlinear optics,” *Science*, vol. 286, no. 5444, pp. 1507–1512, 1999.
- [14] D. E. Spence, P. N. Kean, and W. Sibbett, “60-fsec pulse generation from a self-mode-locked ti:sapphire laser,” *Opt. Lett.*, vol. 16, pp. 42–44, Jan 1991.
- [15] M. Nisoli, S. De Silvestri, and O. Svelto, “Generation of high energy 10 fs pulses by a new pulse compression technique,” *Applied Physics Letters*, vol. 68, no. 20, pp. 2793–2795, 1996.
- [16] C. G. Durfee, A. R. Rundquist, S. Backus, C. Herne, M. M. Murnane, and H. C. Kapteyn, “Phase matching of high-order harmonics in hollow waveguides,” *Phys. Rev. Lett.*, vol. 83, pp. 2187–2190, Sep 1999.
- [17] E. Constant, D. Garzella, P. Breger, E. Mével, C. Dorrer, C. Le Blanc, F. Salin, and P. Agostini, “Optimizing high harmonic generation in absorbing gases: Model and experiment,” *Phys. Rev. Lett.*, vol. 82, pp. 1668–1671, Feb 1999.
- [18] X. Feng, S. Gilbertson, H. Mashiko, H. Wang, S. D. Khan, M. Chini, Y. Wu, K. Zhao, and Z. Chang, “Generation of isolated attosecond pulses with 20 to 28 femtosecond lasers,” *Phys. Rev. Lett.*, vol. 103, p. 183901, Oct 2009.
- [19] H. M. Milchberg, C. G. Durfee III, and T. J. McIlrath, “High-order frequency conversion in the plasma waveguide,” *Phys. Rev. Lett.*, vol. 75, pp. 2494–2497, Sep 1995.
- [20] R. Szipöcs, C. Spielmann, F. Krausz, and K. Ferencz, “Chirped multilayer coatings for broadband dispersion control in femtosecond lasers,” *Opt. Lett.*, vol. 19, pp. 201–203, Feb 1994.

- 
- [21] T. Brabec and F. Krausz, “Intense few-cycle laser fields: Frontiers of nonlinear optics,” *Rev. Mod. Phys.*, vol. 72, pp. 545–591, Apr 2000.
- [22] U. Keller, “Recent developments in compact ultrafast lasers,” *Nature*, vol. 424, pp. 831–838, Aug. 2003.
- [23] C. A. Brau, “Free-electron lasers,” *Science*, vol. 239, pp. 1115–1121, 1988.
- [24] J. M. J. Madey, “Stimulated emission of bremsstrahlung in a periodic magnetic field,” *Journal of Applied Physics*, vol. 42, no. 5, pp. 1906–1913, 1971.
- [25] D. A. G. Deacon, L. R. Elias, J. M. J. Madey, G. J. Ramian, H. A. Schwettman, and T. I. Smith, “First operation of a free-electron laser,” *Phys. Rev. Lett.*, vol. 38, pp. 892–894, Apr 1977.
- [26] S. V. Milton, E. Gluskin, N. D. Arnold, C. Benson, W. Berg, S. G. Biedron, M. Borland, Y.-C. Chae, R. J. Dejus, P. K. Den Hartog, B. Deriy, M. Erdmann, Y. I. Eidelman, M. W. Hahne, Z. Huang, K.-J. Kim, J. W. Lewellen, Y. Li, A. H. Lumpkin, O. Makarov, E. R. Moog, A. Nassiri, V. Sajaev, R. Soliday, B. J. Tie-man, E. M. Trakhtenberg, G. Travish, I. B. Vasserman, N. A. Vinokurov, X. J. Wang, G. Wiemerslage, and B. X. Yang, “Exponential gain and saturation of a self-amplified spontaneous emission free-electron laser,” *Science*, vol. 292, no. 5524, pp. 2037–2041, 2001.
- [27] Andruszkow and *al*, “First observation of self-amplified spontaneous emission in a free-electron laser at 109 nm wavelength,” *Phys. Rev. Lett.*, vol. 85, pp. 3825–3829, Oct 2000.
- [28] A. Tremaine, X. J. Wang, M. Babzien, I. Ben-Zvi, M. Cornacchia, H.-D. Nuhn, R. Malone, A. Murokh, C. Pellegrini, S. Reiche, J. Rosenzweig, and V. Yakimenko, “Experimental characterization of nonlinear harmonic radiation from a visible self-amplified spontaneous emission free-electron laser at saturation,” *Phys. Rev. Lett.*, vol. 88, p. 204801, May 2002.
- [29] V. Ayvazyan and *al*, “Generation of gw radiation pulses from a vuv free-electron laser operating in the femtosecond regime,” *Phys. Rev. Lett.*, vol. 88, p. 104802, Feb 2002.

- [30] W. Ackermann and *al.*, “Operation of a free-electron laser from the extreme ultraviolet to the water window,” *Nat Photon*, vol. 1, pp. 336–342, June 2007.
- [31] T. Shintake and *al.*, “A compact free-electron laser for generating coherent radiation in the extreme ultraviolet region,” *Nat Photon*, vol. 2, pp. 555–559, Sept. 2008.
- [32] P. Emma and *al.*, “First lasing and operation of an angstrom-wavelength free-electron laser,” *Nat Photon*, vol. 4, pp. 641–647, Sept. 2010.
- [33] T. Ishikawa and *al.*, “A compact x-ray free-electron laser emitting in the sub-angstrom region,” *Nat Photon*, vol. 6, pp. 540–544, Aug. 2012.
- [34] L. Young, E. P. Kanter, B. Krässig, Y. Li, A. M. March, S. T. Pratt, R. Santra, S. H. Southworth, N. Rohringer, L. F. DiMauro, G. Doumy, C. A. Roedig, N. Berrah, L. Fang, M. Hoener, P. H. Bucksbaum, J. P. Cryan, S. Ghimire, J. M. Glowina, D. A. Reis, J. D. Bozek, C. Bostedt, and M. Messerschmidt, “Femtosecond electronic response of atoms to ultra-intense x-rays,” *Nature*, vol. 466, pp. 56–61, July 2010.
- [35] Y. Hikosaka, M. Fushitani, A. Matsuda, C.-M. Tseng, A. Hishikawa, E. Shigemasa, M. Nagasono, K. Tono, T. Togashi, H. Ohashi, H. Kimura, Y. Senba, M. Yabashi, and T. Ishikawa, “Multiphoton double ionization of ar in intense extreme ultraviolet laser fields studied by shot-by-shot photoelectron spectroscopy,” *Phys. Rev. Lett.*, vol. 105, p. 133001, Sep 2010.
- [36] A. A. Sorokin, S. V. Bobashev, T. Feigl, K. Tiedtke, H. Wabnitz, and M. Richter, “Photoelectric effect at ultrahigh intensities,” *Phys. Rev. Lett.*, vol. 99, p. 213002, Nov 2007.
- [37] M. G. Makris, P. Lambropoulos, and A. Mihelic, “Theory of multiphoton multielectron ionization of xenon under strong 93-ev radiation,” *Phys. Rev. Lett.*, vol. 102, p. 033002, Jan 2009.
- [38] M. Hentschel, R. Kienberger, C. Spielmann, G. A. Reider, N. Milosevic, T. Brabec, P. Corkum, U. Heinzmann, M. Drescher, and F. Krausz, “Attosecond metrology,” *Nature*, vol. 414, pp. 509–513, Nov 2001.
- [39] R. Kienberger, E. Goulielmakis, M. Uiberacker, A. Baltuska, V. Yakovlev, F. Bammer, A. Scrinzi, T. Westerwalbesloh, U. Kleineberg, U. Heinzmann, M. Drescher,

- and F. Krausz, “Atomic transient recorder,” *Nature*, vol. 427, pp. 817–821, Feb 2004.
- [40] P. B. Corkum and F. Krausz, “Attosecond science,” *Nat Phys*, vol. 3, pp. 381–387, June 2007.
- [41] P. H. Bucksbaum, “The future of attosecond spectroscopy,” *Science*, vol. 317, no. 5839, pp. 766–769, 2007.
- [42] A. Scrinzi, M. Y. Ivanov, R. Kienberger, and D. M. Villeneuve, “Attosecond physics,” *Journal of Physics B: Atomic, Molecular and Optical Physics*, vol. 39, no. 1, p. R1, 2006.
- [43] J. L. Krause, K. J. Schafer, and K. C. Kulander, “High-order harmonic generation from atoms and ions in the high intensity regime,” *Phys. Rev. Lett.*, vol. 68, pp. 3535–3538, Jun 1992.
- [44] P. B. Corkum, “Plasma perspective on strong field multiphoton ionization,” *Phys. Rev. Lett.*, vol. 71, pp. 1994–1997, Sep 1993.
- [45] M. Lewenstein, P. Balcou, M. Y. Ivanov, A. L’Huillier, and P. B. Corkum, “Theory of high-harmonic generation by low-frequency laser fields,” *Phys. Rev. A*, vol. 49, pp. 2117–2132, Mar 1994.
- [46] K. T. Kim, D. M. Villeneuve, and P. B. Corkum, “Manipulating quantum paths for novel attosecond measurement methods,” *Nat Photon*, vol. 8, pp. 187–194, Mar. 2014.
- [47] I. D. Williams, J. McKenna, J. Wood, M. Suresh, W. A. Bryan, S. L. Stebbings, E. M. L. English, C. R. Calvert, B. Srigengan, E. J. Divall, C. J. Hooker, A. J. Langley, and W. R. Newell, “Excited ions in intense femtosecond laser pulses: Laser-induced recombination,” *Phys. Rev. Lett.*, vol. 99, p. 173002, Oct 2007.
- [48] R. López-Martens, K. Varjú, P. Johnsson, J. Mauritsson, Y. Mairesse, P. Salières, M. B. Gaarde, K. J. Schafer, A. Persson, S. Svanberg, C.-G. Wahlström, and A. L’Huillier, “Amplitude and phase control of attosecond light pulses,” *Phys. Rev. Lett.*, vol. 94, p. 033001, Jan 2005.
- [49] A. de Bohan, P. Antoine, D. B. Milošević, and B. Piraux, “Phase-dependent har-

- monic emission with ultrashort laser pulses,” *Phys. Rev. Lett.*, vol. 81, pp. 1837–1840, Aug 1998.
- [50] G. G. Paulus, F. Grasbon, H. Walther, P. Villoryesi, M. Nisoli, S. Stagira, E. Priori, and S. De Silvestri, “Absolute-phase phenomena in photoionization with few-cycle laser pulses,” *Nature*, vol. 414, pp. 182–184, Nov. 2001.
  - [51] A. Baltuska, T. Udem, M. Uiberacker, M. Hentschel, E. Goulielmakis, C. Gohle, R. Holzwarth, V. S. Yakovlev, A. Scrinzi, T. W. Hansch, and F. Krausz, “Attosecond control of electronic processes by intense light fields,” *Nature*, vol. 421, pp. 611–615, Feb. 2003.
  - [52] G. G. Paulus, F. Lindner, H. Walther, A. Baltuška, E. Goulielmakis, M. Lezius, and F. Krausz, “Measurement of the phase of few-cycle laser pulses,” *Phys. Rev. Lett.*, vol. 91, p. 253004, Dec 2003.
  - [53] E. Goulielmakis, M. Schultze, M. Hofstetter, V. S. Yakovlev, J. Gagnon, M. Uiberacker, A. L. Aquila, E. M. Gullikson, D. T. Attwood, R. Kienberger, F. Krausz, and U. Kleineberg, “Single-cycle nonlinear optics,” *Science*, vol. 320, no. 5883, pp. 1614–1617, 2008.
  - [54] M. Y. Shverdin, D. R. Walker, D. D. Yavuz, G. Y. Yin, and S. E. Harris, “Generation of a single-cycle optical pulse,” *Phys. Rev. Lett.*, vol. 94, p. 033904, Jan 2005.
  - [55] G. Sansone, E. Benedetti, F. Calegari, C. Vozzi, L. Avaldi, R. Flammini, L. Poletto, P. Villoryesi, C. Altucci, R. Velotta, S. Stagira, S. De Silvestri, and M. Nisoli, “Isolated single-cycle attosecond pulses,” *Science*, vol. 314, no. 5798, pp. 443–446, 2006.
  - [56] P. M. Paul, E. S. Toma, P. Breger, G. Mullot, F. Augé, P. Balcou, H. G. Muller, and P. Agostini, “Observation of a train of attosecond pulses from high harmonic generation,” *Science*, vol. 292, no. 5522, pp. 1689–1692, 2001.
  - [57] P. Antoine, A. L’Huillier, and M. Lewenstein, “Attosecond pulse trains using high-order harmonics,” *Phys. Rev. Lett.*, vol. 77, pp. 1234–1237, Aug 1996.
  - [58] P. Salières, A. L’Huillier, and M. Lewenstein, “Coherence control of high-order harmonics,” *Phys. Rev. Lett.*, vol. 74, pp. 3776–3779, May 1995.



- 
- [59] M. Lewenstein, P. Salières, and A. L’Huillier, “Phase of the atomic polarization in high-order harmonic generation,” *Phys. Rev. A*, vol. 52, pp. 4747–4754, Dec 1995.
- [60] P. Balcou, P. Salières, A. L’Huillier, and M. Lewenstein, “Generalized phase-matching conditions for high harmonics: The role of field-gradient forces,” *Phys. Rev. A*, vol. 55, pp. 3204–3210, Apr 1997.
- [61] K. Zhao, Q. Zhang, M. Chini, Y. Wu, X. Wang, and Z. Chang, “Tailoring a 67 attosecond pulse through advantageous phase-mismatch,” *Opt. Lett.*, vol. 37, pp. 3891–3893, Sep 2012.
- [62] M. Drescher, M. Hentschel, R. Kienberger, G. Tempea, C. Spielmann, G. A. Reider, P. B. Corkum, and F. Krausz, “X-ray pulses approaching the attosecond frontier,” *Science*, vol. 291, no. 5510, pp. 1923–1927, 2001.
- [63] J. Itatani, F. Quéré, G. L. Yudin, M. Y. Ivanov, F. Krausz, and P. B. Corkum, “Attosecond streak camera,” *Phys. Rev. Lett.*, vol. 88, p. 173903, Apr 2002.
- [64] P. Krehl and S. Engemann, “August toepler - the first who visualized shock waves,” *Shock Waves*, vol. 5, pp. 1–18, 1995.
- [65] M. M. Abraham and J. Lemoine, “Disparition instantanée du phénomène de kerr,” *Compte Rendus*, vol. 129, p. 206, 1899.
- [66] S. R. Leone, C. W. McCurdy, J. Burgdorfer, L. S. Cederbaum, Z. Chang, N. Dudovich, J. Feist, C. H. Greene, M. Ivanov, R. Kienberger, U. Keller, M. F. Kling, Z.-H. Loh, T. Pfeifer, A. N. Pfeiffer, R. Santra, K. Schafer, A. Stolow, U. Thumm, and M. J. J. Vrakking, “What will it take to observe processes in ‘real time’?,” *Nat Photon*, vol. 8, pp. 162–166, Mar. 2014.
- [67] F. Lepine, M. Y. Ivanov, and M. J. J. Vrakking, “Attosecond molecular dynamics: fact or fiction?,” *Nat Photon*, vol. 8, pp. 195–204, Mar. 2014.
- [68] J. C. Baggesen, E. Lindroth, and L. B. Madsen, “Theory of attosecond absorption spectroscopy in krypton,” *Phys. Rev. A*, vol. 85, p. 013415, Jan 2012.
- [69] H. Mashiko, A. Suda, and K. Midorikawa, “Focusing coherent soft-x-ray radiation to a micrometer spot size with an intensity of  $10^{14}$  w/cm<sup>2</sup>,” *Opt. Lett.*, vol. 29, pp. 1927–1929, Aug 2004.

- [70] G. Kolliopoulos, B. Bergues, H. Schröder, P. A. Carpeggiani, L. Veisz, G. D. Tsakiris, D. Charalambidis, and P. Tzallas, “Revealing quantum path details in high-field physics,” *Phys. Rev. A*, vol. 90, p. 013822, Jul 2014.
- [71] A. Zewail, *Femtochemistry Volume I and II*. World Scientific, Singapore, 1994.
- [72] A. Zewail *J. Phys. Chem. A*, vol. 104, p. 5660, 2000.
- [73] R. Berera, R. van Grondelle, and J. T. M. Kennis *Photosynth. Res.*, vol. 101, pp. 101–105, 2009.
- [74] P. Foggi, L. Bussotti, and F. V. R. Neuwahl, “Photophysical and photochemical applications of femtosecond time-resolved transient absorption spectroscopy,” *International Journal of Photoenergy*, pp. 103–109, 2001.
- [75] Z.-H. Loh, M. Khalil, R. Correa, R. Santra, C. Buth, and S. Leone, “Quantum state-resolved probing of strong-field-ionized xenon atoms using femtosecond high-order harmonic transient absorption spectroscopy,” *Physical Review Letters*, vol. 98, p. 143601, Apr. 2007.
- [76] T. Baumert, R. Thalweiser, and G. Gerber, “Femtosecond two-photon ionization spectroscopy of the b state of na<sub>3</sub> clusters,” *Chemical Physics Letters*, vol. 209, no. 1, pp. 29 – 34, 1993.
- [77] A. Assion, M. Geisler, J. Helbing, V. Seyfried, and T. Baumert, “Femtosecond pump-probe photoelectron spectroscopy: Mapping of vibrational wave-packet motion,” *Phys. Rev. A*, vol. 54, pp. R4605–R4608, Dec 1996.
- [78] R. Haight, J. Bokor, J. Stark, R. H. Storz, R. R. Freeman, and P. H. Bucksbaum, “Picosecond time-resolved photoemission study of the inp(110) surface,” *Phys. Rev. Lett.*, vol. 54, pp. 1302–1305, Mar 1985.
- [79] A. Stolow, “Time-resolved photoelectron spectroscopy: Non-adiabatic dynamics in polyatomic molecules,” *International Reviews in Physical Chemistry*, vol. 22, no. 2, pp. 377–405, 2003.
- [80] A. Stolow, A. E. Bragg, and D. M. Neumark, “Femtosecond time-resolved photoelectron spectroscopy,” *Chemical Reviews*, vol. 104, no. 4, pp. 1719–1758, 2004.

- 
- [81] M. Bauer, “Femtosecond ultraviolet photoelectron spectroscopy of ultra-fast surface processes,” *Journal of Physics D: Applied Physics*, vol. 38, no. 16, p. R253, 2005.
- [82] T. Suzuki, “Femtosecond time-resolved photoelectron imaging,” *Annual Review of Physical Chemistry*, vol. 57, no. 1, pp. 555–592, 2006.
- [83] G. Wu, P. Hockett, and A. Stolow, “Time-resolved photoelectron spectroscopy: from wavepackets to observables,” *Phys. Chem. Chem. Phys.*, vol. 13, no. 41, pp. 18447–18467, 2011.
- [84] T. Pfeifer, M. J. Abel, P. M. Nagel, A. Jullien, Z.-H. Loh, M. J. Bell, D. M. Neumark, and S. R. Leone, “Time-resolved spectroscopy of attosecond quantum dynamics,” *Chemical Physics Letters*, vol. 463, no. 1–3, pp. 11 – 24, 2008.
- [85] M. Holler, F. Schapper, L. Gallmann, and U. Keller, “Attosecond electron wave-packet interference observed by transient absorption,” *Phys. Rev. Lett.*, vol. 106, p. 123601, Mar 2011.
- [86] M. Drescher, M. Hentschel, R. Kienberger, M. Uiberacker, V. Yakovlev, A. Scrinzi, T. Westerwalbesloh, U. Kleineberg, U. Heinzmann, and F. Krausz, “Time-resolved atomic inner-shell spectroscopy,” *Nature*, vol. 419, pp. 803–807, Oct. 2002.
- [87] E. Goulielmakis, M. Uiberacker, R. Kienberger, A. Baltuska, V. Yakovlev, A. Scrinzi, T. Westerwalbesloh, U. Kleineberg, U. Heinzmann, M. Drescher, and F. Krausz, “Direct measurement of light waves,” *Science*, vol. 305, no. 5688, pp. 1267–1269, 2004.
- [88] M. Schultze, M. Fieß, N. Karpowicz, J. Gagnon, M. Korbman, M. Hofstetter, S. Neppl, A. L. Cavalieri, Y. Komninos, T. Mercouris, C. A. Nicolaides, R. Pazourek, S. Nagele, J. Feist, J. Burgdörfer, A. M. Azzeer, R. Ernstorfer, R. Kienberger, U. Kleineberg, E. Goulielmakis, F. Krausz, and V. S. Yakovlev, “Delay in photoemission,” *Science*, vol. 328, no. 5986, pp. 1658–1662, 2010.
- [89] M. Uiberacker, T. Uphues, M. Schultze, A. J. Verhoef, V. Yakovlev, M. F. Kling, J. Rauschenberger, N. M. Kabachnik, H. Schroder, M. Lezius, K. L. Kompa, H.-G. Muller, M. J. J. Vrakking, S. Hendel, U. Kleineberg, U. Heinzmann, M. Drescher, and F. Krausz, “Attosecond real-time observation of electron tunnelling in atoms,” *Nature*, vol. 446, pp. 627–632, Apr 2007.

- [90] O. Smirnova, M. Spanner, and M. Y. Ivanov, “Coulomb and polarization effects in laser-assisted xuv ionization,” *Journal of Physics B: Atomic, Molecular and Optical Physics*, vol. 39, no. 13, p. S323, 2006.
- [91] P. Johnsson, J. Mauritsson, T. Remetter, A. L’Huillier, and K. J. Schafer, “Attosecond control of ionization by wave-packet interference,” *Phys. Rev. Lett.*, vol. 99, p. 233001, Dec 2007.
- [92] A. L. Cavalieri, N. Muller, T. Uphues, V. S. Yakovlev, A. Baltuska, B. Horvath, B. Schmidt, L. Blumel, R. Holzwarth, S. Hendel, M. Drescher, U. Kleineberg, P. M. Echenique, R. Kienberger, F. Krausz, and U. Heinzmann, “Attosecond spectroscopy in condensed matter,” *Nature*, vol. 449, pp. 1029–1032, Oct 2007.
- [93] S. Mukamel and D. Abramavicius, “Many-body approaches for simulating coherent nonlinear spectroscopies of electronic and vibrational excitons,” *Chemical Reviews*, vol. 104, no. 4, pp. 2073–2098, 2004.
- [94] W. Pollard, S. Lee, and R. Mathies, “Wave packet theory of dynamic absorption spectra in femtosecond pump–probe experiments,” *The Journal of chemical physics*, vol. 92, p. 4012, 1990.
- [95] M. B. Gaarde, C. Buth, J. L. Tate, and K. J. Schafer, “Transient absorption and reshaping of ultrafast xuv light by laser-dressed helium,” *Phys. Rev. A*, vol. 83, p. 013419, Jan 2011.
- [96] L. Argenti, A. Jiménez-Galán, C. Marante, C. Ott, T. Pfeifer, and F. Martín, “Dressing effects in the attosecond transient absorption spectra of doubly excited states in helium,” *Phys. Rev. A*, vol. 91, p. 061403, Jun 2015.
- [97] R. Santra, V. S. Yakovlev, T. Pfeifer, and Z.-H. Loh, “Theory of attosecond transient absorption spectroscopy of strong-field-generated ions,” *Phys. Rev. A*, vol. 83, p. 033405, Mar 2011.
- [98] M. Lezius, V. Blanchet, D. M. Rayner, D. M. Villeneuve, A. Stolow, and M. Y. Ivanov, “Nonadiabatic multielectron dynamics in strong field molecular ionization,” *Phys. Rev. Lett.*, vol. 86, pp. 51–54, Jan 2001.
- [99] M. A. L. Marques, N. T. Maitra, F. M. S. Nogueira, E. K. U. Gross, and A. Ru-

- bio, eds., *Fundamentals of Time-Dependent Density Functional Theory*, vol. 837 of *Lecture Notes in Physics*. Berlin Heidelberg: Springer, 2012.
- [100] The code can be freely downloaded from <http://www.tddft.org/programs/octopus>.
- [101] M. A. Marques, A. Castro, G. F. Bertsch, and A. Rubio, “octopus: a first-principles tool for excited electron-ion dynamics,” *Computer Physics Communications*, vol. 151, no. 1, pp. 60 – 78, 2003.
- [102] A. Castro, H. Appel, M. Oliveira, C. A. Rozzi, X. Andrade, F. Lorenzen, M. A. L. Marques, E. K. U. Gross, and A. Rubio, “octopus: a tool for the application of time-dependent density functional theory,” *physica status solidi (b)*, vol. 243, no. 11, pp. 2465–2488, 2006.
- [103] X. Andrade, J. Alberdi-Rodriguez, D. A. Strubbe, M. J. T. Oliveira, F. Nogueira, A. Castro, J. Muguerza, A. Arruabarrena, S. G. Louie, A. Aspuru-Guzik, A. Rubio, and M. A. L. Marques, “Time-dependent density-functional theory in massively parallel computer architectures: the octopus project,” *Journal of Physics: Condensed Matter*, vol. 24, no. 23, p. 233202, 2012.
- [104] R. Santra, V. S. Yakovlev, T. Pfeifer, and Z.-H. Loh, “Theory of attosecond transient absorption spectroscopy of strong-field-generated ions,” *Phys. Rev. A*, vol. 83, p. 033405, Mar 2011.
- [105] W.-C. Chu and C. D. Lin, “Photoabsorption of attosecond xuv light pulses by two strongly laser-coupled autoionizing states,” *Phys. Rev. A*, vol. 85, p. 013409, Jan 2012.
- [106] A. D. Dutoi, K. Gokhberg, and L. S. Cederbaum, “Time-resolved pump-probe spectroscopy to follow valence electronic motion in molecules: Theory,” *Phys. Rev. A*, vol. 88, p. 013419, Jul 2013.
- [107] E. Perfetto and G. Stefanucci, “Some exact properties of the nonequilibrium response function for transient photoabsorption,” *Phys. Rev. A*, vol. 91, p. 033416, Mar 2015.
- [108] C. Brif, R. Chakrabarti, and H. Rabitz, “Control of quantum phenomena: past, present and future,” *New Journal of Physics*, vol. 12, p. 075008, July 2010.

- [109] J. Werschnik and E. Gross, “Quantum optimal control theory,” *Journal of Physics B: Atomic, Molecular and Optical Physics*, vol. 40, pp. R175–R211, 2007.
- [110] S. Shi, A. Woody, and H. Rabitz, “Optimal control of selective vibrational excitation in harmonic linear chain molecules,” *The Journal of chemical physics*, vol. 88, no. 11, p. 6870, 1988.
- [111] A. P. Peirce, M. A. Dahleh, and H. Rabitz, “Optimal control of quantum-mechanical systems: Existence, numerical approximation, and applications,” *Phys. Rev. A*, vol. 37, pp. 4950–4964, Jun 1988.
- [112] R. Kosloff, S. A. Rice, P. Gaspard, S. Tersigni, and D. J. Tannor, “Wavepacket dancing: Achieving chemical selectivity by shaping light pulses,” *Chemical Physics*, vol. 139, pp. 201–220, 1989.
- [113] D. G. Luenberger, *Optimization by vector space methods*. New York: John Wiley & Sons, Inc., 1969.
- [114] D. G. Luenberger, *Introduction to Dynamic Systems*. New York: John Wiley & Sons, Inc., 1979.
- [115] P. Brumer and M. Shapiro, “Control of unimolecular reactions using coherent light,” *Chemical Physics Letters*, vol. 126, no. 6, pp. 541 – 546, 1986.
- [116] P. Brumer and M. Shapiro *Faraday Discussions of the Chemical Society*, vol. 82, p. 177, 1986.
- [117] M. Shapiro and P. Brumer, *Principles of the Quantum Control of Molecular Processes*. New York: Wiley, 2003.
- [118] D. J. Tannor and S. A. Rice, “Control of selectivity of chemical reaction via control of wave packet evolution,” *The Journal of Chemical Physics*, vol. 83, no. 10, pp. 5013 – 5018, 1985.
- [119] J. Herek, A. Materny, and A. Zewail, “Femtosecond control of an elementary unimolecular reaction from the transition-state region,” *Chemical Physics Letters*, vol. 228, no. 1-3, pp. 15 – 25, 1994.
- [120] U. Gaubatz, P. Rudecki, M. Becker, S. Schiemann, M. Külz, and K. Bergman,

- “Population switching between vibrational levels in molecular beams,” *Chemical Physics Letters*, vol. 149, no. 5-6, pp. 463 – 468, 1988.
- [121] K. Ohmori, “Wave-packet and coherent control dynamics,” *Annual Review of Physical Chemistry*, vol. 60, no. 1, pp. 487–511, 2009. PMID: 19335221.
- [122] R. S. Judson and H. Rabitz, “Teaching lasers to control molecules,” *Phys. Rev. Lett.*, vol. 68, pp. 1500–1503, Mar 1992.
- [123] C. J. Bardeen, V. V. Yakovlev, K. R. Wilson, S. D. Carpenter, P. M. Weber, and W. S. Warren, “Feedback quantum control of molecular electronic population transfer,” *Chemical Physics Letters*, vol. 280, pp. 151–158, 1997.
- [124] A. Assion, T. Baumert, M. Bergt, T. Brixner, B. Kiefer, V. Seyfried, M. Strehle, and G. Gerber, “Control of chemical reactions by feedback-optimized phase-shaped femtosecond laser pulses,” *Science*, vol. 282, no. 5390, pp. 919–922, 1998.
- [125] J. L. Herek, W. Wohlleben, R. J. Cogdell, D. Zeidler, and M. Motzkus, “Quantum control of energy flow in light harvesting,” *Nature*, vol. 417, pp. 533–535, May 2002.
- [126] V. I. Prokhorenko, A. M. Nagy, S. A. Waschuk, L. S. Brown, R. R. Birge, and R. J. D. Miller, “Coherent control of retinal isomerization in bacteriorhodopsin,” *Science*, vol. 313, no. 5791, pp. 1257–1261, 2006.
- [127] M. F. Kling, C. Siedschlag, A. J. Verhoef, J. I. Khan, M. Schultze, T. Uphues, Y. Ni, M. Uiberacker, M. Drescher, F. Krausz, and M. J. J. Vrakking, “Control of electron localization in molecular dissociation,” *Science*, vol. 312, no. 5771, pp. 246–248, 2006.
- [128] X. Xie, K. Doblhoff-Dier, S. Roither, M. S. Schöffler, D. Kartashov, H. Xu, T. Rathje, G. G. Paulus, A. Baltuška, S. Gräfe, and M. Kitzler, “Attosecond-recollision-controlled selective fragmentation of polyatomic molecules,” *Phys. Rev. Lett.*, vol. 109, p. 243001, Dec 2012.
- [129] G. Cerullo and C. Vozzi, “Viewpoint: Coherent control of chemical reactions on the attosecond time scale,” *Physics*, vol. 5, p. 138, 2012.
- [130] B. J. Sussman, M. Y. Ivanov, and A. Stolow, “Nonperturbative quantum control via the nonresonant dynamic stark effect,” *Phys. Rev. A*, vol. 71, p. 051401, May 2005.

- [131] B. J. Sussman, D. Townsend, M. Y. Ivanov, and A. Stolow, "Dynamic stark control of photochemical processes," *Science*, vol. 314, no. 5797, pp. 278–281, 2006.
- [132] B. J. Sussman, J. G. Underwood, R. Lausten, M. Y. Ivanov, and A. Stolow, "Quantum control via the dynamic stark effect: Application to switched rotational wave packets and molecular axis alignment," *Phys. Rev. A*, vol. 73, p. 053403, May 2006.
- [133] P. J. Bustard, G. Wu, R. Lausten, D. Townsend, I. A. Walmsley, A. Stolow, and B. J. Sussman, "From molecular control to quantum technology with the dynamic stark effect," *Faraday Discuss.*, vol. 153, pp. 321–342, 2011.
- [134] I. R. Sola, J. Gonzalez-Vazquez, R. de Nalda, and L. Banares, "Strong field laser control of photochemistry," *Phys. Chem. Chem. Phys.*, vol. 17, pp. 13183–13200, 2015.
- [135] M. E. Corrales, G. Balerdi, V. Lorient, R. de Nalda, and L. Banares, "Strong field control of predissociation dynamics," *Faraday Discuss.*, vol. 163, pp. 447–460, 2013.
- [136] G. G. Balerdi, M. E. Corrales, G. Gitzinger, J. González-Vázquez, R. Solá, V. Lorient, R. de Nalda, and L. Banares, "Dynamic stark shift of the  $^3r_1$  rydberg state of  $ch_3i$ ," *EPJ Web of Conferences*, vol. 41, p. 02035, 2013.
- [137] C. Sanz-Sanz, G. W. Richings, and G. A. Worth, "Dynamic stark control: model studies based on the photodissociation of  $ibr$ ," *Faraday Discuss.*, vol. 153, pp. 275–291, 2011.
- [138] M. E. Corrales, J. González-Vázquez, G. Balerdi, I. R. Solá, R. de Nalda, and L. Bañares, "Control of ultrafast molecular photodissociation by laser-field-induced potentials," *Nat Chem*, vol. 6, pp. 785–790, Sept. 2014.
- [139] Z.-H. Loh, C. H. Greene, and S. R. Leone, "Femtosecond induced transparency and absorption in the extreme ultraviolet by coherent coupling of the  $he\ 2s2p\ (1po)$  and  $2p2\ (1se)$  double excitation states with 800 nm light," *Chemical Physics*, vol. 350, no. 1-3, pp. 7 – 13, 2008. Femtochemistry and Femtobiology Papers associated with the 8th International Conference on Femtochemistry and Femtobiology.
- [140] H. Wang, M. Chini, S. Chen, C.-H. Zhang, F. He, Y. Cheng, Y. Wu, U. Thumm, and Z. Chang, "Attosecond time-resolved autoionization of argon," *Phys. Rev. Lett.*, vol. 105, p. 143002, Oct 2010.



- 
- [141] S. Gilbertson, M. Chini, X. Feng, S. Khan, Y. Wu, and Z. Chang, “Monitoring and controlling the electron dynamics in helium with isolated attosecond pulses,” *Phys. Rev. Lett.*, vol. 105, p. 263003, Dec 2010.
- [142] H. Geiseler, H. Rottke, N. Zhavoronkov, and W. Sandner, “Real-time observation of interference between atomic one-electron and two-electron excitations,” *Phys. Rev. Lett.*, vol. 108, p. 123601, Mar 2012.
- [143] Z. X. Zhao and C. D. Lin, “Theory of laser-assisted autoionization by attosecond light pulses,” *Phys. Rev. A*, vol. 71, p. 060702, Jun 2005.
- [144] W.-C. Chu, S.-F. Zhao, and C. D. Lin, “Laser-assisted-autoionization dynamics of helium resonances with single attosecond pulses,” *Phys. Rev. A*, vol. 84, p. 033426, Sep 2011.
- [145] J. Zhao and M. Lein, “Probing fano resonances with ultrashort pulses,” *New Journal of Physics*, vol. 14, no. 6, p. 065003, 2012.
- [146] M. Wickenhauser, J. Burgdörfer, F. Krausz, and M. Drescher, “Time resolved fano resonances,” *Phys. Rev. Lett.*, vol. 94, p. 023002, Jan 2005.
- [147] H. Beutler, “über absorptionsserien von argon, krypton und xenon zu termen zwischen den beiden ionisierungsgrenzen  $2p\ 3/2$  und  $2p\ 1/2$ ,” *Z. Phys.*, vol. 93, no. 3-4, pp. 177–196–, 1935.
- [148] U. Fano, “Effects of configuration interaction on intensities and phase shifts,” *Phys. Rev.*, vol. 124, pp. 1866–1878, Dec 1961.
- [149] T. Kampschulte, W. Alt, S. Brakhane, M. Eckstein, R. Reimann, A. Widera, and D. Meschede, “Optical control of the refractive index of a single atom,” *Phys. Rev. Lett.*, vol. 105, p. 153603, Oct 2010.
- [150] S. E. Harris, J. E. Field, and A. Imamoglu, “Nonlinear optical processes using electromagnetically induced transparency,” *Phys. Rev. Lett.*, vol. 64, pp. 1107–1110, Mar 1990.
- [151] M. Fleischhauer, A. Imamoglu, and J. P. Marangos, “Electromagnetically induced transparency: Optics in coherent media,” *Rev. Mod. Phys.*, vol. 77, pp. 633–673, Jul 2005.

- [152] C. D. Lin and W.-C. Chu, “Controlling atomic line shapes,” *Science*, vol. 340, no. 6133, pp. 694–695, 2013.
- [153] A. Castro, J. Werschnik, and E. K. U. Gross, “Controlling the dynamics of many-electron systems from first principles: A combination of optimal control and time-dependent density-functional theory,” *Phys. Rev. Lett.*, vol. 109, p. 153603, Oct 2012.
- [154] M. Hellgren, E. Räsänen, and E. K. U. Gross, “Optimal control of strong-field ionization with time-dependent density-functional theory,” *Phys. Rev. A*, vol. 88, p. 013414, Jul 2013.
- [155] A. Castro, “Theoretical shaping of femtosecond laser pulses for ultrafast molecular photo-dissociation with control techniques based on time-dependent density functional theory,” *ChemPhysChem*, vol. 14, no. 7, pp. 1488–1495, 2013.
- [156] A. Castro and E. K. U. Gross, “Optimal control theory for quantum-classical systems: Ehrenfest molecular dynamics based on time-dependent density-functional theory,” *Journal of Physics A: Mathematical and Theoretical*, vol. 47, no. 2, p. 025204, 2014.
- [157] K. Krieger, J. K. Dewhurst, P. Elliott, S. Sharma, and E. K. U. Gross, “Laser-induced demagnetization at ultrashort time scales: Predictions of tddft,” *Journal of Chemical Theory and Computation*, vol. 0, no. 0, p. null, 0.
- [158] O. B. Malcıoğlu, A. Calzolari, R. Gebauer, D. Varsano, and S. Baroni, “Dielectric and thermal effects on the optical properties of natural dyes: A case study on solvated cyanin,” *Journal of the American Chemical Society*, vol. 133, no. 39, pp. 15425–15433, 2011.
- [159] M. Born and R. Oppenheimer, “Zur quantentheorie der molekeln,” *Annalen der Physik*, vol. 389, pp. 457–484, 1927.
- [160] M. Baer, *Beyond Born-Oppenheimer: Electronic Nonadiabatic Coupling Terms and Conical Intersections*. New York: Wiley, 2006.
- [161] A. Castro and I. V. Tokatly, “Quantum optimal control theory in the linear response formalism,” *Phys. Rev. A*, vol. 84, p. 033410, Sep 2011.

- [162] C. Ullrich, *Time-Dependent Density-Functional Theory: Concepts and Applications*. Oxford University Press, 2012.
- [163] G. Giuliani and G. Vignale, *Quantum Theory of the Electron Liquid*. Cambridge University Press, 2005.
- [164] J. Jensen and A. R. Mackintosh, *Rare Earth Magnetism: Structures and Excitations*. Clarendon Press, 1991.
- [165] J. D. W. Alexander L. Fetter, *Quantum Theory of Many-Particle Systems*. Dover Publications, 2003.
- [166] R. Kubo, “Statistical-mechanical theory of irreversible processes. i. general theory and simple applications to magnetic and conduction problems,” *Journal of the Physical Society of Japan*, vol. 12, no. 6, pp. 570–586, 1957.
- [167] U. Fano, “Sullo spettro di assorbimento dei gas nobili presso il limite dello spettro d’arco,” *Nuovo Cimento*, vol. 12, p. 156, 1935.
- [168] G. Wentzel, “On radiationless quantum jump,” *Z. Phys.*, vol. 43, p. 524, 1927.
- [169] E. Majorana, “Sulla formazione dello ione molecolare di he,” *Nuovo Cimento*, vol. 8, pp. 22–28, 1931.
- [170] E. Majorana, “Teoria dei tripletti p’inclompeti,” *Nuovo Cimento*, vol. 8, pp. 107–113, 1931.
- [171] J. M. Blatt and V. F. Weisskopf, *Theoretical nuclear physics*. Wiley, New York, 1958.
- [172] H. Feshbach, C. E. Porter, and V. F. Weisskopf, “Model for nuclear reactions with neutrons,” *Phys. Rev.*, vol. 96, pp. 448–464, Oct 1954.
- [173] H. Feshbach, “Unified theory of nuclear reactions,” *Annals of Physics*, vol. 5, no. 4, pp. 357 – 390, 1958.
- [174] U. Fano *Citation Classics*, vol. 27, July 4 1977.
- [175] U. Fano, *Atomic Collisions and Spectra*. Elsevier, Amsterdam, 1986.
- [176] A. Vittorini-Orgeas and A. Bianconi, “From majorana theory of atomic autoion-

- ization to feshbach resonances in high temperature superconductors,” *Journal of Superconductivity and Novel Magnetism*, vol. 22, no. 3, pp. 215–221, 2009.
- [177] M. E. Casida, *Time-Dependent Density Functional Response Theory for Molecules*, ch. 5, pp. 155–192. 1995.
- [178] U. De Giovannini, D. Varsano, M. A. L. Marques, H. Appel, E. K. U. Gross, and A. Rubio, “Ab initio angle- and energy-resolved photoelectron spectroscopy with time-dependent density-functional theory,” *Physical Review A*, vol. 85, p. 062515, June 2012.
- [179] K. Capelle, “A bird’s eye view on density functional theory,” *Braz. J. Phys*, vol. 36 (4A), pp. 1318–1343, 2006.
- [180] W. Y. R.G. Parr, *Density-Functional Theory of Atoms and Molecules*. Oxford University Press, 1989.
- [181] R. M. Martin, *Electronic Structure - Basic Theory and Practical Methods*. Cambridge University Press, 2004.
- [182] W. Kohn and L. J. Sham, “Self-consistent equations including exchange and correlation effects,” *Phys. Rev.*, vol. 140, pp. A1133–A1138, Nov 1965.
- [183] N. Helbig, J. I. Fuks, M. Casula, M. J. Verstraete, M. A. L. Marques, I. V. Tokatly, and A. Rubio, “Density functional theory beyond the linear regime: Validating an adiabatic local density approximation,” *Phys. Rev. A*, vol. 83, p. 032503, Mar 2011.
- [184] P. Hohenberg and W. Kohn, “Inhomogeneous electron gas,” *Phys. Rev.*, vol. 136, pp. B864–B871, Nov 1964.
- [185] N. Helbig, I. V. Tokatly, and A. Rubio, “Exact kohn-sham potential of strongly correlated finite systems,” *JOURNAL OF CHEMICAL PHYSICS*, vol. 131, DEC 14 2009.
- [186] P. A. M. Dirac, “Note on exchange phenomena in the thomas atom,” *Mathematical Proceedings of the Cambridge Philosophical Society*, vol. 26, pp. 376–385, 7 1930.
- [187] J. P. Perdew and Y. Wang, “Accurate and simple analytic representation of the electron-gas correlation energy,” *Phys. Rev. B*, vol. 45, pp. 13244–13249, Jun 1992.

- [188] J. P. Perdew and A. Zunger, “Self-interaction correction to density-functional approximations for many-electron systems,” *Phys. Rev. B*, vol. 23, pp. 5048–5079, May 1981.
- [189] J. B. Krieger, Y. Li, and G. J. Iafrate, “Construction and application of an accurate local spin-polarized kohn-sham potential with integer discontinuity: Exchange-only theory,” *Phys. Rev. A*, vol. 45, pp. 101–126, Jan 1992.
- [190] C. Legrand, E. Suraud, and P.-G. Reinhard, “Comparison of self-interaction-corrections for metal clusters,” *Journal of Physics B: Atomic, Molecular and Optical Physics*, vol. 35, no. 4, p. 1115, 2002.
- [191] R. van Leeuwen and E. J. Baerends, “Exchange-correlation potential with correct asymptotic behavior,” *Phys. Rev. A*, vol. 49, pp. 2421–2431, Apr 1994.
- [192] A. D. Becke and E. R. Johnson, “A simple effective potential for exchange,” *The Journal of Chemical Physics*, vol. 124, no. 22, pp. –, 2006.
- [193] A. Karolewski, R. Armiento, and S. Kümmel, “Electronic excitations and the becke-johnson potential: The need for and the problem of transforming model potentials to functional derivatives,” *Phys. Rev. A*, vol. 88, p. 052519, Nov 2013.
- [194] C. A. Ullrich, U. J. Gossmann, and E. K. U. Gross, “Time-dependent optimized effective potential,” *Phys. Rev. Lett.*, vol. 74, pp. 872–875, Feb 1995.
- [195] C. Ullrich, U. J. Gossmann, E. K. U. Gross, and B. Bunsenges *Phys. Chem.*, vol. 99, p. 488, 1995.
- [196] M. Mundt and S. Kümmel, “Optimized effective potential in real time: Problems and prospects in time-dependent density-functional theory,” *Phys. Rev. A*, vol. 74, p. 022511, Aug 2006.
- [197] M. Mundt, S. Kümmel, R. van Leeuwen, and P.-G. Reinhard, “Violation of the zero-force theorem in the time-dependent krieger-li-iafrate approximation,” *Phys. Rev. A*, vol. 75, p. 050501, May 2007.
- [198] N. Troullier and J. L. Martins, “Efficient pseudopotentials for plane-wave calculations,” *Phys. Rev. B*, vol. 43, pp. 1993–2006, Jan 1991.

- [199] W. Kohn, “Nobel lecture: Electronic structure of matter—wave functions and density functionals,” *Rev. Mod. Phys.*, vol. 71, pp. 1253–1266, Oct 1999.
- [200] E. Runge and E. Gross, “Density-functional theory for time-dependent systems,” *Physical Review Letters*, vol. 52, no. 12, pp. 997–1000, 1984.
- [201] R. Baer, L. Kronik, and S. Kümmel, eds., *Open problems and new solutions in time dependent density functional theory*, vol. 391 of *Chemical Physics*. Elsevier, Nov. 2011.
- [202] J. D. Ramsden and R. W. Godby, “Exact density-functional potentials for time-dependent quasiparticles,” *Phys. Rev. Lett.*, vol. 109, p. 036402, Jul 2012.
- [203] M. J. P. Hodgson, J. D. Ramsden, J. B. J. Chapman, P. Lillystone, and R. W. Godby, “Exact time-dependent density-functional potentials for strongly correlated tunneling electrons,” *Phys. Rev. B*, vol. 88, p. 241102, Dec 2013.
- [204] L. Mancini, J. D. Ramsden, M. J. P. Hodgson, and R. W. Godby, “Adiabatic and local approximations for the kohn-sham potential in time-dependent hubbard chains,” *Phys. Rev. B*, vol. 89, p. 195114, May 2014.
- [205] K. Luo, J. I. Fuks, E. D. Sandoval, P. Elliott, and N. T. Maitra, “Kinetic and interaction components of the exact time-dependent correlation potential,” *The Journal of Chemical Physics*, vol. 140, no. 18, pp. –, 2014.
- [206] J. I. Fuks, K. Luo, E. D. Sandoval, and N. T. Maitra, “Time-resolved spectroscopy in time-dependent density functional theory: An exact condition,” *Phys. Rev. Lett.*, vol. 114, p. 183002, May 2015.
- [207] K. Yabana and G. F. Bertsch, “Time-dependent local-density approximation in real time,” *Phys. Rev. B*, vol. 54, pp. 4484–4487, Aug 1996.
- [208] S. Chelkowski, C. Foisy, and A. Bandrauk, “Electron-nuclear dynamics of multi-photon  $H_2^+$  dissociative ionization in intense laser fields,” *Physical Review A*, vol. 57, pp. 1176–1185, Feb. 1998.
- [209] R. Loudon, “One-dimensional hydrogen atom,” *American Journal of Physics*, vol. 27, no. 9, pp. 649–655, 1959.
- [210] N. Helbig, J. Fuks, I. Tokatly, H. Appel, E. Gross, and A. Rubio, “Time-dependent

- density-functional and reduced density-matrix methods for few electrons: Exact versus adiabatic approximations,” *Chemical Physics*, vol. 391, no. 1, pp. 1 – 10, 2011. Open problems and new solutions in time dependent density functional theory.
- [211] D. J. Tannor, *Introduction to Quantum Mechanics: A Time-Dependent Perspective*. University Science Books, 2007.
- [212] L. Allen and J. H. Eberly, *Optical Resonance and Two-level Atoms*. Wiley, 1975.
- [213] R. Kosloff, S. Rice, P. Gaspard, S. Tersigni, and D. Tannor, “Wavepacket dancing: Achieving chemical selectivity by shaping light pulses,” *Chemical Physics*, vol. 139, no. 1, pp. 201 – 220, 1989.
- [214] Y. Ohtsuki, G. Turinici, and H. Rabitz, “Generalized monotonically convergent algorithms for solving quantum optimal control problems,” *The Journal of Chemical Physics*, vol. 120, no. 12, pp. 5509–5517, 2004.
- [215] I. Serban, J. Werschnik, and E. K. U. Gross, “Optimal control of time-dependent targets,” *Phys. Rev. A*, vol. 71, p. 053810, May 2005.
- [216] R. Fletcher, *Practical Methods of Optimization*. Wiley, New York, 2001.
- [217] J. Somló, V. A. Kazakov, and D. J. Tannor, “Controlled dissociation of  $\text{I}_2$  via optical transitions between the x and b electronic states,” *Chemical Physics*, vol. 172, no. 1, pp. 85 – 98, 1993.
- [218] W. Zhu, J. Botina, and H. Rabitz, “Rapidly convergent iteration methods for quantum optimal control of population,” *The Journal of Chemical Physics*, vol. 108, no. 5, pp. 1953–1963, 1998.
- [219] W. Zhu and H. Rabitz, “A rapid monotonically convergent iteration algorithm for quantum optimal control over the expectation value of a positive definite operator,” *The Journal of Chemical Physics*, vol. 109, no. 2, pp. 385–391, 1998.
- [220] D. E. Goldberg, *Genetic algorithms in Search, Optimization, and Machine Learning*. Addison Wesley, Reading, 1993.
- [221] H.-P. Schwefel, *Evolution and Optimum Seeking*. Wiley, New York, 1995.

- [222] J. A. Nelder and R. Mead, “A simplex method for function minimization,” *The Computer Journal*, vol. 7, no. 4, pp. 308–313, 1965.
- [223] M. Powell, *Large Scale Nonlinear Optimization*. Springer, New York, 2004.
- [224] S. Chelkowski and A. D. Bandrauk, “Asymmetries in strong-field photoionization by few-cycle laser pulses: Kinetic-energy spectra and semiclassical explanation of the asymmetries of fast and slow electrons,” *Phys. Rev. A*, vol. 71, p. 053815, May 2005.
- [225] T. Young, “The bakerian lecture: On the theory of light and colours,” *Philosophical Transactions of the Royal Society of London*, vol. 92, pp. 12–48, 1802.
- [226] G. Svaetichin, W. Krattenmacher, and M. Laufer, “Photostimulation of single cones,” *The Journal of General Physiology*, vol. 43, pp. 101–114, July 1960.
- [227] In the first pump probe experiment performed by A. Toepler [P. Krehl and S. Engemann, *Shock Waves* **5**, 1 (1995)], already in the 19th century, the probe was in fact used to photograph the sound waves initiated by the pump.
- [228] J. Alonso, X. Andrade, P. Echenique, F. Falceto, D. Prada-Gracia, and A. Rubio, “Efficient formalism for large-scale ab initio molecular dynamics based on time-dependent density functional theory,” *Physical Review Letters*, vol. 101, p. 096403, Aug. 2008.
- [229] S. Kümmel and J. Perdew, “Optimized effective potential made simple: Orbital functionals, orbital shifts, and the exact kohn-sham exchange potential,” *Physical Review B*, vol. 68, July 2003.
- [230] M. Casula, S. Sorella, and G. Senatore, “Ground state properties of the one-dimensional coulomb gas using the lattice regularized diffusion monte carlo method,” *Physical Review B*, vol. 74, p. 245427, Dec. 2006.
- [231] J. I. Fuks, N. Helbig, I. V. Tokatly, and A. Rubio, “Nonlinear phenomena in time-dependent density-functional theory: What rabi oscillations can teach us,” *Phys. Rev. B*, vol. 84, p. 075107, Aug 2011.
- [232] J. F. Janak, “Proof that  $\frac{\partial \epsilon}{\partial n_i} = \epsilon$  in density-functional theory,” *Phys. Rev. B*, vol. 18, pp. 7165–7168, Dec 1978.



- [233] O. Fojón, A. Palacios, J. Fernández, R. Rivarola, and F. Martín, “Interferences in the photoelectron spectrum of  $\text{h}^+ + 2$  molecules at high energy,” *Physics Letters A*, vol. 350, no. 5-6, pp. 371–374, 2006.
- [234] P. Puschnig, S. Berkebile, A. J. Fleming, G. Koller, K. Emtsev, T. Seyller, J. D. Riley, C. Ambrosch-Draxl, F. P. Netzer, and M. G. Ramsey, “Reconstruction of molecular orbital densities from photoemission data,” *Science*, vol. 326, pp. 702–706, Oct. 2009.
- [235] J. Walkenhorst, U. De Giovannini, A. Castro, and A. Rubio, “Tailored pump & probe transient spectroscopy with time-dependent density-functional theory: Controlling absorption spectra,” *to be submitted*.
- [236] M. Ruggenthaler and D. Bauer, “Rabi oscillations and few-level approximations in time-dependent density functional theory,” *Phys. Rev. Lett.*, vol. 102, p. 233001, Jun 2009.
- [237] S. Raghunathan and M. Nest, “Critical examination of explicitly time-dependent density functional theory for coherent control of dipole switching,” *Journal of Chemical Theory and Computation*, vol. 7, no. 8, pp. 2492–2497, 2011. PMID: 26606623.
- [238] S. Raghunathan and M. Nest, “The lack of resonance problem in coherent control with real-time time-dependent density functional theory,” *Journal of Chemical Theory and Computation*, vol. 8, no. 3, pp. 806–809, 2012. PMID: 26593342.
- [239] M. Goerz, K. Whaley, and C. Koch, “Hybrid optimization schemes for quantum control,” *EPJ Quantum Technol.*, vol. 2, p. 21, 2015.
- [240] C. Herring, “Critique of the heitler-london method of calculating spin couplings at large distances,” *Rev. Mod. Phys.*, vol. 34, pp. 631–645, Oct 1962.
- [241] G. Rastelli, “Semiclassical formula for quantum tunneling in asymmetric double-well potentials,” *Phys. Rev. A*, vol. 86, p. 012106, Jul 2012.